Aix-Marseille Université

Ecole doctorale 353 - Sciences pour l'Ingénieur : Mécanique, Physique, Micro et Nanoélectronique

Laboratoire d'accueil: IRSTEA Aix-En-Provence, UR RECOVER

Thèse présentée pour obtenir le grade universitaire de docteur de l'université d'Aix-Marseille

Spécialité: Mécanique et Physiques des Fluides

par

Zeyd BENSEGHIER

Etude numérique de l'érosion d'un matériau granulaire cohésif par un écoulement fluide

Numerical modeling of fluid flow erosion of a cohesive granular material

---

Soutenue le 04/12/2019 devant le jury composé de:

M. Luc SIBILLE	MCF, Univ Grenoble Alpes	Rapporteur
M. Patrick RICHARD	DR, IFSTTAR Nantes	Rapporteur, Président
Mme. Pascale AUSSILLOUS	MCF, AMU	Examinateur
M. Franck LOMINÉ	MCF, INSA Rennes	Examinateur
M. Pierre PHILIPPE	DR, IRSTEA Aix-en-provence	Directeur de thèse
M. Stéphane BONELLI	DR, IRSTEA Aix-en-provence	Co-directeur de thèse

Acknowledgements

For almost four years, during my thesis work and previously my six months of internship, I had the great privilege of working in a warm environment at IRSTEA, RECOVER research unit, Aix-En-Provence under the direction of Pierre PHILIPPE. I am deeply grateful to him for his research methodology, scientific knowledge, and his help in writing this thesis in a clear and well-reasoned manner. I would also like to thank him for his friendship and for giving me the opportunity and freedom to explore alternative pathways by my own. Thanks also to my co-supervisor Stéphane BONELLI for his insightful suggestions and guidance and his expertise in the geomechanical field.

Let me thank the jury members: Luc SIBILLE, Patrick RICHARD, Pascale AUSSILLOUS, and Franck LOMINÉ for accepting evaluating my work and for their constructive questions and suggestions during my defense.

Besides, I would like to thank the members of my thesis committee: Franck LOMINÉ, Jérome DURIEZ, Jean-Yves DELENNE, and Pablo CUÉLLAR for fruitful discussions. I also acknowledge valuable exchanges with Denis CHAUSSEE (Suez Consulting Corp).

I am especially indebted to Li-Hua LUU for her permanent support, especially, during my defense preparation.

Special thanks go to Pablo CUÉLLAR for his motivation, encouragement, and insightful suggestions. I am also grateful to him and Matthias BAEßLER for offering me the opportunity to work for two months at BAM, Berlin. Also, I would like to thank his brother Vicente CUÉLLAR for his valuable support and expertise in CUDA.

My thanks go to all the people who have supported me to complete this research work directly or indirectly especially friends, other PhD students, researchers, IT, and administrative department colleagues at IRSTEA, Aix-En-Provence.

I am grateful for the financial support provided by "Région Sud, Provence-Alpes-Côte d'Azur". Thanks also to the DAAD organization for a short-term exchange scholarship at BAM, Berlin.

Finally, yet importantly, I would like to express my indebtedness to my parents, my two sisters, and all my family who have given me constant support and love during the completion of the thesis and throughout my whole life.

Zeyd BENSEGHIER, December 2019, Aix-En-Provence

Contents

List of Figures

List of Tables

Abstract

Hydraulic earthworks (e.g. earth-dams, levees and dikes), constructed for both protection against floods and water retention, are subject to the risk of hydraulic failures. The latter are predominantly triggered by erosion as reported in the literature. Accordingly, several erosion tests have emerged to quantify soil's erodibility, such as Jet Erosion Test (JET), Hole Erosion Test (HET), and Erosion Function Apparatus (EFA). However, these tests are based on not sufficiently reliable interpretation models, which require strong assumptions and may, in particular, give different estimations of erodibility for a same soil. Despite several experimental investigations that have been conducted on the subject, there is still a lack of understanding of the erosion mechanisms taking place at the grain level.

From this assessment, the present work aims to study numerically the erosion phenomena at the grain scale, for two different fluid flow configurations both in laminar regime. To this end, the Lattice Boltzmann Method (LBM) is used for the fluid phase and the Discrete Element Method (DEM) for the solid phase, with the addition of a cohesion rheology at grain bonding, including a time-dependent damage model. Taking advantage of GPUs highly parallel compute capabilities, the first task is to improve significantly the computational speed and the efficiency of the code.

Next, we focus on quantifying the threshold conditions for erosion onset for both cohesive and cohesion-less granular samples. In this respect, impinging jet flow, similar to JET, is first chosen as case study. After a preliminary analysis of impinging jet hydrodynamics, we then focus on erosion conditions. The relevance of the classical Shields criterion for cohesion-less samples is recovered while a generalization of this Shields criterion is proposed for weakly cohesive soils with good agreement. Lastly, an adaptation of the classical JET interpretation model is proposed for our 2D laminar situation and the erodibility parameters thus obtained for our cohesive samples are quantified and critically discussed for various inter-particle cohesive bond strength and hydrodynamic conditions.

Finally, a simpler shear-driven fluid flow (i.e. Couette flow) is alternatively studied, enabling to impose a constant shear-stress along the entire upper surface of a sample and therefore to derive more straightforwardly the erosion rate of the cohesive material. A power law function is found to be best suited than the usual linear relation to account for the erosion law at sample scale. A parametric study is then performed, by varying both the inter particles cohesion strength and the particle size, to investigate the link between erodibility obtained at sample scale and input parameters of the micromechanical model.

Keywords: LBM, DEM, erosion, cohesive soil, granular material, impinging jet flow, GPU, numerical modelling.

Résumé

Les ouvrages hydrauliques (digues, barrages, levées, etc.), utilisés pour des fonctions de protection contre les inondations ou de rétention d'eau, sont soumis au risque de rupture par ouverture de brèche. Des analyses statistiques ont montré que ces ruptures étaient déclenchées de façon prépondérante par l'érosion hydraulique des sols constitutifs de ces ouvrages. Plusieurs essais d'érosion ont ainsi été mis au point pour quantifier l'érodabilité des sols, tels que l'essai d'érosion par jet (JET), l'essai d'érosion de conduit (HET) ou encore l'essai d'érosion tangentielle (EFA). Cependant, ces tests reposent sur des modèles d'interprétation qui, du fait d'hypothèses réductrices, restent relativement peu fiables et peuvent, par exemple, amener à des estimations de l'érodabilité notablement différentes pour un même sol. Malgré plusieurs études expérimentales menées sur le sujet, les mécanismes d'érosion à l'échelle des grains restent encore mal compris.

Fort de ce constat, le travail réalisé au cours de cette thèse vise à analyser du point de vue numérique le processus d'érosion de surface à l'échelle du grain, en étudiant deux configurations différentes d'écoulement fluide en régime laminaire. A cette fin, la méthode LBM (Lattice Boltzmann Method) est utilisée pour décrire la phase fluide et la méthode DEM (Discrete Element Method) pour la phase solide, avec l'ajout d'une rhéologie de cohésion au niveau des contacts entre grains, incluant également un modèle d'endommagement dépendant du temps. La première tâche présentée ici consiste à tirer parti des capacités de calcul parallèle sur GPU pour améliorer de manière très significative la vitesse de calcul et l'efficacité d'un code existant.

Le travail s'attache ensuite à la quantification des conditions hydrodynamiques au seuil d'érosion pour des matériaux granulaire, sans ou avec cohésion. Après une analyse préalable de l'écoulement 2D d'un jet impactant laminaire permettant de caractériser au mieux ce type d'écoulement, le seuil d'érosion a été étudié de façon systématique. La pertinence du critère classique de Shields pour les échantillons sans cohésion est confirmée, tandis qu'une généralisation de ce critère est proposée pour les sols faiblement cohésifs avec un accord très satisfaisant. Enfin, le modèle d'interprétation classique de l'essai JET est adapté à notre géométrie 2D et au régime laminaire. Les paramètres d'érodabilité ainsi obtenus pour nos échantillons cohésifs sont analysés en fonction du degré de cohésion et des conditions hydrodynamiques, puis discutés de façon critique.

Enfin, la dernière partie de ce travail explore une configuration hydrodynamique plus simple, celle d'un écoulement tangentiel cisaillant, de type Couette laminaire, qui permet d'imposer une contrainte de cisaillement constante sur toute la surface supérieure d'un échantillon. Le taux d'érosion du matériau cohésif est ainsi mesuré directement à l'échelle macroscopique puis analysé en fonction de la contrainte appliquée. Les lois d'érosion ainsi obtenues apparaissent mieux décrites par une loi de puissance que par la relation linéaire classiquement utilisée. Une étude paramétrique est finalement menée, en faisant varier à la fois la force de cohésion entre particules et la taille de celles-ci, afin d'examiner le lien entre érodabilité d'un échantillon de sol et paramètres d'entrée du modèle micromécanique.

Mots clés: LBM, DEM, érosion, sol cohésif, matériau granulaire, écoulement de jet impactant, GPU, simulation numérique.

Introduction

The actual Global Warming obviously induces a rapid climate change with dramatic consequences such as an intensification of natural disasters, massive ocean and sea rises, increasingly heavy and frequent precipitation events, and subsequent potentially catastrophic floods. Among others, a clearly identified risk concerns the destruction of earthen hydraulic structures (e.g. earth embankment dams, levees, and dikes), which play an essential role in protection against floods or water reservation. The main phenomenon underlying the breakage of such structures is erosion, which is estimated to be responsible for about 95 % of failure cases, causing major economic and social costs worldwide. Recent French examples of disastrous erosional events induced by floods are the failure of several dikes of the Gard river (South-East of France) in September 2002, which cost around a billion euros and claimed the lives of five people. From an international perspective, the spectacular failures of coastal levees in New-Orleans (USA) following the Katrina hurricane in 2005 will be remembered for long. Katrina has killed more than 1,000 people with total damage cost around 100 billion dollars. There is consequently a growing social demand for improving safety management of existing structures and constructing more durable and resistant structures in the future.

However, such erosion induced failures of hydraulic infrastructures is a far complex instability issue which has engendered a number of studies for many years but still claims for a better understanding of both the elementary processes involved at small scale and their progressive combination until global failure at large scale. Many researches are being conducted for studying soil erosion, in particular to identify parameters that trigger erosion or, rather the opposite, inhibiting factors. To this end, several erosion tests have been developed along with their interpretation models. The most common ones are the Jet Erosion Test (JET), the Hole Erosion Test (HET), and the Erosion Function Apparatus (EFA). The main purpose of these tests is to quantify the so-called erodibility of soils, which is basically given by two parameters (an erosion coefficient and a critical shear stress). In practice, both quantities are derived by fitting the experimental data based on a postulated linear surface erosion law that links the soil's erosion rate to the excess fluid shear stress. The slope gives the erosion coefficient while the intercept is the critical shear stress.

The practical utility of soil erodibility can be understood as follows: the erosion coefficient rules the kinetics and consequently allows quantifying the remaining time to failure in times of crisis emergency; the critical shear stress predicts the threshold

at which erosion starts and can be used as a determining factor in construction or remediation of a structure.

Nonetheless, there is still a scientific debate whether the two parameters are intrinsic to the soil or not. This postulate is indeed questionable since different erosion devices usually give different estimations for the erodibility of a same soil. A first possible explanation for this lies in the interpretation models which are often rather crude and over-simplified by a set of assumptions and empirical correlations used to circumvent the difficulty of measuring the local flow parameters. The relevance of the postulated erosion law, namely the linear excess shear-stress, may also be brought into question.

On the other hand, computational fluid dynamic (CFD) models have considerably gained in accuracy and give now access to most of the local flow parameters that are hardly measurable in the experiments, either in small or large-scale engineering applications. Such methods can consistently model erosion of soils, the latter needing for its part a proper modeling. At the scale of an hydraulic structure, the FEM (Finite Element Method) is most commonly used but requires to define in advance erodibility coefficients for the soil through a postulated erosion law or empirical solid transport formulas. Alternatively, accurate numerical methods have been developed during the last years to account at a much smaller scale for mutual interactions between a fluid flow and a population of solid particles, either static or in motion. Thus, efficient simulations are nowadays capable of modeling complex fluid-grains situations for a representative elementary volume (REV) of granular material, by considering the soil as a set of discrete particles and taking into consideration a continuum fluid model (e.g. CFD). This approach is obviously more relevant for studying soil's erosion since no premise on erodibility coefficients nor erosion law is assumed *a priori*. This is clearly the main motivation for the present study.

Hence, this thesis deals with the numerical modeling of the erosion of cohesive granular soils induced by an incompressible fluid flow described by the Lattice Boltzmann Method (LBM) at low to moderate Reynolds numbers (i.e. laminar flow regime). The soil is described locally, at the micro-scale, as set of discrete particles and thus modeled by the Discrete Element Method (DEM), including an inter-granular cohesion and a time-dependent sub-critical damage models. The main purpose of this work is to conduct relevant numerical simulations, building on and improving the numerical tools previously developed by J. Ngoma (2011-2014) during his Ph.D. thesis and P. Cuéllar (2014-2015) during his Post-doc. The present simulations are restricted to two practical cases: impinging jet erosion and shear-driven (or Couette) erosion.

The scientific problems under question here are: to prove the accuracy and the validity of our numerical modeling to simulate fluid flow erosion in a realistic way; to test the relevance of several empirical erosion laws; to find a link between micro parameters (e.g. the cohesive bond strength, particle diameter) and macro parameters (e.g. the erosion rate coefficient and the critical fluid shear stress) through a parametric study. This work is divided into four chapters and organized as follows:

The first chapter presents a state of the art as regards soil erosion. It consists first of a description of the general context underlying this study (i.e. erosion phenomena

in hydraulic earthworks). Secondly, a brief review is proposed about several theoretical and experimental aspects of erosion of both granular and cohesive materials (i.e hydrodynamics, onset of surface erosion, erosion test devices and their interpretation models). Finally, some numerical methods from the literature are presented for modeling soil erosion induced by a fluid flow.

We propose in the second chapter a detailed description of the numerical methods that will be used in this study, namely the Lattice Boltzmann Method (LBM) and the Discrete Element Method (DEM), along with the coupling technique between both methods. Next, the GPU parallelization technique, as well as the validation of the LBM/DEM coupling, is presented.

In chapter 3, the previous numerical tools are applied in the context of soil erosion by an impinging jet. Two-dimensional laminar free jet is first simulated and validated against the free jet theory. Then, from jet impingement on a smooth wall and a fixed granular surface, we derive an empirical formula that correlates the fluid shear stress at the impingement surface to the free jet self-similar model for laminar regime in two-dimensional configuration. The second part of the chapter is dedicated to a parametric study of impinging jet erosion, successively for cohesion-less and cohesive soils, with a special focus on the erosion onset (erosion threshold) for both cases. The results are plotted in the Shields diagram and favorably compared to previous experimental results. For the case of cohesive soil, the erosion threshold is found to be well described by an extension of the classical Shields criterion used for cohesion-less materials to moderately cohesive soils. Furthermore, the subsequent scouring process is investigated using image processing techniques, and we provide a 2D analysis of the evolution of the scour depth (erosion rate) versus the fluid shear stress at the upper bed surface. Then the mathematical model of the Jet Erosion Test (JET) is adapted to our two-dimensional geometry and allows implicitly deriving at the macro scale the erodibility parameters of soils (i.e. erosion coefficient and critical shear stress) for different micro cohesion strengths.

The last chapter (Chapter 4) presents a study of an alternative erosion test which consists of applying a shear-driven (or Couette) fluid flow at the upper surface of a cohesive granular sample. Since the fluid shear stress is kept approximately constant, the erodibility of the cohesive material is easily derived without the need for an interpretation model. The additional use of the time-dependent damage model allows extending the results to lower fluid shear stress values. Also, we found that a power erosion law fits well our numerical data, still using the excess shear-stress quantity. A parametric study is performed by varying the inter-particles cohesion and the particle size to investigate the relationship between the erosion parameters and the cohesive contact laws.

Finally, we close this work with a general conclusion and provide some perspectives for future research.

Chapter 1

State of the art

Contents

1.1 Introduction

The aim of this chapter is first to describe the general context of this thesis, whose topic deals with erosion phenomena, more specifically applied to hydraulic earthworks, and, second, to introduce the major factors responsible for erosion of either cohesion-less or cohesive soils. Then, we compile a summary of the main devices used to quantify soil's resistance to erosion (e.g. JET, HET, EFA), including their interpretation models, with a specific focus on impinging jet hydrodynamics. The last section is finally dedicated to a review of some numerical methods previously developed in the literature for modeling the coupling between fluid flow and grains, which is at the heart of erosion of cohesive soils. A more detailed insight is proposed for the methods that will be implemented in this study, namely Lattice Boltzmann Method (LBM) and Discrete Element Method (DEM).

1.2 Erosion of hydraulic earthworks

Erosion, either internal or external, is far ahead the main cause of breakage for earthen hydraulic structures (e.g. dikes and dams). Statistically speaking, it contributes to 90 to 95 % of failure cases reported worldwide after (Foster et al., 2000). For illustrative purpose, Figure 1.1 shows two recent failures of hydraulic structures caused by erosion. As regards France, which accounts for more than 700 large dams, ten thousand small dams (i.e. with height less than 15 m), nearly 8,000 km of dikes for navigation channels, and 10,000 km of protective levees, erosion is usually responsible for an average of one dam and one dike breakage annually, most of these ruptures occurring during floods. The damage costs are estimated to more than 100 million euros per year.

Fig. 1.1. Failure of the Algodões dam (Piau, Brazil, 2009) (left) ; Failure of the Lianfeng dam (Urumqi, China, 2013) (right).

After Foster et al. (2000), the erosion mechanisms likely to trigger earthen hydraulic structure failures can be classified into two distinct categories: internal erosion and external erosion. External erosion refers to hydrodynamic stresses at the outer surface of the structure, usually due to an overflow (see Fig. 1.2a). If the

soil's sub-layer is not resistant enough to erosion, the overflow may cause substantial degradation, possibly leading to the creation of a breach, and, eventually, to the rupture of the structure. This type of erosion represents approximately 50 % of reported earth dam failures Foster et al. (2000).

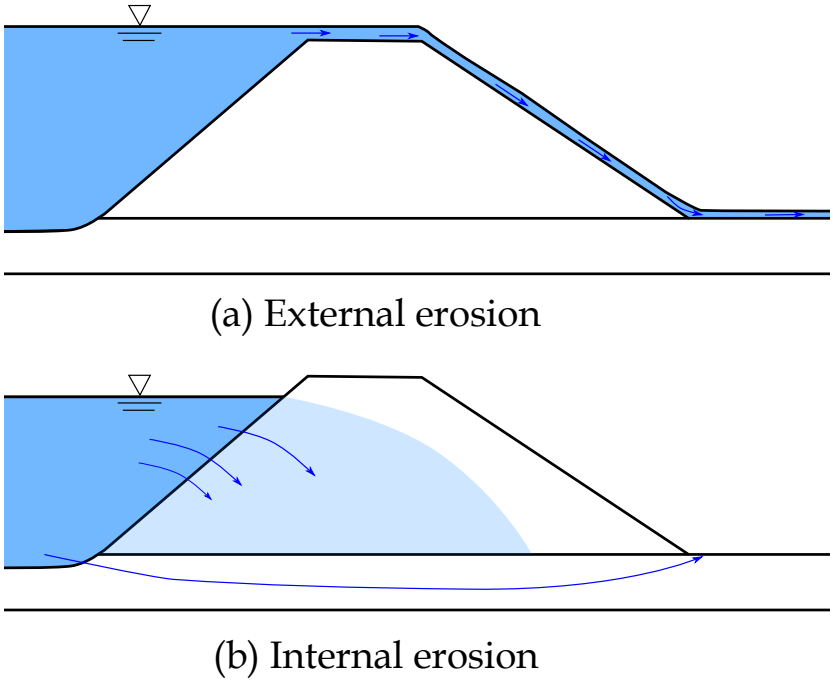

Fig. 1.2. Two types of erosion: (a) External erosion ; (b) Internal erosion.

Even though there is no overflow, almost the same proportion of failures, around 45 %, are due to internal erosion, a general term that includes all erosional processes occurring inside the earthen embankment. Internal erosion is a generally much more slower and far less apparent phenomenon, initiated by the water infiltration through the structure or its foundations (see Fig. 1.2b). Four different initiation mechanisms of internal erosion are reported (Fell and Fry, 2007), as summarized in Fig. 1.3: concentrated leak erosion, backward erosion, contact erosion, and suffusion. Concentrated leak erosion may occur when there already exists a preferential path for the flow through the structure. Such a pre-existing path can be caused for instance by differential settlement, hydraulic fracture in clayey core walls, or desiccation in voids adjacent to a concrete wall or conduits, as well as the presence of transverse pipe, roots or animal burrows (Zhang et al., 2016). Backward erosion is first initiated at the toe of the structure, where a seepage flow exits the foundations, either by an uplift or a sand boil (i.e. granular soil fluidization) depending on the nature (i.e. cohesive versus granular) of the soil's sub-layer. Once formed, such a cavity expands backwards from downstream to upstream, in the opposite direction to the flow. Contact erosion is a selective erosion of fine particles, at the interface between two layers of different soil types and grain size, driven by a seepage flow through the coarser layer. Suffusion is also a selective erosion of fine particles, which get transported by the flow through the pores that pre-exist between the coarser particles.

Note that these four initiation mechanisms, with initially relatively slow kinetics (i.e. evolution over years), may progressively accelerate and, in combination with others processes (settlement, sinkhole, collapse, etc.), lead ultimately to the failure of the structure by a piping flow passing through the entire structure. This phenomenon, called piping erosion, usually corresponds to the final stage of an embankment dam failure for which the remaining time before rupture can be counted in hours rather than days (Bonelli and Benahmed, 2011).

Furthermore, piping erosion can be regarded locally as surface erosion and is consequently comparable to external erosion even if the flow conditions are different, namely open-channel versus closed-conduit flow. Thus the same surface erosion laws can be applied in both cases. Moreover, many other internal mechanisms as concentrated leak erosion, backward erosion, and contact erosion give rise to similar situations where, at small scale, a soil is stressed by a superficial flow.

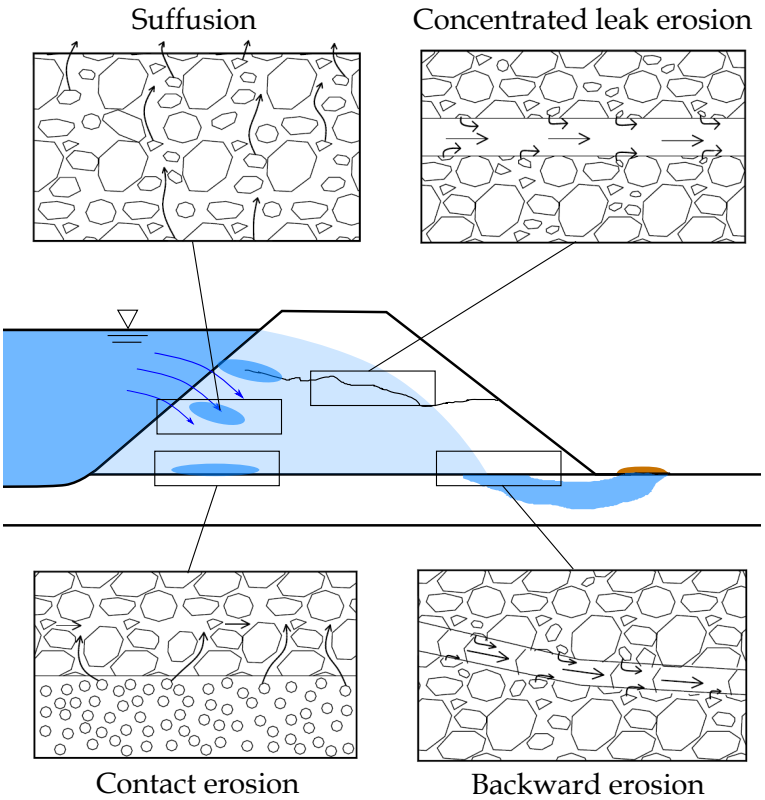

Fig. 1.3. Four different initiation mechanisms for internal erosion: concentrated leak erosion, backward erosion, contact erosion, and suffusion. Redrawn from (Zhang et al., 2016).

As shown in Fig. 1.4, we can distinguish three kinds of necessary conditions to trigger internal erosion: geometric, hydraulic, and mechanical conditions. At least two of these conditions need to be simultaneously fulfilled to initiate internal erosion. The inter-relations are multiple: a weaker hydraulic gradient is required for fine particle erosion, compaction of soil improves the resistance to erosion, or the critical gradient differs under different mechanical conditions (e.g stress states) (Zhang et al.,

2016).

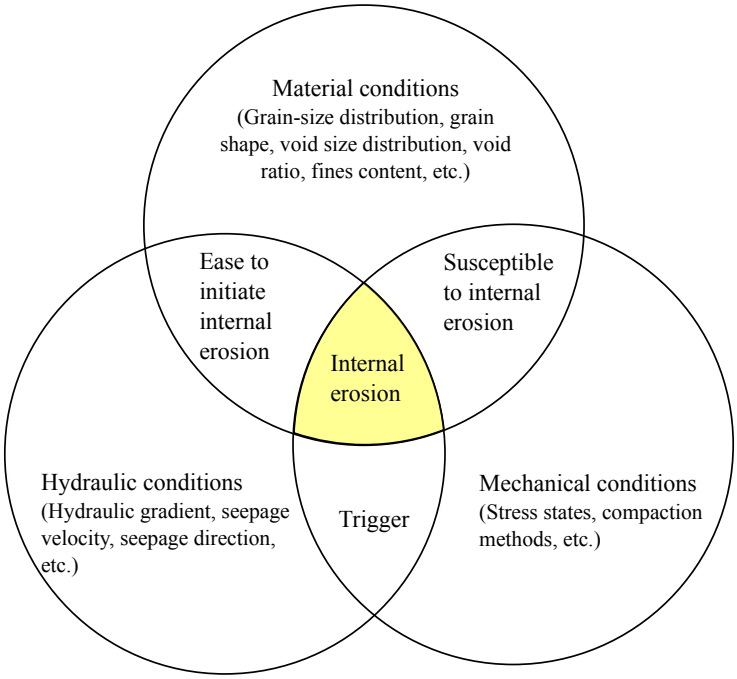

Fig. 1.4. Conditions that trigger internal erosion (Zhang et al., 2016).

1.3 Hydrodynamics involved in erosion of soils

Sediment transport consists of three main processes: erosion, transport, and deposition of sediment particles. The process of concern in this study is erosion, which can be defined as the detachment of sediment particles from the soil mass (or matrix) under the action of fluid flow. The erosion processes occur when the hydrodynamic forces exceed the soil's resistance forces and many researchers have investigated incipient erosion criteria for decades. As will be detailed in forthcoming section 1.4, a distinction must be drawn between cohesion-less materials (typically sand or gravel) and cohesive soils (as clay or loam). In short, the quantitative determination of erosion onset in the case of cohesion-less soils is usually based on the dimensionless Shields number Sh_τ, which is the ratio of the critical bed shear stress to the apparent weight of the particles. The empirical Shields curve almost collapses all the experimental data together. For cohesive soils, several surface erosion laws have emerged, relating surface erosion rate to some relevant hydrodynamic quantities. Here again, bed shear stress is often used to account for a fluid flow acting on a soil. Namely, a critical shear stress τ_c is found, corresponding to the soil's resistance to erosion, and the rate of soil particles detachment by the flow is given as a function of the fluid's excess shear stress, $\tau - \tau_c$. Whatever the sediment type (cohesion-less versus cohesive), it is essential to gain accurate knowledge of the exact fluid flow according to the different flow regimes.

1.3.1 Flow regimes

Flow regimes are classified in terms of the dimensionless Reynolds number Re, which represents the ratio of inertial to viscous forces and reads:

$$Re = \frac{\mathcal{U}\mathcal{L}}{\nu} \tag{1.1}$$

where L is a characteristic length of the flow (e.g. grain diameter or water depth), $\mathcal{U}$ is a typical fluid flow velocity and ν is the fluid's kinematic viscosity.

Based on the Reynolds number, three flow regimes can be distinguished (as shown in Fig. 1.5): laminar flow for low Reynolds numbers $Re < 10^2$, transition flow when $10^2 < Re < 10^3$, and turbulent flow for high Reynolds numbers $Re > 10^3$. Note that the viscous forces are dominant when $Re << 1$, whereas the inertial forces predominate for $Re >> 1$.

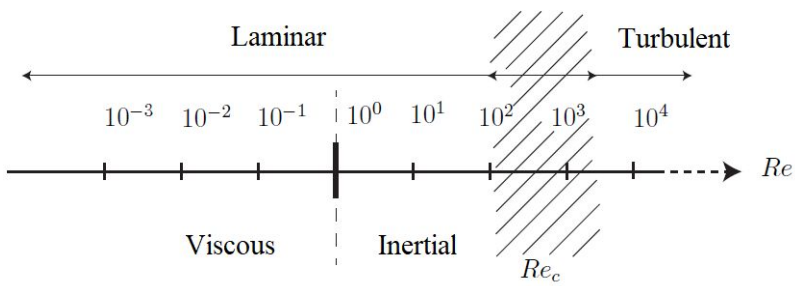

Fig. 1.5. Flow regimes as a function of the Reynolds number Re. The hatched zone represents the transition from laminar to turbulent regime for $10^2 < Re < 10^3$. Figure extracted from (Badr, 2014).

1.3.2 Fluid shear stress induced by steady uniform flow in open channels

As mentioned, the estimation of the bed shear stress is essential for evaluating the erosion onset or incipient of motion. In laminar regime, the flow can be viewed as sliding layers, without any mixing between them, and the shear stress can be described by Newton's viscosity law.

$$\tau = \rho_f \nu \frac{du}{dy} \tag{1.2}$$

where ρ_f and ν are the density and kinematic viscosity of the fluid, respectively. The bottom shear stress is often represented by a friction velocity u_*^2 defined as:

$$\tau = \rho_f u_*^2 \tag{1.3}$$

Note that, in practice, it is nontrivial to deduce the friction velocity u_*, or equivalently the shear stress. However, the shear stress can be alternatively estimated at

the bottom from the measured average velocity U, thus τ will be:

$$\tau = \rho_f u_*^2 = \frac{1}{2}\rho_f C_f U^2 \tag{1.4}$$

where C_f stands for the friction coefficient of the bed that is a purely empirical coefficient.

However, common flows are mostly turbulent in nature. The turbulence is generated by instabilities in the flow resulting in velocity fluctuations. Therefore, the velocity field in turbulent flow can be decomposed into two parts as:

$$u = \overline{u} + u^{'} \tag{1.5}$$

where $\overline{u}$ is the time-averaged velocity, and $u^{'}$ the instantaneous velocity fluctuation. The latter term can be significantly higher in amplitude for strongly turbulent regimes, but its time average value tends to zero by definition.

The total shear stress τ is therefore decomposed into viscous τ_v and turbulent τ_t shear components, as:

$$\tau = \tau_v + \tau_t = \rho_f \frac{d\overline{u}}{dy} + (-\rho_f \overline{u_x' u_y'}) \tag{1.6}$$

Based on the velocity profile $\overline{u_x} = f(y)$ from the bottom surface (y being the distance from the bottom position), several horizontal layers can be distinguished, as shown in Fig 1.6. These flow layers, starting from the bottom, are successively: (1) the viscous sub-layer, (2) the transition layer, (3) the turbulent layer, and finally (4) the turbulent outer layer.

The viscous sub-layer corresponds to the usually very small zone, at the bottom boundary, where the flow is laminar, of Couette type, and generates a constant viscous shear stress τ_s, denoted bed or bottom shear stress, that can be calculated from Eq. 1.4. In the transition layer, also called buffer layer, viscous and turbulent forces are comparable in magnitude and the same global shear stress τ_s holds. Finally, within the turbulent logarithmic layer, the viscous forces become negligible and, as derived from Prandtl's mixing length concept, the mean velocity profile is logarithmic and reads:

$$\overline{u}(y) = \frac{u_*}{k} \ln \frac{y}{y_0} \tag{1.7}$$

with $k = 0.41$ is the Von Karman constant, and y_0 is an integration constant corresponding to zero velocity ($u_{y=y_0} = 0$). Finally, the mean velocity reaches an almost constant value in the turbulent outer layer.

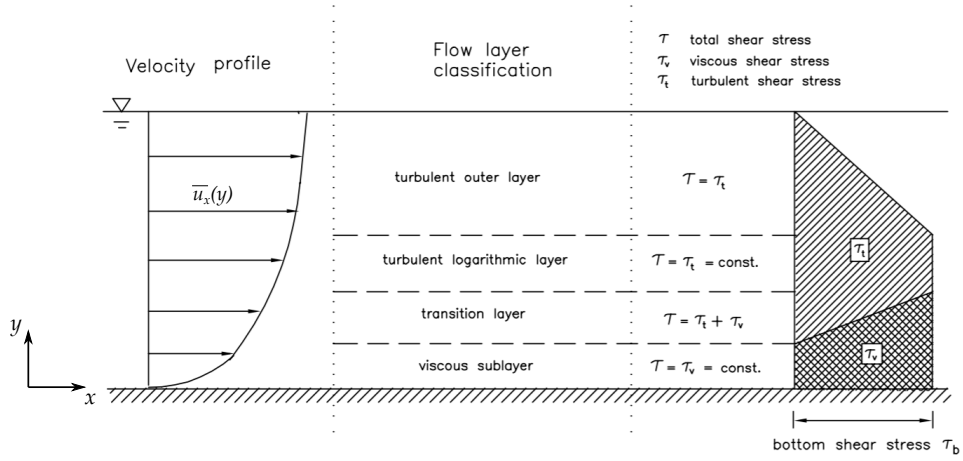

Fig. 1.6. Velocity profile and layer classification for turbulent flow in open channels.

1.4 Onset of surface erosion for a soil layer

We now focus on the situation where such a tangential flow occurs at the upper surface of a soil layer. Owing that a relevant characteristic diameter d is obtained from the soil's grain size distribution, then a particle Reynolds number Re_p can be introduced, by replacing the characteristic length $\mathcal{L}$ by d, and reads:

$$Re_p = \frac{\mathcal{U}d}{\nu} \tag{1.8}$$

Additionally, a boundary or shear Reynolds number Re_τ can be defined based on the bed shear stress τ_s, or equivalently the friction velocity $u_* = \sqrt{\frac{\tau_s}{\rho_f}}$ defined previously. This shear Reynolds number is:

$$Re_\tau = \frac{u_* d}{\nu} \tag{1.9}$$

1.4.1 Case of a cohesion-less soil

The erosion onset of cohesion-less sediment at the particle scale brings us approximately in the previous flow situation except the bottom boundary is now an horizontal bed made of a grains, with a mean (or median) particle size d, and interacting through friction at contacts. Consequently, the onset of erosion by the fluid flow is here based on the incipient motion of an individual grain. From the pioneer work of Shields (Shields, 1936), it has been demonstrated experimentally and analytically that a grain starts moving when the drag forces F_{drag} induced by the flow around the particle exceed the buoyant weight of the grain W. As $F_{drag} \propto \tau_s d^2$ and $W \propto (\rho_g - \rho_f) g d^3$, with ρ_g and ρ_f the grain and fluid densities, respectively, and τ_s the bed shear stress, Shields conveniently introduced a dimensionless group,

denoted since that time Shields number, or Shields criterion, and given by:

$$Sh_\tau = \frac{\tau_s}{(\rho_g - \rho_f)gd} \tag{1.10}$$

At the erosion onset (i.e. incipient motion), we can define a critical value of Shields criterion Sh_τ^*, based on the critical fluid shear stress τ_s^*. Shields proposed to use a diagram where the critical Shields number is plotted versus the shear Reynolds number Re_τ^* (see definition in previous section 1.3.2) which is also a critical value deduced from τ_s^*:

$$Re_\tau^* = \sqrt{\frac{\tau_b^*}{\rho_f}}\frac{d}{\nu} \tag{1.11}$$

From this representation, Shields found roughly a unique curve for several data obtained with different types of sediment and proposed the existence of a one-to-one relation between both parameters, also denoted Shields curve:

$$Sh_\tau^* = \frac{\tau_s^*}{(\rho_g - \rho_f)gd} = f(Re_\tau^*) \tag{1.12}$$

Nevertheless, it can be noted that, throughout history, many researchers failed to reproduce the Shields curve. According to Buffington (1999), it appears that the original results of Shields encounter some uncertainties and raise some flaws, mainly in the method used to define the incipient motion by extrapolating stress-transport curves to a zero transport level. Moreover, the results are significantly scattered mixtures sized sediments are used instead of uniform ones. Furthermore, using either mean or median grain size of the sediment seems to affect the results for the same data set (Buffington, 1999).

Several empirical approximations have been subsequently proposed to fit the Shields curve. Amongst them, the explicit formulation proposed by Guo (1997, 2002) will be used in the rest of this manuscript and reads:

$$Sh_\tau^* = \frac{0.106}{Re_\tau^*} + 0.0545\left[1 - \exp\left(-0.158{Re_\tau^*}^{0.52}\right)\right] \tag{1.13}$$

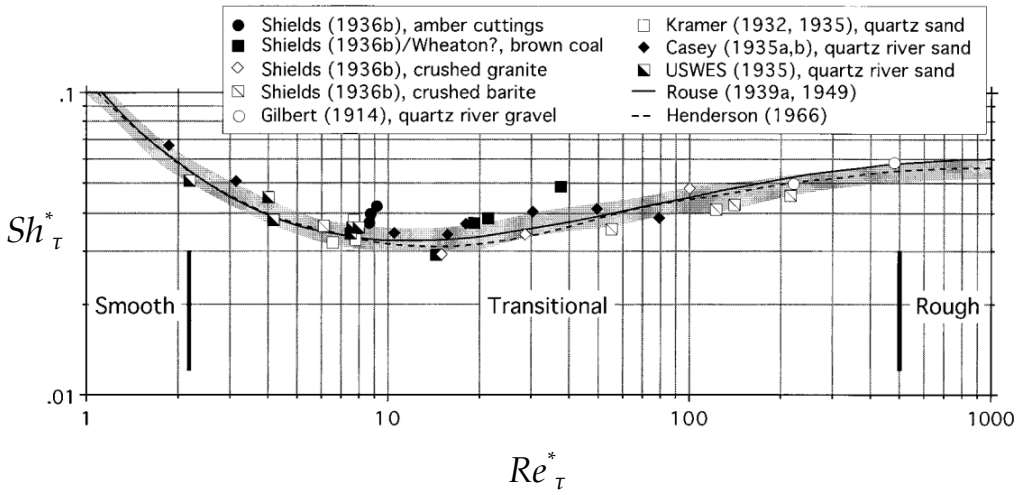

Fig. 1.7. Shields Diagram: Critical Shields number Sh^*_τ as a function of the critical shear Reynolds number Re^*_τ. Figure extracted from Buffington (1999).

1.4.2 Case of cohesive soils

In contrast to the cohesion-less case, estimating erosion onset for cohesive soils is nontrivial and far more complex. As substantial attractive forces now exist in-between soil's particles, there is no more a clear understanding of what is soil's mobilization by a fluid flow. Indeed, friction and buoyant weight are not the only causes for soil's resistance to erosion. On the contrary, these forces often become negligible compared to the soil's cohesive strength. Consequently, the previous Shields approach will no longer be valid, at least in its standard version, since the simple picture of incipient motion of individual grains is no more relevant. Collective behaviors are indeed likely to predominate here, for instance through the entrainment of soil's particles by "flocs" (Righetti and Lucarelli, 2007).

Coleman and Nikora (2008) have shown the influence of the inter-particle forces on the evolution of the critical Shields number. As can be seen in Fig. 1.8, Sh_c increases with Re_p (or equivalently the viscous diameter D_*) in the presence of adhesion or cohesion forces between particles.

In nature, cohesive soils generally consist of fine-grained soils (silt and mineral clay particles) where the grains interact, and possibly adhere together, by physical-chemical forces. Attractive forces can also exist between larger grains in presence of solid bonds or capillary bridges. In both cases, the soil's mechanical strength increases substantially, thus the material becomes more resistant to erosion or scouring. More precisely, a distinction is often proposed between cohesion and adhesion (Coleman and Nikora, 2008; Delenne, 2002; Righetti and Lucarelli, 2007; Jacobs et al., 2011; Chen et al., 2018):

Adhesion: Adhesion stands for surface microscopic forces between two bodies without the presence of a third one. These forces are susceptible to bring nearer the two bodies or to maintain them in contact. Generally, these forces are very strong

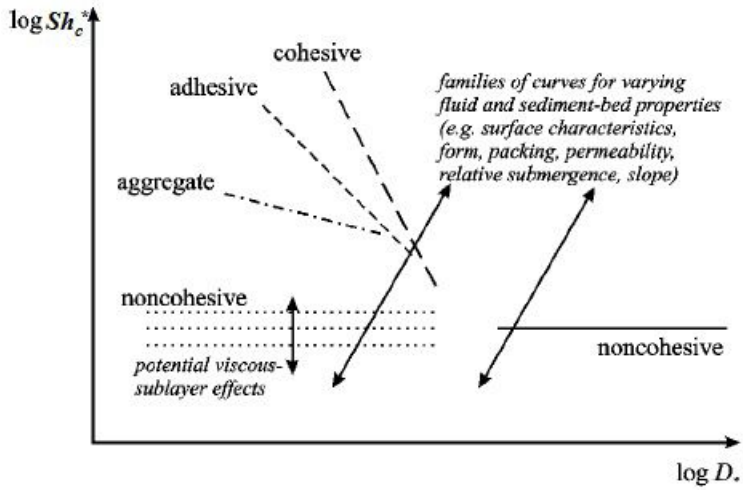

Fig. 1.8. Evolution of the critical Shields number as a function of , for steady uniform 2D flows and with different sediment, fluid, and flow parameters (Coleman and Nikora, 2008).

at short distance but quickly vanish beyond.

Cohesion: Cohesion is described at a macroscopic scale as the result of multiple interactions and links between particles (including adhesive forces). Cohesion can involve a third body as liquid capillary bridges in unsaturated soils, solid bridges in cemented soils, or a mixed behavior related to the presence of particles and clay "matrix". In soil mechanics, cohesion refers to the extrapolated shear strength under zero normal stress, deduced from the intercept of a material's failure envelope (as Mohr-Coulomb) with the shear stress axis in the shear stress-normal stress space (Lu and Likos, 2013).

As microscopic adhesion leads cohesive behavior at the macroscopic scale, we will only focus in the following on cohesive granular soils under the assumption that microscopic actions can be described by cohesive bonds in-between larger grains which do not interact directly, physical-chemically speaking, except by friction.

It is known from a long time that both the onset and the kinetics of soils erosion heavily depend on this internal cohesion. Specific erosion experiments have thus been developed to estimate, either in the lab or in-situ, soils'erosion rate under given hydraulic loadings. Among these erosion testing devices, the most common ones are the Hole Erosion Test (HET), the Jet Erosion Test (JET), and the Erosion Function Apparatus (EFA) (see further descriptions in sec. 1.5). Each device is associated with its own interpretation model to quantify for a given soil the onset and the kinetics of erosion, usually denoted "erodibility" parameters. To this end, an assumption is required as regards local erosion law at the boundary between a cohesive soil and a fluid flow. Most of the interpretation models are based on the linear excess shear stress model, described hereafter. Tentative correlations between these erodibility parameters and some geotechnical and physical-chemical properties of the soils have also emerged (Fell and Fry, 2007), as will be discussed later.

1.4.2.1 Surface erosion laws

To account quantitatively for erosion of a fluid flow at the boundary of a soil layer, it is first needed to fix both space and time scales. Indeed, very different kinds of erosion can be envisaged whether considering seconds or geological times, as well as millimetres or kilometers. These scales prescribe notably how the amount of eroded matter and the hydro-dynamical load exerted by the fluid flow can be quantified. Here, we only focus on erosion in a soil mechanics perspective, typically at centimetre scale over time periods of seconds to minutes. Even in this restricted frame, erosion of a cohesive soil remains a rather generic term and only little is known about the real processes at work at particle scale. Winterwerp and Van Kesteren (2004) postulated the existence of four erosion modes: entrainment, floc erosion, surface erosion and mass erosion. In particular, surface erosion process is defined as follows: "when the mean flow- and/or wave-induced stresses are considerably larger than the true critical shear stress for erosion, large layers of sediment are eroded and mobilized"(Winterwerp and Van Kesteren, 2004). Soil's erosion is described as a complex combination of very specific, and always commonly accepted, sub-processes: head-cut erosion, sidewall sloughing, tunneling and micro-piping, slaking, piping and sapping (Bryan et al., 1989; Bryan, 1990; Zhu et al., 1995; Owoputi and Stolte, 1995; Rapp, 1998).

Another issue deals with the relevance of a hydrodynamic quantity that is able to account for the action of the fluid flow over the surface of a soil, particularly for turbulent flows as is the case in most practical situations. For simplicity, a time average value is often used although more realistic statistical approaches can be proposed but are difficult to implement. Either flow-rate, pressure drop, shear-stress, or energy have been used as actual hydrodynamic load. In coherence with the Shields framework, the fluid's mean shear stress appears as the most common choice and will be used in the rest of this manuscript.

It should additionally be noted that the use of a unique set of parameters to account for soil's sensitivity to erosion is also problematic since resistance to erosion is likely to vary from one location to another inside a given soil sample. Soils indeed are often heterogeneous.

In practice, several empirical laws have been proposed in order to relate the soil's rate of erosion to the hydrodynamic load, quantified here by the fluid time average shear stress. An excess shear stress was first proposed by Partheniades (1965) and remains the most popular formulation. It is based on the assumption that the erosion rate $\dot{m}$, i.e. the eroded mass per surface and time units ($\mathrm{Kg\,m^{-2}\,s^{-1}}$), varies linearly with the fluid shear stress τ:

$$\dot{m} = \begin{cases} k_{er}(\tau - \tau_c) & if \quad \tau \geq \tau_c \\ 0 & if \quad \tau < \tau_c \end{cases} \tag{1.14}$$

The linear relationship directly defines a critical shear stress τ_c (in Pa) while the other parameter, k_{er} (in $\mathrm{s\,m^{-1}}$), is called erosion coefficient. It can alternatively be expressed as $k_{er} = \rho_g k_d$, with k_d in $\mathrm{m^3\,N^{-1}\,s^{-1}}$, if the erosion rate is now defined as an eroded depth per time unit: $\dot{\epsilon}$.

The two parameters τ_c and k_{er}, or k_d, characterize the soil's erodibility. More precisely, τ_c predicts the erosion threshold at which the detachment of particles occurs while the erosion coefficient k_{er} (or k_d) quantifies the kinetics of erosion when the threshold is exceeded. Under some additional assumptions, the latter parameter can be used to predict the remaining time to failure in emergency situation, when a piping flow erosion occurs (Bonelli and Benahmed, 2011).

Note that a slightly more elaborate law is sometimes used, where the linear relation is replaced by a power law. Rather similar formulations have been proposed, for instance by Van Rijn (1984) or Foster (1982). It can read as follows:

$$\dot{m} = \begin{cases} k_{er}(\tau - \tau_c)^n & if \quad \tau \geq \tau_c \\ 0 & if \quad \tau < \tau_c \end{cases} \tag{1.15}$$

The previous expression is obviously recovered for $n = 1$. However, n can be higher or lower than one, accounting either for a convex or concave shape. This exponent n is merely a fitting parameter of experimental or numerical data and does not provides relevant physical significance (Bonelli and Brivois, 2008). However, although the linear law (Eq. 1.15) remains most commonly used for its simplicity, it is yet no more suitable for high shear stress and long slopes whereas the power erosion law gives better agreement of the erodibility parameters for low to medium shear stresses (Zhu et al., 2001). Lastly, Knapen et al. (2007) stated that "no consensus on the nature of the relation between $\dot{\epsilon}$ and τ exists and theoretical explanations for linearity or non-linearity have not been tested yet".

Finally, some alternative laws can be cited. Foster and Meyer (1972) proposed a power law formulation but without critical condition: $\dot{\epsilon} = k_d\tau^{3/2}$. Also an exponential law was introduced by Parchure and Mehta (1985): $\dot{\epsilon} = k_d\tau_c \exp[\alpha(\tau - \tau_c)^\beta]$. More recently, Walder (2016) developed several dimensionless erosion laws.

As will be presented in more detail in the following section 1.5, interpretation models are used to estimate soil's erodibility from one or several erosion tests. However, even if a same erosion law is assumed, the erodibility values obtained for a same material are scattered. This is partly due to the type of erosion device that does not systematically rely on similar fluid flows. In addition, as already mentioned, the erosion laws are based on a time average value of the shear stress. As mainly turbulent flows induce fluctuations in fluid pressure and velocity over time and space, the local shear stress at the interface may therefore occasionally exceed the soil's critical threshold τ_c even if its time average value is far below. This results in intermittent particle extraction and thus maintains a non-zero erosion rate over time (Philippe et al., 2017). To address this issue, statistical approaches have emerged using probability density functions for both the flow hydraulics (e.g. shear stress or other) and the soil's erodibility parameters (Nearing, 1991; Sidorchuk, 2001, 2005). For instance, Van Prooijen and Winterwerp (2010) proposed a statistical distribution of the shear stress based on a Gaussian distribution of the average velocity. A similar use of statistical distribution to account for space variability was implemented by Beguin et al. (2013) in the context of contact erosion.

1.4.2.2 Erodibility parameters (k_d and τ_c)

Almost all erosion laws agree on involving the two empirical parameters k_d and τ_c. Consequently, the latter are traditionally considered as an intrinsic material feature of a cohesive soil, called soil's erodibility. Over the past decade, great effort has been devoted to achieve a better understanding of the erodibility parameters, mainly by systematic confrontation and interlinking with some of the typical properties of natural soils such as particle size, density, water content, and many other quantities including consolidation time (Black et al., 2002; Parchure and Mehta, 1985; Kimiaghalam et al., 2014). In this sense, a very large variety of empirical relations has been proposed in the literature (see e.g. (Grabowski et al., 2011; Winterwerp and Van Kesteren, 2004; Zhu et al., 2008)), mostly regarding the critical shear stress τ_c. However, the erosion rate parameter k_d (sometimes also denoted k_{er} when mass loss is considered instead of volume loss) has received considerably less attention since it is far more difficult to evaluate experimentally, especially *in situ*, even if a theoretical derivation has already been proposed by Winterwerp and Van Kesteren (2004).

Regardless of the direct dependencies with other soil properties, some authors (Hanson and Simon, 2001; Karamigolbaghi et al., 2017) have also proposed the existence of an intrinsic relationship between τ_c and k_d in the following form: $k_d \propto \tau_c^{-\gamma}$. Even if an exponent of $\gamma = 0.5$, as initially suggested in Hanson and Simon (2001), was consistent with a dimensional analysis (Andreotti et al., 2013), the extremely larger range of exponent values subsequently proposed by other authors (Daly et al., 2015; Julian and Torres, 2006; Karamigolbaghi et al., 2017; Karmaker and Dutta, 2011; Konsoer et al., 2016; Layzell and Mandel, 2014; Nguyen et al., 2017; Thoman and Niezgoda, 2008), from $\gamma \approx 0.4$ to $\gamma \approx 2.4$, appears to discourage any attempt of generalization, particularly in view of the very strong scattering of these erodibility data (see for instance (Kimiaghalam et al., 2014)) and considering the significant impact of the test interpretation model (at least for JET measurements) (Karamigolbaghi et al., 2017) as well as some contradicting analyses that show an absence of correlation between τ_c and k_d (Knapen et al., 2007). In this respect, it merely appears appropriate to state, in a qualitative manner, that a less(more) resistant soil is generally prone to suffer higher(lower) erosion rates in equivalent hydrodynamic conditions.

1.5 Erosion test devices

1.5.1 Hole Erosion Test (HET)

The Hole Erosion Test (HET) is one of the most commonly used erosion tests. It was first developed by Wan and Fell (2004) for modeling a controlled piping erosion in the laboratory and characterizing the resistance against erosion of cohesive soils. As regards hydrodynamics, the HET consists of applying a tangential flow along an initially cylinder pipe within a soil specimen, under either constant flow rate or constant pressure drop conditions. Note however that the second protocol is far more

difficult to implement in practice. Before the start of the experiment, a cylindrical hole is drilled across the soil sample to be tested. Then, the flow passes through this pipe, inducing erosion, mass loss, and pipe enlargement. The HET device is shown in Fig. 1.9.

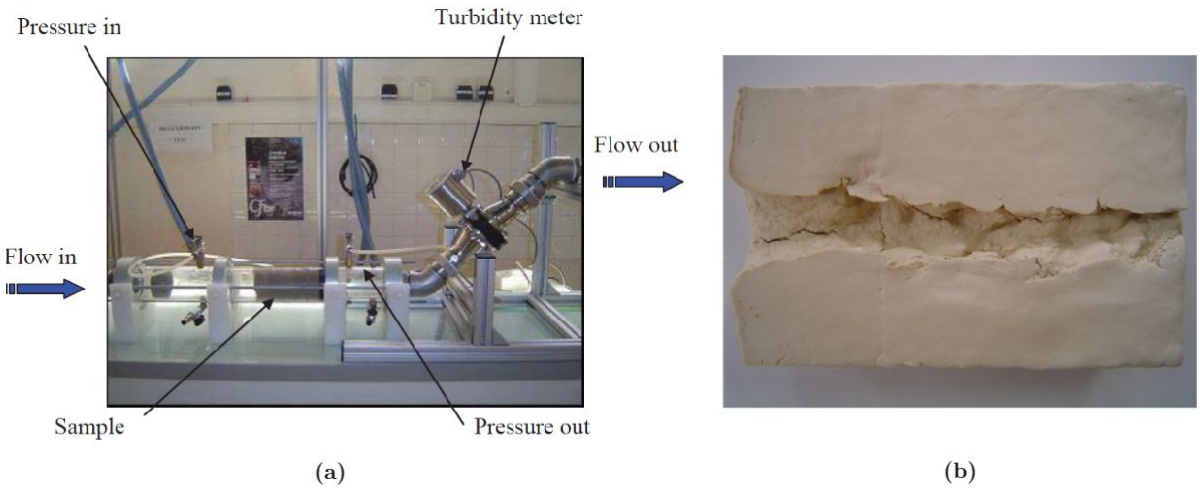

Fig. 1.9. (a) Photograph of the experimental Hole Erosion Test device. (b) A typical soil sample after erosion by HET.

The first HET interpretation was proposed by Wan and Fell (2004) and allows determination of the erodibility parameters (k_d and τ_c) based on a linear regression of the erosion rate versus fluid shear stress curve, but making several questionable assumptions, especially as regards hydrodynamics.

A second and more elaborate interpretation model was proposed by Bonelli et al. (2006), still considering the linear excess stress erosion law and using now a more realistic modelling of the pipe flow based based on the Navier-Stokes equations of an incompressible fluid in cylindrical geometry. Assuming that the pipe keeps a cylinder shape, the eroded mass allows for estimating the erodibility k_d and the critical fluid shear stress τ_c parameters of the tested materials as described below.

The radius evolution over time gives the erosion rate and can be expressed from the linear excess shear erosion law in Eq. 1.15 with ρ_d the soil's dry density:

$$\dot{m} = \rho_d \frac{dR}{dt} = k_{er}(\tau - \tau_c) = \rho_d k_d (\tau - \tau_c) \tag{1.16}$$

Yet the fluid shear stress at the interface can be calculated based on both the pressure drop ΔP and the pipe radius (supposed to evolve uniformly as already mentioned):

$$\tau = \frac{R(t)\Delta P}{2L} \tag{1.17}$$

where L is the pipe length and $R(t)$ its mean radius that progressively increases over time as erosion occurs.

If a constant pressure drop ΔP is first considered, then, based on Eqs 1.17 and 1.16, one gets:

$$\frac{1}{R_c}\frac{dR}{dt} = k_d\frac{\Delta P}{L}(\frac{R}{R_c} - 1) \quad \text{with} \quad R_c = \frac{2\tau_c L}{\Delta P} \tag{1.18}$$

After integration, the time evolution of the pipe radius is found to simply follow an exponential law during the erosion test with constant pressure drop (Bonelli and Brivois, 2008):

$$R(t) = R_0 + (R_0 - R_c)(e^{t/t_{er}} - 1) \tag{1.19}$$

with a characteristic time $t_{er} = \dfrac{2L}{k_d \Delta P} = \dfrac{R_c}{k_d \tau_c}$.

The erodibility parameters (k_d, τ_c) are lastly determined by exponential adjustment with experimental data. However, as previously mentioned, the protocol with a constant pressure drop is quite difficult to implement experimentally as both pipe radius and flow rate quickly diverge.

The second protocol with constant flow rate is consequently far more frequently performed. Unfortunately, in this case, the fluid shear stress at the soil's interface can be only estimated in an empirical manner:

$$\tau = f\frac{\rho_f Q^2}{2\pi^2 R^4} \tag{1.20}$$

where $Q = \pi R^2 \bar{U}$ is the constant flow rate, $\bar{U}$ is the mean flow velocity in the pipe cross-section, and f is the so-called friction coefficient. This coefficient f is estimated from semi-empirical and often implicit formulas, as a function of the Reynolds number Re and, consequently, of the pipe radius $R(t)$.

As a first approximation, the friction coefficient f can be assumed to be constant. Then, based on Eqs 1.16 and 1.20, the pipe radius satisfies the following differential equation:

$$\frac{1}{R_c}\frac{dR}{dt} = \frac{k_d f \rho_f Q^2}{2\pi^2 R_c^5}\left[\left(\frac{R_c}{R}\right)^4 - 1\right] \quad \text{with} \quad R_c = \left(\frac{f\rho_f Q^2}{2\pi^2 \tau_c}\right)^{1/4} \tag{1.21}$$

Next, an implicit solution is obtained for the evolution of the pipe radius with time (Bonelli et al., 2006):

$$F\left(\frac{R(t)}{R_c}\right) = F\left(\frac{R_0}{R_c}\right) + \frac{t}{t_{er}} \tag{1.22}$$

with again $t_{er} = \dfrac{R_c}{k_d \tau_c}$ and $F(x) = \dfrac{1}{2}(\tan^{-1} x + \tanh^{-1} x) - x$.

Finally, the erodibility parameters (k_d, τ_c) are determined by indirect adjustment of the previous expression, as shown in Fig. 1.10.

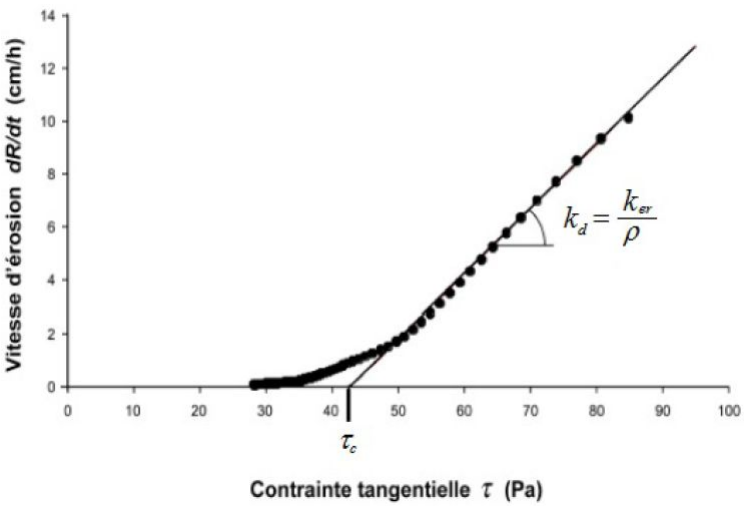

Fig. 1.10. Interpretation of a typical HET test results for the assessment of erodibility parameters τ_c and k_d (Benahmed and Bonelli, 2012).

1.5.2 Erosion Function Apparatus (EFA)

The EFA is shown in Fig. 1.11. It was developed by Briaud et al. (2001) to study scouring of soils around a bridge pier and quantifying the related erodibility parameters. Contrarily to the HET which is restricted to substantially cohesive soils (silt, clay), capable of holding a transverse pipe in a sample of soil, the EFA can also estimate erodibility parameters of coarse grained soils (sand, gravel). The EFA consists of a closed circuit with a channel of rectangular cross-section. The water is driven through the channel by a pump and the flow is regulated by a valve to maintain a constant mean velocity in the range 0.1 m/s to 6 m/s. A piston, placed at the bottom end of the channel, is used to push upward the tested soil sample. Thus the soil sample is maintained in a flush position, 1 mm above the inner surface of the channel. This height adjustment is proceeded by the experimenter, manually and visually through a plexiglass window. The time required for this 1 mm sub-layer of soil to be eroded is recorded and used to determine the erosion rate as follows:

$$\dot{z} = \frac{h}{t} \tag{1.23}$$

where $\delta h = 1$ mm is the length of soil sample depth eroded during the time t. The sample is then lifted again 1 mm above the channel bottom for another measurement.

By the end, an average erosion rate is calculated for a given channel mean flow velocity v. The formulation in terms of the fluid shear stress τ at the channel bottom is based on the following empirical expression:

$$\tau = \frac{1}{8} f \rho_f v^2 \tag{1.24}$$

where f is the friction factor obtained from the Moody chart and ρ_f is the water density ($1,000$ kg/m^3).

To plot the erosion rate against different shear stress values (Fig. 1.12), the experiment must be repeated for several velocity values. First, the critical velocity is determined when the soil begins to erode and the critical shear stress of the soil can be derived directly from this velocity. Next, starting from the critical velocity, the velocity is gradually increased. Figure 1.12 represents a typical erosion curve, i.e. erosion rate versus fluid shear stress, for two different soil samples, namely coarse and fine grained.

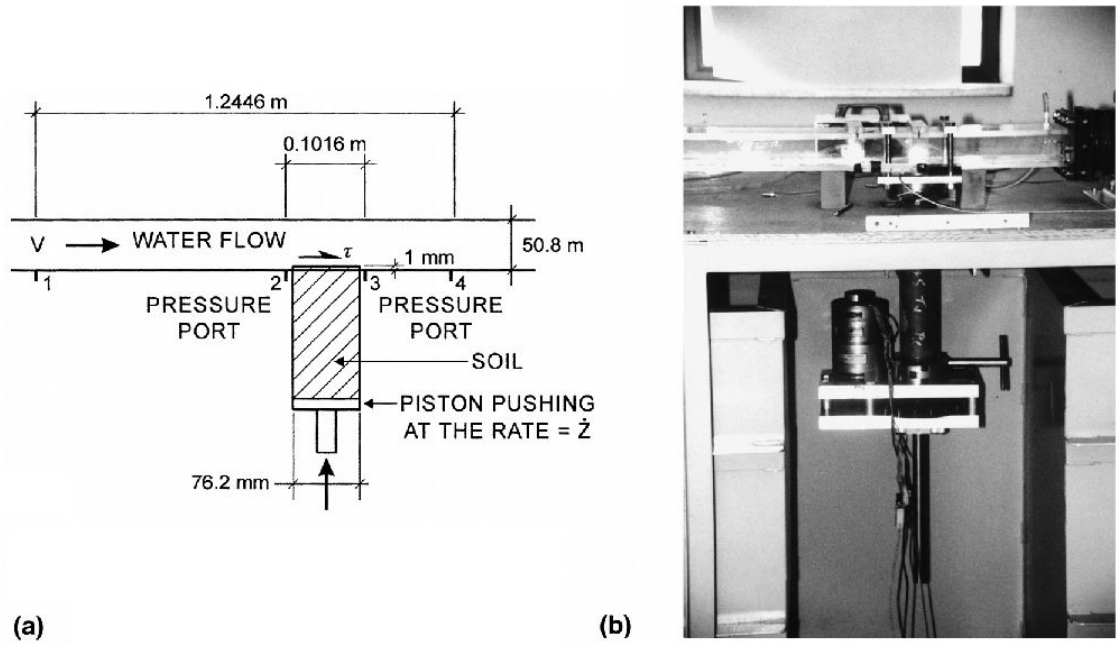

Fig. 1.11. EFA: (a) Conceptual diagram; (b) Photograph of the test section. Figure extracted from (Briaud et al., 2001).

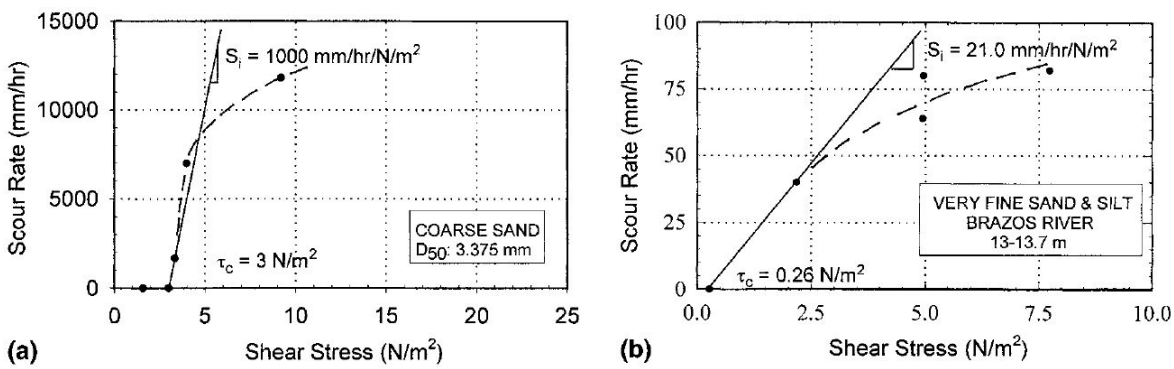

Fig. 1.12. Erosion curve obtained from EFA for: (a) Coarse sand; (b) Mixture of a very fine sand with silt (Brazos River). Figure extracted from (Briaud et al., 2001).

1.5.3 Jet Erosion Test (JET)

The Jet Erosion Test (JET), sketched in Fig. 1.13, was first introduced by Hanson and Cook (2004). It has the great advantage that it can be used either in laboratory or *in-situ* and requires a rather low fluid load. The *in-situ* condition is particularly interesting as it can preserve intact the original structure of the soil, contrarily to the HET. The JET consist of applying, in a large submerged circular tank, a downward vertical jet flow, impinging the upper surface of a soil sample and progressively forming a crater. The scour depth H is measured over time and used to quantify the erosion rate $\dot{\epsilon} = \frac{dH}{dt}$.

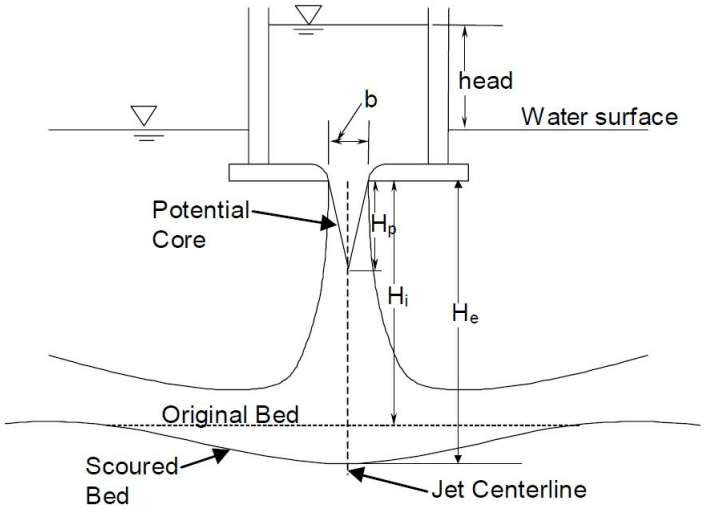

Fig. 1.13. Sketch of the jet erosion test (JET).

The impinging jet flow is naturally complex and numerous simplifications are necessary to achieve some analytical derivations and propose an interpretation model. To clarify, the flow can be decomposed into three main parts: free jet flow up a certain distance from the nozzle exit, tangential flow at the bed surface and far from the jet center-line, and re-circulation flow inside the crater once it is formed. The assumptions are mostly made for estimating the flow characteristics at the bed surface. Nonetheless, the free jet theory (Schlichting, 1960; Bickley, 1937) and the experimental results about bottom shear stress on a smooth wall (Beltaos and Rajaratnam, 1977, 1974; Hanson et al., 1990) can be applied to quantify the hydraulic shear stress on the soil surface. Finally, the soil's erodibility paraemeters τ_c and k_d can be deduced from adjustment of the experimental data.

Note that the JET interpretation model proposed by Hanson and Cook (2004) is based on the estimation of the velocity on the bed surface U using the free jet self-similar model

$$U(H) = \begin{cases} U_0 & if \quad H < H_p \\ U_0 \frac{H_p}{H} & if \quad H > H_p \end{cases} \tag{1.25}$$

where $H_p = C_d b$ is the potential core length, $U_0 = \sqrt{2g\Delta H}$ is the mean jet inlet velocity, C_d is the diffusion coefficient (see more details in the next section).

Furthermore, the fluid shear shear stress reads:

$$\tau = \frac{1}{2}\rho_f C_f U^2 \tag{1.26}$$

with C_f the bed coefficient of friction. Typical values of C_f around 4×10^{-3} and $C_d = 6.2$ are used for turbulent flow conditions (Albertson et al., 1950).

At the equilibrium (i.e. for a crater depth at which the interface shear stress is no longer sufficient to erode the soil), the final depth H_e is used to calculate the critical stress through the following equation:

$$\tau_c = \tau_0 \left(\frac{H_p}{H_e}\right)^2 \tag{1.27}$$

where the 0-index refers to the initial condition. The evolution of the scour depth dH/dt can be given from the surface erosion law, as follows:

$$\dot{\epsilon} = \frac{dH}{dt} = k_d \left[\tau_0 \left(\frac{H_p}{H}\right)^2 - \tau_c\right] \tag{1.28}$$

A relevant non-dimensionalization, initially proposed by Hanson and Cook (1997), provides, after time integration of Eq. 1.28, the following implicit expression for the scour depth versus time t:

$$t = t_{er} \left[0.5 \ln\left(\frac{1+H^*}{1-H^*}\right) - H^* - 0.5 \ln\left(\frac{1+H_i^*}{1-H_i^*}\right) + H_i^*\right] \tag{1.29}$$

where $t_{er} = H_e/(k_d \tau_c)$, $H^* = H/H_e$, and $H_i^* = H_i/H_p$. Then, the erodibility parameters τ_c and k_d are obtained from the crater depth evolution with this analytical expression by minimization of the sum of squared errors between the measured data and the analytical solution of Eq. 1.29.

Note that, as H_e may not be reached in field testing due to the high time required for equilibrium state, the excess stress τ_c can be alternatively predetermined from H_e by fitting the scour data versus time to an hyperbolic function for predicting the equilibrium depth, as proposed by Blaisdell et al. (1981). Then, k_d can be determined by curve-fitting measured values of H versus t for Eq. 1.29. However, this method proposed by Hanson and Cook (1997) does not always converge to a reasonable solution compared to the previous one as pointed out by Daly et al. (2013).

1.6 Focus on impinging jet hydrodynamics

This section is dedicated to the state of the art as regards free and impinging jets flows, with a closer scope on laminar regime and planar geometry. This specific focus is motivated by the greater complexity of impinging flows in comparison with usual tangential flows as presented in previous sections. Indeed, the jet flow, whether

laminar or turbulent, is first perfectly vertical and can be described by a self-similar free jet model. Then, as it gets closer to the impinged wall, the flow progressively deviates tangentially and also creates a stagnation point at the apex of the jet's center-line. It was pointed out that the type of impingement surface can significantly change the flow behavior.

The empirical interpretation model for Jet Erosion Test (JET) briefly described in the previous section is based on both free jet theory and experimental results of impinging jets on flat smooth surfaces. Consequently, in the following, we will first focus on free jet, specifically on self-similar models in the laminar regime since our numerical model is laminar and bi-dimensional, as will be detailed later, and next present some data from the literature about jet impingement on a smooth wall, particularly as regards the shear stress distribution.

1.6.1 Self-similar free jet models

Free jets are widely observed in the nature and often used in experiments. They can be described as a fluid flow issued from a source into the same fluid at rest or in motion. Shear stress at the boundary between the jet flow and the ambient fluid generate instabilities and mixing to a certain extent according to the flow regime, from laminar to turbulent. The main characteristic of the free jet is based on the postulate that the momentum remains constant. Under this assumption, the jet flow continues to develop in the downstream direction, with a regular decrease of the center-line velocity and a lateral widening of the flow area in order to compensate the extra mass that enters the flow. The self-similar model of turbulent round free jet was briefly presented in the previous section. Here we focus specifically on the bi-dimensional laminar case, which will be studied in detail in chapter 3.

Ideal jets The governing equations of the self-similar jet model are based on the boundary-layer approximation. This free jet boundary-layer solution was first provided by Schlichting (1960) to describe a round jet through a numerical integration, while Bickley (1937) gave an analytical expression for the two-dimensional case. The latter relies on the assumptions that (i) the jet is issued from a point source with an infinite velocity, (ii) the momentum flux M remains constant, and (iii) the jet flow is self-similar according to x, the downstream distance from the point source. For the remainder, we introduce the index ($\tilde{}$) to denote the theoretical variables and distinguish them from the simulated ones presented later in chapter 3.

The self-similarity of a free plane jet implies that the longitudinal velocity u of the fluid at any point downstream of the nozzle can be described by:

$$\tilde{u}(x, y) = \tilde{u}_m(x) f(\eta) \tag{1.30}$$

where y is the coordinate transverse to the jet's axis and $\tilde{u}_m$ is the fluid velocity along the jet axis, also denoted center-line velocity, and corresponds to the maximal velocity at the horizontal position x. The function f reads:

$$f(\eta) = \mathrm{sech}^2(\eta) = \frac{1}{\cosh^2(\eta)} \tag{1.31}$$

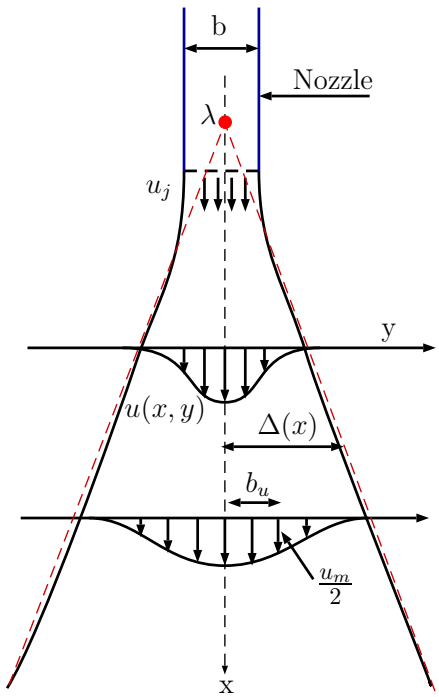

Fig. 1.14. Sketch of a plane free jet with a virtual origin λ located above the nozzle exit.

with the self-similar variable $\eta = y/\tilde{\Delta}(x)$ and $\tilde{\Delta}(x)$ the jet's half-width at the downstream distance x (see Fig. 1.14).

Defining $\tilde{b}_u$ as the value of y where $\tilde{u} = \frac{1}{2}\tilde{u}_m$, the relationship between $\tilde{\Delta}$ and $\tilde{b}_u$ is simply given by:

$$\tilde{b}_u(x) = \text{argch}(\sqrt{2})\tilde{\Delta}(x) \tag{1.32}$$

The analytical solutions for the jet's center-line velocity and half-width are provided by Bickley (1937) and read, respectively:

$$\tilde{u}_m(x) = \left(\frac{3M^2}{32\rho_f^2\nu x}\right)^{1/3} \tag{1.33}$$

$$\tilde{\Delta}(x) = \left(\frac{48\rho_f\nu^2x^2}{M}\right)^{1/3} \tag{1.34}$$

In the present case of 2D jet, the constant momentum flux M is defined by:

$$M = \int_{-\infty}^{+\infty} \rho_f\tilde{u}^2 dy \tag{1.35}$$

If a 2D Poiseuille flow is assumed at nozzle inlet, the constant momentum flux reads $M = (6/5)\rho_f u_j^2 b$, after integration of the velocity profile over the injection section.

From the mass flux conservation, the center-line velocity $\tilde{u}_m$ can be expressed at any downstream location:

$$\tilde{u}_m(x) = \frac{3}{10} u_j \left(\frac{5Re_j}{x/b} \right)^{1/3} \tag{1.36}$$

where $u_j = \frac{2}{3}U_0$ is the mean jet velocity, with U_0 the maximum jet injection velocity in the nozzle and $Re_j = u_j b/\nu$ the jet Reynolds number.

Similarly, the jet's half-width reads:

$$\tilde{\Delta}(x) = 40^{1/3} b Re_j^{-2/3} \left(\frac{x}{b} \right)^{2/3} \tag{1.37}$$

Adaptation to real jets Practically, whether in experiments or numerical simulations, the flow of a real jet deviates from the previous analytical solution. Such a jet is indeed very sensitive to the boundary conditions and, even for a same Reynolds number, the flow may differ from an experimental apparatus to another. To reproduce identical results can be rather challenging.

The main observed difference between real and theoretical jets concerns the center-line velocity $u_m(x)$ which does not start decreasing right after issuing from the jet's nozzle exit but it remains almost constant up to a certain distance downstream. This region, called the potential core, depends on the flow regime, i.e. laminar, transitional, or turbulent. It is noteworthy that the potential core region can be extended up to around $6b$ for turbulent flows according to the literature (Hanson and Cook, 2004; Beltaos and Rajaratnam, 1977). This potential core may also require a slight modification in Eq. 1.36 by introducing a coefficient in order to fit with the experimental data.

Moreover, the analytical solution features a singular point at $x = 0$, due to the assumption that the jet flow emerges from a narrow source of infinitesimal width (Bickley, 1937; Schlichting, 1960), while a real jet flow is injected from a finite size nozzle. Consequently, the previous analytical equations need to be modified by introducing a virtual origin $\tilde{\lambda}$ (see Fig. 1.14) in order to fit the theoretical predictions with both the experimental and simulated data. This virtual origin corresponds to the source point from which the jet appears to emerge when observed sufficiently far from the outlet and has been estimated theoretically in previous works (Andrade and Tsien, 1937; Andrade, 1939; Revuelta et al., 2002). Revuelta et al. (2002) gave for instance a numerical estimation of $\tilde{\lambda}$ for both plane and round jets as a function of Re_j and b. Thus, in relation with the flow studied later in chapter 3, the expression of $\tilde{\lambda}$ for a laminar plane free jet with a Poiseuille injection reads:

$$\tilde{\lambda} = 0.029 Re_j b \tag{1.38}$$

In practice, the virtual origin $\tilde{\lambda}$ can be obtained by extrapolation to 0 of either the jet width $\Delta(x)$ or the inverse center-line velocity $[u_m(x)]^{-1}$. The corresponding x-intercept gives the value of the virtual origin $\tilde{\lambda}$ and is used to translate the x-axis from x to $x + \tilde{\lambda}$. This method will be used in forthcoming chapter 3. So finally,

after introduction of the virtual origin, the center-line velocity (previous Eq. 1.36) and the jet's half-width (previous Eq. 1.37) become:

$$\tilde{u}_m(x) = \frac{3}{10} u_j \left(\frac{5Re_j}{(x+\tilde{\lambda})/b} \right)^{1/3} \tag{1.39}$$

$$\tilde{\Delta}(x) = 40^{1/3} b Re_j^{-2/3} \left(\frac{x+\tilde{\lambda}}{b} \right)^{2/3} \tag{1.40}$$

1.6.2 Impinging jets

The impinging jet is encountered in numerous natural and industrial applications, such as heat transfer (heating, cooling and drying) (Martin, 1977; Jambunathan et al., 1992) or head-cut erosion (Bennett and Alonso, 2005). As previously presented, it is also used to quantify the resistance against erosion of cohesive soils (Hanson and Cook, 2004). This particular jet flow configuration has been profusely studied in the past both from theoretical and experimental perspectives (Beltaos and Rajaratnam, 1973, 1974; Rajaratnam, 1976; Hanson et al., 1990; Looney and Walsh, 1984; Poreh et al., 1964; Ghaneeizad et al., 2014; Phares et al., 2000). These studies focused on the evolution of the flow characteristics at the impingement surface, notably the velocity and the fluid shear stress distribution. Obviously, the presence of an horizontal plane surface downstream of the jet exit affects drastically the overall behavior of the jet, separating the flow into three main regions sketched in Fig. 1.15. Within each region, a particular fluid flow can be distinguished (see e.g. Beltaos and Rajaratnam (1973)): a free jet region (zone I) where the flow remains self-similar; an impingement region (zone II) in which the impinged surface increasingly affects the jet flow; a wall jet region (zone III), where the flow becomes parallel to the impinged surface.

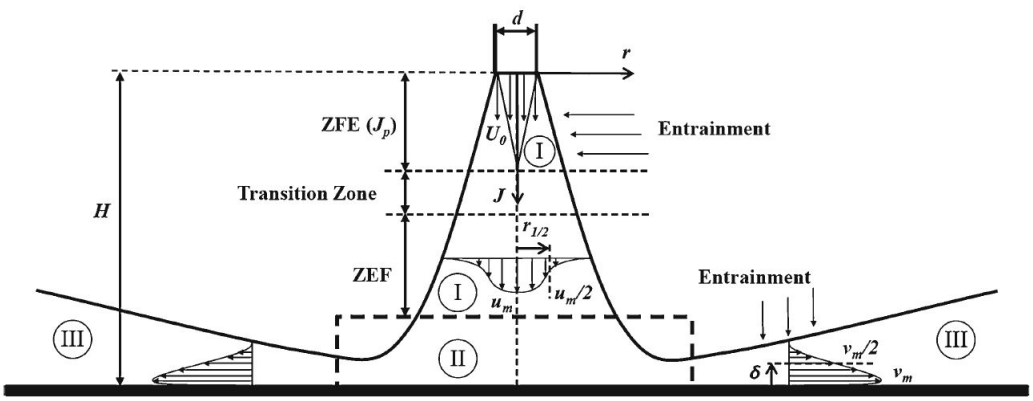

Fig. 1.15. Schematic of the three distinct flow regions for an axi-symmetric impinging (after (Ghaneeizad et al., 2014; Beltaos and Rajaratnam, 1974))

In the impingement region (zone II), the presence of the horizontal wall makes the center-line velocity decrease down to zero at the impingement (i.e. stagnation

point) and the flow be diverted laterally. Note that the distance from the impinging wall from which the center-line velocity starts to deviate from the free-jet analytical prediction until its final stagnation at the wall is rather short and represents approximately only 15-20% of the total distance H between the jet's outlet and the wall (Badr, 2014). Beltaos and Rajaratnam (1974) predicted that the axial velocity of the plane jet near the wall (i.e. for $0.75 \leq \frac{x}{H} \leq 1$) varies according to the following law:

$$\frac{u_m(x)}{u_j} = 5.5\sqrt{1 - \frac{x}{H}}\sqrt{\frac{b}{H}} \tag{1.41}$$

Beltaos and Rajaratnam (1974) also gave a Gaussian-type distribution of the shear stress for turbulent round jets, which is given by:

$$\frac{\tau}{\tau_m} = 0.18(\frac{1 - e^{-114\sigma^2}}{\sigma}) - 9.43\sigma e^{-114\sigma^2} \tag{1.42}$$

where $\sigma = r/H$ is the dimensionless distance from the jet center-line axis and τ_m is the maximal shear stress on the plane surface.

The transverse component of the velocity generally follows a pattern known as wall jet. The velocity profile in the wall jet region (zone III) can for instance be described by the following self-similarity equation proposed by Verhoff (1963) for a turbulent wall jet:

$$\frac{v}{v_m} = 1.48\eta^{1/7}\left[1 - erf(0.68\eta)\right] \tag{1.43}$$

where $\eta = x_1/b_1$ is the self-similar variable, x_1 is the vertical distance from the impinged wall and b_1 is the wall jet's half-width which corresponds to the distance x_1 from the wall where $v = \frac{v_m}{2}$.

Similarly to the self-similar free jet model, the present study will be restricted to the case of 2D laminar jet impingement, as detailed later in chapter 3. To our knowledge, there is no theoretical or empirical expressions in the literature for these specific conditions.

1.7 Numerical modeling of fluid flow induced erosion

Numerical models are nowadays gaining growing relevance for the study of small to large-scale geotechnical engineering applications and enable some difficulties of the experimental situations, where for instance several quantities can be hardly measurable, to be overcome. In the context of fluid flow induced erosion, using such customized numerical simulations can indeed provide a relevant insight into local parameters of the flow and accurate values of all the hydrodynamic quantities. This may considerably improve the interpretation models developed to estimate the soils erodibility parameters which, as shown previously, are based on several assumptions and use empirical or semi-analytical relations, as for JET or HET, respectively. By

now, there is no universal interpretation model capable of working for any erosion device or other real-life situations.

The challenge for numerical simulations is to accurately describe the erosion phenomena and, more generally, saturated porous media, which are highly coupled fluid-solid interaction problems. Appropriate numerical models are required, capable of modeling many interacting effects: the motion of the fluid and solid phases as well as the interface between both phases, the action of the fluid (i.e. hydrodynamic forces) on a solid which possibly moves or even deforms under fluid pressure, the effect of a moving solid on the ambient fluid, and the inter-particle interactions, with possibly cohesive interactions as in the present modeling of cohesive granular materials subject to erosion. Such a complex phenomenon obviously requires fully coupled hydro-mechanical models, where fluid-particle and particle-particle interactions are taken into account. We give in this section an overview of different numerical approaches that are capable of adequately describing the physical mechanisms of fluid-particle interactions in immersed granular materials and for which two main approaches can be distinguished.

First, the continuum approach, where the fluid and solid are considered as continuum phases. Three models can be envisaged: mono-phasic, bi-phasic, and tri-phasic approaches. The mono-phasic approach consists of solving directly the Navier-Stokes equations for the fluid flow alone, possibly using several different turbulence models. Erosion and solid phase are only accounted for through the water/soil interface, considered as a Lagrangian boundary. In the bi-phasic approach, two separate phases are defined (solid and fluid) and the interface is considered as singular. The Navier-Stokes equations can be applied to model the fluid phase while, for instance, the Darcy-Brinkman equation is assumed for the solid phase. Finally, in the tri-phasic approach, a third fluidized solid phase is introduced to model the solid-fluid interface, for instance again through the Darcy-Brinkman equation. For each phase, the corresponding mass balance equations are established, a source term is introduced to account for particle erosion and transport between phases (Vardoulakis et al., 1996).

Second, a combined multi-scale approach (i.e. Micro-Micro or Meso-Micro approaches) can be also envisaged, where the soil is modeled as a collection of discrete particles described by Newton's second law of motion (e.g. with the Discrete Element Method, or DEM) while the fluid flow calculation is based on suitable continuum models. Such fluid models include classical computational fluid dynamics method (CFD), solving the Navier-Stokes or the Boltzmann equations (see Fig. 1.16), or specially developed scheme as the Pore-scale Finite Volume (PFV) model (Catalano, 2012). Given that the pertinence and validity of the erosion law are the main concerns here, the latter multi-scale approach has several advantages for simulating the erosion phenomena since, in this case, no erosion law needs to be postulated *a priori*.

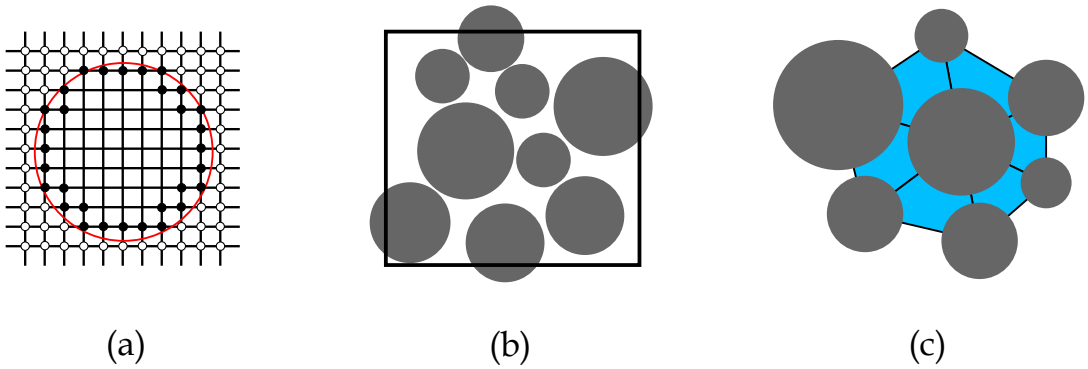

Fig. 1.16. Description scale for different fluid-solid coupling approaches: (a) LBM-DEM; (b) CFD-DEM; (c) PFV-DEM.

1.7.1 Continuum approaches of fluid flow induced erosion

1.7.1.1 Mono-phasic method

Mercier et al. (2014) adapted an Eulerian-Lagrangian approach to simulate the JET and HET configurations for turbulent flows. The Navier-Stokes equations are directly solved for the fluid flow, the water/soil interface being thus considered as a Lagrangian boundary which is regularly updated using a suitable erosion law. This approach provides good precision at the interface, especially in the turbulent regime, but requires in return frequent re-meshing of the calculation domain which ultimately leads to a higher computational time.

1.7.1.2 Bi-phasic method

In the two-phase or bi-phasic approach, both the fluid and the solid (i.e. the soil's particles) are considered as continuum phases. Note that each phase alone is bi-phasic in the sense that the soil contains a given water content and the water flow includes the eroded soil particles in suspension. Both phases are separated by a singular interface. The mass conservation equations of fluid/particle mixture and the eroded particle phase, as well as the balance equation of momentum of the mixture, is applied in order to model both phases. Closure laws are required to model the fluid/solid interface, usually obtained by semi-empirical correlations. The classical surface erosion law, i.e. the linear excess shear-stress law, can be introduced to describe the movement of the fluid/cohesive soil interface (Lachouette et al., 2008). Contrarily to the mono-phasic approach proposed by Mercier et al. (2014) which requires frequent and costly remeshing, the bi-phasic model uses a fixed mesh but the determination of the flow variables at the interface remains however difficult.

It is noteworthy that Lachouette et al. (2008) used a bi-phasic method for modeling the HET of cohesive soils in a laminar flow regime. These authors found that the quantity of eroded mass in the fluid phase is sufficiently small to be considered as negligible. This is very likely due to an obvious separation of the velocity scales as the flow velocity is several orders of magnitude greater than the erosion velocity

prescribed by the erosion law. A mono-phase model (i.e. Eulerian approach with a fixed mesh) for both solid and fluid phases was therefore developed by the authors, where the movement of the interface, due to progressive change in the velocity field, is tracked on the fixed mesh using the Level-Set method proposed by (Stanley and James A., 1988).

1.7.1.3 Triphasic method

A numerical modeling of soil's erosion was first proposed by Vardoulakis et al. (1996). In addition to fluid and solid phases, these authors introduced a third phase, denoted fluidized solid, for which the Darcy-Brinkman equations are implemented. The erosion of the solid phase is described by introducing a source term in the mass conservation equations, which ensures relevant mass exchanges between the soil and fluid phases.

Later, Papamichos and Vardoulakis (2005) proposed another soil's erosion model in the specific context of sand production, a major process in oil industry. The erosion of a granular soil by a laminar flow is modeled by use of the same three-phase concept (Vardoulakis et al., 1996). The overall behavior of the solid matrix (which is erodible, fluid-saturated, and stressed by a fluid flow) is described by mass conservation equations for the three phases. The Darcy law models the poro-elastic system (solid-fluid system) at the equilibrium while a constitutive law for the porous solid medium allows taking into account the rate of eroded mass. The problem is then solved numerically by a Finite element method.

Although this approach is rather relevant for describing the erosion of a saturated granular medium, it is too restrictive to be applied to the erosion of cohesive soils. The erosional mechanisms involved are indeed much more complex in the case of cohesive soils than in the case of grains independent of each other (Mercier, 2013).

Bonelli and Marot (2011) adapted this approach to model the suffusion (one of the internal erosion processes as presented earlier in this chapter), which can be described, at the macroscopic scale, as a source term in the mass balance equations. These authors introduced the previous surface erosion law with a threshold (i.e. the so-called linear excess shear stress law) to take into account eroded mass under the assumption that suffusion, at the micro-scale, can be viewed as a clay/water interface erosion.

1.7.2 Micro/Meso-micro approaches of fluid flow induced erosion

1.7.2.1 DNS/CFD-DEM

CFD-DEM is a computational approach used to model fluid-particle systems. In this method, the particle behavior is modeled by the Discrete Element Method (DEM) that will be extensively detailed in the next chapter. For its part, the fluid flow is computed by solving the Navier-Stokes equations in general CFD (Computational Fluid Dynamics) calculated.

In this method, the Navier-Stokes equations can be volume averaged on a coarse regular grid whose mesh size is mesoscopic, that is larger than the diameter of the individual particles (i.e. a fluid cell usually holds many particles). The solid properties (e.g. porosity, velocity, etc.) are averaged on each cell and introduced as field variables for the continuum equations (i.e. volume averaged Navier-Stokes equations). Note that an empirical correlation for drag and lift forces is required. Among the studies that have been carried out using this approach, we can cite Kuang et al. (2013) who presented a 3D two-way coupling CFD-DEM model of a turbulent round air jet impinging on a granular bed, focusing mainly on the crater formation induced by the air jet.

The CFD-DEM method can be alternatively used to simulate fully resolved fluid-particle problem at the micro-scale for both fluid and particles, meaning that the fluid cell sizes are now smaller than the particle sizes. This method is often referred to DNS-DEM (for Direct Numerical Simulation) and shares some features of LBM-DEM (for Lattice Boltzmann Method) that will be presented hereafter. This method has the great advantage that the hydrodynamic forces acting on the particles are directly calculated by integration of the fluid stresses on the surfaces of the particles without any empirical correlation for drag and lift forces. However, compared to CFD-DEM at meso-scale, it is extremely expensive in term of computational time and resources (number of CPUs, memory consummations) due to the finer mesh needed around the surface of the particles, in order to correctly integrate the fluid stresses, and the frequent re-meshing of the grid to adapt to the new positions of the particles.

Nonetheless, neither of these methods are capable to simulate large deformations because the mesh endures huge distortions. It is for these reasons that particle-based methods, with or without mesh, such as the LBM, the PFV (Pore-scale Finite Volume), and the SPH (Smoothed Particles Hydrodynamics) methods, are preferred for solving small scale problems. All of them can be coupled with other methods to solve fluid-particle interaction problems, especially to the DEM as in the following examples for the LBM-DEM (Cook et al., 2004), the SPH-DEM (Potapov et al., 2001), or the PFV-DEM (Catalano, 2012). These approaches are particularly suited for fluid-solid interface problems with account for large deformations.

1.7.2.2 PFV-DEM

The PFV-DEM coupling is a numerical method for the behavior of dense saturated granular media (Catalano, 2012; Chareyre et al., 2012; Catalano et al., 2014). The method consists of discretizing the pore domain (i.e. complementary to the granular packing) into a connected pore network by a regular Delaunay triangulation and their dual Voronoi graphs as shown in Fig. 1.17. This allows decomposing the pore volume into tetrahedra (in 3D), whereas the centers of the Voronoi cells represent the fluid paths between adjacent pores. In each pore, a linear system is solved combining the continuity equations and the conductance equation, the latter being obtained under the assumption of a linear relation between fluxes and inter-pore gradient, as is the case for a laminar pipe flow. The hydrodynamic forces exerted

on each particle derives from the pressure field through a momentum conservation equation.

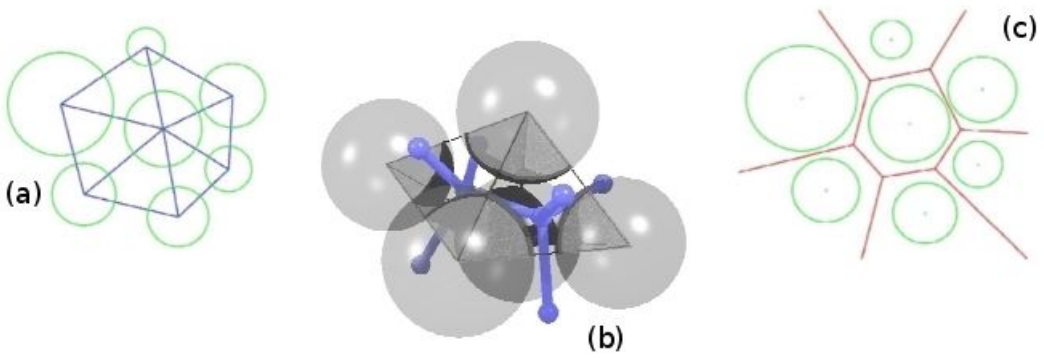

Fig. 1.17. Adjacent tetrahedra in the regular triangulation and dual Voronoi network, in 2D (a,b) and in 3D (c) (Catalano, 2012).

Several applications of the PFV-DEM method can be cited as regards the simulation of soil's erosion. First, Tejada et al. (2016) used a fully coupled DEM-PFV approach in order to investigate the transport of passive particles in porous media. Next, the PFV-DEM method was adapted for describing suffusion, with a focus on the internal instability of the granular media, respectively through a one-way coupling (Aboul Hosn et al., 2018) and a two-way coupling (Wautier et al., 2017).

Despite the advantages offered by this method in decreasing the computational cost by reducing the fluid's degrees of freedom, it remains mainly restricted to simulate internal Stokes (or viscous) fluid flow within compact granular materials. The method loses indeed accuracy whenever large pores exist in the system since it is based on pores discretization. However, quite recently, localized fluidization of grains was consistently modeled (Montellà et al., 2016).

1.7.2.3 LBM-DEM

In recent years, the Lattice Boltzmann Method (LBM) has become one of the most commonly used Computational fluid dynamics (CFD) methods for solving fluid-solid coupling problems. Moreover, when the solid phase is discrete (i.e. solid particles), the LBM was successfully coupled with the discrete DEM approach to model the behavior of granular materials subject to a great variety of fluid flows. Unlike traditional CFD methods, the LBM consists in solving the Boltzmann equation, instead of the Navier-Stokes equations, to simulate the fluid behavior. This method will be given full details in the next chapter. In a few words, the fluid domain in the LBM is partitioned by a fixed regular grid where fictitious fluid particles are represented by probability distribution functions. The movement of these fluid particles is discretized in a limited number of discrete velocity vectors for fluid particle populations. The evolution of the fluid flow is characterized by two main steps (Sukop and Thorne Jr, 2006): a collision step, defined as a process of relaxation towards

an equilibrium state , and a streaming (or propagation) step, where information are exchanged between adjacent cells in terms of momentum and energy.

The major strengths of the LBM lie in its implementation simplicity of the algorithm, its great versatility in dealing with complex boundaries (whether fixed or moving) present in the flow, and also its ability to simulate flows at high Reynolds number. However, owing that the method is based on fluctuations in fluid density, or equivalently fluid pressure since both are related via a state law, simulating incompressible fluid flows imposes the fluid velocity to be kept very small compared to the lattice velocity, in order to reduce the compressibility effect (i.e. small Mach number). Moreover. This method also requires large memory resources and high computational cost, especially when dealing with 3D problems. The method is thus usually limited to small scale applications. However, the LBM-DEM is easily parallelizable and we propose in forthcoming section 2.5 a possible GPU parallelization technique for LBM-DEM.

As regards implementation of the LBM-DEM in modeling geotechnical problems, numerous works can be cited on several practical issues as for instance porous flows (Han and Cundall, 2013), consolidation (Boutt et al., 2007), fluidization of soils (Cui et al., 2014; Ngoma et al., 2018), immersed granular avalanches (Mutabaruka et al., 2014), or hydraulic fracture (Boutt et al., 2007). Concerning more specifically the surface erosion of cohesive soils, the LBM was coupled with the DEM for a 2D modeling of the HET test in the laminar flow regime (Lominé et al., 2013) as well as a micro-mechanical simulation of the 2D laminar impinging jet (Cuéllar et al., 2015, 2017). The latter constitutes the basis for the present study where extended scope and model are proposed.

Given the great advantages offered by the LBM to simulate fluid flows with complex solid boundaries and by the LBM-DEM coupling to model the erosion phenomenon at the grain scale (owing that a precise description of fluid-particle interactions is provided), this approach was adopted in the present work and a far more detailed description of both methods and of the coupling technique is given in next Chapter 2.

Chapter 2

Numerical methods

Contents

2.1 Introduction

As advocated in the previous chapter, the motivation behind the choice of LBM-DEM to model the erosion phenomena of cohesive materials by a fluid flow are that the fluid-particle coupling can be described at the scale of the particles (Micro-scale). Moreover, it should be emphasized the possibility offered by the DEM to introduce cohesive-adhesive contact laws, and the simplicity of LBM to model fluid behavior even in presence of complex moving boundaries.

We provide in this chapter a detailed presentation of DEM for describing the behavior of the granular materials with the possibility to include a solid cohesive bond model. Then, LBM is displayed for describing the fluid phase. Following that, the coupling method between LBM-DEM is explained, to account properly for fluid-particle interaction, as well as the GPU parallelization technique for our LBM-DEM code. Validation of the LBM-DEM coupling in the GPU version of the code is finally implemented.

2.2 Discrete Element Method (DEM)

In the past years, the Discrete Element Method (DEM) has known great and regularly increasing popularity in terms of granular material modelings. This method was introduced by Cundall and Strack (1979) in the 80's, derived from Molecular Dynamic (DM) algorithms. The DEM consists of describing the whole behavior of solid particles by integrating Newton's equations of motion for translation and rotation via explicit numerical schemes. The interactions between particles are controlled by contact models. Note that, in the Molecular Dynamic (DM) approach, a slight penetration between particles is allowed in order to calculate the interaction force. This interpenetration at the contact point can be viewed as a local deformation. On this basis, the contact forces can be determined from simple models such as spring/dash-pot/mass systems.

The numerical integration of Newton's equations for translation and rotation accurately describes the evolution of each particle (positions, velocities, accelerations), defining its instantaneous motion (translation and rotation) in the whole system:

$$m_i \frac{d^2 \boldsymbol{x_i}}{dt^2} = \boldsymbol{F_i}, \quad and \quad I_i \frac{d\boldsymbol{\omega_i}}{dt} = \boldsymbol{T_i} \tag{2.1}$$

where m_i and I_i are the mass and the moment of inertia, $\boldsymbol{x_i}$ and $\boldsymbol{\omega_i}$ are the position and the angular velocity of the grain i. $\boldsymbol{F_i}$ is the total force acting on the particle i and reads:

$$\boldsymbol{F_i} = \sum_{j \neq i} \boldsymbol{F_{ij}} + \boldsymbol{F_i^{ext}} \tag{2.2}$$

with $\boldsymbol{F_{ij}}$ the interaction force applied by grain j on grain i, $\boldsymbol{F_i^{ext}}$ the resulting external force (e.g., gravity $m_i \boldsymbol{g}$ or hydraulic forces in the presence of fluid). The interaction force at the contact between a pair of particles can be decomposed into

two components, normal and tangential, as follows:

$$\boldsymbol{F}_{ij} = F_n \boldsymbol{n} + F_t \boldsymbol{t} \tag{2.3}$$

where $\boldsymbol{n}$ and $\boldsymbol{t}$ are normal and tangential unit vectors of the local origin (at the contact), and can be calculated as:

$$\boldsymbol{n} = \frac{\boldsymbol{x_i} - \boldsymbol{x_j}}{\|\boldsymbol{x_i} - \boldsymbol{x_j}\|} \tag{2.4}$$

$$\boldsymbol{t} = \boldsymbol{z} \wedge \boldsymbol{n} \tag{2.5}$$

with $\boldsymbol{x_j}$ and $\boldsymbol{x_i}$ the position vectors of the grain i and j, respectively.

The contact forces (normal and tangential) plus the corresponding torque are calculated as soon as two particles overlap, which means that $\delta_n \leq 0$, where the overlap δ_n is calculated as follows:

$$\delta_n = \|\boldsymbol{x_i} - \boldsymbol{x_j}\| - r_i - r_j \tag{2.6}$$

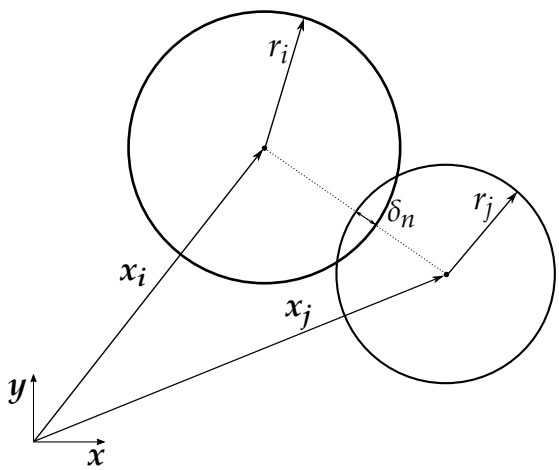

Fig. 2.1. Sketch of two particles at contact with an overlap δ_n. The particle radii are r_i and r_j, respectively.

2.2.1 Frictional contact law

The normal force F_n is calculated based on a visco-elastic linear model (Fig. 2.2a):

$$f_n = -k_n \delta_n - \gamma_n v_n, \qquad F_n = \begin{cases} 0, & f_n \leq 0 \\ f_n, & f_n > 0 \end{cases} \tag{2.7}$$

where $v_n = (\boldsymbol{v_i} - \boldsymbol{v_j}) \cdot \boldsymbol{n}$ is the relative velocity in normal direction, k_n is the normal stiffness and γ_n is the normal viscous damping.

The tangential force at contact F_t is computed using a visco-elastic linear model as well, except that the tangential "shear" force is limited by the Coulomb's friction law $|f_t| \leq \mu_s F_n$ (Fig. 2.2b):

$$f_t = -k_t \delta_t - \gamma_t \frac{d\delta_t}{dt}, \qquad F_t = \begin{cases} \mathrm{sgn}(F_t)\mu F_n, & |f_t| \geq \mu F_n \\ f_t, & |f_t| < \mu F_n \end{cases} \tag{2.8}$$

where k_t is the tangential stiffness, μ_s is the friction coefficient, γ_t is the tangential viscous damping, δ_t is the cumulative relative shear displacement at the contact given by:

$$\frac{d\delta_t}{dt} = v_t = (\boldsymbol{v_i} - \boldsymbol{v_j}) \cdot \boldsymbol{t} - (r_i \boldsymbol{w_i} + r_j \boldsymbol{w_j}) \times \boldsymbol{n} \tag{2.9}$$

where v_t is the relative tangential velocity.

The torque due to friction force is calculated by:

$$\boldsymbol{T_i} = -(r_i \boldsymbol{n}) \times (F_t \boldsymbol{t}) \tag{2.10}$$

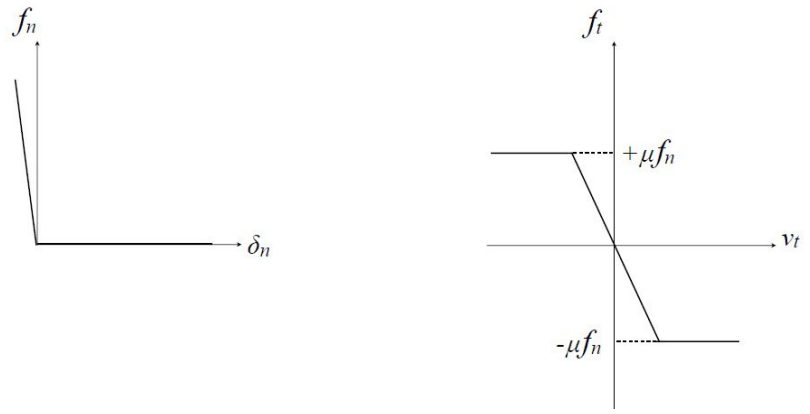

(a) Linear contact model **(b)** Coulomb friction model

Fig. 2.2. Normal and friction contact laws.

Rolling resistance

In reality, it is well known that if a sphere moves by rolling on a horizontal plate with an initial translation velocity, it will stop after a certain distance due to the gradual loss in its kinetic energy. However, this it is not the case in the simulation for perfectly spherical (3D) or circular (2D) particles, which will continue to move indefinitely since the friction force determined by Coulomb's law is null. In order to take energy dissipation during relative rotation into consideration, which is important for dynamic flow conditions, and provide stability in packing particulate system, which is important in static system (Ai et al., 2011), a rolling resistance at the contact is often introduced (Zhou et al., 2001; Ai et al., 2011) as follows:

$$\boldsymbol{T_{roll}} = -\frac{\boldsymbol{v_r}}{|\boldsymbol{v_r}|}\mu_r R_{eff} f_n \tag{2.11}$$

with $\boldsymbol{v_r} = \boldsymbol{\omega_i} - \boldsymbol{\omega_j}$ the rolling velocity ($\boldsymbol{\omega_i}$ and $\boldsymbol{\omega_j}$ being the angular velocities of grain i and j, respectively), $R_{eff} = (r_i r_j)/(r_i + r_j)$ the corrected radius, and μ_r the rolling coefficient.

2.2.2 Additional cohesive contact laws

The DEM rheology (i.e. contact model) introduced above only reproduces the mechanics of frictional contacts. However, there are several rheological models able to introduce cohesion in the material, such as contact cohesion models (e.g. JKR (Johnson et al., 1971) or DMT (Derjaguin et al., 1994)), capillary bridges (Urso et al., 2002) or solid bonds (Delenne et al., 2004). A detailed description of these models can be found in (Radjai and Dubois, 2010).

For the specific case of solid bonds, Delenne et al. (2004) have developed a 2D model based on elastic rheology associated with three degrees of freedom: normal translation δ_n (along normal unit vector $\boldsymbol{n}$), tangential translation δ_t (along tangential unit vector $\boldsymbol{t}$), and rotation angle γ as shown in Figure 2.3. δ_n is the same as in the frictional case (in Eq. 2.6), the other two degrees of freedom can be expressed as follows, with the notations and quantities defined on the sketch of Fig 2.3:

$$\delta_t = \boldsymbol{I}_i \boldsymbol{I}_j \cdot \boldsymbol{t} \tag{2.12}$$

$$\gamma = \theta_i - \theta_j \tag{2.13}$$

where $\boldsymbol{I}_{i,j}$ are the reference point of a cohesive solid bond of particle i and j at the initial configuration (initial overlap). $\theta_{i,j}$ are the rotation angles of particle i and j.

The forces associated with these degrees of freedom are the normal force F_n, the shear force F_t and the bending force M, respectively. These three forces can be applied at the same time at the interaction point and can be calculated only for small displacements and rotation via a linear elastic rheology. The traction-compression, shear, and bending forces are indeed associated by normal, shear, and moment stiffness: $k_{n,b}$, $k_{t,b}$ and $k_{\gamma,b}$. The solid bond law can be written as:

$$\begin{pmatrix} F_n \\ F_t \\ M \end{pmatrix} = -\begin{pmatrix} k_{n,b} & 0 & 0 \\ 0 & k_{t,b} & 0 \\ 0 & 0 & k_{\gamma,b} \end{pmatrix} \begin{pmatrix} \delta_n \\ \delta_t \\ \gamma \end{pmatrix} \tag{2.14}$$

To evaluate these forces, a list of cohesive bonds is initially created at $t = 0$, based on the initial normal overlap $\delta_n < 0$ between particles. The list holds all the cohesive bond information. After exposure to external loads, some cohesive bonds may break. The failure mechanism is based on a parabolic yield surface (ξ_u):

$$\xi_u = \left(\frac{F_n}{C_n}\right) + \left(\frac{F_t}{C_t}\right)^2 + \left(\frac{M}{M_b}\right)^2 - 1 \tag{2.15}$$

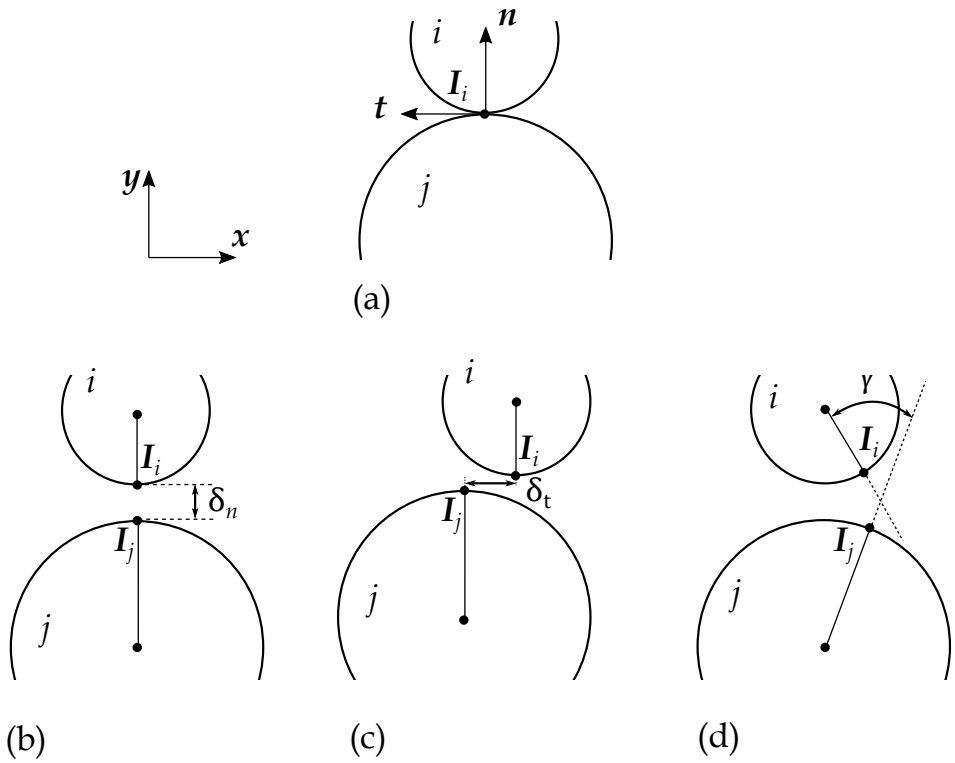

Fig. 2.3. Degrees of freedom of the cohesive solid bond at the local scale: (a) Initial state; (b) Normal displacement; (c) Tangential displacement; (d) Rotation (Delenne et al., 2004).

Initially, the solid bond is intact and follows the elastic rheology. However, the rupture only occurs when the bond solicitation reaches or exceeds the yield surface (i.e. when $\xi_u \geq 0$) and the contact becomes subsequently purely frictional.

It can be seen from the yield surface that the failure mechanism is a combination of the three mechanisms: traction, shearing, and bending. Also, in compression ($\delta_n < 0$), no failure occurs and the normal stiffness is taken as in the purely frictional model $k_{n,b} = k_n$ (i.e. no cohesion).

It is worth emphasizing that this model was calibrated experimentally by Delenne et al. (2004) using cylindrical rollers through a set of comparative numerical and experimental tests (e.g. tension, compression, shearing, and moment, as well as combined tests). Ultimately, the conducted parametric study allowed to fix the threshold parameter values in normal, shear, and bending solicitations: C_n, C_t and M_b, respectively. Moreover, these three thresholds are found to depend on a single parameter C through Mohr-Coulomb failure criterion (Delenne et al., 2004). This

parameter is adapted here to account for particle diameters and reads:

$$C = C_n = 2 \times C_t = \frac{M_b}{0.25 \times d_{mean}} \tag{2.16}$$

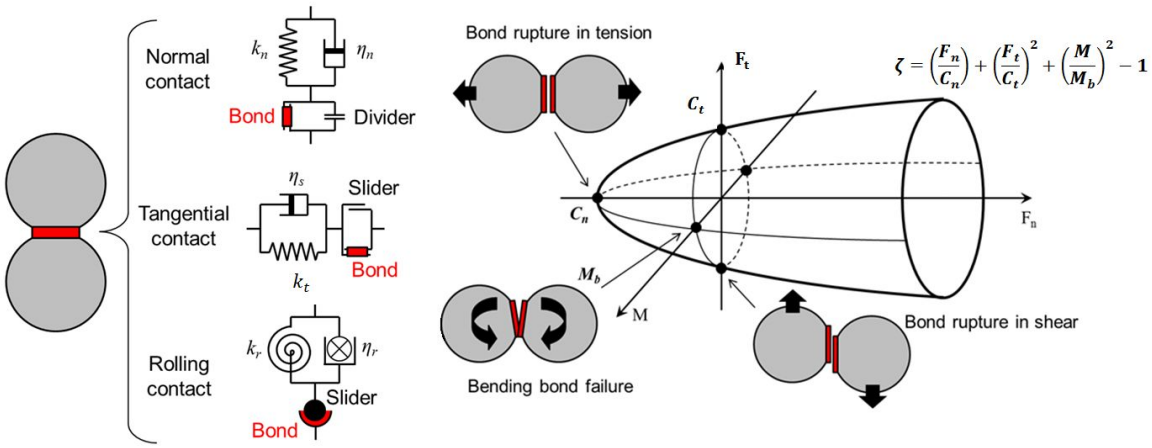

Fig. 2.4. Rheological model of solid contacts (left) and yield surface of cohesive bonds in the space of interaction forces (right). Figure redrawn from (Delenne et al., 2004).

This description holds many features as regards failure mechanisms and can model complex behaviors, such as plasticity and damage at the local scale, through its ability to handle crack formation and propagation inside a cohesive material (Delenne et al., 2004). Also, this model has the possibility to account for a large variety of material behaviors, from brittle clustering materials (low M_b ratios) to "diffusive de-cohesion" (remote debonding, with low C_s ratios) (Philippe et al., 2017).

The solid bond model may be considered as a “static” cohesion approach due to its lack of transience beyond the binary state-disjunctive, where only intact and fully broken bond states are possible, with sudden state transitions (Benseghier et al., 2019). However, this model can be enriched to take into account a gradual evolution, or damage, of the cohesive bond. Among the possibilities, we selected a time-dependent damage model (Silvani et al., 2009), that introduces a damage variable to ensure a progressive evolution of the cohesive bonds over time.

2.2.3 Enrichment with a time-dependent damage model

All the simulations that will be presented in chapter 3 are based on the standard solid bond model detailed in the previous section. However, as will be demonstrated in chapter 4, the addition of a time-dependent damage model was proved convenient and useful to study erosion in moderate shear stress conditions.

This time-dependent damage model allows to degrade the yield surface ξ_u over time to an ultimate interior damage surface ξ_0 as shown in Figure 2.5. The displace-

ment of both surfaces is ensured by a damage parameter d, whose time evolution is given by:

$$\dot{d} = \frac{\langle \xi_0(F_n, F_t, M, d) \rangle}{\eta C_0} \tag{2.17}$$

where $\langle . \rangle$ denotes the MacCauley brackets (i.e. $\langle x \rangle = x$ if $x \geq 0$; $\langle x \rangle = 0$ if $x < 0$), η is a characteristic damage time, $m > 0$ is a softening parameter, and C_0 is the initial damage threshold.

Based on Figure 2.5 which illustrates the time-dependent damage model extended to the cohesion model of Delenne et al. (2004) in the space of normal and shear forces (the third moment space is not presented in the figure for clarity), three main regions can be identified:

1. ($\xi_0 \leq 0$ and $\dot{d} = 0$) corresponds to a cohesive bond with no damage evolution.
2. ($0 < \xi_0$ and $\xi_u < 0$) corresponds to a cohesive bond with a time-dependent damage evolution.
3. ($0 \leq \xi_u$) corresponds to an instantaneous break of the cohesive bond.

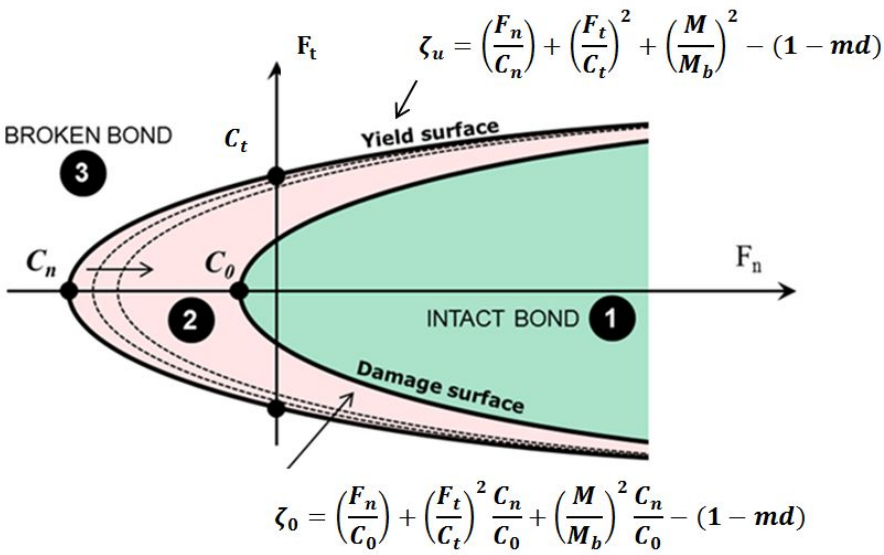

Fig. 2.5. Time-dependent damage model in the space of normal and shear forces. The third dimension (i.e. rolling moment) has not been shown for the sake of simplicity.

Silvani et al. (2009) studied the influence of the damage parameters (η, m, C_0, and C_n) on the evolution of the damage for a system composed of two bonded particles under simple tension test as well as 2D rigid bonded particulate system under oedometric compression test. The main finding for two bonded particles with one parameter being fixed, and the other being varied are as follow:

The characteristic time parameter η is inversely proportional to the evolution rate of damage (i.e. the higher η the longer the breakage will be delayed). Moreover, η is the relevant non-dimensional parameter when the other damage parameters (m, C_0, and C_n) are fixed. On this basis, this parameter will be varied therefore in our study, more specifically in Chapter 4.

2.2.4 Integration scheme

Once all the contact forces and the external forces (e.g. hydraulic forces) are determined at a time t, integration algorithms are required in order to compute the new kinematic variables of the grain i at time $t + \Delta t$. The velocity Verlet integration algorithm (Swope et al., 1982) is used in this study for its implementation simplicity and its numerical stability.

The velocity Verlet integration algorithm for the case of translation and rotation reads:

$$\boldsymbol{x}_i(t + dt) = \boldsymbol{x}_i(t) + \boldsymbol{v}_i(t)dt + \frac{1}{2}\boldsymbol{a}_i(t)dt^2 \tag{2.18}$$

$$\boldsymbol{\theta}_i(t + dt) = \boldsymbol{\theta}_i(t) + \boldsymbol{\omega_i}(t)dt + \frac{1}{2}\dot{\boldsymbol{\omega}}_{\boldsymbol{i}}(t)dt^2 \tag{2.19}$$

The translation and angular velocities are evaluated at an intermediate time step $t + \frac{1}{2}dt$:

$$\boldsymbol{v_i}(t + \frac{1}{2}dt) = \boldsymbol{v_i}(t) + \frac{1}{2}\boldsymbol{a_i}(t) \tag{2.20}$$

$$\boldsymbol{\omega_i}(t + \frac{1}{2}dt) = \boldsymbol{\omega_i}(t) + \frac{1}{2}\dot{\boldsymbol{\omega}}_{\boldsymbol{i}}(t) \tag{2.21}$$

Afterward, the accelerations are obtained, based on Newton's principle in Eq. 2.1.

$$\boldsymbol{a_i}(t + dt) = \frac{1}{m_i}\boldsymbol{F}_i \tag{2.22}$$

$$\dot{\boldsymbol{\omega}}_{\boldsymbol{i}}(t + dt) = \frac{1}{I_i}\boldsymbol{T}_i \tag{2.23}$$

Finally, the velocities at $t + dt$ are corrected as follows:

$$\boldsymbol{v_i}(t + dt) = \boldsymbol{v_i}(t + \frac{1}{2}dt) + \frac{1}{2}\boldsymbol{a}(t + dt)dt \tag{2.24}$$

$$\boldsymbol{\omega_i}(t + dt) = \boldsymbol{\omega_i}(t + \frac{1}{2}dt) + \frac{1}{2}\dot{\boldsymbol{\omega}}_{\boldsymbol{i}}(t + dt)dt \tag{2.25}$$

2.2.5 Numerical stability

In order to obtain a stable simulation and correctly integrate the equations of motion (Eq. 2.1), the time step Δt_{DEM} is chosen below a critical value Δt_{cr} which represents the contact duration (half of the oscillation period) of two overlapping particles with a linear elastic model at the equilibrium. The differential equation of an oscillating mass around the point of contact is:

$$m\ddot{\delta}_n(t) + k_n\delta_n(t) = 0 \tag{2.26}$$

and the analytical solution of the normal oscillation is given by:

$$\delta_n(t) = \delta_n^{max}\sin(\sqrt{\frac{k_n}{m}}(t - t_{cr})) \tag{2.27}$$

The contact duration corresponds to the time difference $\Delta t_{cr} = \pi\sqrt{m/k_n}$ between two successive cancellations of the normal distance. Note that this is only an estimation of the time step, since many contacts can be involved at the same time. In practice, the time step should be chosen smaller than Δt_{cr}, thus a time step factor λ_t is introduced to reduce the time step chosen with λ_t around 0.1. Additionally, Δt_{cr} is calculated based on the smallest mass in the system m_{min} as $\Delta t_{cr} = \pi\sqrt{m_{min}/k_n}$. The DEM time step will finally be:

$$\Delta t_{DEM} = \lambda_t\Delta t_{cr} = \lambda_t\pi\sqrt{m_{min}/k_n} \tag{2.28}$$

In the case of a system with a viscous damping, the critical damping coefficient will be: $\gamma_{cr} = 2\sqrt{mk_n}$. Note that only the under-damped regime is considered here, when $0 \leq \gamma_n < \gamma_{cr}$. Generally, we introduce a coefficient $\lambda_e \in [0, 1[$ which control the damping ratio compared to the critical damping, this coefficient can be calculated can be determined from the coefficient of restitution e as (Ting and Corkum, 1992)

$$\lambda_e = -\frac{ln(e)}{\sqrt{\pi^2 + ln(e)^2}} \tag{2.29}$$

Thus the viscous damping coefficient γ_n will be:

$$\gamma_n = \lambda_e\gamma_{cr} = -\frac{2ln(e)\sqrt{k_n m_{eff}}}{\sqrt{\pi^2 + ln(e)^2}} \tag{2.30}$$

where the effective mass $m_{eff} = m_i m_j/(m_i + m_j)$ and the coefficient of restitution e are chosen between 0 and 1. Note that the normal stiffness k_n is taken sufficiently high to avoid excessive overlap which could affect the overall behavior of the granular assembly.

2.3 Lattice Boltzmann Method (LBM)

2.3.1 A brief history of the LBM

Before describing the Lattice Boltzmann Method, it is worth introducing the historical background and the origin of the method. The LBM was first derived from

the Lattice Gas Automata (LGA) method, also called lattice gas model and Boltzmann's kinetic theory. The LGA is a simplified method to simulate fluid flows, the fluid being described by a set of particles located on a regular lattice (hexagonal and square lattices for FHP and HPP schemes, respectively). During a time step, the fluid particles can solely move and propagate to the nearest nodes, with respect to the lattice shape. Within these conditions, special collision rules are implemented in a given site so that mass and momentum conservation is satisfied. Two main lattice and collision rules were proposed to simulate a given fluid flow. First, a simple LGA model with square lattice (i.e. HPP scheme) was introduced by Hardy et al. (1973). Although, the model was able to ensure mass and momentum conservation, it suffers in retrieving the symmetry of the Navier-Stokes equation. Then, Frisch et al. (1986) introduced the FHP model with an hexagonal lattice to overcome the drawback of HPP.

The motion of particles can be described as a Boolean function $n_i(\boldsymbol{x}, t)$ that describes, at time t, the occupation of a particle at a given site x (a particle is whether present or absent):

$$n_i(\boldsymbol{x} + \boldsymbol{c}_i \Delta t, t + \Delta t) = n_i(\boldsymbol{x}, t) + \Omega_i(\boldsymbol{x}, t), \quad i = 0, ...\alpha, \tag{2.31}$$

where $\boldsymbol{c}_i$ is the discrete velocity of the particle, Δt the time step, and $\Omega_i(x, t)$ a collision operator that includes all possible collisions. α stands for all the available directions (e.g. four for HPP and six for FHP). Equation 2.31 is mainly solved in two steps.

1/ Collision step:

$$n_i^{'}(\boldsymbol{x}, t) = n_i(\boldsymbol{x}, t) + \Omega_i(\boldsymbol{x}, t) \tag{2.32}$$

2/ Streaming step:

$$n_i^{'}(\boldsymbol{x} + \boldsymbol{c}_i \Delta t, t + \Delta t) = n_i^{'}(\boldsymbol{x}, t) \tag{2.33}$$

The macroscopic fluid variables, such as density and velocity, can be derived from the averages of the occupation functions $f_i = \langle n_i \rangle$:

$$\rho = \sum_i f_i, \qquad \rho \boldsymbol{u} = \sum \boldsymbol{c}_i f_i \tag{2.34}$$

It can be seen from the LGA equations that the implementation of the method is straightforward and, since the basic equation rely on Boolean operations, the round-off errors can be eliminated. Despite the advantages offered by the LGA, the method suffers however dramatically from statistical noise due to the use of Boolean variables.

Based on these limitations, the Lattice Boltzmann Equation (LBE) was first introduced by McNamara and Zanetti (1988) in order to reduce the statistical noise found in the LGA by replacing the Boolean variables n_i by the distribution functions f_i, which takes a real-valued number between 0 and 1. Despite the effective improvement, the collision operator used was still nonlinear. Afterward, Higuera and Jiménez (1989) proposed a collision operator linearized around its equilibrium and written in matrix form. However, the equilibrium distribution function was

still derived from the LGA and not from kinetic theory. Finally, a simplified linear collision operator was proposed by Chen et al. (1991); Koelman (1991); Qian et al. (1992), based on the BGK model from kinetic theory. Therefore, the LBE gets completely independent of the LGA and depends only on the Boltzmann equation. Since then, the LBM has become a stand-alone method and has made significant progress in the modeling of complex fluid dynamic problems.

2.3.2 Derivation of the LBE from the Boltzmann equation

We have shown so far that the LBM is no longer based on the LGA, but on the discrete form of the Boltzmann equation. The Boltzmann equation without external force can be written as follows:

$$\frac{\partial f}{\partial t} + \boldsymbol{c}.\nabla_x f = \boldsymbol{\Omega}(f) \tag{2.35}$$

where $f = f(\boldsymbol{x}, \boldsymbol{c}, t)$ represents the particle distribution function at time t, position $\boldsymbol{x}$ and with a velocity $\boldsymbol{c}$. $\boldsymbol{\Omega}(f)$ stands for the collision operator. By introducing the BGK approximation (Bhatnagar et al., 1954), which is based on the assumption that the particle collisions can be described as a relaxation of the particles towards an equilibrium state with a given relaxation time τ_0, the collision operator reads:

$$\boldsymbol{\Omega}(f) = -\frac{1}{\tau_0}\left(f - f_{eq}\right) \tag{2.36}$$

where f_{eq} is the Maxwell-Boltzmann distribution function at equilibrium.

From a numerical point of view, it is difficult to discretize the Boltzmann equation (Eq. 2.35) since a triple discretization is necessary (i.e. in space, velocity, and time). Therefore, certain restrictions are needed. First, the velocity space $\boldsymbol{c}$ is discretized into a finite set of velocities $\boldsymbol{c}_i$ (in a direction i). Hence, the discrete-velocity distribution function can be derived from the distribution function by introducing a weight parameter w_i associated with the velocity $\boldsymbol{c}_i$ as: $f_i(x,t) = w_i f(\boldsymbol{x}, \boldsymbol{c}_i, t)$. Secondly, simple lattice structures (or lattice velocity models) are introduced with space dimension d and q velocity directions, generally denoted as DdQq models (Qian et al., 1992). The models D3Q15, D3Q19 and D3Q27 are the most used for 3D simulation (see Fig. 2.6). For 2D simulations, the classical D2Q9 model is the most common and will be used in this study.

By discretization of the Boltzmann equation (Eq. 2.35) we can write the Lattice Boltzmann equation as follows:

$$f_i(\boldsymbol{x} + \boldsymbol{c}_i \Delta t, t + \Delta t) = f_i(\boldsymbol{x}, t) + \boldsymbol{\Omega}_i(\boldsymbol{x}, t) \tag{2.37}$$

There are many LBM collision models. The simplest one is the Bhatnagar-Gross-Krook (BGK) operator already presented in Eq 2.36 and written as follows on a lattice:

$$\boldsymbol{\Omega}_i^{BGK}(\boldsymbol{x}, t) = -\frac{1}{\tau}\left(f_i(\boldsymbol{x}, t) - f_i^{eq}(\boldsymbol{x}, t)\right) \tag{2.38}$$

where $\tau = \tau_0/\Delta t$.

The equilibrium distribution function f_α^{eq} is given as:

$$f_\alpha^{eq}(\rho, \boldsymbol{u}) = \rho w_\alpha \left[1 + \frac{\boldsymbol{u}.\boldsymbol{c}_\alpha}{c_s^2} + \frac{(\boldsymbol{u}.\boldsymbol{c}_\alpha)^2}{2c_s^4} - \frac{\boldsymbol{u}.\boldsymbol{u}}{2c_s^2}\right] \tag{2.39}$$

where $c_s = c/\sqrt{3}$ is the speed of sound in the lattice system while $c = \frac{\Delta x}{\Delta t}$ is the characteristic lattice speed. The relation between the relaxation time τ and the kinematic viscosity ν of the fluid reads:

$$\tau = \frac{\nu}{\Delta t c_s^2} + \frac{1}{2} \tag{2.40}$$

The density ρ and velocity $\boldsymbol{u}$ of the fluid, can be derived from the distribution function as follows:

$$\rho = \sum_\alpha f_\alpha \tag{2.41}$$

$$\boldsymbol{u} = \frac{1}{\rho} \sum_\alpha f_\alpha \boldsymbol{c}_\alpha \tag{2.42}$$

The fluid pressure is directly given by the following state equation:

$$p = c_s^2 \rho \tag{2.43}$$

As shown in Figure 2.7, in the D2Q9 model referring to two-dimensional space and nine velocity vectors $\boldsymbol{c}_\alpha$, the discrete velocities are defined as:

$$\boldsymbol{c}_\alpha \begin{cases} (0,0) & \alpha = 0 \\ (1,0),(0,1),(-1,0),(0,-1) & \alpha = 1,2,3,4 \\ (1,1),(-1,1),(-1,-1),(1,-1) & \alpha = 5,6,7,8 \end{cases} \tag{2.44}$$

where the weights are $w_0 = 4/9$, $w_\alpha = 1/9$ for $||c_\alpha|| = 1$, and $w_\alpha = 1/36$ for $||c_\alpha|| = \sqrt{2}$.

Eq. 2.37 with the BGK collision operator is classically solved in two main steps:
1/ Collision step:

$$f_\alpha^{out}(\boldsymbol{x}, t) = f_\alpha(\boldsymbol{x}, t) + \Omega_\alpha^{BGK} \tag{2.45}$$

2/ Streaming step:

$$f_\alpha(\boldsymbol{x} + \boldsymbol{c}_\alpha \Delta t, t + \Delta t) = f_\alpha^{out}(\boldsymbol{x}, t) \tag{2.46}$$

where f_α^{out} represents the post-collision distribution function.

Note that the LB equation (Eq. 2.37) can retrieve the incompressible Navier-Stokes equation when the Mach number is small compared to unity ($Ma << 1$). The Mach number is defined as the ratio of the maximum velocity to the lattice speed $c = (\Delta x)/(\Delta t)$.

Notwithstanding the simplicity of the BGK collision model and its rapidness for calculations, it suffers from well-known stability issues, particularly for high Reynolds number or, equivalently, when τ approaches 0.5. However, these deficiencies can be overcome using more complicated collision models such as two or multi-relaxation collision models.

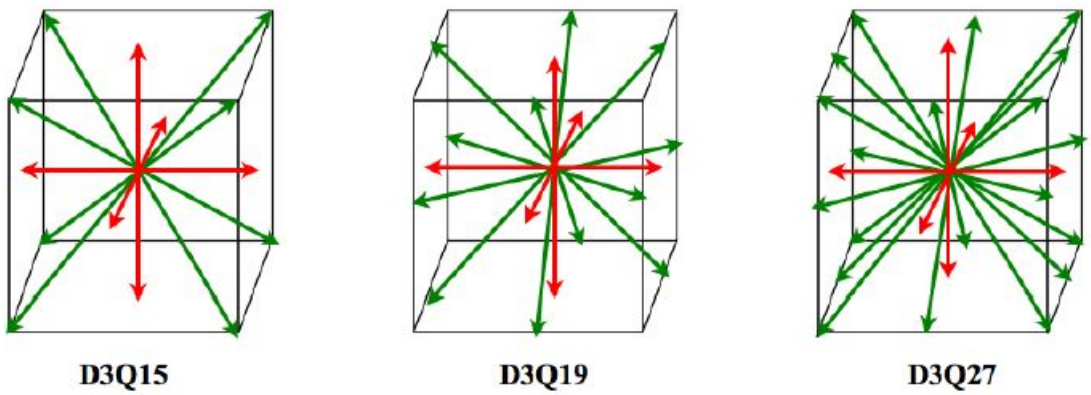

Fig. 2.6. 3D lattice models.

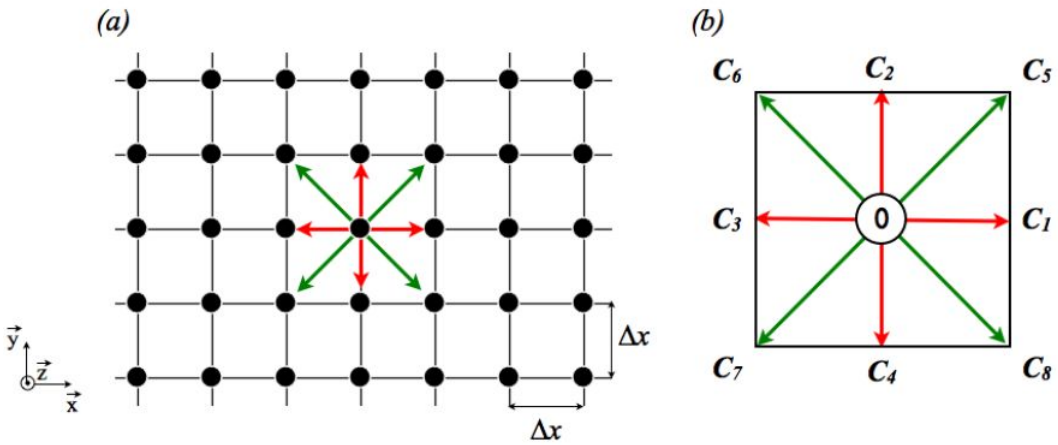

Fig. 2.7. (a) Uniform structured grid. (b) D2Q9 lattice model.

2.3.3 More sophisticated collision operators

2.3.3.1 Two Relaxation Time (TRT)

The two-relaxation-time (TRT) collision operator was proposed by Ginzburg et al. (2008). The probability distribution function is now decomposed into positive and negative parts:

$$f_\alpha = f_\alpha^+ + f_\alpha^- \qquad f_\alpha^{eq} = f_\alpha^{eq,+} + f_\alpha^{eq,-}$$

$$f_\alpha^+ = \frac{f_\alpha + f_{\bar{\alpha}}}{2} \qquad f_\alpha^{eq,+} = \frac{f_\alpha^{eq} + f_{\bar{\alpha}}^{eq}}{2}$$

$$f_\alpha^- = \frac{f_\alpha - f_{\bar{\alpha}}}{2} \qquad f_\alpha^{eq,-} = \frac{f_\alpha^{eq} - f_{\bar{\alpha}}^{eq}}{2}$$

where $\bar{\alpha}$ stands for the opposite direction of the index α. The TRT collision operator is therefore calculated as:

$$\Omega_\alpha^{TRT} = -\omega^+ \left(f_\alpha^+(\boldsymbol{x},t) - f_\alpha^{eq,+}(\boldsymbol{x},t)\right) - \omega^- \left(f_\alpha^-(\boldsymbol{x},t) - f_\alpha^{eq,-}(\boldsymbol{x},t)\right) \tag{2.47}$$

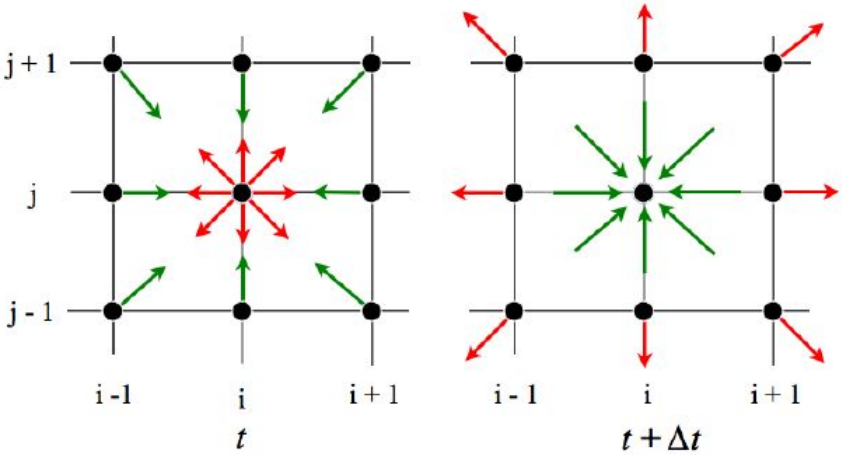

Fig. 2.8. Streaming step.

where $\omega^+ = 1/\tau$ and ω^- is a constant to be tuned in order to find a stable condition for a given simulation. However, it is often calculated based on the so-called "magic" parameter $\Lambda = (1/\omega^+ - 1/2)(1/\omega^- - 1/2)$. It was found indeed that the magic parameter $\Lambda = 1/4$ provides the most stable simulations (Ginzburg et al., 2010). It therefore will be used in the present work.

The LBE with the TRT collision model reads:

$$f_\alpha(\boldsymbol{x} + \boldsymbol{c}_\alpha \Delta t, t + \Delta t) = f_\alpha(\boldsymbol{x}, t) - \omega^+ \left(f_\alpha^+(\boldsymbol{x}, t) - f_\alpha^{eq,+}(\boldsymbol{x}, t)\right) - \omega^- \left(f_\alpha^-(\boldsymbol{x}, t) - f_\alpha^{eq,-}(\boldsymbol{x}, t)\right) \tag{2.48}$$

2.3.3.2 Multi-Relaxation Time (MRT)

The idea of this model is that the moments $\boldsymbol{m}$ of the distribution functions can be relaxed with different relaxation times. In contrast to the BGK and the TRT operators, the collision step is carried out in the moment space instead of using the distribution functions directly. The link between the distribution function vector $\boldsymbol{f} = [f_0, f_1, \ldots, f_8]^T$ and their moment vector $\boldsymbol{m} = [\rho, e, \epsilon, j_x, q_x, j_y, q_y, P_{xx}, P_{xy}]^T$ is ensured by the invertible transformation matrix $\boldsymbol{M}$ as:

$$\boldsymbol{m} = \boldsymbol{M}\boldsymbol{f} \tag{2.49}$$

Note that the elements of the moment vector $\boldsymbol{m}$ consist of conserved and non-

conserved quantities. Eq. 2.49 can be defined in matrix form as:

$$\begin{pmatrix} \rho \\ e \\ \epsilon \\ j_x \\ q_x \\ j_y \\ q_y \\ P_{xx} \\ P_{xy} \end{pmatrix} = \begin{pmatrix} 1 & 1 & 1 & 1 & 1 & 1 & 1 & 1 & 1 \\ -4 & -1 & -1 & -1 & -1 & 2 & 2 & 2 & 2 \\ 4 & -2 & -2 & -2 & -2 & 1 & 1 & 1 & 1 \\ 0 & 1 & 0 & -1 & 0 & 1 & -1 & -1 & 1 \\ 0 & -2 & 0 & 2 & 0 & 1 & -1 & -1 & 1 \\ 0 & 0 & 1 & 0 & -1 & 1 & 1 & -1 & -1 \\ 0 & 0 & -2 & 0 & 2 & 1 & 1 & -1 & -1 \\ 0 & 1 & -1 & 1 & -1 & 0 & 0 & 0 & 0 \\ 0 & 0 & 0 & 0 & 0 & 1 & -1 & 1 & -1 \end{pmatrix} \begin{pmatrix} f_0 \\ f_1 \\ f_2 \\ f_3 \\ f_4 \\ f_5 \\ f_6 \\ f_7 \\ f_8 \end{pmatrix} \tag{2.50}$$

where ρ is the fluid density, e is the energy, ϵ is related to energy square, $j_x = \rho u_x$ and $j_y = \rho u_y$ are the x and y components of momentum j, P_{xx} and P_{xy} are the diagonal and off-diagonal components of the stress tensor, q_x and q_y are the x and y components of the energy flux.

The multi-relaxation-time lattice Boltzmann equation can be written as:

$$f_\alpha(\boldsymbol{x} + \boldsymbol{c}_\alpha \Delta t, t + \Delta t) = f_\alpha(\boldsymbol{x}, t) - M^{-1}\boldsymbol{S}\left[m_\alpha(\boldsymbol{x}, t) - m_\alpha^{eq}(\boldsymbol{x}, t)\right] \tag{2.51}$$

where $\boldsymbol{S}$ is the diagonal relaxation matrix $\boldsymbol{S} = diag\left[s_0, s_1, s_2, s_4, s_4, s_5, s_6, s_7, s_8\right]$. For the D2Q9 model, the coefficients $s_{1,2,4}$ are constants, to be chosen in the range $[0, 2]$ for stability reasons, and $s_7 = s_8 = 1/\tau$, where τ is the relaxation time as in the BGK scheme (Eq. 2.40). It should also be mentioned that $s_{0,3,5}$ have no effect on the calculation because these relaxation values are directly related to collision invariants ρ and $\rho\boldsymbol{u}$. Practically, they are set equal to zero.

Note that, in this context, the BGK and the TRT collision models are particular cases of the MRT scheme: all the coefficients on the diagonal of $\boldsymbol{S}$ are identical (i.e, $s_0, s_1, \ldots, s_8 = 1/\tau$) for BGK; all even-order moments (i.e, $\rho, \epsilon, q_x, q_y, P_{xy}$) are relaxed with ω^+ and odd moments (i.e, e, j_x, j_y, P_{xx}) with ω^- for TRT.

After Lallemand and Luo (2000), the following relaxation rates are used in the rest of this manuscript: $s_1 = 1.63$; $s_2 = 1.14$; $s_4 = s_6 = 1.92$.

Finally, the equilibrium moment vector $\boldsymbol{m}^{eq}$ is defined as:

$$m^{eq} = \begin{pmatrix} \rho \\ -2\rho + 3(j_x^2 + j_y^2)/\rho \\ \rho - 3(j_x^2 + j_y^2)/\rho \\ j_x \\ -j_x \\ j_y \\ -j_y \\ (j_x^2 - j_y^2)/\rho \\ j_x j_y/\rho \end{pmatrix} \tag{2.52}$$

2.3.4 Nondimensionalization (Working with units)

For the sake of simplicity, the key implementation element of the LBM is to work with Lattice units instead of using directly the real physical units. For example, the

time and space steps in lattice units are equal to unity $\bar{\Delta t} = \bar{\Delta x} = 1$. Objectively, it can be ambiguous to work with lattice units. However, some rules can be applied to convert from lattice to physical units and *vice versa*. These rules are summarized in Table 2.1.

Variables	Physical	Lattice	Relationship
Density	ρ	$\bar{\rho} = 1$	$\rho = \rho_0 \bar{\rho}$
Space stap	Δx	$\bar{\Delta x} = 1$	-
Time step	Δt	$\bar{\Delta t} = 1$	-
Lattice speed	$c = \frac{\Delta x}{\Delta t}$	$\bar{c} = 1$	-
Coordinates	$\boldsymbol{x}$	$\bar{\boldsymbol{x}}$	$\boldsymbol{x} = \bar{\boldsymbol{x}} \Delta x$
Time	t	$\bar{t}$	$t = \bar{t} \Delta t$
Velocity	$\boldsymbol{u}$	$\bar{\boldsymbol{u}}$	$\boldsymbol{u} = c\bar{\boldsymbol{u}}$
Kinematic viscosity	ν	$\bar{\nu}$	$\nu = \bar{\nu} c \Delta x$
Force	$\boldsymbol{F}$	$\bar{\boldsymbol{F}}$	$\boldsymbol{F} = \rho c^2 \Delta x \bar{\boldsymbol{F}}$
Torque	$\boldsymbol{T}$	$\bar{\boldsymbol{T}}$	$\boldsymbol{T} = \rho c^2 \Delta x^2 \bar{\boldsymbol{T}}$

Table 2.1. Table illustrating the conversion from physical to dimensionless (i.e. lattice) quantities.

2.3.5 Boundary conditions

In the LBM, the pressure or velocity boundary conditions can not be directly imposed, as they derive from the particle distribution functions f_α. Thus, the unknown distribution functions must be defined to set the desired values of the hydrodynamic quantities at the boundary nodes.

Non-slip boundary conditions (Bounce-back) The so-called bounce-back scheme imposes the non-slip boundary condition between the fluid and a stationary solid wall. The wall is supposed to be located between solid and fluid nodes, exactly in the middle. During the streaming step, the wall boundary nodes will reflect back any incoming distribution of neighboring fluid nodes into the opposite direction. Called half-way bounce-back, this scheme has proven to give a second order numerical accuracy (Zou and He, 1997). The explicit form of the half-way bounce-back, as illustrated in Fig. 2.9, is: $f_7 = f_3$, $f_8 = f_4$, $f_1 = f_5$. The general numerical form reads:

$$f_{\bar{\alpha}}(\boldsymbol{x_b}, t + \Delta t) = f_\alpha^{out}(\boldsymbol{x_b}, t) \tag{2.53}$$

Pressure and velocity boundary conditions Pressure and velocity boundary conditions can be set using the method proposed by Zou and He (1997), which is based on the assumption that the non-equilibrium part of a distribution function

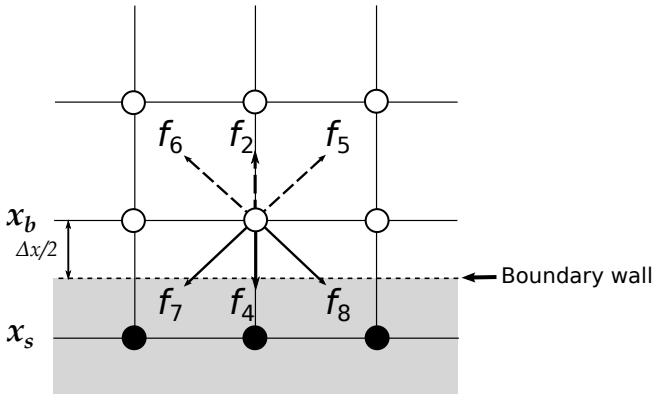

Fig. 2.9. Bounce-back boundary condition at a bottom wall, where the boundary wall is located in the middle between solid (solid circles) and fluid nodes (open circles). The grey shaded domain is the wall region and the dashed line corresponds to its boundary while $\boldsymbol{x_b}$ and $\boldsymbol{x_s}$ denote boundary fluid and solid nodes, respectively. The dashed arrows represent the reflected distribution.

normal to the boundary is supposed to be constant. To find the unknown distribution functions at the boundary, a system of equations must be solved.

To explain the method, we consider, for example, a pressure BC at the top of a domain as illustrated in figure 2.10. Therefore, the density needs to be specified ($\rho = \rho_0 = P_0/c_s^2$) while the velocity reads $\boldsymbol{u} = \begin{bmatrix} 0 \\ v \end{bmatrix}$. From Eq. 2.41 and 2.42, the following relations can be obtained, respectively:

$$f_4 + f_7 + f_8 = \rho_0 - (f_0 + f_1 + f_2 + f_3 + f_5 + f_6) \tag{2.54}$$

$$f_4 + f_7 + f_8 = \rho_0 v - (f_2 + f_5 + f_6) \tag{2.55}$$

$$0 = f_1 + f_5 + f_8 - (f_6 + f_3 + f_7) \tag{2.56}$$

To solve this system of 3 equations with 4 unknowns (f_4, f_7, f_8, and v), an additional equation is needed. After Zou and He (1997), the gap from equilibrium of normal functions (f_2 and f_4) at the boundary is supposed constant:

$$f_2 - f_2^{eq} = f_4 - f_4^{eq} \tag{2.57}$$

Finally, by solving the system, one gets:

$$\begin{aligned}
v &= 1 - \frac{(f_0 + f_1 + f_3) + 2(f_2 + f_5 + f_6)}{\rho_0} \\
f_4 &= f_2 - \frac{2}{3}\rho_0 v \\
f_7 &= f_5 + \frac{1}{2}(f_1 - f_3) - \frac{1}{6}\rho v \\
f_8 &= f_6 - \frac{1}{2}(f_1 - f_3) - \frac{1}{6}\rho v
\end{aligned}$$

In this context, it is possible, by simply changing the control variable (i.e. $\boldsymbol{u}$ is imposed and ρ is unknown), to impose velocity boundary conditions of Neumann type (flux Boundary), with the presumption that the velocity component parallel to the boundary is always zero. The unknown quantities: ρ, f_4, f_7, and f_8 can be derived after arranging the equations as below:

$$\begin{aligned}
\rho &= \frac{(f_0 + f_1 + f_3) + 2(f_2 + f_5 + f_6)}{1 + v_0} \\
f_4 &= f_2 - \frac{2}{3}\rho_0 v \\
f_7 &= f_5 + \frac{1}{2}(f_1 - f_3) - \frac{1}{6}\rho v \\
f_8 &= f_6 - \frac{1}{2}(f_1 - f_3) - \frac{1}{6}\rho v
\end{aligned}$$

Despite the fact that the Zou & He boundary condition was found to be second-order accurate, the method lacks in stability at high Reynolds numbers (Latt et al., 2008). However, here again, many alternative methods are available to efficiently impose pressure or velocity. Two methods are detailed below and were used in this study, namely regularized and equilibrium methods.

Regularized method The regularized method is an alternative method for imposing pressure or velocity boundary conditions, which was proposed by Latt et al. (2008) for enhancing stability at the boundary without affecting the accuracy. The particle populations on the boundary are split into two parts, equilibrium and non-equilibrium, and their values are replaced by the following equations:

$$f_\alpha = f_\alpha^{eq}(\rho, \boldsymbol{u}) + \frac{w_\alpha}{2c_s^4}\boldsymbol{Q}_\alpha : \boldsymbol{\Pi}^{(1)} \quad for \quad \alpha = 0, .., 8 \tag{2.58}$$

where w_α are the lattice weights and $\Pi^{(1)}$ is the reconstructed first order stress tensor from the known off-equilibrium parts of the particle population $f_\alpha^{neq} = f_\alpha - f_\alpha^{eq}(\rho, \boldsymbol{u})$:

$$\Pi^{(1)} = \sum_{i=0}^{8} \boldsymbol{c}_\alpha \boldsymbol{c}_\alpha f_\alpha^{neq} \tag{2.59}$$

The unknown part of f_α^{neq} will take the value of the known parts in opposite direction ($f_\alpha^{neq} = f_{opp(\alpha)}^{neq}$) while the tensor $\boldsymbol{Q}_\alpha$ is defined as: $\boldsymbol{Q}_\alpha = \boldsymbol{c}_\alpha \boldsymbol{c}_\alpha - c_s^2 \boldsymbol{I}$.

On the D2Q9 model and in the inlet boundary located at the top of the domain, as shown in Fig. 2.10, the $\boldsymbol{\Pi}^{(1)}$ can be reconstructed from the known non-equilibrium populations:

$$\begin{aligned}
\Pi_{xx}^{(1)} &= f_6^{neq} + f_2^{neq} + 2(f_7^{neq} + f_1^{neq}) \\
\Pi_{yy}^{(1)} &= 2(f_1^{neq} + f_8^{neq} + f_7^{neq}) \\
\Pi_{xy}^{(1)} &= 2(f_7^{neq} - f_1^{neq})
\end{aligned} \tag{2.60}$$

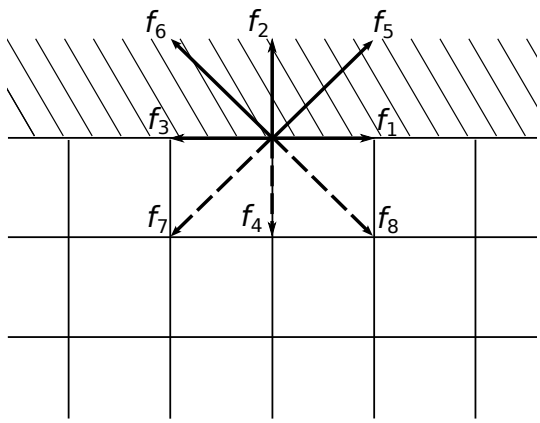

Fig. 2.10. Inlet boundary located at a top boundary. The dashed vectors represent the unknown populations.

Equilibrium boundary conditions It is possible to impose either pressure or vVelocity directly by reconstructing all the particle populations (known and unknowns) by their equilibrium parts as follows:

$$f_\alpha = f_\alpha^{eq}(\rho, \boldsymbol{u}) \quad for \quad \alpha = 0, .., 8 \tag{2.61}$$

However, an extrapolation between the boundary nodes and the nearby fluid nodes is required to obtain additional information at the boundary. Namely, we extrapolate velocity when imposing pressure and *vice versa*. The equilibrium boundary was found to be less precise than both the Zou & He method (Zou and He, 1997) and the regularized method, as demonstrated in Figure 3.3b, but far much easier to implement.

2.3.5.1 Wall shear stress

The wall shear stress exerted by the fluid on a given surface can be calculated using the deviatoric shear stress tensor τ_{xy}, which, for a two-dimensional incompressible flow, is given by:

$$\tau_{xy} = \rho\nu(\partial_x u_y + \partial_y u_x) \tag{2.62}$$

To calculate the wall shear stress, a linear extrapolation is used to evaluate the velocity gradient at the wall. For the case of horizontal wall (located at $y = 0$) and if $\frac{du_y}{dx}$ is supposed negligible, the wall shear stress will be:

$$\tau_{xy,w} = \rho\nu \left.\frac{du_x}{dy}\right|_{y=0} \tag{2.63}$$

In the LBM, the shear stress tensor can be calculated from the non-equilibrium part of the distribution functions as proposed by Mei et al. (2002):

$$\tau_{xy} = (1 - \frac{1}{2\tau}) \sum_\alpha f_\alpha^{neq}(\boldsymbol{x}, t)\,(c_{\alpha,x} c_{\alpha,y}) \tag{2.64}$$

where $f_\alpha^{neq} = f_\alpha - f_\alpha^{eq}$ while $c_{\alpha,x}$ and $c_{\alpha,y}$ are the x and y components of the velocity vector α, respectively.

Since, in our case, the wall surface boundary is not located on a fluid node, we linearly extrapolate the shear stress to the wall boundary as follows :

$$\tau_{xy,w} = \tau_{xy}^{y=1} + \Delta(\tau_{xy}^{y=1} - \tau_{xy}^{y=2}) \tag{2.65}$$

where $y = 1$ and $y = 2$ are the locations, in lattice units, of the two nearest neighbors fluid nodes in the normal direction from the wall. Δ is the relative distance from the fluid node to the wall (see Fig. 2.11). Since the half-way bounce-back scheme is used, Δ is expected to be equal to 0.5.

Mei et al. (2002) found that using the non-equilibrium part of the distribution functions to calculate the shear stress (Eq. 2.64) is more accurate than using directly the velocity gradient.

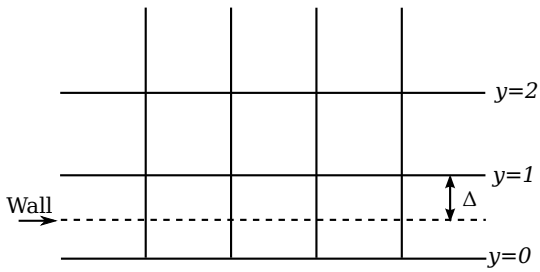

Fig. 2.11. Illustration of the location of the wall

2.4 Fluid-Particle interaction

The main advantage of the LBM is its simplicity and robustness when it comes to fluid-solid interactions, with simple but also complex shapes, while keeping the numerical errors small with reasonable computational costs.

As presented previously, the LBM is based on a regular static grid in which the nodes are regarded as fluid nodes. Furthermore, the boundary conditions presented so far are either located exactly at the boundary node, or in the middle at the adjacent cell, while the boundaries are rather stationary. On this basis, several questions can be raised: How does the LBM deal with arbitrary shapes? What if the boundaries move? How to couple the LBM with other different solvers?. However, to answer these questions, several techniques and algorithms were developed in the past years such as the Bouzidi scheme and the Partially Saturated Method (PSM) to apply non-slip condition at moving and/or arbitrary-shaped solid boundary. What they share in common is the idea to map the solid domain (i.e. the DEM particles) into the fluid domain (i.e. the LBM nodes) by changing the state of the lattice nodes: solid node if it is occupied by a particle and, oppositely, fluid node.

2.4.1 Momentum exchange method with the Bouzidi scheme

The non-slip condition can be applied to fluid-solid interactions via the bounce-back scheme in the restricted case of circular particles in our study. In addition, for moving particles (or solids), the bounce-back scheme can be improved by some adjustments proposed by Lallemand and Luo (2003). However, this condition considers that the solid boundary is located in the middle between solid and fluid nodes. Therefore, the exact boundary is represented by a staircase approximation shape. To solve this issue, Bouzidi et al. (2001) has proposed a modified bounce-back scheme to retrieve roughly the exact curvature of the boundary through linear interpolation, involving post-collision distribution functions and using two-fluid nodes $\boldsymbol{x}_f$ and $\boldsymbol{x}_{ff}$, as shown in Fig.2.12. The Bouzidi scheme considers two interpolation situations

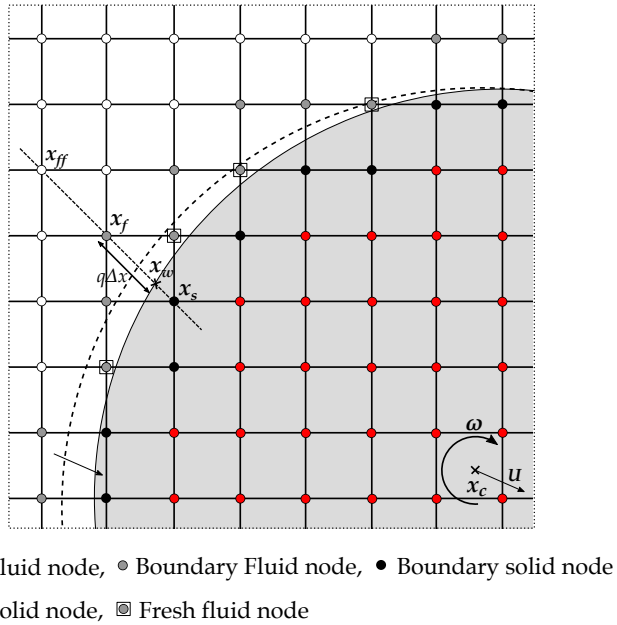

Fig. 2.12. Representation of a moving particle where the dash line stands for the previous position of the particle. As a consequence, fresh fluid nodes appear as depicted by the open squares.

(Eq. 2.66), based on the relative distance $q = \dfrac{|\boldsymbol{x}_f - \boldsymbol{x}_w|}{|\boldsymbol{x}_f - \boldsymbol{x}_x|}$ between the boundary fluid node $\boldsymbol{x}_f$ and the solid intersection point $\boldsymbol{x}_w$:

$$\begin{cases} f_{\bar{\alpha}}(\boldsymbol{x}_f, t+\Delta t) = 2q f_{\alpha}^{out}(\boldsymbol{x}_f, t) + (1-2q) f_{\alpha}^{out}(\boldsymbol{x}_{ff}, t) + 2 w_\alpha \rho_w \frac{\boldsymbol{c}_{\bar{\alpha}} \boldsymbol{u}_w}{c_s^2}, & q < 1/2 \\ f_{\bar{\alpha}}(\boldsymbol{x}_f, t+\Delta t) = \frac{1}{2q} f_{\alpha}^{out}(\boldsymbol{x}_f, t) + \frac{(2q-1)}{2q} f_{\bar{\alpha}}^{out}(\boldsymbol{x}_f, t) + \frac{1}{q} w_\alpha \rho_w \frac{\boldsymbol{c}_{\bar{\alpha}} \boldsymbol{u}_w}{c_s^2}, & q \geq 1/2 \end{cases} \tag{2.66}$$

where $\boldsymbol{c}_{\bar{\alpha}}$ is the opposite direction of $\boldsymbol{c}_\alpha$ and $\boldsymbol{u}_w$ is the wall velocity at the intersection point $\boldsymbol{x}_w$. This velocity $\boldsymbol{u}_w$ is computed from the particle velocity $\boldsymbol{U}$, the angular velocity $\boldsymbol{\omega}$, and the center of mass $\boldsymbol{x}_c$:

$$\boldsymbol{u}_w = \boldsymbol{U} + \boldsymbol{\omega} \times (\boldsymbol{x}_w - \boldsymbol{x}_c) \tag{2.67}$$

One of the issues associated with this scheme deals with the situation where the solid boundary is in motion. As a consequence, some of the solid nodes may convert to fluid nodes and the unknown distribution functions must therefore be recovered. Several techniques were proposed by Lallemand and Luo (2003) to address this problem. In this study, the unknown distribution functions of the fresh fluid nodes are simply approximated using the equilibrium distribution function $f_\alpha^{eq}(\rho, \boldsymbol{u}_w)$, computed using the averaged fluid density in the system, that fluctuates around 1, and the wall velocity at the specified node position just before it converts into a fluid node (Mansouri et al., 2017).

The total forces acting on a given particle by the fluid are calculated by summation of the momentum-exchange between the solid boundary nodes and the fluid nodes, based on the momentum exchange algorithm (Ladd, 1994):

$$\boldsymbol{F} = \sum_{all\,\boldsymbol{x}_f} \sum_{\alpha} \left[f_\alpha^{out}(\boldsymbol{x}_f, t) + f_{\bar{\alpha}}(\boldsymbol{x}_f, t + \Delta t) \right] \boldsymbol{c}_\alpha \tag{2.68}$$

The total torque reads:

$$\boldsymbol{T} = \sum_{all\,\boldsymbol{x}_f} \sum_{\alpha} (\boldsymbol{x}_w - \boldsymbol{x}_c) \times \left[f_\alpha^{out}(\boldsymbol{x}_f, t) + f_{\bar{\alpha}}(\boldsymbol{x}_f, t + \Delta t) \right] \boldsymbol{c}_\alpha \tag{2.69}$$

2.4.2 Partially saturated method (PSM)

Another possible method, called the Partially Saturated Method (PSM) and proposed by Noble and Torczynski (1998), is adapted in this study for applying the non-slip boundary condition to moving solid boundary nodes. It is based on the local solid fraction ε of each lattice cell that can be fluid ($\varepsilon = 0$), solid ($\varepsilon = 1$), or mixed (i.e. partially saturated with $0 < \varepsilon < 1$), as shown in Figure 2.13. Since there is no interpolation used in this method and no explicit object mapping, the parallelization is straightforward and makes the method best candidate to be used in GPU (CUDA) as will be presented in forthcoming section 2.5. The PSM is based on the following modified BGK equation:

$$f_\alpha(\boldsymbol{x} + c_\alpha \Delta t, t + \Delta t) = f_\alpha(\boldsymbol{x}, t) + (1 - B)\Omega_\alpha^{BGK} + B\Omega_\alpha^s \tag{2.70}$$

where Ω_α^s is the additional collision operator for solid nodes that depends on the solid fraction ε and reads:

$$\Omega_\alpha^s = (f_{\bar{\alpha}}(\boldsymbol{x}, t) - f_{\bar{\alpha}}^{eq}(\rho, \boldsymbol{u})) - (f_\alpha(\boldsymbol{x}, t) - f_\alpha^{eq}(\rho, \boldsymbol{u_s})) \tag{2.71}$$

where $\boldsymbol{u}$ and $\boldsymbol{u_s} = \boldsymbol{u_p} + \boldsymbol{\omega} \times (\boldsymbol{x} - \boldsymbol{x_c})$ are the local fluid velocity and the particle velocity at a given location x.

$$\Omega_\alpha^s = f_\alpha^{eq}(\rho, \boldsymbol{u_s}) - f_\alpha(\boldsymbol{x}, t) + (1 - \frac{1}{\tau})(f_\alpha(\boldsymbol{x}, t) - f_\alpha^{eq}(\rho, \boldsymbol{u})) \tag{2.72}$$

Noble and Torczynski (1998) proposed two possibilities to calculate the local weighting parameter B as a function of the local solid fraction ε:

$$B(\varepsilon, \tau) = \frac{\varepsilon(\mathbf{x}, t)(\tau - 1/2)}{[1 - \varepsilon(\mathbf{x}, t)] + (\tau - 1/2)} \tag{2.73}$$

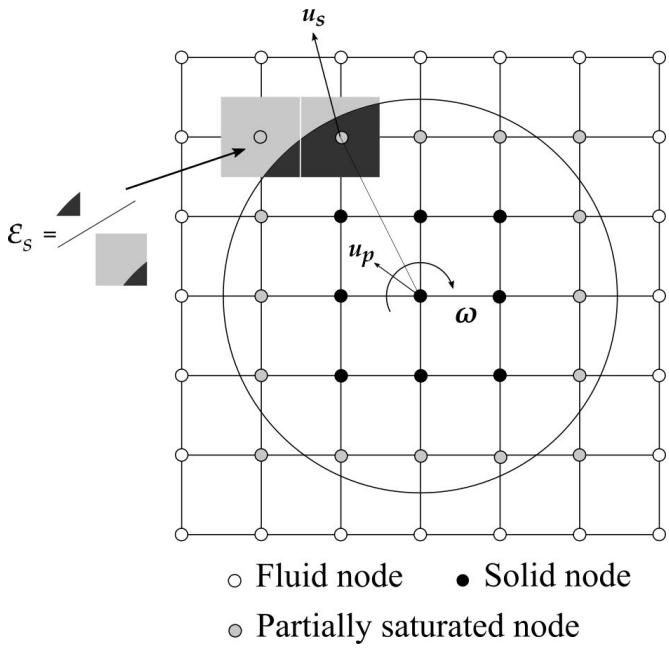

Fig. 2.13. Sketch of the Partial Saturation Method (PSM), redrawn from Wang et al. (2017).

$$B(\varepsilon, \tau) = \varepsilon(\mathbf{x}, t) \tag{2.74}$$

In the case of many particles, with s solid intersects with a given cell, the lattice solid fraction will be $\varepsilon(\mathbf{x}, t) = \sum_s \varepsilon_s(\mathbf{x}, t)$, thus $B(\varepsilon, \tau) = \sum_s B_s(\varepsilon_s, \tau)$.

Solid fraction calculation: As pointed out above, the PSM is highly dependent on the evolution of the local solid fraction at each time step and for each cell. This part can be very expensive (computationally speaking) for complex-shaped particles. Fortunately, we are dealing here with circular particles where the intersection with the square cell and the particle can be calculated analytically. Practically, the solid fraction ε can be estimated in several ways. The simplest one, that will be used here, consists in dividing the lattice cell into several small cells (sub-cells) and then count the sub-cells that are solid thus the solid fraction will be the total number of solid sub-cells divided by the number of sub-cells in the lattice cell n_{sub}^2 (in 2D) (see Fig. 2.14).

Fluid-solid interaction force The force and torque acting on the boundary can be computed as proposed by Cook et al. (2004):

$$\boldsymbol{F}(t) = \frac{\Delta x^2}{\Delta t} \sum_{\boldsymbol{x_n}} B(\boldsymbol{x_n}) \sum_{\alpha} \Omega_\alpha^s(\boldsymbol{x_n}) \boldsymbol{c_\alpha} \tag{2.75}$$

$$\boldsymbol{T}(t) = \frac{\Delta x^2}{\Delta t} \sum_{x_n} B(\boldsymbol{x_n})(\boldsymbol{x_n} - \boldsymbol{x_c}) \times \sum_{\alpha} \Omega_\alpha^s(\boldsymbol{x_n}) \boldsymbol{c_\alpha} \tag{2.76}$$

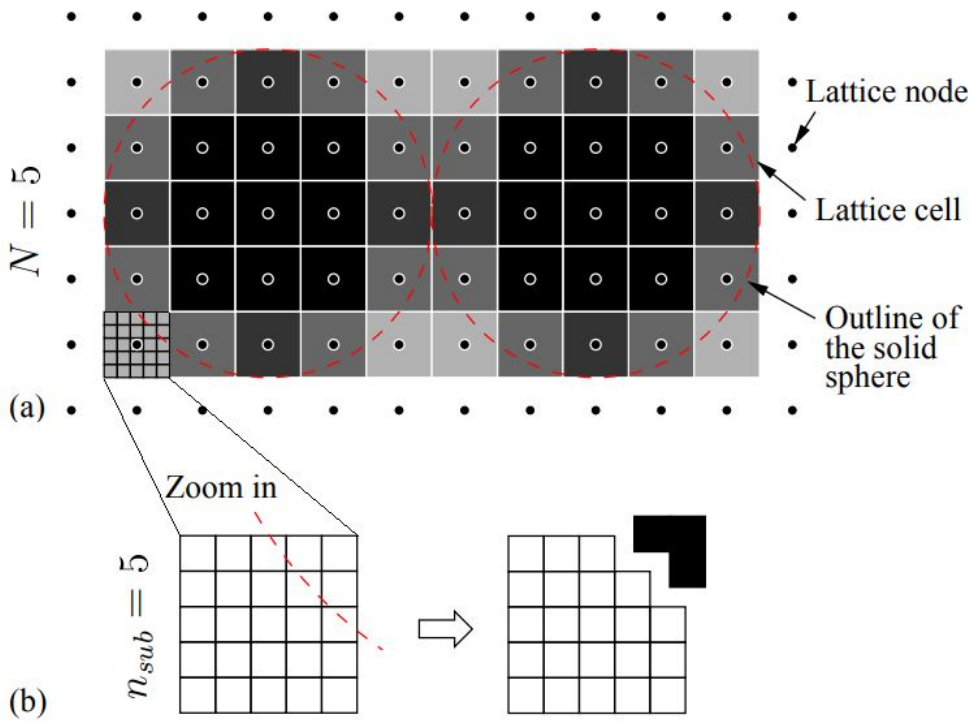

Fig. 2.14. (a) Distribution of the solid fraction ε represented by gray-scale values, from white ($\varepsilon = 0$, fluid) to black ($\varepsilon = 1$, solid cells). The red dashed lines represent two particles boundaries. (b) Zoom on a partially saturated cell where the solid fraction ε is calculated via a cell decomposition method with 5 sub-slices (Yang et al., 2018).

where $\boldsymbol{x_n}$ stand for all the lattice nodes which are totally, or partially, solid (i.e. all nodes with $\varepsilon > 0$) and $\boldsymbol{x_c}$ is the location of the center of mass of the particle.

Further improvement As already mentioned, the BGK collision model has some deficiencies and since the PSM method is based on the BGK model, we propose here to use the TRT collision model instead. Thus Equation 2.70 becomes:

$$f_\alpha(\boldsymbol{x} + \boldsymbol{c_\alpha}\Delta t, t + \Delta t) = f_\alpha(\boldsymbol{x}, t) + (1 - B)\Omega_\alpha^{TRT} + B\Omega_\alpha^s \tag{2.77}$$

As with the Lattice Boltzmann equation with the BGK scheme (Eq. 2.37), Eq. 2.70, or equivalently Eq. 2.77, is solved in two main steps as follows: Collision step:

$$f_\alpha^{out}(\boldsymbol{x}, t) = f_\alpha(\boldsymbol{x}, t) + (1 - B)\Omega_\alpha^{BGK;TRT} + B\Omega_\alpha^s \tag{2.78}$$

Streaming step:

$$f_\alpha(\boldsymbol{x} + \boldsymbol{c}_\alpha\Delta t, t + \Delta t) = f_\alpha^{out}(\boldsymbol{x}, t) \tag{2.79}$$

2.4.3 Coupling approach for LBM-DEM

The LBM-DEM coupling technique used in this study is fully-resolved (or four-way coupling), meaning that we take into account both the particle-fluid and the particle-

particle interactions. As regards the effect of particles on fluid, it is modeled by applying non-slip boundary conditions whether by the PSM or the Bouzidi scheme. Therefore, the resulting total force and torque (Eqs. 2.68 and 2.69 for the Bouzidi scheme or Eqs. 2.75 and 2.76 for the PSM scheme) are introduced in the DEM calculation using Eq. 2.1 after conversion to physical units (see Table 2.1).

It should be noted that the buoyancy effect is also introduced by simply multiplying the gravitational acceleration by $(1 - \rho/\rho_g)$.

2.4.3.1 Space and time discretization

The LBM-DEM coupling imposes certain restrictions on both sides (fluid and solid), such as the choice of space and time steps in order to maintain a stable simulation. For the solid part, only the time step can be imposed. For the LBM calculation, the situation is much complicated since space and time discretizations of fluid depend on the physical phenomena to be modeled. As we have shown, the time and space steps and the relaxation time τ for the LBM are directly related to the physical kinematic viscosity ν (Eq. 2.40) while the space discretization is straightforwardly linked to the particle diameter $d/\Delta x$. For the case of poly-disperse particles, d is chosen as the smallest diameter of the particles d_{min}. The space resolution should be fixed high enough to minimize the computational errors in the hydraulic force calculation. The resolution ratio $d_{min}/\Delta x$ is set at 10 in order to obtain an accurate force evolution on a given particle as recommended by Yu et al. (2003). This ratio sets the discretization parameter Δx.

To correctly simulate an incompressible flow, it is required that the computational Mach number $Ma = |u_{max}|/c_s$ should be kept small compared to unity, which means that the maximum velocity in the system u_{max} should be smaller enough compared to the sound speed c_s. Usually the limit value is set to $Ma \leq 0.1$ after the literature. However, once the lattice velocity $c = \Delta x/\Delta t$ is correctly fixed the Mach number remains below 0.1.

From these values of the fluid viscosity ν and of the discretization parameter Δx from the known solid (particles) domain, Δt is finally derived.

2.4.3.2 Sub-cycling

As we have shown above, the LBM and the DEM have different time steps and, despite the restrictions in the fluid part, the DEM time step is often smaller than the LBM time step. However, both approaches can always be combined with the introduction of the sub-cycle concept for the DEM calculation (Han et al., 2007). This concept allows to perform more than one DEM cycle before going to the next LBM step. The number of the DEM cycles can be introduced by an integer parameter n_p, which can be calculated as follows:

$$n_p = \frac{\Delta t_{LBM}}{\Delta t_{DEM}} \tag{2.80}$$

In practice, the parameter λ_t introduced in section 2.2.5 is slightly modified for n_p to be an integer. In the present study, n_p has a maximal value of 2.

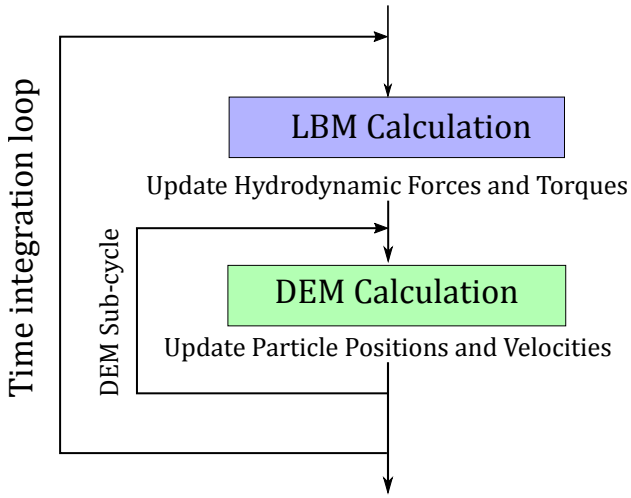

Fig. 2.15. Diagram illustrating the sub-cycling in the LBM-DEM time loop.

2.4.3.3 Hydraulic radius

A 2D densely packed disk sample under gravity has a very low porosity and prevents the fluid to pass through pores, giving rise to a zero permeability. To address this issue, a hydraulic radius r_h for the grains is introduced in the LBM calculation while the reference radius r is kept unchanged in the DEM part. This idea was first introduced by Boutt et al. (2007) and Cui et al. (2012) who both recommended a ratio r_h/r equal to 0.8.

It is worth noting that this concept not only solves this problem, allowing a finite non-zero permeability in the system but makes it possible also to correct the interpolation of the post-collision distribution between fluid nodes in the Bouzidi scheme and avoid high solid fraction calculations in the PSM scheme, when two particles overlap.

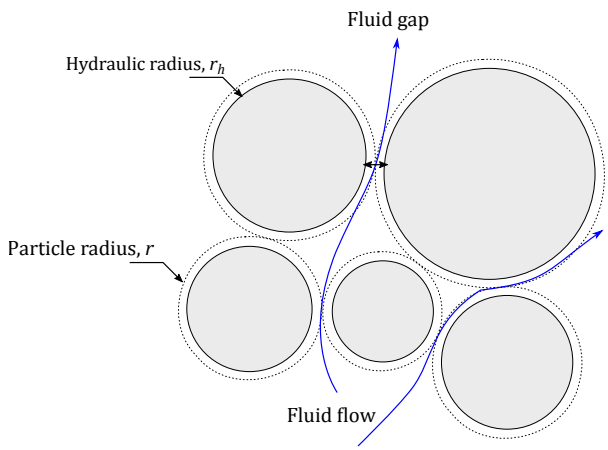

Fig. 2.16. Illustration of the hydraulic radius solution.

2.5 Gpu parallelization

In the previous sections, we have described the two different numerical methods, one for simulating discrete particles (DEM) and the other for fluid flow (LBM), and the coupling techniques between both methods. We have also shown that both methods are explicit in time and easily "parallelizable".

The applications of the LBM-DEM are still restricted to small-scales academic studies. This is partly due to the extremely high computational cost involved for the discrete simulations of soils at a representative scale (e.g. millions of soil grains interacting with a structure) in combination with the necessary high refinement degree of the fluid mesh in order to fully resolve the flow around the solid particles (around 10 to 30 fluid divisions per grain diameter depending on the application, see (Tran et al., 2017)).

However, this limitation on modeling large scale engineering problems is being gradually overcome by means of the high-performance parallel computation (HPC), which addresses these issues by domain decomposition, efficient distribution of data among the multiple processors, synchronization protocols, and local communication between neighboring processors/domains. There are several parallelization techniques that can be used such as OpenMP (Open Multi-Processing), which is based on shared memory architecture, and Message Passing Interface (MPI) which allows the program to run in several non-shared memory systems (CPU clusters). Regardless of the difference of both libraries, both are CPU based libraries (i.e. designed to allow the code to run in multiple CPU processors). Due to the slow increase in the CPU performance over the past years compared to the GPU performance, which increases dramatically, and based on the advantages offered by the GPUs, we have chosen the GPU parallelization technique.

Before diving into the parallelization chapter, it is worth clarifying the history of the numerical code that will be used in this study. First, the serial LBM-DEM code was developed during the PhD thesis work of J. Ngoma (2011-2014) (Ngoma, 2015; Ngoma et al., 2018), written in C/C++ programming language. Next, P. Cuéllar (Cuéllar et al., 2015, 2017) enriched the code with the cohesion and time-dependent damage models during a one year post-doc position (2014-2015).

Concerning the new development made during this thesis, the Partially saturated method (PSM) was first added into the code before the parallelization of the CPU version of the code. The programming environment used is CUDA (Compute Unified Device Architecture) which allows NVIDIA GPUs to execute programs written in C, C++, FORTRAN, and other programming languages. A typical CUDA code comprises a set of *kernels* [1]. The kernel execution is divided first into grid of *blocks* (see Fig. 2.17). A block consists of a group of threads, each thread within a block executes instantaneously the kernel in parallel. A unique ID is assigned to each block and thread, thus the data in the GPU memory is easily accessible using block and thread indices. Also, the data is stored in both CPU memory and GPU global memory to allow transfer. Furthermore, CUDA programming is based on the idea

[1] Functions to be executed in parallel on the GPU

that the main parts of the code that are parallelizable, or segments that are susceptible to be computationally expensive (e.g. the collision step in LBM or collision detection phase in DEM, etc), should be rewritten in separate kernels. Thus, in this work, the main parts of the initial (serial) code are rewritten in CUDA in order to exploit the full potential of the GPU: both DEM and LBM parts, as well as the coupling technique, are rewritten in separate kernels. The implementation technique will be explained in the following sections and the validity of the implementation is briefly discussed in terms of classical benchmark cases, namely the drag coefficient of a settling particle as well as the so-called DKT phenomenon (draft-kiss-tumble trajectories) of a pair of settling grains.

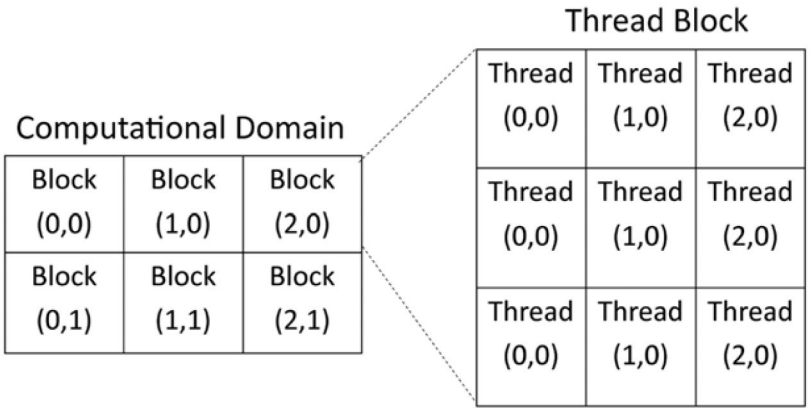

Fig. 2.17. Blocks and threads in CUDA.

2.5.1 Parallelization of the DEM part

In this section, we explain the main parallelization technique of the DEM part of the code. The method can be summarized in the time integration loop shown in Figure 2.18. The method can be divided into three main parts. First, the positions and velocities of the particles are updated based on known forces. Then the contacts are detected and the interaction forces computed. Note that this part is very expensive in terms of computational time. However, several techniques can be used to speed-up the calculation. Two different algorithms for contact detection are explained in the following section. The last part deals with the calculation of acceleration and subsequent velocity correction. In part 1 and 3 the parallelization is straightforward since each thread will be assigned to one particle. The second part requires more complex parallelization techniques.

2.5.1.1 Data structure

The CUDA programming requires that the data should be declared in memory in a coalesced manner. Therefore, we adapted our data structure from an Array Of Structure (AOS) to a Structure Of Array (SOA) to allow efficient memory access.

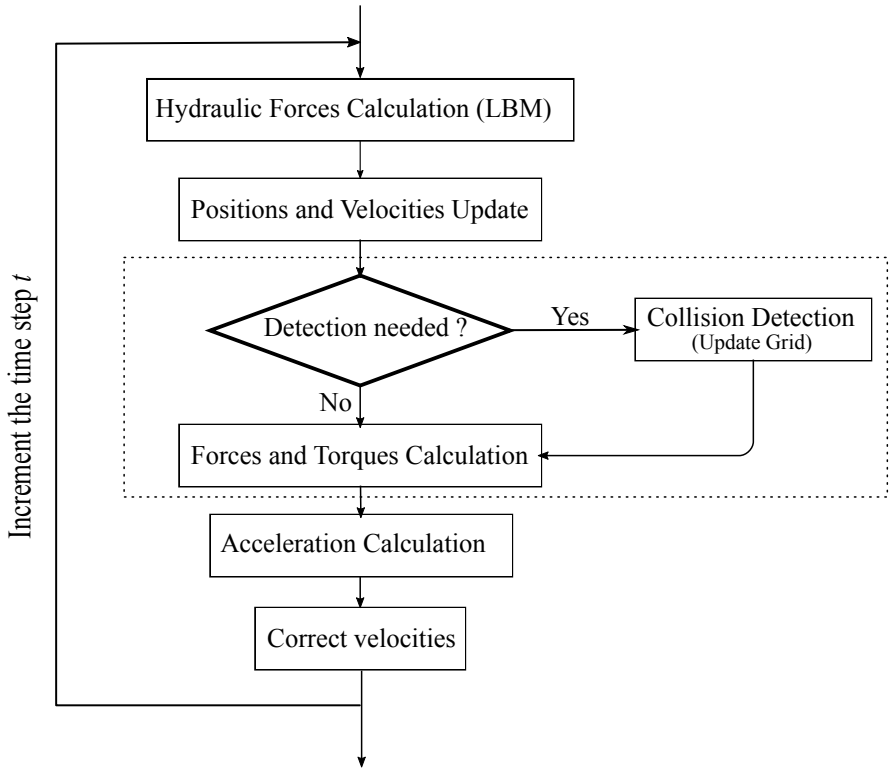

Fig. 2.18. Illustration of the DEM algorithm. The collision detection part is showed inside dashed rectangle.

In other words, all state variables (ID, positions, velocities, accelerations, etc) are stored in arrays of size N_p [2] and organized in a common structure as shown in Figure 2.19.

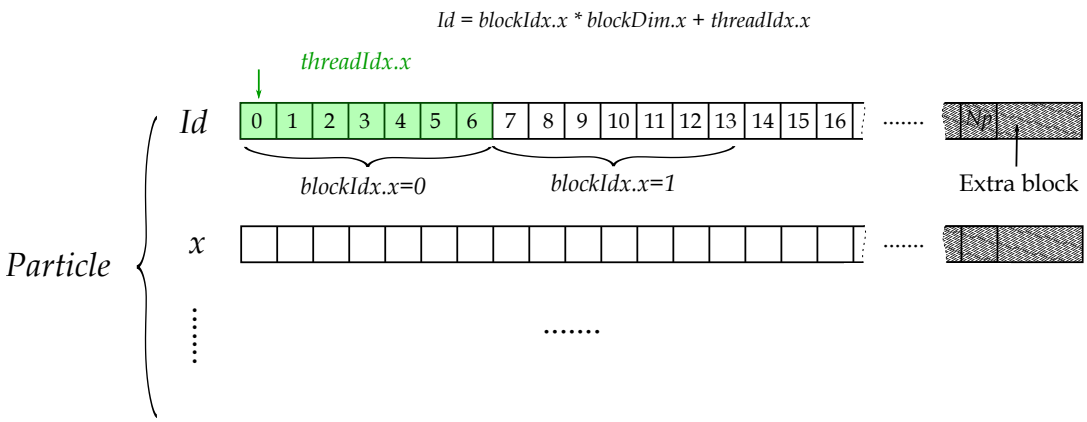

Fig. 2.19. Illustration of particle structure: Decomposition into blocks and threads inside a CUDA kernel and data load from global memory.

[2] N_p is the number of particles

2.5.1.2 Collision Detection

Collision detection is a fundamental part of the DEM calculation and also the most expensive one, since the DEM requires to evaluate the distance between particles at each time step, or frequently, to check whether they overlap or not. In the case of overlapping particles, the distance will be used later to calculate the interaction forces. A naive inefficient approach, by evaluating all the distances between a particle i and all $N_p - 1$ others, results in a great complexity of $O(N_p^2)$. Therefore, an efficient algorithm for neighboring search is needed to shorten this very expensive process. Fortunately, there are several approaches to be used, based on the restriction of the calculations to only a small number of pairs, listed hereinafter.

Verlet lists

The Verlet lists algorithm, as shown in Fig. 2.20(a), consists of storing for each particle i a list of neighbors that are situated in a distance d_v. The collisions are performed on the stored pairs if there is an overlap. The neighboring list should be updated frequently. This algorithm can reduce the computational costs up to $O(\frac{N_p(N_p-1)}{2})$ iterations and is much adapted for serial calculation in (CPU).

Linked-Cell list

The Linked-Cell list presented in Fig. 2.20(b) consists of dividing the computational domain into cells (sub-domains). The particles IDs are assigned to the cells based on their center point. The Linked-Cell list is much adapted for GPUs and it is implemented here.

The Linked-Cell list algorithm can be summarized as follows. First, we go through the particles inside the collision detection kernel then we get the cell ID that holds the particle. The collision process will be performed only on the neighboring cells ($3 \times 3 = 9$) in total and for the particles that have smaller ID number ($i < j$), since the contact forces between two overlapping particles are equal in magnitude and opposite in direction ($F_i = -F_j$) [3]. This algorithm reduces the calculation up to $O(N_p)$ times. This method is much adapted to equal sized particles and for a low polydispersity. However, for broad particle size distributions, an adaptive cell division is required in function of the grain sizes.

For a low polydispersity, as is the case in the present study, the cells discretization should be at least the size of the largest particle in the population. The grid resolution is set at $\Delta x_{DEM} = 2.1 \times r_{max}$ and each cell will contain probably a maximum number of particles set at 5, which is explicitly defined.

As in the Verlet list, the algorithm needs to be updated frequently, thus it is scheduled every 100 time steps. Note that this value is set optionally, for the reason that particles do not move that much inside the fluid and to avoid rebuilding the grid at each time step and ultimately reducing the computational cost.

[3] It was observed that doing half of the collision we do not gain in overall performance as it seems. This is maybe because of the atomic operation used to increment forces.

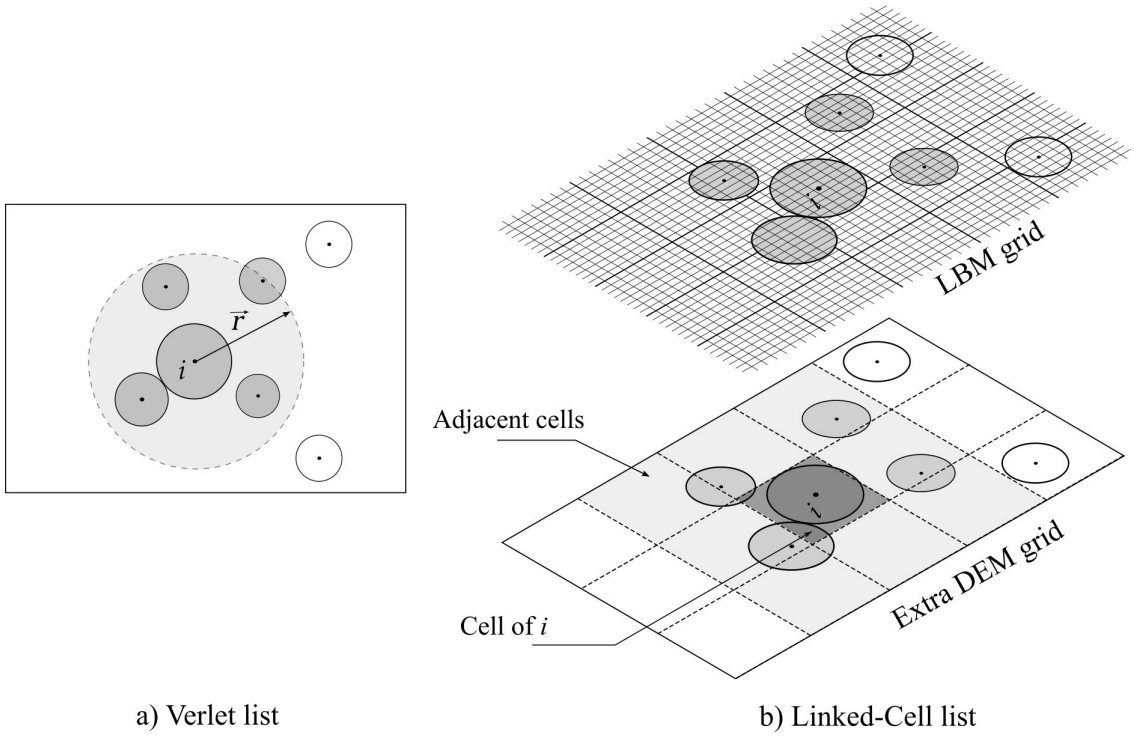

Fig. 2.20. Alternative choices for neighboring search algorithms: (a) Verlet list; (b) Linked-cell list, where the computational domain is divided into an additional cell-grid for the DEM particles with a cell-size of $2.1 \cdot r_{max}$ possible interactions for a given particle i are only explored for the particles contained in the adjacent (grey) cells

2.5.1.3 Mechanical behaviour of the contacts

After detecting the collision, a device (GPU) functions will be launched depending on the two particles state whether cohesive "collideCohparticles" or dry "collideDryparticles". For the cohesive case, the cohesive bond state will be checked first to determine if it is active or not. Checking a cohesive bond state requires a special data structure, which will be explained in the following subsection.

Cohesive bond data structure

The same procedure can be used for the identification of cohesive bonds in the case of bonded granular sample, where the particular bond data (i.e. bond state, strength, orientation, etc..) can be stored in the lower part of a symmetric matrix structure with both dimensions equal to the number of particles. For further efficiency, the storage of this big sparse bond matrix can be done using a Compressed Sparse Column format (CSC). The idea is to decompose the sparse matrix into three lists: the first "indices" contains the row indices corresponding to the non-zero values (neighboring bonded particles), the second "data" contains the non-zero values (cohesive bond information), and the third "indptr" stores the indices where each column starts. The format used is first explained by the following 11x11 matrix and the

corresponding schematic as illustrated in Figs. 2.21 and Fig. 2.22. For symmetry reasons, only the lower part of the sparse cohesive matrix is used to construct the three lists (indices, data, and indptr) based on the initial overlap, before entering into the time loop.

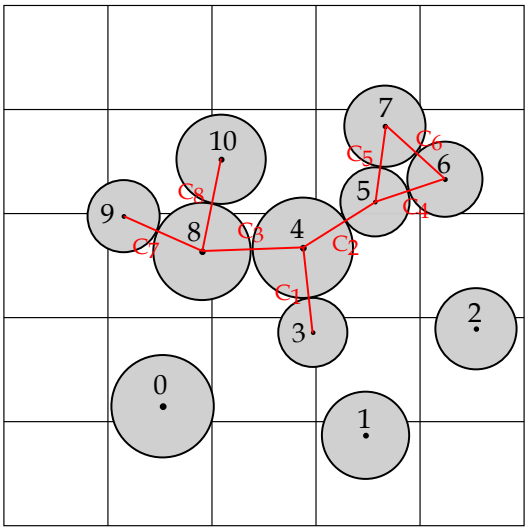

Fig. 2.21. Schematic illustrating an assembly of particles. The red line represents the cohesive bonds and the bonds are labelled from C_1 to C_8.

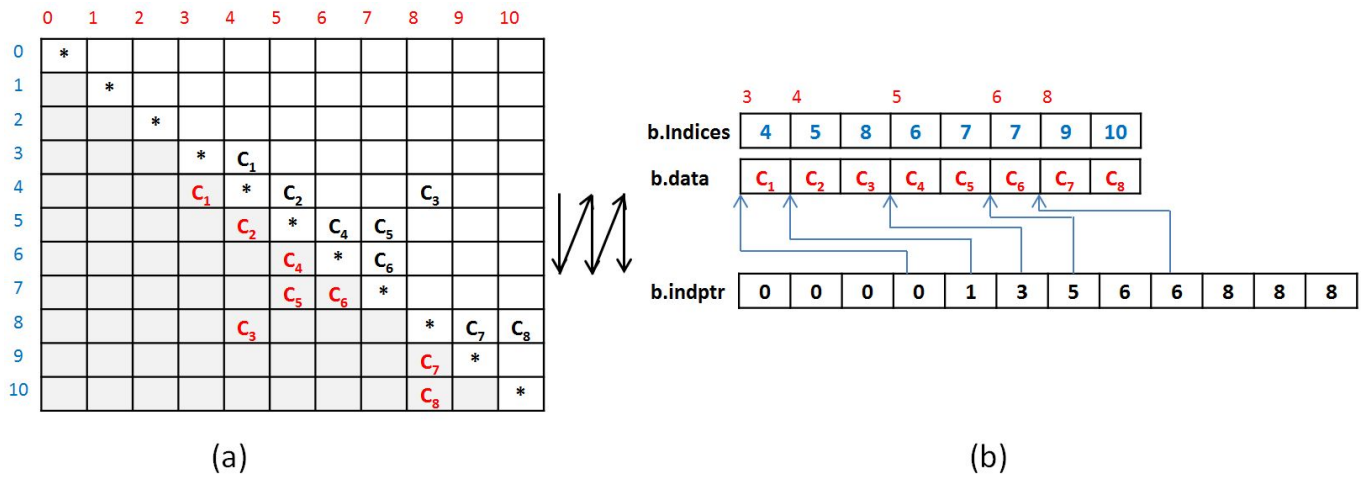

Fig. 2.22. (a) Illustration of the symmetric sparse bond matrix generated based on the cohesion bonds as shown in Fig. 2.21. (b) Corresponding CSC matrix structure.

The following listing shows the function that gets the ID of the cohesive bond from two pairs of particles i and j. If there is a cohesive link between the two particles, the function will return an integer > 0 otherwise -1 will be returned. The function can be used either in the host (CPU) or in the device (GPU).

Listing 2.1. Function that get a bond Id

```
__host__ __device__ int GetIdbond(int i, int j, int * indptr, int * id) {
    int idbond=-1;
    int nbcurgrain=indptr[i+1]-indptr[i];//Number of cohesive bonds linked to i
    for (int k=0; k<nbcurgrain; k++) {
        if (nbcurgrain>0){
        if (id[indptr[i]+k]==j){
            idbond=k+indptr[i];
            break;
        }
        }
    }
    return idbond;
}
```

2.5.2 Parallelization of the LBM part

As in the DEM part, the LBM steps are also divided into a set of kernels, which are then executed by the threads. The implementation is designed so that each thread operates at one location in the fluid domain (i.e. one thread for each lattice node) Obrecht et al. (2013). In contrast to the DEM, the two-dimensional LBM domain will be divided into a grid of two-dimensional CUDA blocks, each block is divided into arrays of threads running the same tasks in parallel. The parallel threads inside the blocks are fixed at (16×16). Note that this value is optional and it could be $(N_{threads,X} \times N_{threads,Y} < 1024)$ for most of the current graphic cards. Moreover, there is an optimal value where the peak performance can be reached and it is recommended to use a multiple of the warp size value (32 threads).

The total number of blocks are controlled by the LBM domain, N_x and N_y respectively in the x and y directions. Extra blocks (or buffers) are added in case the LBM domain would be larger than the GPU grid at the end of the domain in x and y directions. A return condition is set when the thread is in the extra buffer (layer). Doing so, we avoid access to non declared (undesired) memory location. Fig. 2.23 shows a two-dimensional example of threads and blocks. The division of threads and blocks can be in one, two or three dimensions[4].

The probability distribution functions $f_\alpha(\boldsymbol{x}, t)$ are then stored as a single array in the GPU global memory and it can be addressed as:

$$f[i + j \times Nx + \alpha \times Nx \times Ny] \tag{2.81}$$

where i and j are the x and y location of the LBM grid, respectively. These locations can be addressed from the GPU grid as shown in Eq. 2.82. Two copies of f are used, one for post collision f_{out} and the other for after streaming step f_{in}. Using two copies, we ensure that the data dependency is not violated.

$$\begin{aligned} i &= blockIdx.x \times blockDim.x + threadIdx.x \\ j &= blockIdx.y \times blockDim.y + threadIdx.y \end{aligned} \tag{2.82}$$

[4]2D blocks and threads for the LBM, and 1D for the DEM.

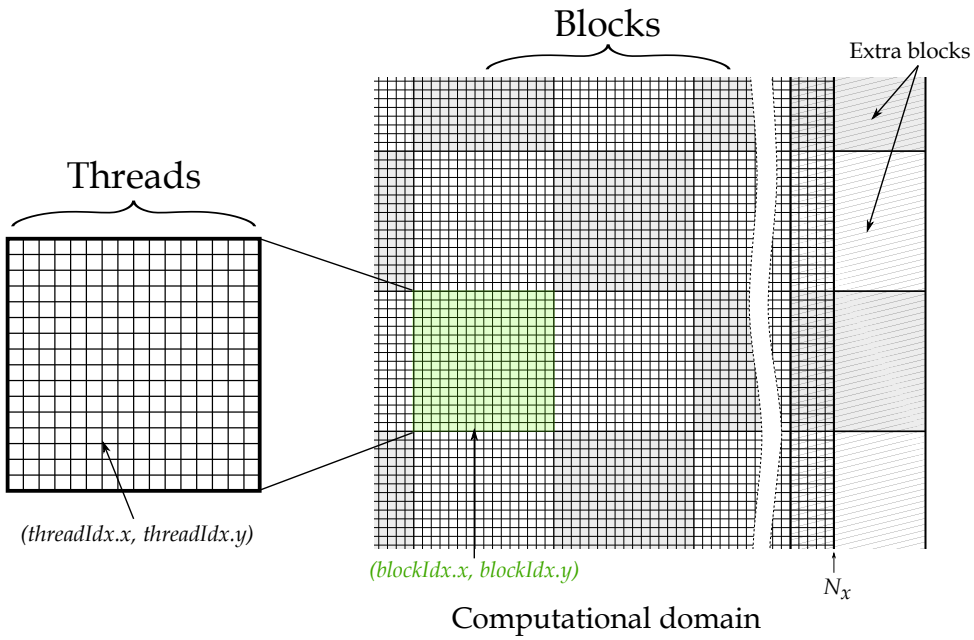

Fig. 2.23. Part of the computation domain with the decomposition into blocks and threads in CUDA. Each grid intersection represents a fluid (LBM) node and also one thread.

The collision and streaming steps with the PSM scheme is summarized in Algorithm 1.

2.5.3 LBM-DEM coupling

As explained in the previous chapter, the coupling between LBM and DEM can be ensured in this context either with the PSM or the Bouzidi schemes. However, both were implemented in the GPU version of the code and they need to be specified optionally at the beginning, i.e. before compiling the code. The main GPU implementation of the LBM-DEM code is summarized in Flowchart 2.24 for the Partially Saturated Method (PSM) and the Bouzidi scheme. Note that in the Bouzidi scheme, the collision and streaming steps are separated into two kernels since synchronization is needed in order to perform the bounce-back scheme, the latter being implemented in the middle also as a separate kernel.

2.5.4 Code performance

The performance of the present parallel GPU (CUDA) code is compared to the serialized CPU version. Keep in mind that the serialized CPU version is not well optimized and the Verlet list algorithm is used for particles neighboring search.

Algorithm 1 Collision and streaming kernel with the PSM scheme.

Get fluid node position i and j from Eq. 2.82.
if $(i < 0) \,||\, (i > N_x - 1) \,||\, (j < 0) \,||\, (j > N_y - 1)$ **then**
  return;
end if
Compute macro variables ρ and $\boldsymbol{u}$, from Eq. 2.41 and 2.42 respectively.
Compute $f_\alpha^{eq}(\rho, \boldsymbol{u})$, from Eq. 2.39.
Get the solid fraction ε_s.
if $\varepsilon_s > 0$ **then**
  Get particle ID then particle velocity, $\boldsymbol{u_s}$.
end if
Compute Ω_α^s from Eq. 2.71.
Apply PSM collision operator, Eq. 2.78
if $\varepsilon_s > 0$ **then**
  Get particle ID.
  Increment hydro forces on particle and torque Eq. 2.75 and 2.76 respectively [5].
end if
Stream to neighbors, Eq. 2.79

The Jet Erosion Test (JET) that will be described in Chapter 3 is chosen as a benchmark test with 5000 particles and $Nx = 1551$ and $Ny = 1001$ lattices units in x and y directions, respectively. A fixed space resolution ratio $N = \frac{2R_{min}}{dx}$ is set at 10 lattice nodes, the characteristic speed is $c = 30\ \mathrm{m\,s^{-1}}$ and the kinematic viscosity $\nu = 40 \times 10^{-6}\ \mathrm{m^2\,s^{-1}}$.

The results are summarized in Fig. 2.25. Different GPU cards were used for the benchmark test (see Table 2.2). Note that the calculation is done in single precision floating point, this explains the high performance achieved. The speedup was measured as the ratio of the number of iterations per second of the GPU calculation to the reference single CPU thread:

$$Speedup = \frac{Iteration\ persecond\ (GPU)}{Iteration\ persecond\ (CPU)} \tag{2.83}$$

where the iteration per second is calculated every one "LBM+DEM+visualization" cycle at each output frequency ($OutFreq$) set here at 4000. It is obvious to set a higher value of $OutFreq$ to minimize the memory transfer between GPU and CPU for the visualization step, which takes, in this case, 0.02% of the overall performance. It was found that, when the TRT collision model is used, the performance slightly dropped about 0.97% compared to the BGK model. Moreover, it was observed that using the cohesion model, or not, does not affect the overall performance in GPU calculation.

The profiling of the test in GPU is shown in Fig. 2.26. We see that the collision and streaming kernel takes the most part of the calculation with 84.28%, followed by the particle mapping and solid fraction calculation kernel with 9.76%. Also, it is to note that the DEM calculation part is negligible compared to the LBM one. From

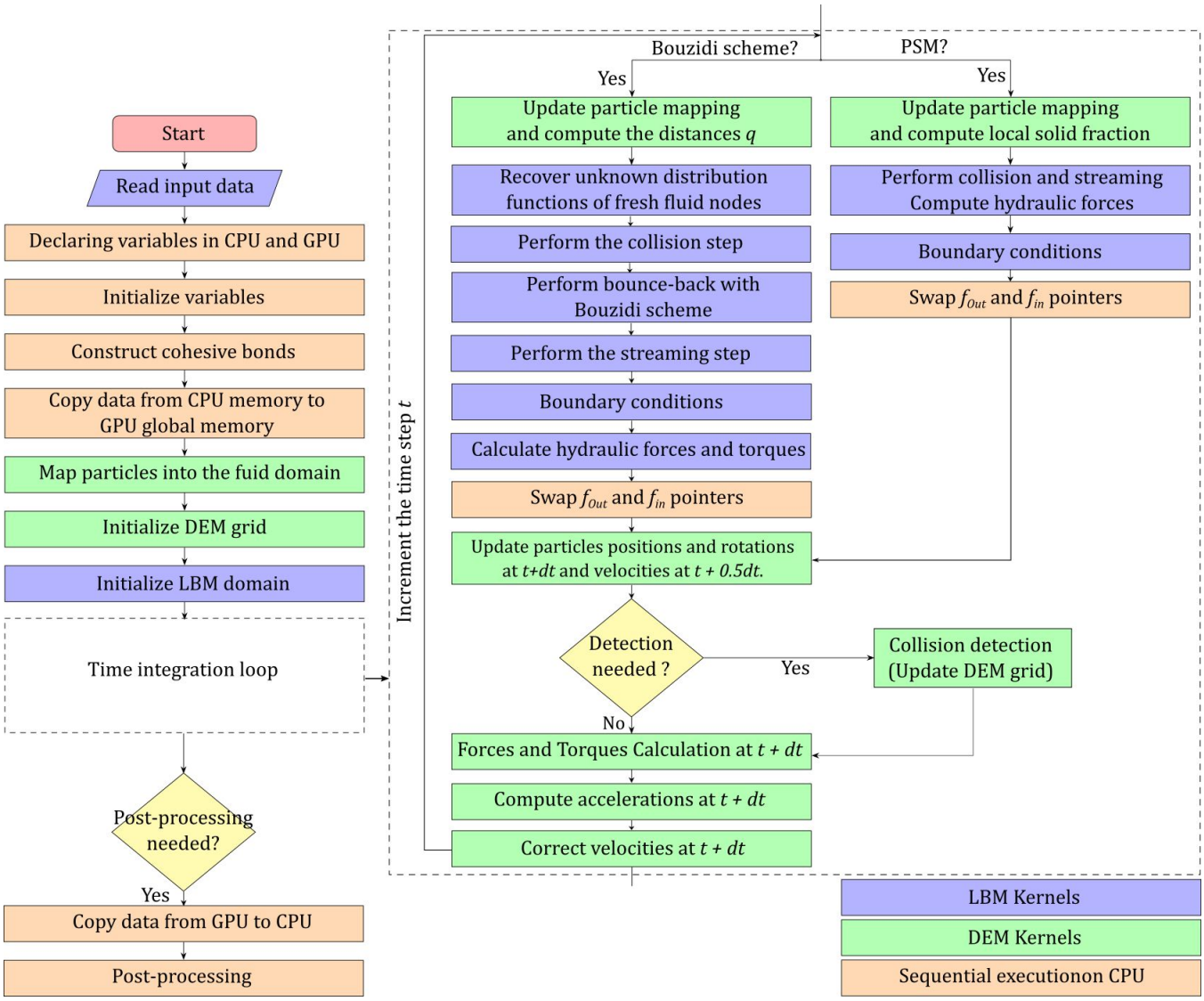

Fig. 2.24. Flowchart of general GPU implementation of the micromechanical simulation model featuring both alternative coupling schemes in the frame of the momentum-exchange (Bouzidi) and partial saturation method (PSM).

the profiling chart, we identified the bottlenecks that slow down the computations and will therefore be optimized in further work.

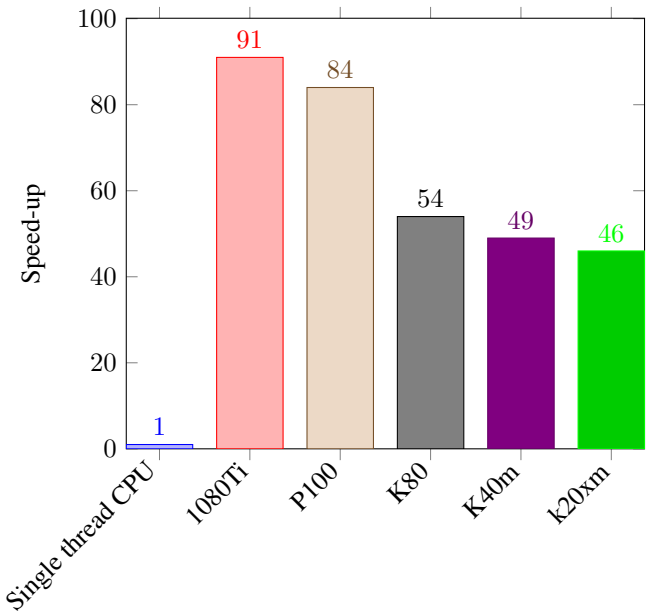

Fig. 2.25. Performance comparison between the GPU implementation of the code and the single thread CPU version. Different Nvidia cards are used, whose specifications are summarized in Table 2.2. The CPU used is Intel(R) Xeon(R) CPU E5-4617 @ 2.90 GHz with 129 GB memory.

Table 2.2. Graphic cards specifications used for the benchmark

GPU name	GTX 1080Ti	Tesla P100 PCIe	Tesla K80	Tesla K40m	Tesla k20xm
Architecture	Pascal	Pascal	Kepler	Kepler	Kepler
Memory (MB)	11264	16384	12288	12288	6144
CUDA cores	3584	3584	2496	2880	2688
FP32*	11,340	9,526	4,373	4,291	3,935
FP64**	1:32	1:2	1:3	1:3	1:3

*FP32 (GFLOPS): single precision (float) performance.
**FP64 (GFLOPS): double precision (double) performance compared to FP32.

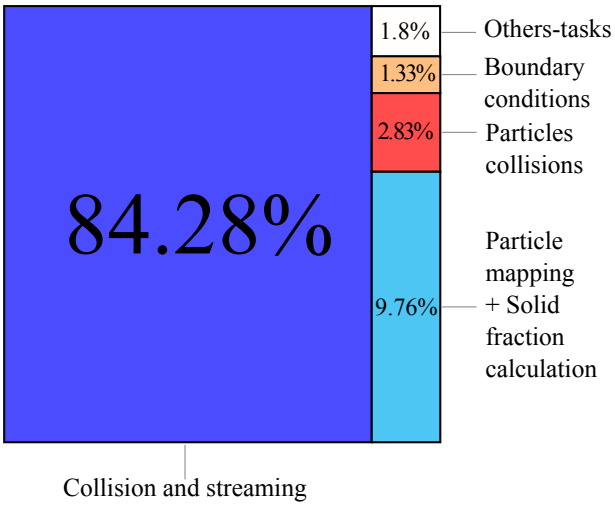

Fig. 2.26. Profiling of the JET CUDA program, the kernels with higher time consumption percentage are shown.

2.6 Validation of the LBM-DEM coupling

2.6.1 Sedimentation of a single particle

In this section we are interested in validating the LBM-DEM GPU code as well as the workability of the GPU implementation in terms of hydraulic forces. Sedimentation of a single particle is chosen as a benchmark because of its simplicity and for the huge number of experimental and theoretical data available in the literature for either a settling particle (in 2D) or the flow past a circular cylinder. The drag coefficient C_D of the particle is related to its terminal settling velocity v_p and is a function of the particle Reynolds number $Re = \frac{v_p D}{\nu}$:

$$C_D = \frac{\pi(\rho_g - \rho_f)gD}{2\rho_f v_p^2} \tag{2.84}$$

where ν is the fluid kinematic viscosity.

The domain is a large rectangle of height $H = 80D$ and width $L = 50D$ and the particle diameter D is set at 20 lattice units. The particle is placed at the center of the width at a height of $72D$ from the bottom wall. Bounce-back (non-slip) boundary conditions were applied at the four walls. To obtain different sedimentation velocities, a series of simulations were conducted, by varying the fluid kinematic viscosity in the range $[0.2, 0.005]$ in lattice units, with a ratio between the particle and fluid density fixed at $\frac{\rho_g}{\rho_f} = 1.01$, and the gravity acceleration being $g = 9.81$ $\mathrm{m\,s^{-2}}$.

Figure 2.27 shows our simulation results for the drag coefficient C_D versus the particle Reynolds number Re, using the two collision models BGK (Bhatnagar et al., 1954) and TRT (Ginzburg et al., 2008) for the PSM (with the magic number $\Lambda = 1/4$) and the MRT model with the Bouzidi scheme. For comparison, the results of fluid flow past a circular cylinder from Tritton (1959) (experiments) and Fornberg (1980) (theory) are also plotted. As can be seen from the figure, our results agree nicely with that found in the literature, except for large Reynolds numbers ($Re > 100$). It is interesting to see that both collision models give close results, even though there are slight fluctuations in the pressure fields around the particle in the BGK collision model at low kinematic viscosity as shown in Fig. 2.28. However, the fluctuations are eliminated using the TRT collision model.

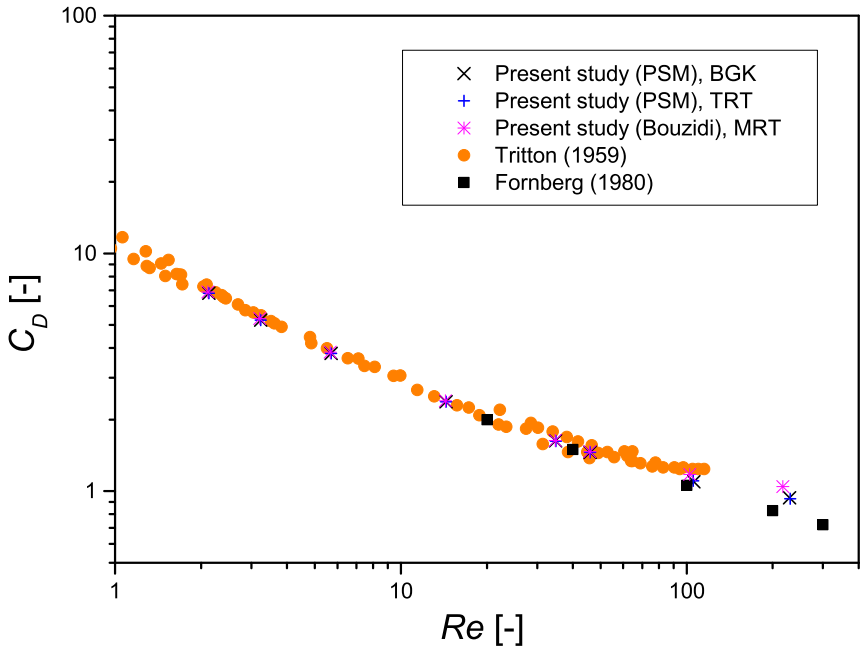

Fig. 2.27. Drag coefficient C_D of a settling particle versus particle Reynolds number Re.

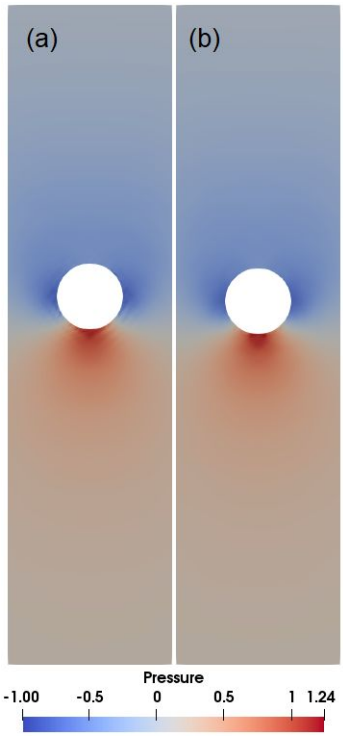

Fig. 2.28. Pressure fields for $\nu = 0.025$ in lattice units: (a) BGK collision model; (b) TRT collision model.

2.6.2 Sedimentation of two particles

To involve additionally inter-particle collisions, sedimentation of two particles in a channel is now simulated. In order to validate the results obtained by our model, the simulation conditions are similar to those presented previously in the literature (Feng and Michaelides, 2004; Wang et al., 2014). The configuration of the numerical test is given in Figure 2.29. The domain is rectangular with 2cm width and 8cm height.

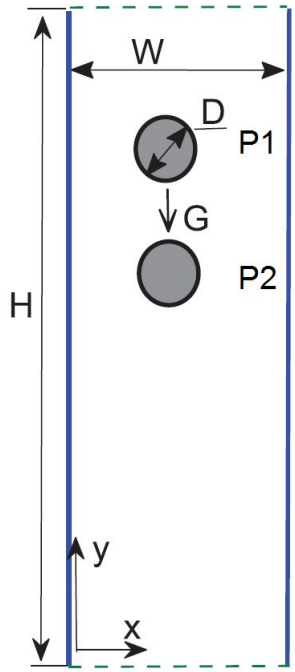

Fig. 2.29. Schematic for the sedimentation of two particles under gravity.

Initially, particle 1 (P1) and particle 2 (P2) are placed at the center of the channel at a height of 7.2 cm and 6.8 cm, respectively. The particle P1 is shifted from the center by one lattice unit. The density and the kinematic viscosity of the fluid are ρ_f=1000 kg/m^3 and $\nu = 10^{-6}$ m^2/s, respectively. The particles have the same properties with a density ρ_g=1010 kg/m^3 and a diameter D=0.2 cm. The normal stiffness is $k_n = 1.1 \times 10^5$ N/m, the shear stiffness $k_t = 1.1 \times 10^5$ N/m, the friction coefficient $\mu = 0$, and the gravitational acceleration $g = 9.81$ m/s^2.

The grid size is set to 201×801, the relaxation time is fixed at $\tau = 0.65$ with $\Delta t = 5 \times 10^{-4}$ s. The Bounce-back (non-slip) boundary conditions were applied at the lateral and lower walls, while outlet with zero pressure is applied at the upper boundary. Fig. 2.30 shows the velocity contours at three different times of the simulation, illustrating the so-called "drafting-kissing-tumbling" scenario. The results are compared to the simulation of Wang et al. (2014), as shown in Fig. 2.31, through the trajectories (transverse and longitudinal coordinates) of the two particles over time. We can see that the behavior of the particles is accurately captured and the

results are in close agreement, except a slight discrepancy for the final transverse motion of particle P1.

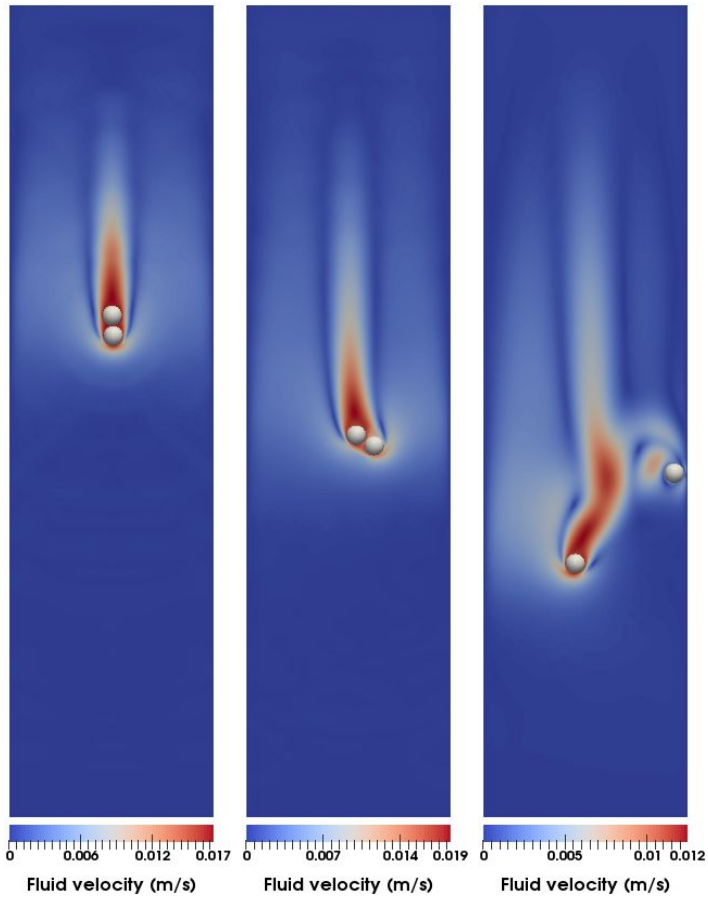

(a) t=1.8s **(b)** t=2.5s **(c)** t=3.5s

Fig. 2.30. Snapshots of the velocity contours during the settling of two particles at three arbitrary times showing the so-called DKT-pattern (drafting-kissing-tumbling).

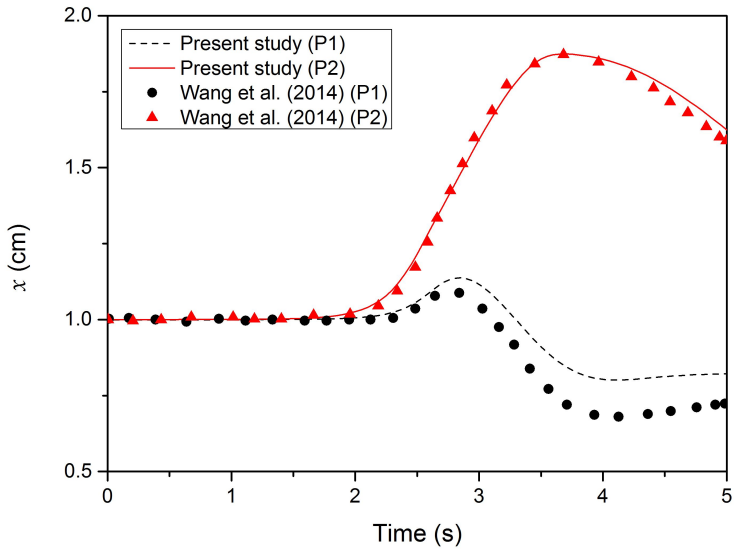

(a)

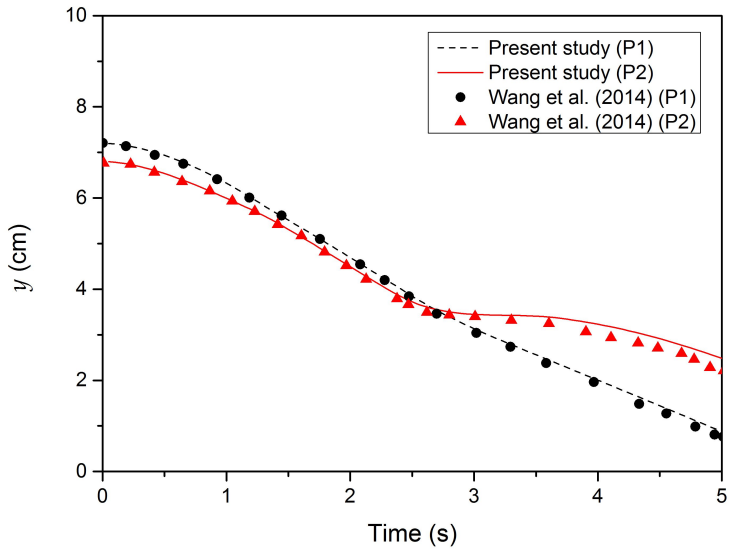

(b)

Fig. 2.31. Time evolution of the two particle coordinates: (a) transverse (x); (b) longitudinal (y). The numerical results of Wang et al. (2014) are also plotted as symbols for comparison purpose.

2.7 Summary

We have shown in this chapter the numerical methods that will be used in this thesis work, which are the Discrete Element Method (DEM) and the Lattice Boltzmann

Method (LBM), as well as the coupling technique between both methods.

Also, we have shown the pertinence of LBM-DEM coupling technique in dealing with fluid-particle interactions. Moreover, the necessity of a robust parallelization technique, since combining both methods are highly costly in terms of simulation time, in this sense, a GPU parallelization approach is adopted to resolve this issue.

Once the numerical tool has been properly validated, it will serve for studying soil erosion with two different configurations: impinging jets and Tangential flow erosion.

Chapter 3

Numerical simulation of impinging jet erosion

Contents

3.1 Introduction

The aim of this chapter deals with an adaptation of the numerical tools presented in Chapter 2 for studying the impinging jet erosion process at the scale of a representative elementary volume (REV) of the tested material. The goal behind is first to quantity the flow characteristics at the granular surface, namely the maximum shear stress and the maximum tangential fluid velocity, and discuss their relation with the bi-dimensional free plane jet model in laminar regime. Then the onset erosion is evaluated and plotted in the so-called Shields diagram. This part covers a slightly more elaborate version of the work that has been accepted for publication in Journal of Hydraulic Engineering (Benseghier et al., 2020).

The second part of this chapter is dedicated to impinging jet erosion of cohesive material and aims to test the proposal by Brunier-Coulin et al. (2017) to extend the classical Shields criterion used for cohesion-less materials to weakly cohesive soils. Furthermore, the scouring process is investigated, using image processing techniques, and a 2D analysis of the time evolution of the scour depth (i.e. erosion rate). The latter is compared to an adapted version of the mathematical model for the Jet Erosion Test (JET) experiment (Hanson and Cook, 2004), which includes the expression of the fluid shear stress at the upper bed surface and the assumption of an excess shear-stress erosion law. This model allows to derive implicitly, at the sample scale, the erodibility parameters of our cohesive samples (i.e. erosion coefficient and critical shear stress) for different micro cohesion strengths.

3.2 Numerical study of 2D jet flow

This section draws on simulation results, obtained for various jet flow conditions, aiming to identify the possible relationship between the free jet self-similar theory and the flow characteristics at the impinged surface in laminar regime, in terms of the maximum velocity V and wall shear stress τ_m, as illustrated in Fig. 3.1. Firstly, we analyze the free plane jet in laminar regime, for jet Reynolds numbers Re_j ranging between 20 and 130, and validate our results with the well-known analytical self-similar solution Schlichting (1960); Bickley (1937). Afterward, we investigate impinging laminar jets on both a smooth wall and a fixed granular layer. It is noteworthy that the present study is restricted to plane (two-dimensional), laminar and unconfined (i.e. no influence of the lateral boundaries) conditions.

The jet flow configurations selected for this study are illustrated in Fig. 3.2. On the left, a free plane jet with a nozzle width b. On the right, an impinging jet with two different impact surfaces: smooth wall (case W) and granular surface with fixed particles (case G).

The boundary conditions are given as follows: the bounce-back boundary condition (Chen et al., 1996) is applied for the solid walls (i.e. for the nozzle boundaries and, eventually, for the impinged surface), while we assume a Zou/He condition with zero pressure (Zou and He, 1997) at the (outer) exterior boundaries. For the velocity inlet (i.e. for the jet's nozzle of width b), we implement a Poiseuille profile

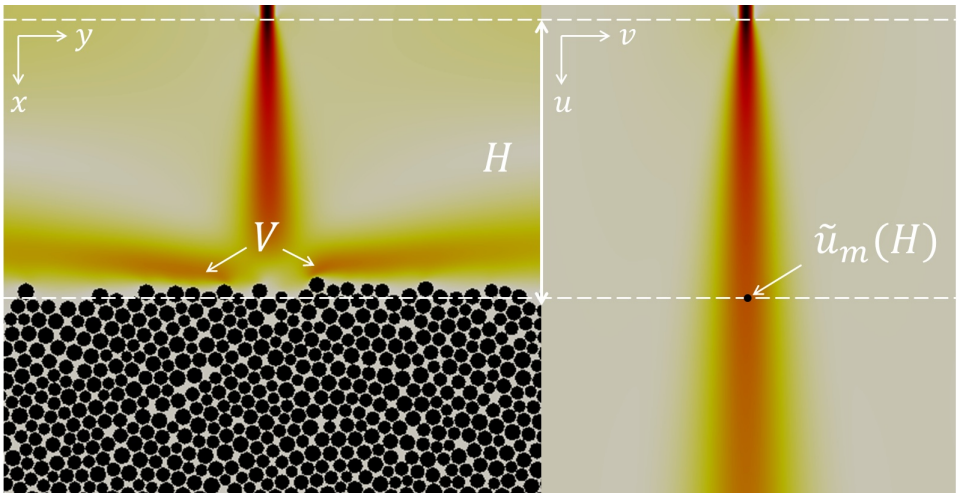

Fig. 3.1. Paradigm of free jet and impinging jet on a granular sample. The hydrodynamic variable $\tilde{u}_m(H)$ represents the free jet center-line velocity at a distance equal to the impingement height H, while V is the maximal fluid velocity over the impinged surface.

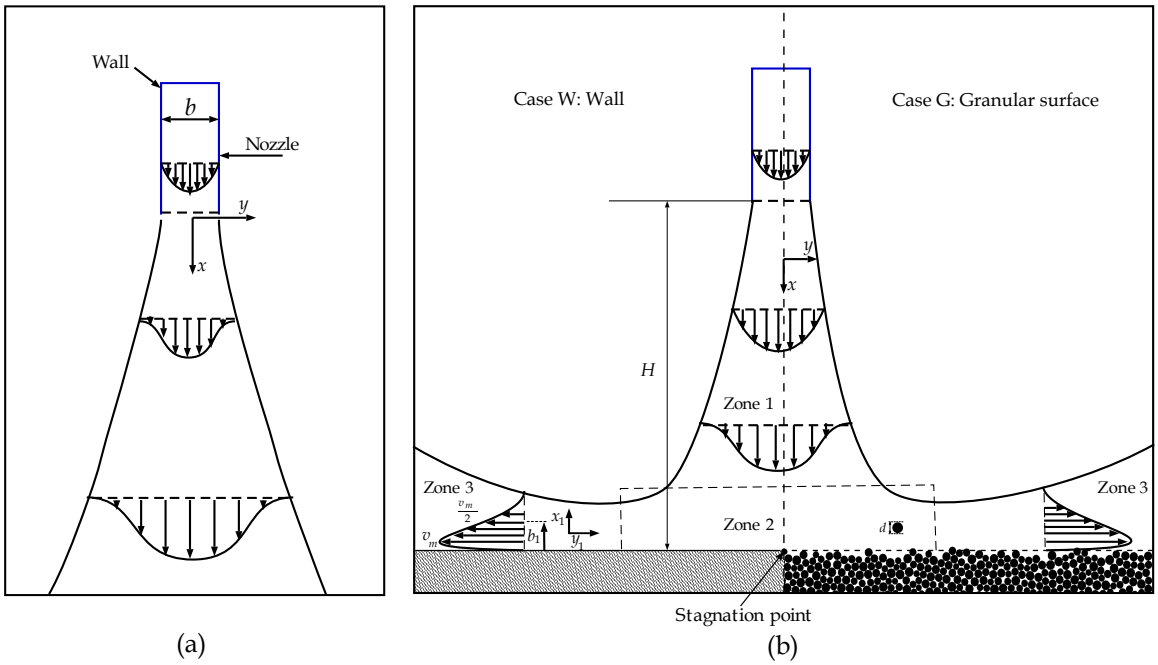

Fig. 3.2. Sketch of the different study cases for jet analysis. (a) Free jet configuration. (b) Impinging jet on either a smooth wall (case W) or on a fixed granular surface (case G), with distinction of the three characteristic jet flow regions: Zone 1 (free jet), zone 2 (impingement region), zone 3 (wall jet).

with both regularized and equilibrium methods as introduced in Eqs. (2.58) and (2.61). The mean velocity of the Poiseuille jet injection at the nozzle width b reads consequently $u_j = \frac{2}{3}U_0$ with U_0 being the maximal inlet velocity. The jet Reynolds

number is defined as: $Re_j = u_j b/\nu$.

Note that, in the impinging jet configuration and more specifically for case (W), the simulation procedure and conditions are the same as in the free jet case except for the horizontal smooth wall which is added to the computational domain and located at an axial distance H from the nozzle exit. While for case (G), the solid smooth wall is replaced by a fixed granular surface at the same distance H (Fig. 3.2). The granular surface is constructed with a uniform particle size distribution: $d_{min} < d < d_{max}$ and $d_{max}/d_{min} = 1.5$. An effective hydraulic radius factor $\varepsilon_h = r_h/r = 0.8$ is introduced in the simulation as well.

The input parameters for the parametric study of the free jet are summarized in Table 3.1, while the ones used for the impinging jet in both cases are given in Table 3.2. In case (G), two different particle diameters have been used: $d = 3$ and 5 mm.

Table 3.1. Input parameters used for the free jet simulations

U_0 (m/s)	b (mm)	$\nu \times 10^{-5}$ (m^2/s)	Re_j (-)
0.37	5.2	3.30	38.9
0.37	5.2	6.60	19.4
0.185	10.8	1.65	80.7
0.185	5.2	1.65	38.9
0.185	10.8	3.30	40.4
0.185	5.2	3.30	19.4
0.74	5.2	3.30	77.7
0.37	10.8	3.30	80.7
0.37	6.8	3.30	50.8
0.37	8.4	3.30	62.8
0.37	12.4	3.30	92.7
0.62	5.2	1.65	130.3
0.53	5.2	1.65	111.4

3.2.1 Two-dimensional laminar free jet

Figure 3.3a and 3.3b present typical velocity contours and plots of the center-line velocities u_m versus y, the distance from the nozzle exit, for a Poiseuille inlet velocity profile with both regularized and equilibrium methods (see section 2.3.5). The free jet characteristics are $U_0 = 0.37$ m/s, $\nu = 33 \times 10^{-6}$ m^2/s and $b = 5.2 \times 10^{-3}$ m.

The numerical results are compared with the 2D analytical solution with the adjustment of the virtual origin (Eq. 1.38 and 1.39). It is clearly noticeable that the profiles slightly deviates from the analytical solution, particularly for the equilibrium method. However, it can be stated that the simulation results are in overall agreement with the analytical solution, especially when using the regularized method.

Table 3.2. Input sets used for the simulation of impinging jet

Case	U_0 (m/s)	b (mm)	$\nu \times 10^{-6}$ (m^2/s)	Re_j (-)	H (mm)
W, G	0.37	5.2	33	38.9	90.4
W, G	0.74	5.2	33	77.7	90.4
W, G	0.5	5.2	33	52.5	90.4
W, G	0.6	5.2	33	63.03	90.4
W, G	0.37	6.8	33	50.8	90.4
W, G	0.74	6.8	33	101.7	90.4
W	0.37	5.2	33	38.9	73.2
W	0.74	5.2	33	77.7	73.2
W	0.37	6.8	33	50.8	73.2
W	0.37	5.2	33	38.9	108
W	0.74	5.2	33	77.7	108
W	0.37	6.8	33	50.8	108
W	0.74	5.2	10	256.5	90.4
W	0.37	5.2	10	128.3	90.4
W	0.74	5.2	100	25.7	90.4
W	0.37	5.2	100	12.8	90.4

A typical transverse profiles of the vertical fluid velocity plotted in Fig. 3.4a decreases continuously from its maximal value u_m at the center-line with lateral distance y. As stated in Chapter 1, these profiles are supposed to follow a self-similar pattern. Denoting b_u the lateral distance where $u = u_m/2$, a normalized plot of these profiles is drawn in Fig. 3.4b, where the vertical velocity, divided by its maximal velocity u_m at center-line, is plotted as a function of the transverse distance y divided by b_u. It can be underlined that these normalized curves nicely collapse all together. This confirms the analytical prediction of a self-similar velocity profile described by $\mathrm{ch}^{-2}[\mathrm{ach}(\sqrt{2})y/b_u]$ up to $x > 1.5b$, i.e. up to the point where the free jet exits from the potential core region.

Fig. 3.5a shows the variation of $(u_j/u_m)^3$ and $(b_u/b)^{3/2}$ at various distances x/b from the nozzle outlet for a jet Reynolds number $Re_j = 38.9$. As expected from Eqs. (1.39) and (1.37), the profiles are linear, with slopes denoted α and β, and x-intercepts denoted A and B, respectively. Consequently, the proportional relations between u_m and $x^{-1/3}$ as well as between b_u and $x^{2/3}$ are clearly confirmed. Since the x-intercepts are different from zero, it is also obvious that the jet is not originating from the nozzle exit, but rather from a virtual point source located at a distance λ above it (i.e. $A, B < 0$).

Up to this point, the results of only one simulation have been shown. Thus, in the next investigation, a series of simulations was performed following the same analysis shown above in order to confirm the validity of our simulation for various flow conditions, i.e. by varying the jet Reynolds number.

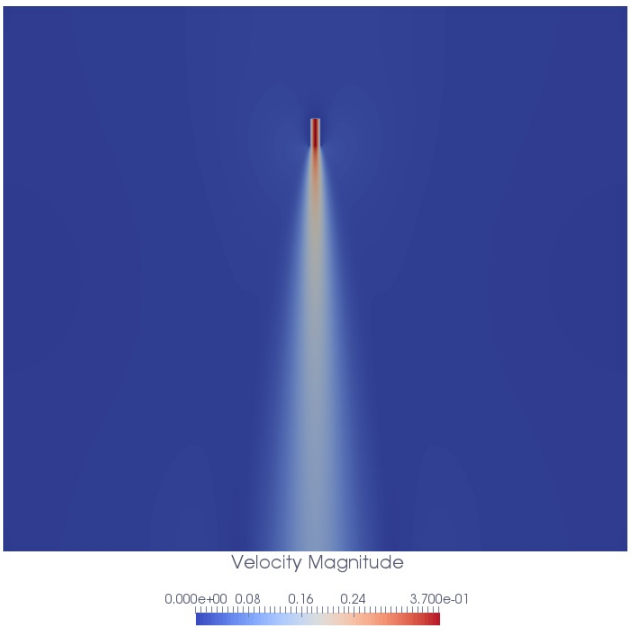

(a)

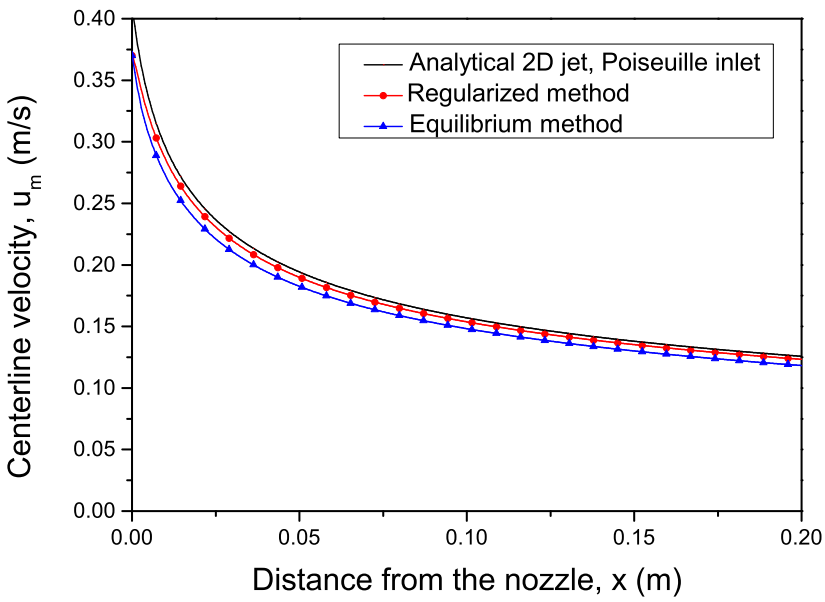

(b)

Fig. 3.3. Simulation results of laminar 2-D free jet for $U_0 = 0.37$ m/s and $b = 5.2 \times 10^{-3}$ m: (a) contours of velocity magnitude with Poiseuille inlet; (b) centerline velocity u_m at different distance x from the nozzle with comparison between analytical solution of 2-D laminar free jet and numerical results using the regularized and equilibrium methods for Poiseuille inlet boundary condition.

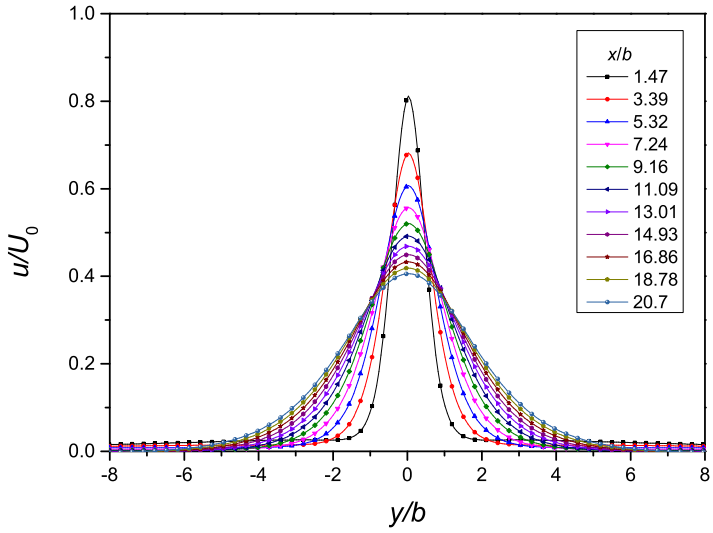

(a)

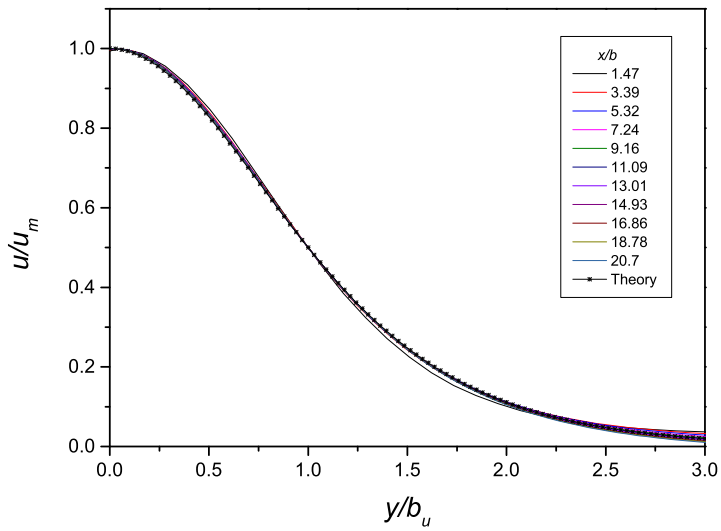

(b)

Fig. 3.4. Transverse profiles of the vertical fluid velocity u: (a) with u divided by the injection velocity U_0 versus the dimensionless distances x/b from the jet's nozzle; (b) with u normalized by its maximum value u_m (at the center-line) versus the transverse distance y normalized by b_u, the transverse distance where $u(b_u) = \frac{1}{2}u_m$.

As specified in section 1.6.1, the theory predicts that the slopes α and β are proportional to Re_j^{-1} as expressed in Eqs. (1.39) and (1.37), respectively. This means that a -1 slope is expected in a log-log representation. The analytical prediction is well verified by the simulation for almost the whole range $37 < Re_j < 120$ as

confirmed in Fig. 3.5b, which shows the variation of the slopes α and β for various jet Reynolds numbers in a log-log plot. By linear regression, the slope of α and β versus Re_j are equal to -1.11 (with a correlation coefficient $R^2 = 0.9982$) and -1.04 (with a correlation coefficient $R^2 = 0.9998$), respectively. Not surprisingly, a slight difference with the analytical slope -1 is expected for α since there is some departure in the center-line velocities (u_m) between the simulation and analytical results, as shown in Fig. 3.3b. However, the relationships $\alpha, \beta \propto Re_j^{-1}$ suggested by Eqs. (1.39) and (1.37), respectively, are almost confirmed by our numerical results.

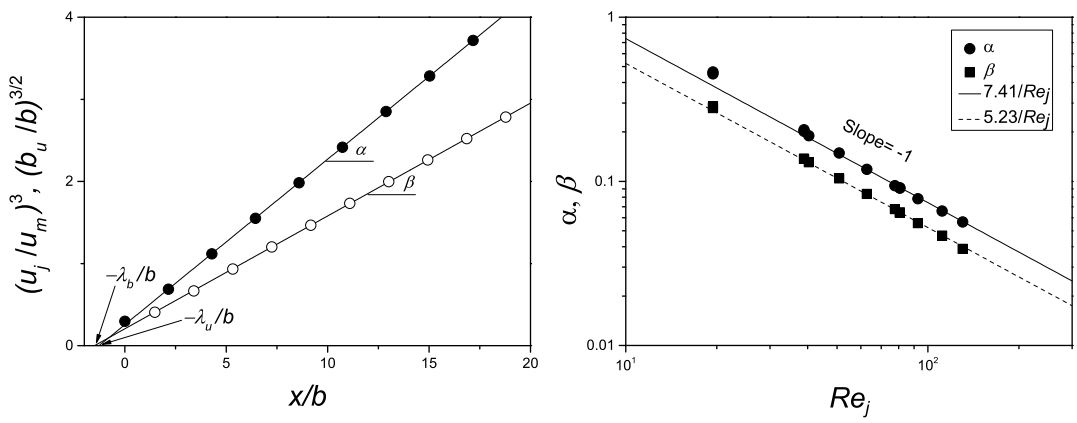

(a) **(b)**

Fig. 3.5. (a) Variation of $(u_j/u_m)^3$ (filled circle) and $(b_u/b)^{3/2}$ (open circle) with the normalized distance from the nozzle x/b for $Re_j = 38.9$. (b) Log-log representation of the slopes α and β versus Re_j. The lines represent the theoretical predictions in Eq. 1.39 and Eq. 1.37, respectively.

We have shown so far that both the simulated jet's center-line velocity and half-width agree well with the analytical predictions given in Eq. 1.39, Eq. 1.37, and Eq. 1.32, respectively, and that the jet is originated from a virtual source point instead of the exact nozzle exit. One last point to be confirmed is thus the quantitative value of this virtual origin λ. The dimensionless quantity λ/b can be simply identified from the x-intercepts, A and B, of both linear profiles $(u_j/u_m)^3 = f(x/b)$ and $(b_u/b)^{3/2} = g(x/b)$ (see Fig. 3.5a). In Figure 3.6, the two corresponding values are plotted against the jet Reynolds numbers Re_j and compared to each other. As can be concluded, the two estimations of λ/b seem to agree fairly well, with a mean relative error of 13%, and can be accurately fitted with a proportional relation (with a correlation coefficient $R^2 = 0.995$), that appears slightly higher than the existing solution in the literature $\lambda/b = 0.029Re_j$ (Revuelta et al., 2002), and reads:

$$\lambda = 0.036 Re_j b \tag{3.1}$$

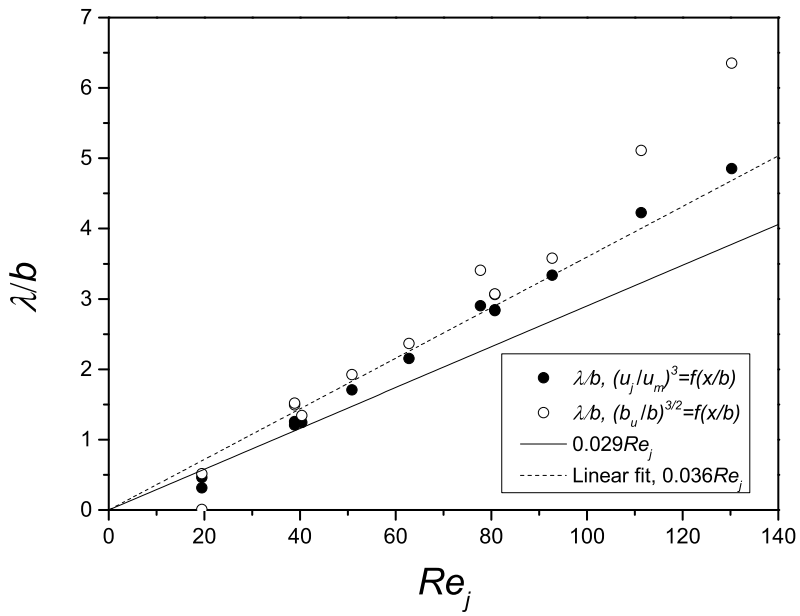

Fig. 3.6. Variation of the dimensionless virtual origin λ/b versus the jet Reynolds number Re_j obtained from the linear regression of the profiles $(u_j/u_m)^3 = f(x/b)$ (black filled dots) and $(b_u/b)^{3/2} = f(x/b)$ (unfilled dots). The linear trend fitting the data is shown as a dashed line and the black solid line is a plot of Eq. 1.38 as predicted by Revuelta et al. (2002).

3.2.2 Jet impingement on a smooth wall and fixed granular layer

As regards impinging jets, three main fluid flow regions can generally be distinguished (Beltaos and Rajaratnam, 1973) as sketched in Fig. 3.2: a free jet region (zone 1) where the flow remains self-similar; an impingement region (zone 2) where the impinged surface affects the jet flow, the center-line velocity decreasing down to zero at the impingement (stagnation) point and diverting the flow to the lateral directions; a wall jet region (zone 3) where the flow becomes parallel to the impinged surface.

Many studies have examined in detail the velocity, pressure, and wall shear stress fields in these different regions, e.g. Rajaratnam (1976). However, the quantification of jet impingement for the prediction of soil erosion still remains largely empirical. No simple analytical approach has been proposed so far for such prediction of flow quantities at either the impingement region or at the wall jet region (zones 2 and 3, respectively). In this respect, most of the estimations proposed in the literature are based on the free jet model (zone 1). We therefore address in this section the influence of both the jet Reynolds number and the impingement height H on the distributions of fluid velocity and shear stress on a smooth impinged surface. Thereby, we explore firstly the relationship between the theoretical free-jet center-

line velocity at the impingement height $\tilde{u}_m(H)$ and the actual maximal velocity V of the impinging jet near the wall surface in zone 3, turning afterward the attention to the corresponding maximal shear stress τ_m.

Velocity field

Figure 3.7 shows the velocity magnitude and streamlines for an impinging jet over a smooth wall, while the variations of the normalized center-line velocity u_m/U_0 with x/b for different impingement height H/b are shown in Figure 3.8a. The center-line velocity follows the theoretical prediction of the free jet up to a distance around $0.6H$, before starting to decrease with a greater gradient until reaching zero at the impingement point. Despite the difference in flow regimes of the impinging jet, namely laminar for our simulation versus turbulent for the experiments of Beltaos and Rajaratnam (1973), the behavior of the impinging jet obtained in the present simulation agrees well, in terms of the center-line velocity and the distance before the deviation from the free jet curve, with the experimental results for plane turbulent impinging jets, as can be seen in Figure 3.8b)

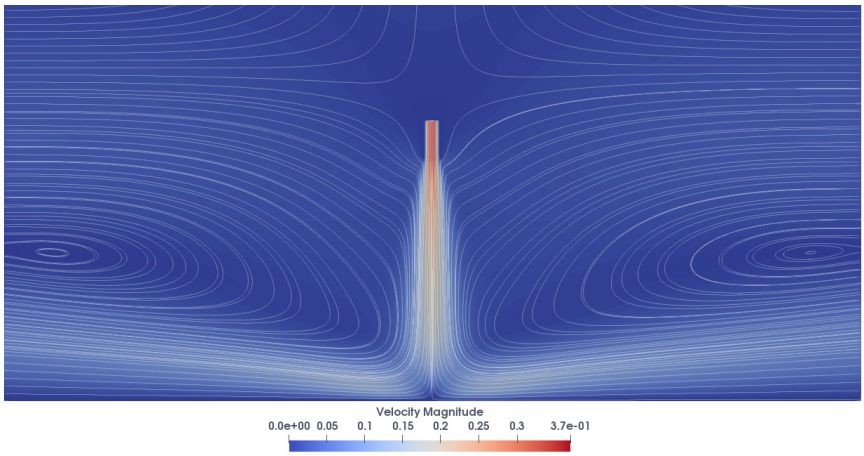

Fig. 3.7. Snapshot of the steady state velocity contours and streamlines for a jet impinging on a smooth wall with $H = 90.4$ mm, $U_0 = 0.37$ m/s, $b = 5.2$ mm, and $\nu = 33 \times 10^{-6}$ m^2/s.

Figure 3.9 shows the transverse profiles of the fluid velocity at different downstream distances x/H from the nozzle, normalized as in Fig. 3.4b. These velocity profiles appear to remain self-similar up to at least $x/H \approx 0.75$. For higher values of x/H, the wall starts to influence increasingly the jet flow velocity as observed by the impingement jet experiments.

Figures 3.10a and 3.10b present the profiles of the transverse velocity v at different distances x_1 from the impinged surface for case (W) and case (G), respectively. An example of velocity contours for the impinging jet over a granular surface is also shown in Figure 3.11. All profiles show a monotonic increase of the velocity up to a maximum value v_m and a subsequent continuous decrease with growing distance y from the jet's axis. The local maximum v_m of the transverse velocity v_m for each

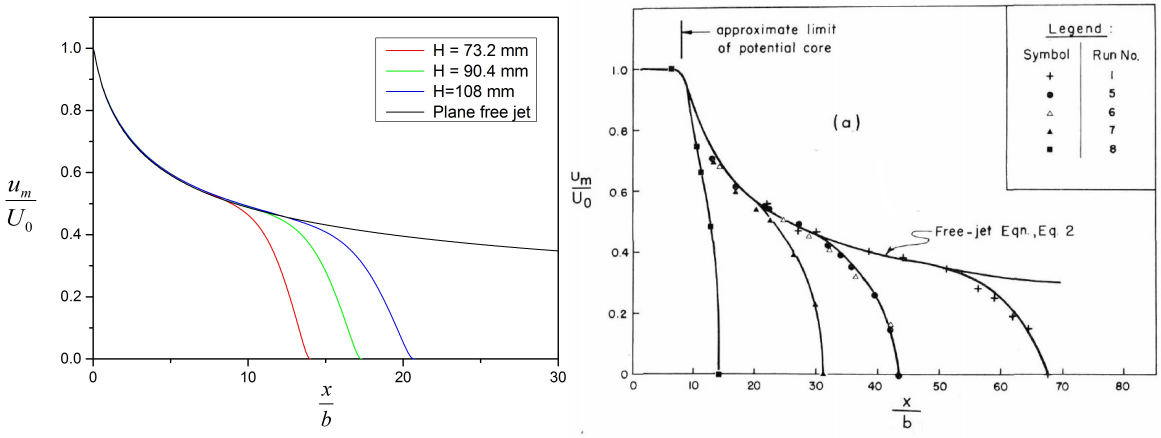

(a) **(b)**

Fig. 3.8. Normalized center-line velocity u_m/U_0 versus x/b with $Re_j = 38.9$ and for different wall distances. (a) Our simulation results with $H = 73$ mm, $H = 90.4$ mm, and $H = 107.8$ mm, the black solid line corresponds to the plane free jet simulation case. (b) Experimental results of Beltaos and Rajaratnam (1973) for plane turbulent impinging jets with: (Run 1) $Re_j = 3767$ and $H = 150.9$ mm, (Run 5) $Re_j = 4733$ and $H = 97.5$ mm, (Run 6) $Re_j = 3513$ and $H = 97.5$ mm, (Run 7) $Re_j = 4647$ and $H = 69.2$ mm, (Run 8) $Re_j = 3513$ and $H = 31.4$ mm.

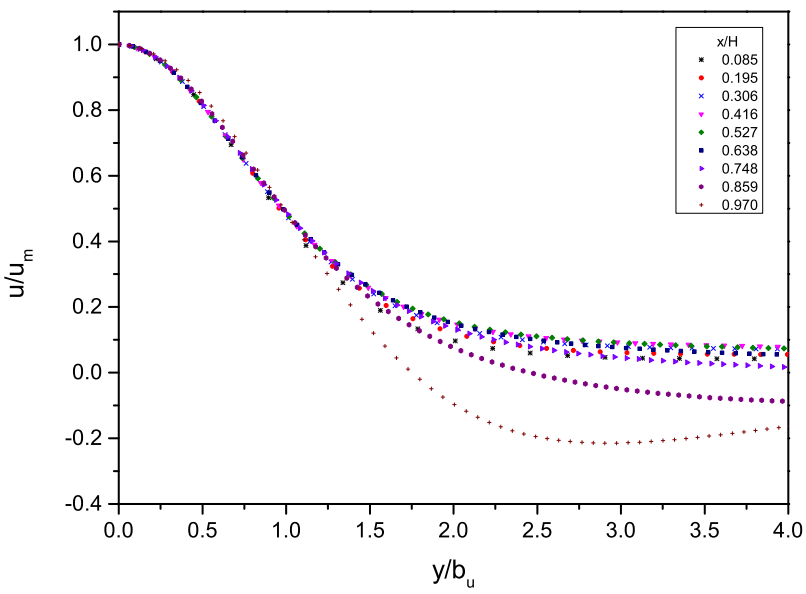

Fig. 3.9. Transverse profiles of the normalized fluid velocity, u/u_m versus y/b_u, of an impinging jet for various downstream distances x/H from the nozzle.

profile increases rapidly with x_1, until reaching a global maximum $V = max(v_m)$, and then decays slowly.

The global maximum of the fluid velocity V over the impinged surface can then be extracted for different flow conditions and samples (i.e. different mean grain sizes), and subsequently be plotted against the free-jet maximum velocity $\tilde{u}_m(H+\lambda)$ at the corresponding distance from the nozzle (Eq. 1.39) which is used here as a reference velocity.

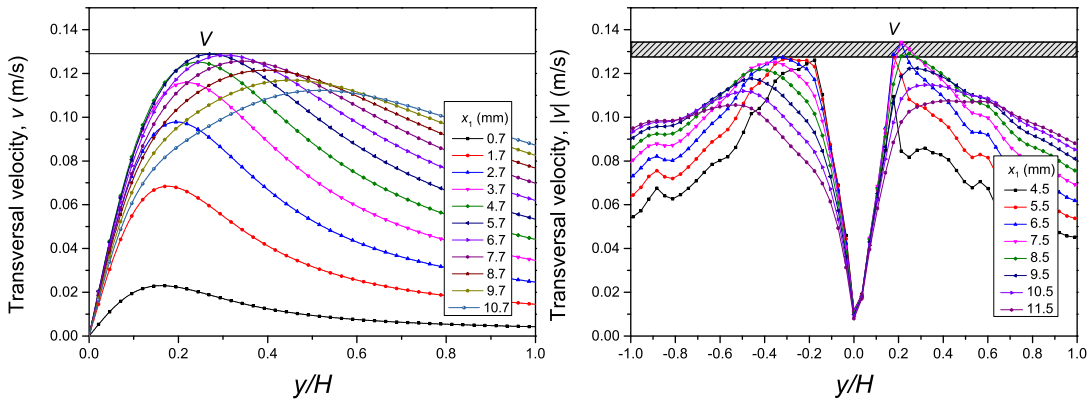

(a) Smooth wall **(b)** Granular surface

Fig. 3.10. Profiles of transverse velocity v at different distances from the impingement surface x_1: (a) smooth wall; (b) granular surface with mean grain size $d = 5$ mm. The other simulation parameters are here $H = 90.4$ mm, $U_0 = 0.37$ m/s, $b = 5.2$ mm, and $\nu = 33 \times 10^{-6}$ m^2/s.

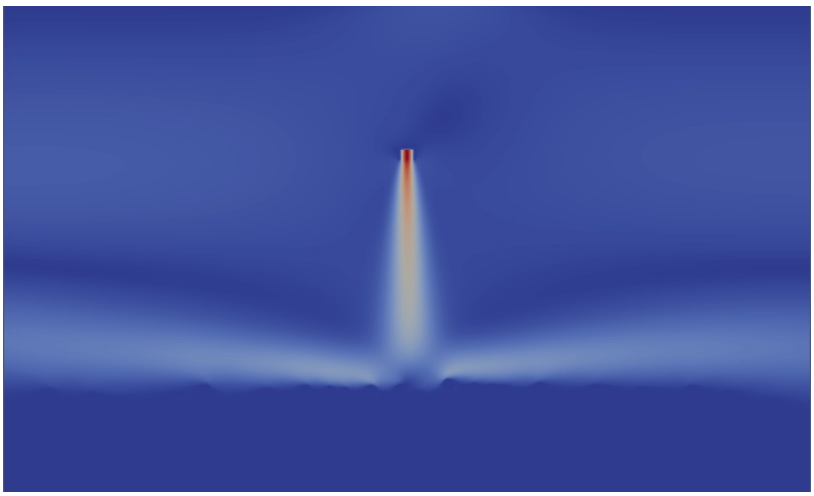

Fig. 3.11. Snapshot of the steady state velocity contours for a jet impinging on a granular surface with mean grain size $d = 5$ mm. The simulation parameters are here $H = 90.4$ mm, $U_0 = 0.37$ m/s, $b = 5.2$ mm, and $\nu = 33 \times 10^{-6}$ m^2/s.

As shown in Figure 3.12, with additional comparison to the smooth-wall results, we can appreciate a close agreement of the data for the low velocity range, with slight growing deviations for higher fluid velocities and higher particle size due to the irregular form of the bed surface. We notice also that the variation is almost proportional with a slope equal to 0.821 in case (W) (with a correlation coefficient $R^2 = 0.999$), consistently for any given jet Reynolds number Re_j and distance H within the range of our simulation sets. We have considered thereby the virtual origin found previously (i.e. replacing H by $H + \lambda$), namely $\lambda/b = 0.036Re_j$, although the effect of λ on the slope appears to be negligible. These results therefore confirm that the maximum velocity near a smooth impinged surface can be consistently estimated by means of the free jet theory. In this respect, it appears also reasonable to approximate the maximum velocity near the granular surface using the smooth wall case at least for the case of low Reynolds numbers.

In addition, the sensitivity to the impact point location was also tested for the same inlet flow condition. To this end, several calculations were performed after a slight lateral displacement of the nozzle (up to 3 times the minimal diameter) in either directions. In all cases, the maximal velocity V was found consistent to a mean value within a reasonable error bar estimated to less than 5% from the standard deviation values. The same relative error is used for the other inlet flow conditions.

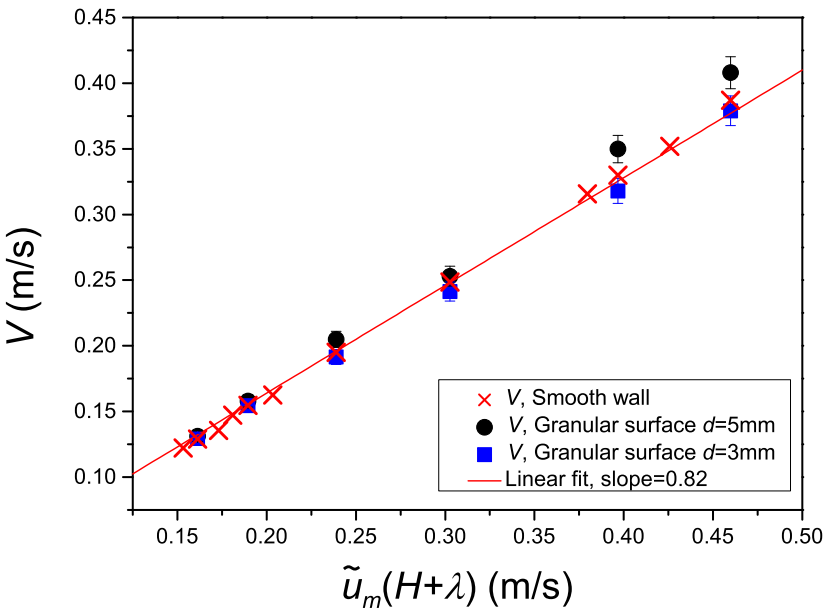

Fig. 3.12. Variation of maximum velocity V versus the free jet velocity $\tilde{u}_m(H+\lambda)$ at the corresponding downstream distance $x = H$ for two grain sizes $d = 3$ mm and 5 mm and impingement on a smooth wall.

Figure 3.13 shows the velocity profiles at various distances y/H from the original jet's axis. These profiles are normalized using the maximum velocity v_m, while the

distance x_1 from the wall is divided by b_1, which corresponds to the distance from the wall where $v = v_m/2$. It can be seen on Fig. 3.13 that both simulated results agree fairly well with Eq. 1.43 as well as with the experimental data of Ghaneeizad et al. (2014). We notice that the velocity profiles appear here self-similar roughly starting from a distance $y/H \geq 0.22$, in contrast to the value of $r/H \geq 0.15$ given in the literature for turbulent round jets Ghaneeizad et al. (2014).

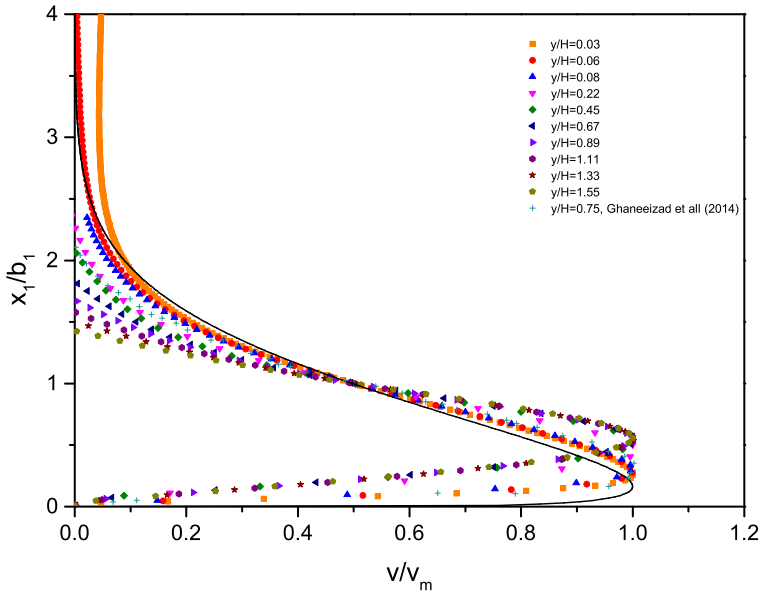

Fig. 3.13. Self-similarity of the normalized velocity profiles v/v_m versus x_1/b_1 in the wall-jet region. The solid line corresponds to Eq. 1.43.

Wall shear stress

The estimation of the shear stress at the bed surface is essential to determine the erodibility of soils, especially to specify the critical shear stress at which the onset of erosion takes place.

A typical distribution of the dimensionless wall shear stress obtained from our simulation is plotted in Figure 3.14 for different combinations of impingement height H/b and jet Reynolds number Re_j. It is also compared to the estimation by Beltaos and Rajaratnam (1974) (see Eq. 1.42). Despite the difference in flow configurations (2D laminar versus round turbulent jet), the dimensionless shear stress distribution agrees quite well with the one given by Beltaos and Rajaratnam (1974). The profiles start with a zero value in the impingement region then increase to a maximum value τ_m before starting to decrease slowly.

The maximal value of the shear stress, denoted τ_m, is commonly assumed to be proportional to the squared maximal velocity V as follows (Beltaos and Rajaratnam,

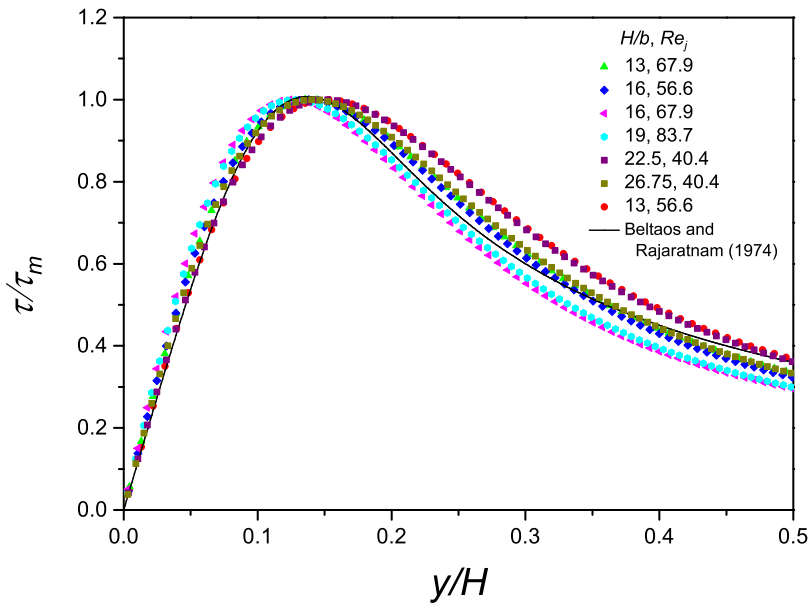

Fig. 3.14. Distributions of the normalized wall shear stress versus y/H for different combinations of normalized impingement height H/b and jet Reynolds number Re_j. The solid line stands for the estimation by Beltaos and Rajaratnam (1974).

1977):

$$\tau_m = \frac{1}{2} C_f \rho_f V^2 \tag{3.2}$$

where C_f is the local friction coefficient and ρ_f is the fluid density.

It is noteworthy that there are no estimations of C_f for laminar impinging jets found in the literature. Thereby we can use our simulation results to estimate C_f based on Eq. 3.2 for the different jet Reynolds numbers and impingement heights H shown in Table 3.2.

A plot of the maximum shear stress τ_m versus $\rho_f V^2/\sqrt{Re_j}$ is shown in Fig. 3.15, suggesting a proportional dependency that allows, from a linear regression (with a correlation coefficient $R^2 = 0.9978$), to estimate C_f as:

$$C_f = \frac{1.53}{\sqrt{Re_j}} \tag{3.3}$$

This way, Eq. 3.2 becomes:

$$\tau_m = \frac{0.765 \rho_f V^2}{\sqrt{Re_j}} = \frac{0.52 \rho_f (\tilde{u}_m(H))^2}{\sqrt{Re_j}} \tag{3.4}$$

By introducing Eq. 1.39 and Eq. 3.1, it then reads:

$$\tau_m = \frac{0.137 \rho_f u_j^2 {Re_j}^{1/6}}{(H/b + 0.036 Re_j)^{2/3}}. \tag{3.5}$$

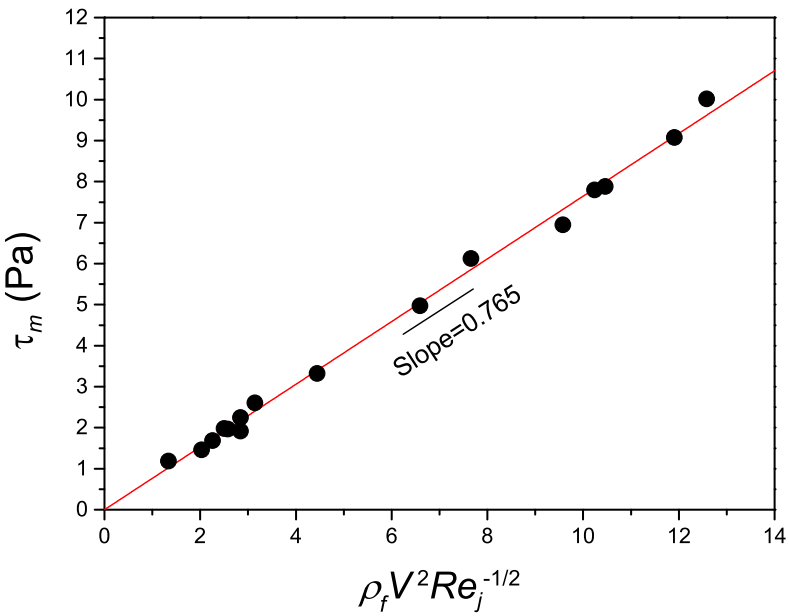

Fig. 3.15. Maximum shear stress τ_m on a smooth impinged surface versus $\rho_f V^2/\sqrt{Re_j}$. The line stands for a proportional relation with a slope 0.765 and a correlation coefficient $R^2 = 0.9978$.

Surprisingly, we found that the simulation results give rather close results compared to an estimation based on the Blasius friction law for laminar flows over a flat plate: $\bar{C}_f = \frac{1.328}{\sqrt{Re}}$ (Streeter and Wylie, 1975), where $\bar{C}_f$ is the average friction coefficient over a plate of length L and $Re = U_\infty L/\nu$.

Summing up, these results show that the local friction coefficient at the maximum shear stress seems to be almost proportional to $1/\sqrt{Re_j}$ for laminar jet impingements on a smooth wall, just as predicted by the laminar boundary layer theory on flat plates at zero incidence. The maximum shear stress on a smooth wall can therefore be estimated using the approximation given in Eq. 3.5 and based on our simulation results.

Concerning the wall shear stress distribution at the granular surface, huge fluctuations in shear stress are observed, most probably due to the irregularity of the impinged surface, and preclude the appearance of smooth distributions such as shown in Fig. 3.14.

Nevertheless, in absence of more specific estimations and regarding the strong similarity observed as regards maximal velocity (see Fig. 3.12), it appears acceptable to derive herein the wall shear stress using the previous approximation based on the maximum velocity V found for the smooth-wall case (i.e. Eq. 3.4).

3.3 Impinging jet erosion: cohesion-less soil

We now focus on jet erosion, i.e. detachment of solid particles under the action of an impinging jet, starting with the case of a cohesion-less granular bed. In this section, the solid particles are no more fixed and can move freely, only constrained by purely frictional interactions (i.e. zero cohesion) and hydrodynamic stresses imposed by the impinging jet. The aim of this section is first to compare our simulation results with the experimental results of Badr et al. (2014) in their proposed "inertial" Shields diagram (i.e. Sh_i vs Re_p). Second, we present a way to plot both results in the classical Shields diagram, using the approximation of the bed shear stress τ_b for the 2D laminar impinging jet from Eq. 3.4, or equivalently Eq. 3.5, as found in the previous section.

3.3.1 Erosion onset

In order to determine the erosion threshold (i.e. the minimum shear stress required to mobilize the solid particles) for a given cohesion-less granular sample in our micro-mechanical jet erosion test (JET) simulations, the maximal injection velocity U_0, or equivalently the mean inlet velocity u_j, is progressively increased with time until ultimately reaching a fully developed erosive state, as shown in Fig. 3.16. Then, we identify the critical inlet velocity U_0^c based on the observation of the first grain motion. This onset time is not easy to determine accurately. Typically, the initiation of grain motion takes place in time sequences of varying duration, up to 10 images, giving this way a substantial uncertainty for the critical inlet velocity. The corresponding error bars are reported in the following graphs. Consistently, the initiation of grain motion can be alternatively detected by the evolution of the total particle's kinetic energy as shown in Fig. 3.17. It can be seen that this method is more accurate than the direct observation of first grain motion by naked-eyes and this method shows indeed a substantial delay time (hatched area) beyond which the erosion progressively starts.

To provide a large range of variation within the Shields diagram this procedure was repeated for various jet Reynolds numbers and three different granular samples: d_{mean}=2, 3, and 5 mm, respectively, with a uniform size distribution ranging from $d_{min} = 0.8d_{mean}$ to $d_{max} = 1.2d_{mean}$. The input parameters for this systematic study are summarized in Table 3.3.

We observe that erosion first takes place at a certain distance from the impingement, that roughly corresponds to the location of the maximal shear stress predicted in our previous analysis of jet impingement over a smooth wall, consistently with the fact that there is a stagnation point at the intersection of the bed surface with the jet's axis. However, with increasing the inlet velocity, we observe eventually lateral oscillations of the jet caused by the irregularities of the bed surface, which also increase with the on-going scouring process. Due to both the jet's oscillations and the increasing depth of the crater, the location of the maximal shear stress appears then to shift towards the jet's axis, thereby creating a deeper crater right at the impingement. This behavior is illustrated by the typical graphical sequence

Table 3.3. Input parameters for our systematic study of the erosion threshold of cohesion-less samples

Solid particles	Fluid
Density ρ_g: 2230 kg/m^3	Density ρ_f: 847 kg/m^3
Mean diameter d_{mean}: 2, 3, or 5 mm	Kinematic viscosity ν:
Normal stiffness k_n: 1.10×10^5 N/m	30 to 50×10^{-6} m^2/s
Shear stiffness k_t: 1.10×10^5 N/m	Nozzle diameter b: 5.2 mm
Friction coefficient μ: 0.30	Impingement height H: 90 mm
Rolling friction μ_r: 0.1	
Restitution coefficient e: 0.2	
Gravitational acceleration g: 9.81 m/s^2	

shown in Fig. 3.16 where a threshold in the particle's kinetic energy (translation plus rotation) has been introduced to highlight the eroded grains. The value of this energy threshold E_c is set implicitly based on the observation of particles detachment on previous simulations. A more in-depth explanation about the exact value to be chosen for E_c will be given in Chapter 4.

3.3.2 Representation in the Shields diagram

Here it is worth noting that, for practical use, the Shields number (Eq. 1.12) is sometimes rather inconvenient, especially in complex flow configurations such as the impinging jet. Indeed, the bed shear stress τ actually appears in both x-axis (i.e. Shields number) and y-axis (i.e. shear Reynolds number $Re_\tau = \sqrt{\frac{\tau}{\rho_f}}\frac{d}{\nu}$) variables of the Shields diagram. However, this can be circumvented with the alternative approach proposed by Badr et al. (2014) and later adopted also by Brunier-Coulin et al. (2017), representing an equivalent form of the Shields number for the impinging jet. The idea here is to assume an inertial expression for the bed shear stress which is therefore simply proportional to $\rho_f u^2$, regardless of the flow regime. Here, the velocity u is the mean fluid velocity around the eroded particle, which can be directly estimated from the free jet model $\tilde{u}_m(H)$ instead of the shear velocity u_* at the impinged surface which requires the exact value of the bed shear stress since $u_* = \sqrt{\frac{\tau}{\rho_f}}$.

As a first test, we can compare quantitatively our simulation results to the experimental data of Badr et al. (2014) carried out with a plane jet, since their quasi-2D configuration is closely consistent with the two-dimensional conditions of our model. The equivalent Shields diagram proposed by Badr et al. (2014) relates the critical value of the inertial Shields number, Sh_u^*, to the critical particle Reynolds number $Re_p^* = \frac{ud}{\nu}$ as follows:

$$Sh_u^* = \frac{\rho_f u^2}{(\rho_g - \rho_f)gd} = \frac{\rho_f u^2}{\Delta\rho g d} = f(Re_p^*) \tag{3.6}$$

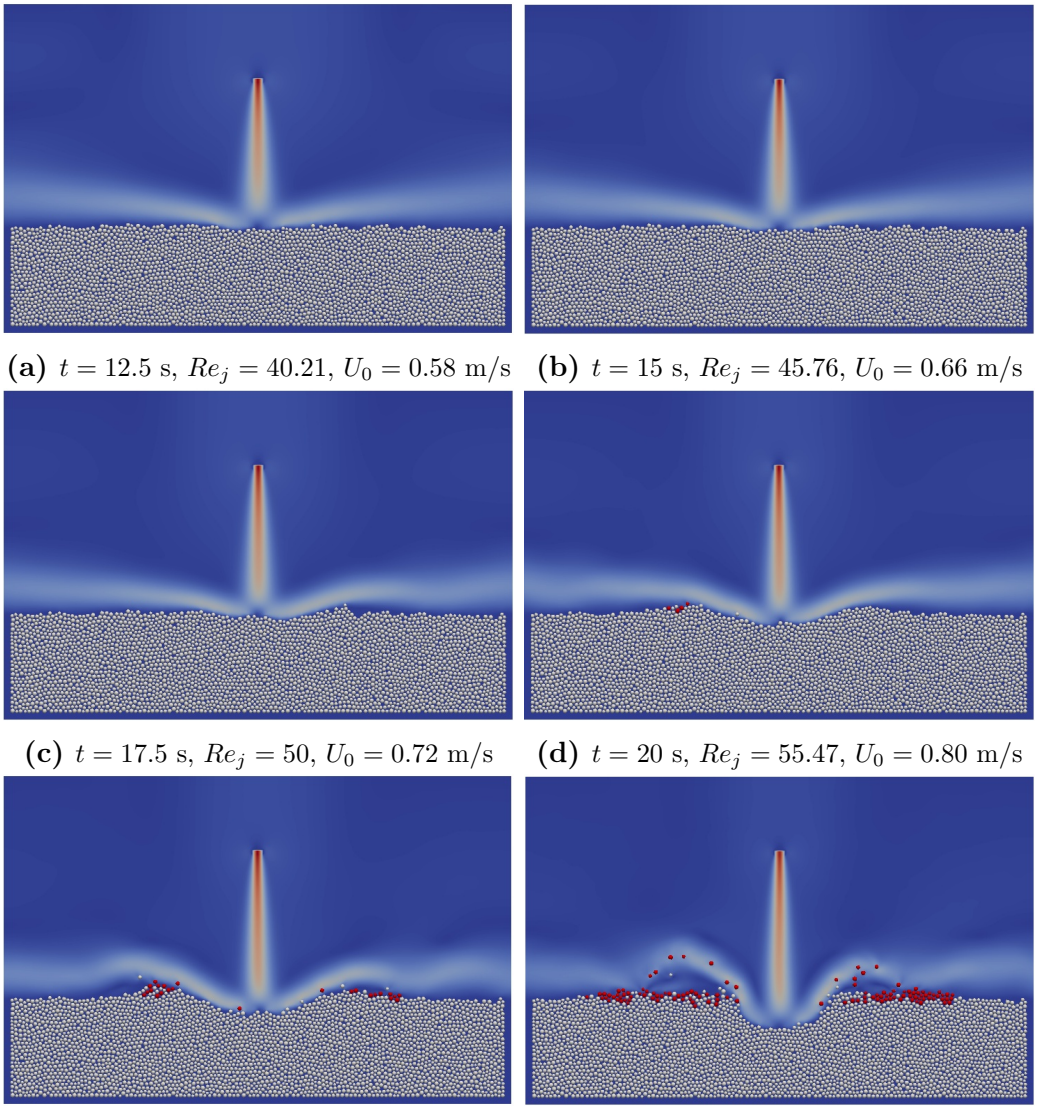

(a) $t = 12.5$ s, $Re_j = 40.21$, $U_0 = 0.58$ m/s **(b)** $t = 15$ s, $Re_j = 45.76$, $U_0 = 0.66$ m/s

(c) $t = 17.5$ s, $Re_j = 50$, $U_0 = 0.72$ m/s **(d)** $t = 20$ s, $Re_j = 55.47$, $U_0 = 0.80$ m/s

(e) $t = 22.5$ s, $Re_j = 61.01$, $U_0 = 0.88$ m/s **(f)** $t = 25$ s, $Re_j = 69.33$, $U_0 = 1.00$ m/s

Fig. 3.16. Time sequence of jet erosion for a frictional granular sample composed of 3000 particles with $d_{mean} = 2$ mm, $\nu = 50 \times 10^{-6}$ m^2/s, and $b = 5.2$ mm. A color scale is used for the fluid velocity magnitude from zero (blue) to the maximal inlet velocity U_0 (red). Solid particles with kinetic energy above a critical threshold value $E_c = 2.0 \times 10^{-4}$ J are classified as eroded (here depicted in red colour).

where ρ_g is the particle density and $\Delta\rho = \rho_g - \rho_f$.

Sh_u^* and Re_p^* are therein evaluated for the equivalent free jet velocity $u = \tilde{u}_m(H)$ using the expression of $\tilde{u}_m(H)$ given in Eq. 1.39, where u_j is deduced from the critical inlet velocity U_0^c obtained for each simulation at the onset of erosion, namely $u_j = \frac{2}{3}U_0^c$.

Here it is also important to note that, for a quantitative comparison, the expression of the inertial Shields number Sh_u has to be modified for the simulated results to account for the dimensional discrepancy of the solid particles, i.e. simulated disks in

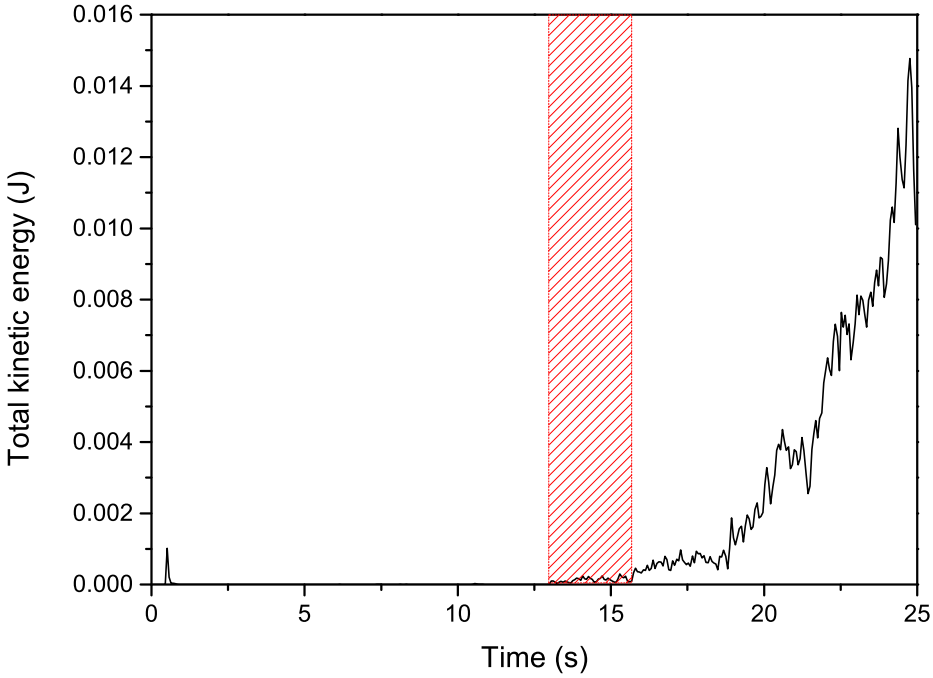

Fig. 3.17. Time evolution of the total kinetic energy of the grains during a jet erosion for a cohesionless sample shown in Fig. 3.16.

a plane versus solid spheres in the quasi-2D experimental configuration of Badr et al. (2014). The correction employed here is explained as follows. First, we assume that the ratio of the hydrodynamic drag force to the buoyant weight for a given particle is the same for both disks and spheres. This ratio reads $\frac{\tau_f S}{\Delta\rho g V} = Sh\frac{Sd}{V}$ where S and V are the cross-section and volume of the particle, respectively. For disks or cylindrical particles, this expression leads to $\frac{Sd}{V} = \frac{4}{\pi}$, while for the case of a sphere $\frac{Sd}{V} = \frac{3}{2}$ is obtained. As a consequence, the inertial Shields number from the simulations needs to be multiplied by $\frac{3\pi}{8}$ to be quantitatively comparable to the experimental data. Moreover, the reduced (hydraulic) diameter $d_h = 0.8d$ is also taken into account, as explained in section 2.4.3.3.

Figure 3.18 shows that a fair agreement between numerical and experimental data can be achieved this way. Our numerical values for Sh_u^* are here in the range 1.16 ± 0.33 and compares well with the results of Badr et al. (2014), which suggested an almost constant value of $Sh_u^* = 1.2 \pm 0.6$ for a comparable range of Re_p^*, from laminar to turbulent flows. However, our numerical data are more compatible with a slight but substantial decrease of Sh_u^* with Re_p^*.

In order to plot Badr et al. (2014) data in the classical Shields graph, namely Sh_τ^* vs Re_τ^*, we start from their experimental results as presented in Figure 3.19 which is directly extracted from their article. Note that l^* denotes the dimensionless distance from the jet inlet: $l^* = l/b$ with b the jet's width at injection. More precisely,

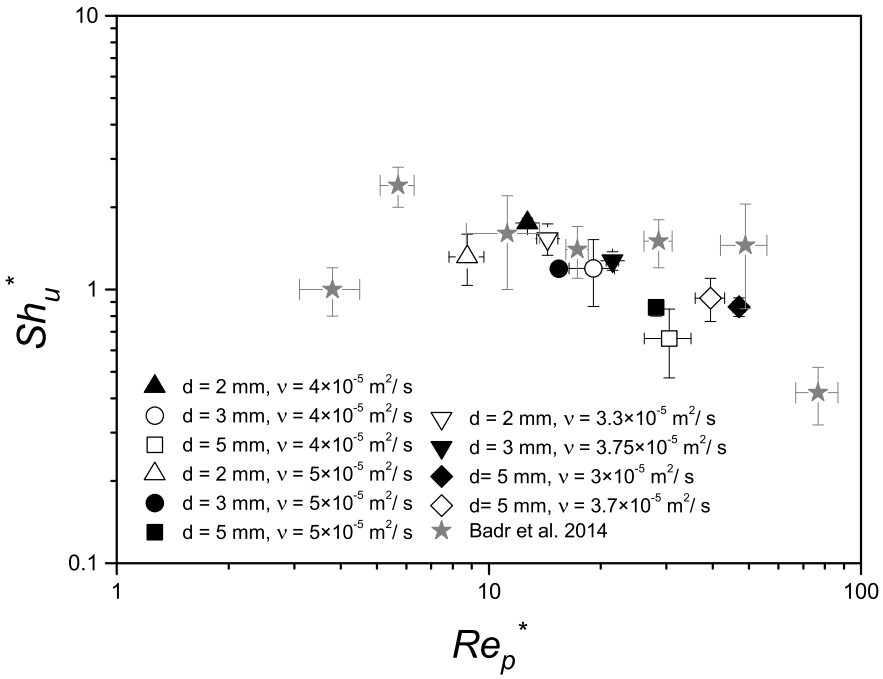

Fig. 3.18. Critical values of inertial Shields number Sh_u^* versus particle Reynolds number Re_p^* for the simulated jet erosion of frictional granular beds, as compared to the experimental results of Badr et al. (2014). The simulations were performed with different values of mean particle size d and fluid kinematic viscosity ν.

Fig. 3.19a is based on a viscous Shields parameter Sh_{Jv}, calculated as: $Sh_{Jv} = \frac{\eta U_J}{\Delta\rho g d^2}$.

From this graph, the critical inlet jet velocity U_{Jc} can then be easily deduced and, next, the local velocity at the bed surface u_{lc} using the expression from the free jet theory. This way and as illustrated in Figure 3.20a, we obtain for each of the 7 sets of parameters (see caption of Fig. 3.19 for more detail) the critical values of both the inlet velocity U_{Jc} and the local Shields number Sh_{lc}, based this time on an inertial definition: $Sh_{lc} = \frac{\rho_f u_{lc}^2}{\Delta\rho g d}$. In the particular case shown in Fig. 3.20b, a local Shields $Sh_{lc} \approx 1.2$ is found, corresponding to a local velocity $u_{lc} = 5.4 \pm 0.4$ cm/s at the sediment bed surface. Note that Badr et al. (2014) systematically observed the local Shields numbers to stagnate at a plateau value, either in laminar or turbulent regime, and consequently stated that "the nature (turbulent or laminar) of the jet does not have a significant influence on the erosion threshold".

However, Badr et al. (2014) were not able to relate locally, at the bed surface, the fluid velocity and the flow shear stress needed to calculate the usual Shields number Sh_τ. But, based on Eq. 3.4 obtained in Section 3.2.2, that is to say under the assumption that the same expression holds for the fluid friction coefficient C_f (i.e. Eq. 3.3), this difficulty can be now circumvented and both previous results can be plotted in the classical Shields diagram through Eq. 1.10 (see Chapter 1). The corresponding values of the critical Shields numbers Sh_τ^* for both experimental

and numerical results are shown in Figure 3.21 as a function of the shear Reynolds number Re_τ^* together with the explicit formulation by Guo (1997) given in Eq. 1.13.

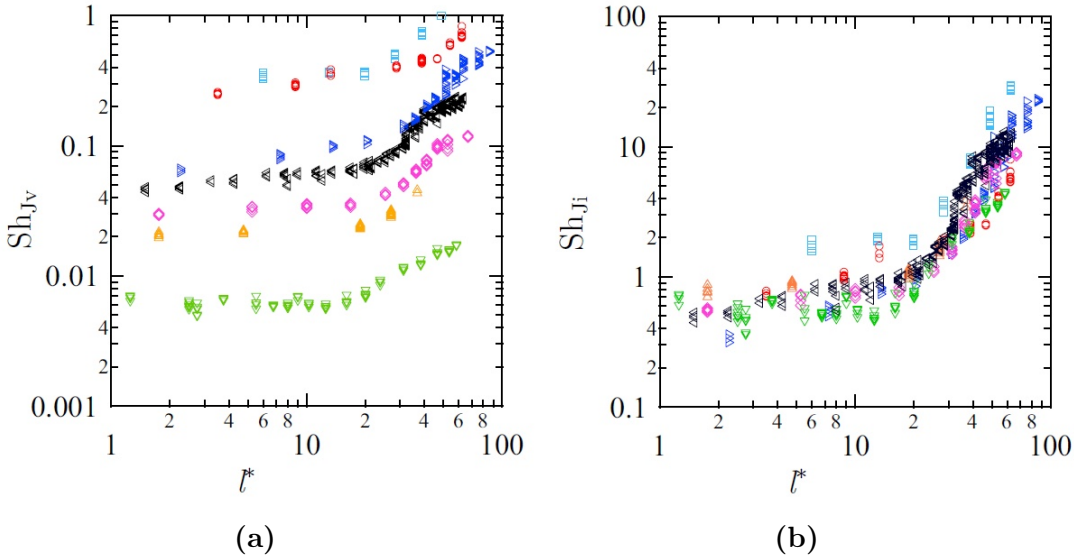

Fig. 3.19. Shields parameter versus the non-dimensional nozzle-sediment distance $l^* = l/b$. (a) Viscous Shields number $Sh_{Jv} = \frac{\eta u_J}{\Delta\rho g d^2}$ and (b) inertial Shields number $Sh_{Ji} = \frac{\rho_f u_J^2}{\Delta\rho g d}$, with different fluids kinematic viscosities ν and glass beads of different diameters d: $d = 0.1$ mm (□), $d = 0.25$ mm (◁), $d = 0.35$ mm (◇), $d = 0.5$ mm (△), and $d = 1$ mm (▽) in water ($\nu = 10^{-6}$ m^2/s) and $d = 0.25$ mm in in water-glycerol mixing of viscosity (▷) $\nu = 1.6 \times 10^{-6}$ m^2/s and $\nu = 4 \times 10^{-6}$ m^2/s (○). Data from Badr (2014)

In contrast to previous Fig. 3.18 using the inertial Shields number Sh_u^* and the particle Reynolds number Re_p, the comparison between numerical and experimental results is less in agreement when using the usual Shields parameter (Eq. 1.10) and the shear Reynolds number. Nevertheless, both data sets appear however relatively close to the explicit Shields curve by Guo (1997) (Eq. 1.13), with the simulated data laying slightly above it and the experimental ones slightly below. Furthermore, a small decrease of Sh_τ^* with Re_τ^* can now be more clearly observed for this range of Reynolds number Re_τ^*, almost consistent with the trend shown by the Shields curve.

In summary, the threshold condition for erosion by impinging jets of a granular sample can be rather satisfactorily described by the non-dimensional Shields parameter, based either on inertial or complete expression of bed shear stress. The Shields parameter Sh_τ based on the actual fluid shear stress is *a priori* more suitable for describing particle detachment at the onset condition than the inertial Shields, especially since the inertial representation of Shields is roughly a constant value whatever the jet regime (laminar or turbulent) and restricted for a particle Reynolds number Re_p greater than unity and less than 100 (Badr et al., 2014). Moreover, the classical Shields representation takes into account the fluid friction coefficient at the bed surface, thus much accurate representation of the flow, and can be easily extended

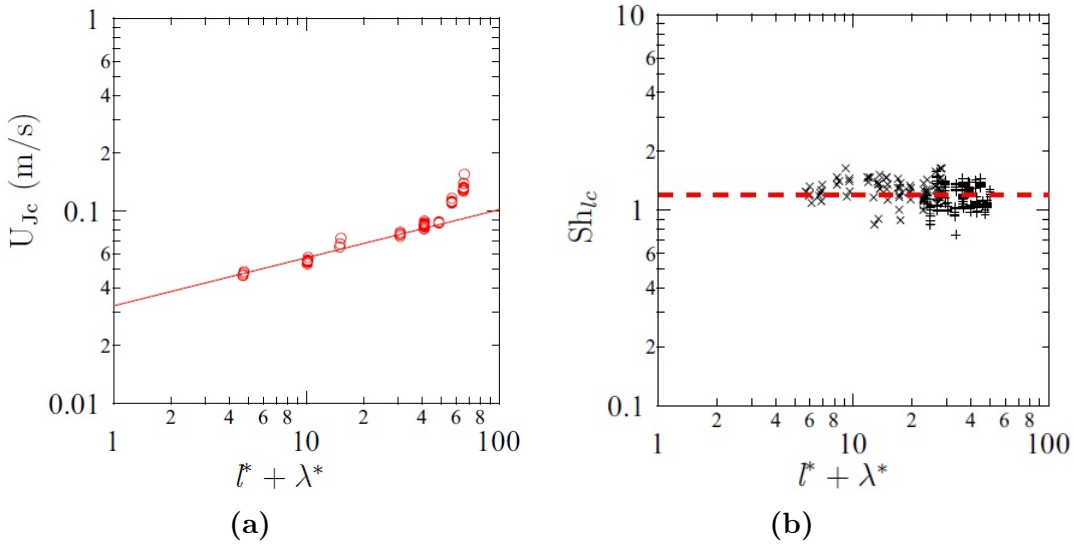

Fig. 3.20. (a) Critical jet velocity U_{Jc} versus the non-dimensional distance $l^* + \lambda^*$ (including the dimensionless virtual origin λ^*) for glass beads of diameter $d = 0.25$ mm immersed in a water-glycerol mixture ($\nu = 4 \times 10^{-6}$ m^2/s). The red solid line is a fit from the self-similar laminar model of free jet. (b) Local Shields number Sh_l at erosion threshold versus the non-dimensional distance $l^* + \lambda^*$, both for ($\times$) laminar model and ($+$) turbulent model. Data from Badr et al. (2014).

to turbulent flow regime, since the corresponding values of C_f are well known in the literature, at least empirically.

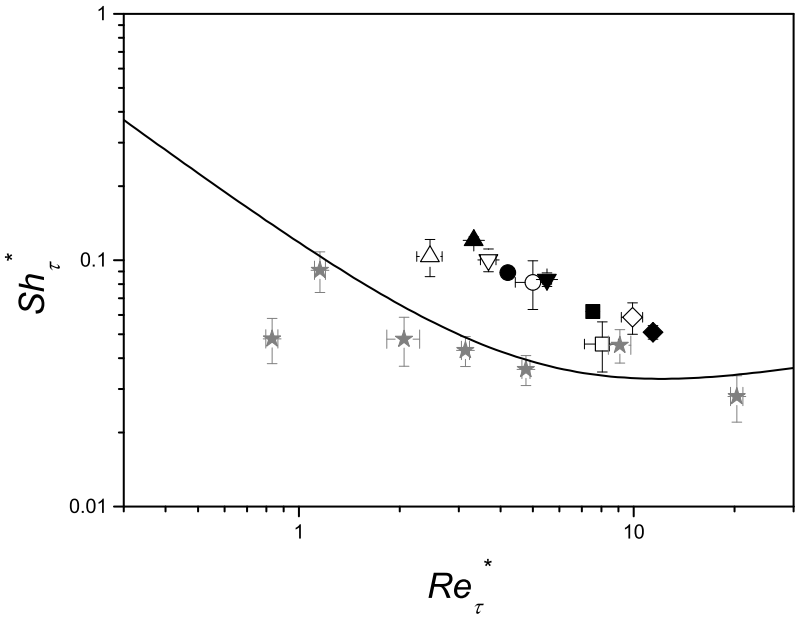

Fig. 3.21. Critical Shields number Sh^*_τ versus shear Reynolds number Re^*_τ. The solid line stands for the explicit formulation of the Shields curve by Guo (1997) (Eq. 1.13). The symbols are the same as those used in Fig. 3.18.

3.4 Impinging jet erosion: cohesive soil

3.4.1 Erosion onset and Shields diagram

In this section, we are interested in quantifying the erosion threshold by jet erosion test (JET) in presence of cohesion between particles.

In order to determine the erosion threshold for a given cohesive granular sample, the same protocol is used, progressively increasing the mean inlet velocity u_j over time until reaching a fully developed erosive state, as shown in Figure 3.22. The velocity growth rate is linear and fixed at 0.05 every second, and the ultimate velocity is fixed at $U_f = 2.5$ m/s. The simulation duration is fixed at 20 s. Then, we identify the critical inlet velocity U_0^c based on the observation of the initiation of bonds breakage at the bed surface (at time around $t = 4.86$ s in the illustrative sequence shown in Fig. 3.22). This velocity will subsequently be used to estimate the critical shear stress of the cohesive sample. Contrarily to the cohesion-less case, the onset is more easily determined here and, as can be seen in Fig. 3.23 showing the time evolution of the total kinetic energy of the grains, an uncertainty below ± 0.03 s (i.e. one picture before or after) can be estimated for the critical time, inducing an error of $\pm 3.0 \times 10^{-3}$ m/s on the corresponding critical velocity. In practice, the error bars are smaller than the size of the symbols and are consequently not plotted in the following graphs.

Here again a systematic study was carried out with rather similar ranges for the

fluid and granular parameters as shown in Table 3.4.

The critical inlet velocities at the erosion threshold U_0^c for different bond strength C are shown in Figure 3.24. Obviously, the critical inlet velocity increases with the bond strength. It is also observed that the lower the mean diameter, the higher the critical inlet velocity required to erode the particles. In other words, particles having lower sizes become more sticky and thus more difficult to be eroded. This is most probably due to the fact that the cohesive forces are more significant compared to the submerged particle weight in the case of fine particles compared to larger ones. However, the cohesion strength C used in our bond model could be scaled explicitly to account for particles sizes, especially if broad grain size distributions are considered, which is not the case here but could be envisaged in future works.

Table 3.4. Input parameters for our systematic study of the erosion threshold of cohesive samples

Solid particles	Fluid
Density ρ_g: 2500 kg/m^3	Density ρ_f: 1000 kg/m^3
Normal stiffness k_n: 1.10×10^5 N/m	Kinematic viscosity ν:
Shear stiffness k_t: 1.10×10^5 N/m	5×10^{-5} to 1×10^{-4} m^2/s
Friction coefficient μ: 0.30	Nozzle diameter b: $5 - 6.7$ mm
Rolling friction μ_r: 0.1	Impingement height H: 70 mm
Restitution coefficient e: 0.2	
Gravitational acceleration g: 9.81 m/s^2	

As already mentioned several times, the critical Shields number, as defined for cohesion-less sediments, is calculated from the fluid shear stress, $Sh_\tau^* = \frac{\tau^*}{\Delta\rho g d}$, and is assumed to be a function of the shear Reynolds number Re_τ^* as given in Eq. 1.10. Then, from the critical values of the inlet velocity, the corresponding critical values of the fluid shear stress τ^* can be estimated using here again the formula in Eq. 3.5 obtained for a laminar impinging jet over a smooth wall.

In presence of cohesion, the forces between particles are substantially larger than the submerged particle weight, keeping the particles together and forming a global matrix. When subjected to erosion, or scouring, to a sufficient level, the particles start to detach under the hydrodynamic forces from this matrix, possibly forming clumps of soil rather than individual particles, and the time required for the first grain detachments is larger compared to the cohesion-less case. In the present situation, it is not only the weight of the particle, with additional contribution of friction, that determines the threshold condition, but also, and mostly, the cohesion forces between particles.

As a consequence, the classical Shields number will no longer be valid for describing the erosion onset for the case of cohesive samples and a huge deviation from the cohesion-less curve is indeed observed on the Shields diagram as shown in Figure 3.25. More precisely, the classical critical Shields number Sh_τ^* (open symbols in the figure) increases almost linearly with Re_τ^*, gradually and drastically departing

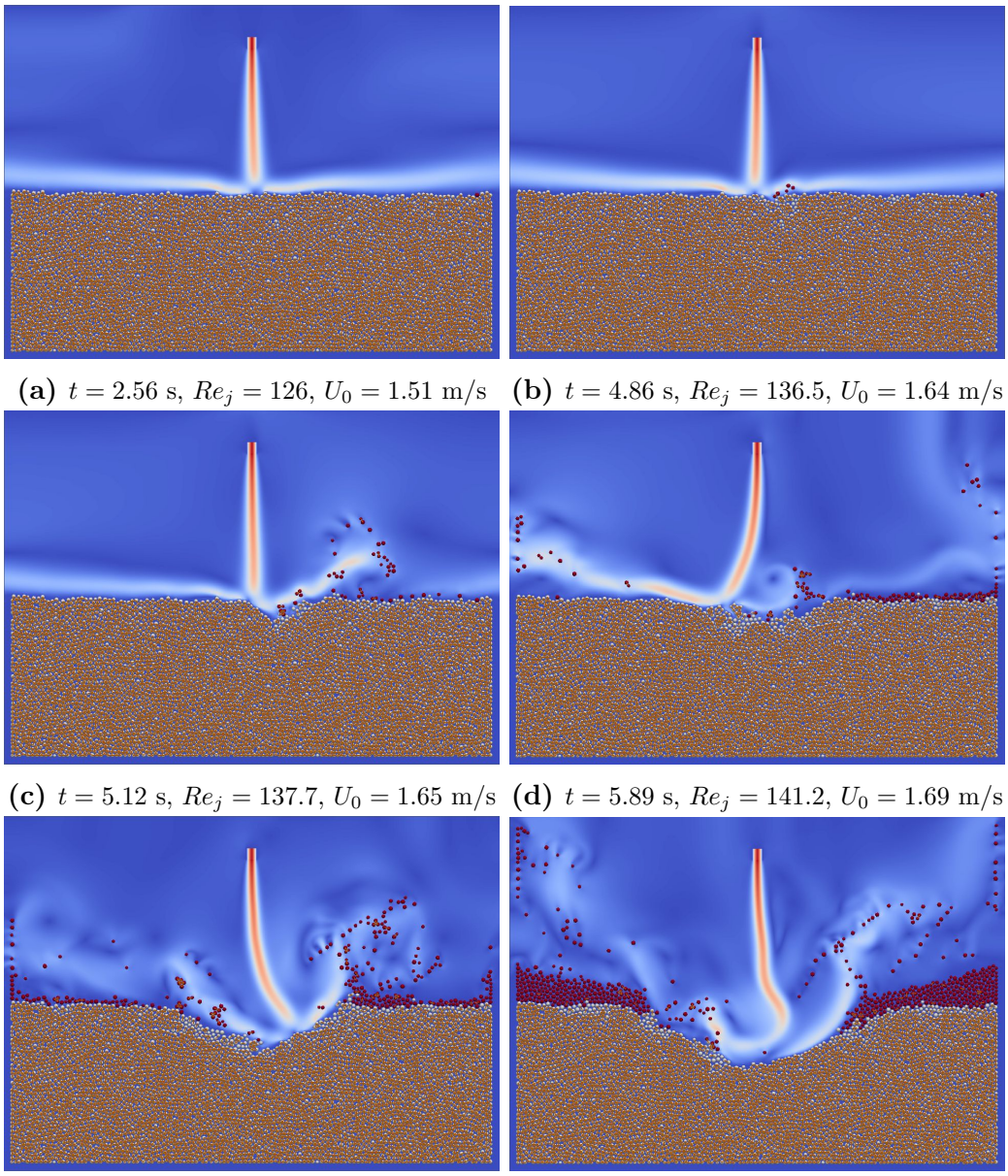

(a) $t = 2.56$ s, $Re_j = 126$, $U_0 = 1.51$ m/s **(b)** $t = 4.86$ s, $Re_j = 136.5$, $U_0 = 1.64$ m/s

(c) $t = 5.12$ s, $Re_j = 137.7$, $U_0 = 1.65$ m/s **(d)** $t = 5.89$ s, $Re_j = 141.2$, $U_0 = 1.69$ m/s

(e) $t = 6.4$ s, $Re_j = 143.6$, $U_0 = 1.72$ m/s **(f)** $t = 8.96$ s, $Re_j = 155.4$, $U_0 = 1.87$ m/s

Fig. 3.22. Time sequence of a jet erosion on a cohesive granular sample, of cohesion strength $C = 1.2$ N, composed of 5000 particles with $d_{mean} = 2$ mm, $\nu = 40 \times 10^{-6}$ m^2/s, and $b = 5$ mm. A color scale is used for the fluid velocity magnitude from zero (blue) to the maximal inlet velocity U_0 (red). Solid particles with a kinetic energy above a critical threshold value $E_c = 2.0 \times 10^{-4}$ J are classified as eroded (here depicted in red colour). The cohesive bond network is displayed in orange.

from the Shields curve. in addition, the data do not collapse on a unique trend as expected.

With the aim of overcoming this problem, a tentative approach to account for cohesion consists in a generalization of the cohesion-less Shields number. Such a

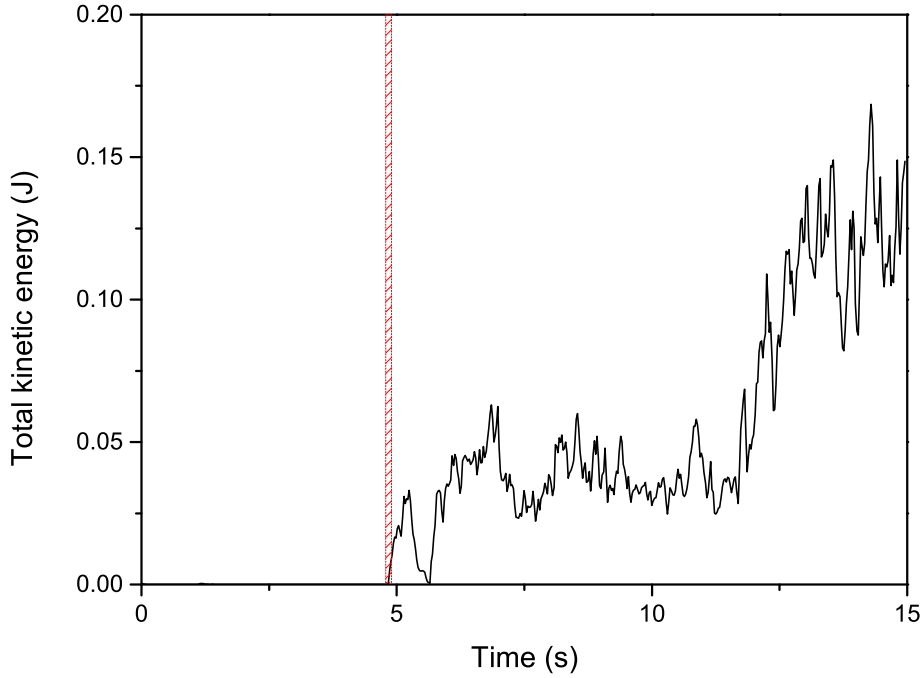

Fig. 3.23. Time evolution of the total kinetic energy of the grains during a jet erosion for a cohesive sample as shown in Fig. 3.22.

generalized shields parameter for cohesive particles has been previously introduced by several authors, as for instance Ternat et al. (2008) who suggested the multiplication of the Shields number by a cohesion function f_c defined by:

$$f_c = 1 + \frac{F_c}{\Delta\rho g d^3} \tag{3.7}$$

where F_c is the mean resultant cohesion force acting on a particle.

More recently, Brunier-Coulin (2016) proposed to add to the buoyant weight stress σ_{bw} the extra contribution of the cohesion stress σ_{coh}, the latter being taken directly proportional to the macroscopic yield tensile stress τ_t. Dimensionally, one gets $\sigma_{bw} \propto \Delta\rho g d^3$ while $\tau_t \approx 1.25 F_c/d^2$ as suggested by Brunier-Coulin (2016) from Rumpf equation (Pierrat and Caram, 1997).

By analogy, in our 2D configuration, this latter proportionality would read $\sigma_{coh} \approx F_c/d$. Note that this cohesion stress is expressed abusively in N/m instead of Pa, since we are dealing here with a 2D geometry. More precisely, in the following, the cohesive force F_c is chosen equal to the yield value of the normal tensile force C used in our cohesive bond model (see section 2.2.2). Shearing and bending failure of the cohesive bonds are not directly taken into account for simplicity reasons. However, in most cases, these thresholds in shearing and bending will be chosen simply proportional to the one in traction (i.e. C). The three failure modes are

consequently considered in the following dimensional analysis and their inclusion allows for aggregates of cohesive bonds to be detached from the cohesive matrix rather than solely pairs of bonded particles. Furthermore, some numerical traction tests were implemented, aiming to find a link between macro tensile stress and micro cohesive force, as presented with more detail in Appendix. A.

Next, denoting Sh_{coh} the corresponding cohesive Shields parameter, we can propose the following generalized definition for Sh_{coh}:

$$Sh_{coh} = \frac{\tau_b}{\Delta\rho g d + \alpha\sigma_{coh}} = \frac{Sh_\tau}{1 + \alpha Bo_g} \tag{3.8}$$

where Bo_g is the granular Bond number, already introduced in the literature (Castellanos, 2005; Claudin and Andreotti, 2006; Anand et al., 2009), which compares cohesion and buoyant weight, and reads:

$$Bo_g = \frac{\sigma_{coh}}{\Delta\rho g d} = \frac{C}{\Delta\rho g d^2}. \tag{3.9}$$

A high level of cohesion is reached when $Bo_g \gg 1$ while, in the cohesion-less case, Bo_g tends to zero and the cohesive Shields number Sh_{coh} coincides in Eq. 3.8 with the usual definition Sh_τ. Note also that the constant α, which comes from the dimensionless coefficients in the expression of the two contributing resistant stresses (namely cohesion and buoyant weight), is unknown and will consequently be used hereafter as a free parameter. A value of the order of 1 is consistently expected.

The pertinence of the generalized cohesive Shields number Sh_{coh} in the present 2D configuration and for our cohesive granular samples is tested in Fig. 3.25 where, in addition to the usual critical Shields number which is further and further away from the Shields curve as already discussed above, the generalized cohesive Shields number is also reported (red solid symbols in the figure) with the coefficient α being fixed to the value 2.7. This particular choice is obtained by direct comparison of the usual critical Shields number Sh^*_τ with the Shields curve, here approximated by the explicit formulation by Guo (1997) denoted Sh^*_{Guo} and given by Eq. 1.13. To this end, the value of $\left(\frac{Sh^*_\tau}{Sh^*_{Guo}} - 1\right)$ is plotted in Figure 3.26 versus the granular Bond number Bo_g, calculated from Eq. 3.9. As expected from Eq. 3.8, an almost linear relation is found and the corresponding slope α can be accurately estimated by linear regression, namely $\alpha = 2.69 \pm 0.06$ with a correlation coefficient $R^2 = 0.977$. Note that, coherently, α is indeed rather close to unity.

From Fig. 3.25 and Fig. 3.26, it can be concluded that the generalized Shields number is fairly relevant to describe the erosion onset for cohesive granular samples contrarily to the classical Shields number. The generalized Shields number can thus be used as a reference value for predicting the critical shear stress of our cohesive materials.

Then, the corresponding expression of the critical shear stress τ_c, deduced from the generalized Shields number, thus reads:

$$\tau_c = \Delta\rho g d \times Sh^*_\tau \times (1 + \alpha B_o) \tag{3.10}$$

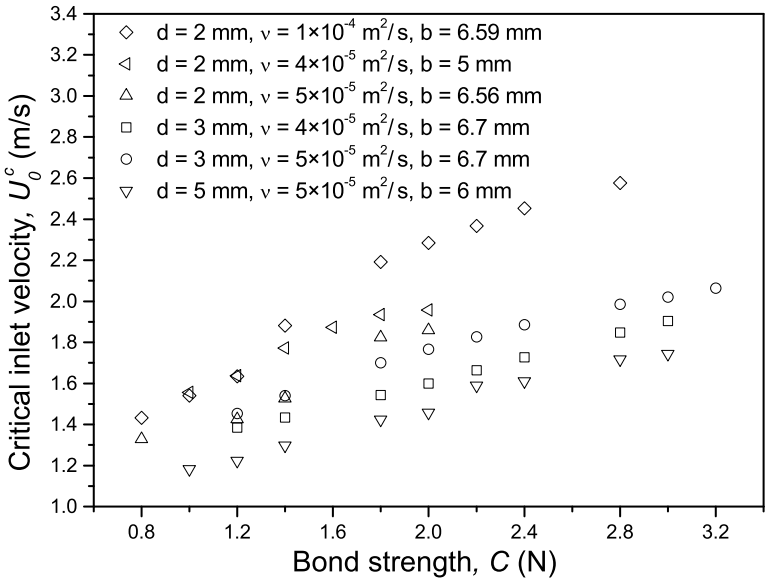

Fig. 3.24. Critical values of the inlet velocity U_0^c versus bond strength C for the simulated jet erosion tests of cohesive granular beds performed with the different values in mean particle size d and fluid kinematic viscosity ν as specified in Table 3.4.

where the classical Shields number Sh_τ^* can estimated from the explicit expression of Guo (1997), with $\alpha = 2.7$ and $B_o = \frac{C}{\Delta\rho g d^2}$.

Finally, τ_c can also be written in the initial form of two distinct contributions to the resistance to erosion:

$$\tau_c = \underbrace{\Delta\rho g d \times Sh_\tau^*}_{\text{buoyant weight + friction}} + \underbrace{\frac{\alpha \times Sh_\tau^* \times C}{d}}_{\text{cohesion/adhesion}} \tag{3.11}$$

Note that, in this expression, the hydrodynamics aspects are included implicitly in $Sh_\tau^*(Re_\tau)$.

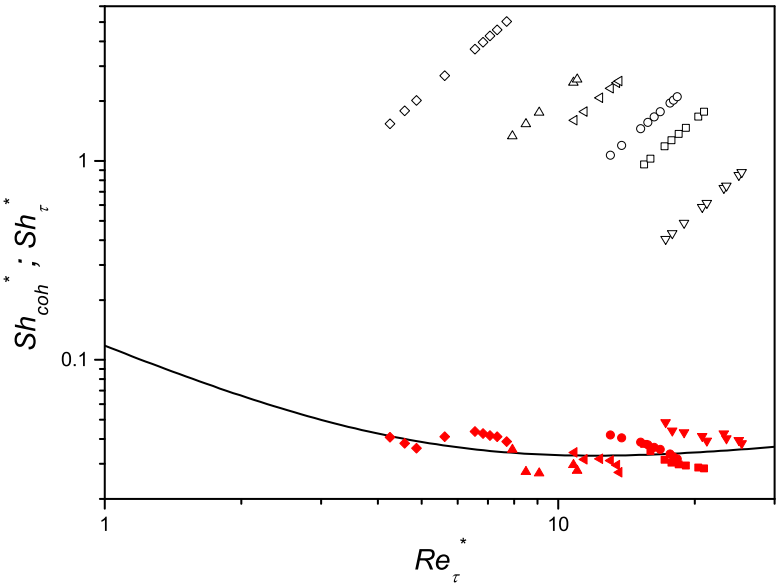

Fig. 3.25. Critical values of the usual Shields number Sh^*_τ and of the generalized Shields number Sh_{coh} versus shear Reynolds number Re^*_τ for the simulated jet erosion of cohesive granular beds with the different values in mean particle size d and fluid kinematic viscosity ν as specified in Table 3.4. The open symbols, which represent Sh^*_τ, are the same as those used in Fig. 3.24 while the red solid symbols for Sh_{coh} are calculated from Eq. 3.8 with $\alpha = 2.7$. The solid line represents the explicit Shields equation by Guo (1997) (Eq. 1.13).

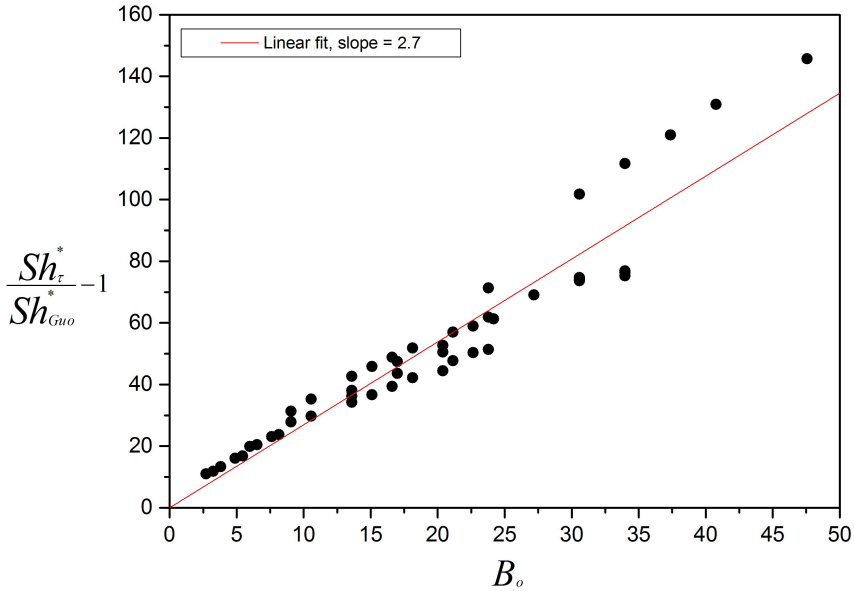

Fig. 3.26. Plot for all data of $\frac{Sh_\tau^*}{Sh_{Guo}^*} - 1$ versus the granular Bond number Bo_g, where Sh_τ^* is the critical Shields number obtained in the simulation and Sh_{Guo}^* is given by the implicit formulation by Guo (1997) in Eq. 1.13. The solid line represents a linear fit where the slope α is equal to 2.69 ± 0.06 with a correlation coefficient $R^2 = 0.977$.

3.4.2 Scour kinetics and erosion law

In this section, we provide an insight into the cohesive soil erosion and scouring induced by impinging jets in the laminar regime. Moreover, a JET interpretation model for the two-dimensional case is provided, aiming to estimate the erodibility parameters (i.e. k_d and τ_c) for our cohesive granular samples.

3.4.2.1 Adaptation of the JET interpretation model

Based on the classical interpretation of the JET presented in section 1.5.3, we propose here an adaptation to our particular situation of a 2D jet in laminar regime. As sketched in Fig. 3.27, it is here again assumed that the scour depth evolution $\frac{dx}{dt}$ (i.e. erosion rate) is given by the excess shear stress erosion law (Partheniades, 1965), with addition of a power law exponent n for a widespread applicability:

$$\dot{\epsilon} = \frac{dx}{dt} = k_d(\tau - \tau_c)^n \tag{3.12}$$

Note that the fluid shear stress at the impingement surface τ can be deduced from the previous impinging jet analysis (Sec. 3.2), and reads:

$$\tau = \tau_m = 0.137\rho_f u_j^2 Re_j^{1/6}\left(\frac{x+\lambda}{b}\right)^{-2/3} \tag{3.13}$$

where $Re_j = \frac{u_j b}{\nu}$ is the jet Reynolds number and λ the virtual origin given by Eq. 3.1.

The exponent n is usually set equal to unity ($n = 1$) in JET experiments. However, we add the exponent as a free parameter since, in the range $0.7 < n < 1.2$, it was found to correctly fit our numerical results presented in the forthcoming Chapter 4.

At equilibrium ($\frac{dx}{dt} = 0$), as the final scour depth x_∞ is reached, Eq. 3.12 can be rewritten as:

$$\tau = \tau_c \iff x_\infty + \lambda = b\left(\frac{0.137\rho_f u_j^2 Re_j^{1/6}}{\tau_c}\right)^{3/2} = 0.051 b\rho_f^{3/2} u_j^3 Re_j^{1/4}\tau_c^{-3/2}. \tag{3.14}$$

It follows for the critical fluid shear stress τ_c will be:

$$\tau_c = 0.137\rho_f u_j^2 Re_j^{1/6}\left(\frac{x_\infty+\lambda}{b}\right)^{-2/3}. \tag{3.15}$$

By introducing Eq. 3.13 and Eq. 3.15 into the erosion law (Eq. 3.12), one gets:

$$\frac{dx}{dt} = 0.137\rho_f u_j^2 Re_j^{1/6} k_d\left[\left(\frac{x+\lambda}{b}\right)^{-2/3} - \left(\frac{x_\infty+\lambda}{b}\right)^{-2/3}\right]^n \tag{3.16}$$

Then, a new variable $\xi = (\frac{x+\lambda}{b})^{-2/3}$ can be defined and substituted to x into Eq. 3.16, as follows:

$$\frac{dx}{dt} = -\frac{3}{2}b\xi^{-5/2}\frac{d\xi}{dt} = 0.137\rho_f u_j^2 Re_j^{1/6} k_d(\xi - \xi_\infty)^n \tag{3.17}$$

After separation of variables, it becomes:

$$\frac{d\xi}{\xi^{5/2}(\xi-\xi_\infty)^n} = -\frac{2}{3}\frac{0.137\rho_f u_j^2 Re_j^{1/6} k_d}{b}dt = -\frac{dt}{t_{er}} \tag{3.18}$$

with

$$t_{er} = \frac{10.95b}{\rho_f u_j^2 Re_j^{1/6} k_d}. \tag{3.19}$$

The integration of Eq. 3.18 from the initial condition, i.e. $\xi = \xi_0$ and $t = t_0$, gives:

$$F(\xi) = \int_{\xi_0}^{\xi(t)} \frac{d\xi}{\xi^{5/2}(\xi-\xi_\infty)^n} = -\frac{t}{t_{er}} \tag{3.20}$$

As one can see, the integral $F(\xi)$ is simply the opposite of the dimensionless time t/t_{er} and depends merely on ξ_0 and ξ_∞, with $F(\xi) \to \infty$ when $\xi \to \xi_\infty$.

Next, the following procedure was used in order to find the erodibility parameters (k_d and τ_c) for several scouring simulations.

- Determination of $\xi_0 = (\frac{x_0}{b})^{-2/3}$ and $\xi_\infty = (\frac{x_\infty}{b})^{-2/3}$ from image processing (see below).
- Plot of $f(\xi) = \xi^{-5/2}(\xi-\xi_\infty)^{-n}$ in the range $[\xi_\infty, \xi_0]$.
- Numerical integration of $f(\xi) = \xi^{-5/2}(\xi-\xi_\infty)^{-n}$ between ξ_0 and ξ_∞ using N intervals. Namely, $F(\xi) = \int_{\xi_0}^{\xi} f(\xi)d\xi = \sum F_i$ with, for $1 \leq i \leq N$, $\xi_i = \xi_0 + \frac{(\xi_0-\xi_\infty)}{N-1}(i-1)$ and $\frac{x_i}{b} = (\xi_i)^{-3/2}$.
- Introduction of the crater depth $\Delta x_i = x_i - x_0$ and plot of $\frac{\Delta x_i}{b}$ as a function of $-F_i = \frac{t_i}{t_{er}}$.
- Adjustment of the numerical results $\frac{\Delta x}{b}$ vs t/t_{er}, using t_{er} as a free parameter, and deduction of k_d from Eq. 3.19.
- Direct calculation of the critical shear stress τ_c from Eq. 3.15.

3.4.2.2 Time measurement of crater depth

The determination of the scour depth Δx is based on the assumption that Δx is directly proportional to the square root of the surface A of the crater. The evolution of the scour depth thus reads:

$$\Delta x = \Delta x_\infty \left(\frac{A}{A_\infty}\right)^{1/2} \tag{3.21}$$

This assumption is relevant in the context of a self-similar crater profile, with the width of the crater being proportional to its depth.

The surface of the crater A can be found using image processing techniques with the help of the free software *ImageJ*. Δx_∞ and A_∞ are the depth and the surface of

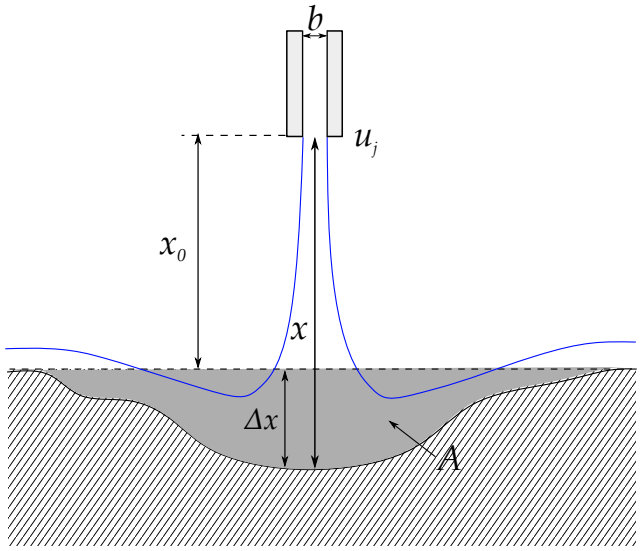

Fig. 3.27. Illustration of the jet erosion test where x_0 is the initial height, x the actual height, and Δx the scour depth. The grey zone is the scoured area denoted A.

the crater at equilibrium, respectively. They are determined here by time average of the sequential images of the evolution of the crater (see Fig. 3.30), once equilibrium is reached. The result of the time average is shown in Figure 3.31.

The crater depth Δx can also be estimated straight forwardly from tracking the interface of the crater at its center. From Fig. 3.28, we can check that both methods (area and interface) give rather close results, especially at the equilibrium since they both reach approximately the same plateau Δx_∞. As a consequence, both methods will give the same estimation of τ_c. However, they will give different k_d values, since the evolution of both curves before reaching the plateau are not similar, the estimation from the area presenting a faster kinetics.

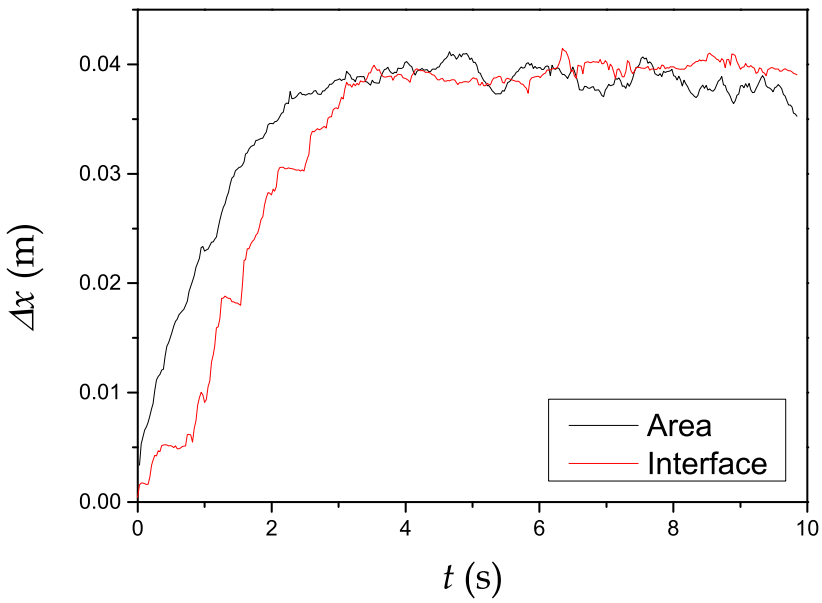

Fig. 3.28. Different methods used to evaluate the evolution of the crater depth Δx versus time for $C = 1.2$ N and $u_0 = 2$ m s^{-1}.

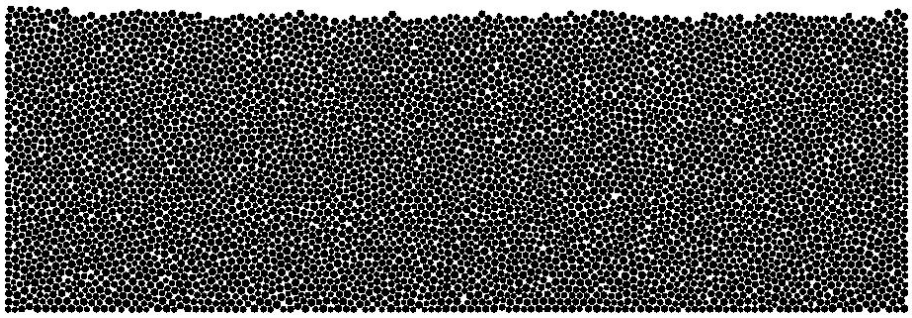

Fig. 3.29. Initial sample used for the JET simulation and composed of 5000 particles with $d_{mean} = 2$ mm.

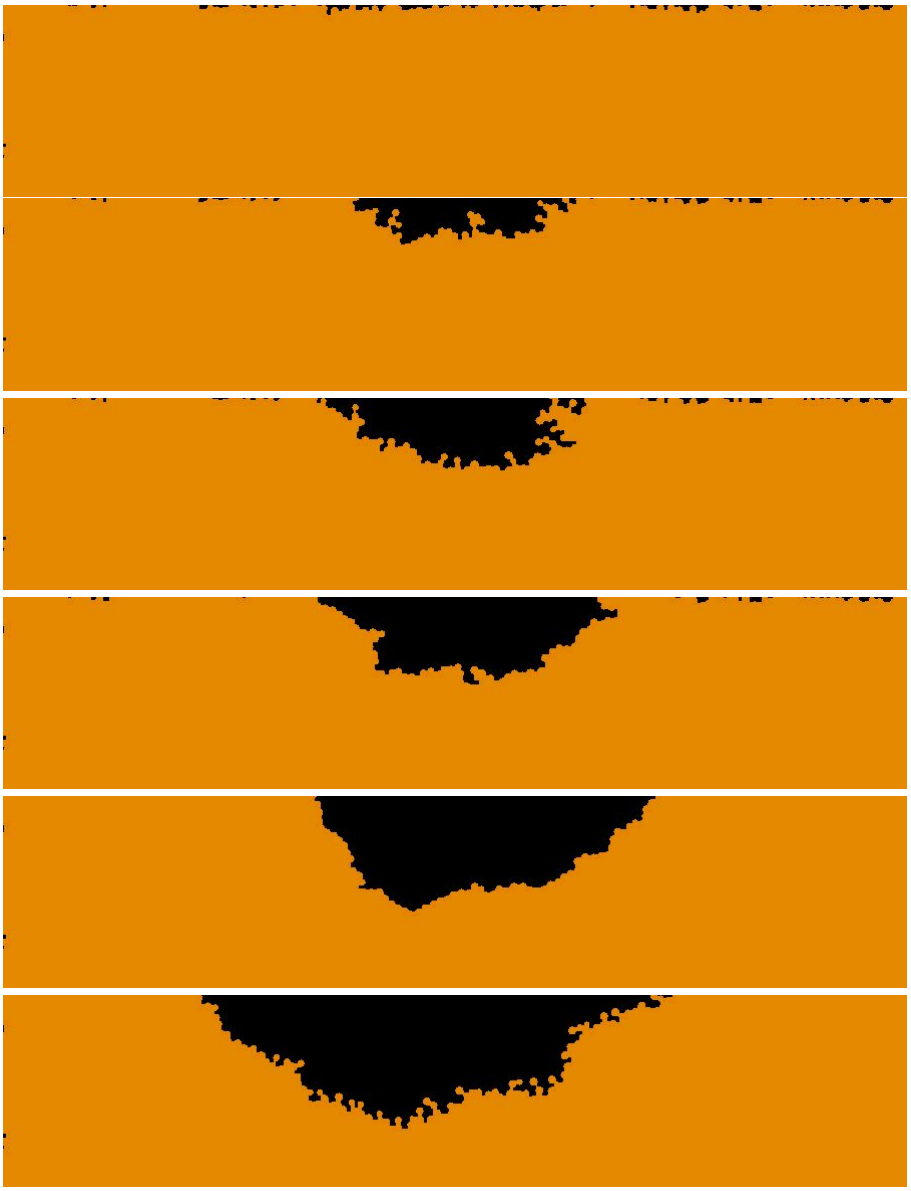

Fig. 3.30. Snapshots of the crater evolution for a 2D Jet Erosion Test at increasing times obtained after some image processing.

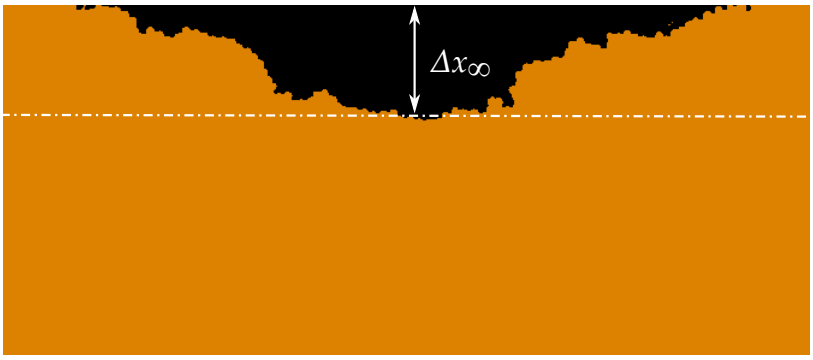

Fig. 3.31. A typical image resulted from post-processing techniques, using time average of the evolution of the scour area (black surface) once equilibrium is reached for $\nu = 40 \times 10^{-6}$ m^2/s, $u_0 = 2$ m/s, $C = 2$ N, $x_0 = 70$ mm, and $\Delta x_\infty = 23.5$ mm.

3.4.2.3 Test of the interpretation model

In order to test the validity of this interpretation model proposed above for our 2D erosion test (JET), a series of simulation is performed by fixing the maximal jet inlet velocity U_0 (or equivalently the mean inlet velocity $u_j = \frac{2}{3}U_0$), while the cohesive bond strength C is varied systematically in the range [1.0-2.0] N. Three values are chosen for U_0: 1.9, 2.0, and 2.2 m/s. The simulation input parameters are summarized in Table 3.5. The initial sample used for the simulation is shown in Figure 3.29.

Table 3.5. Input parameters for our systematic study of the numerical jet erosion test (JET)

Solid particles	Fluid
Density ρ_g: 2500 kg/m^3	Density ρ_f: 1000 kg/m^3
Normal stiffness k_n: 1.10×10^5 N/m	Kinematic viscosity ν:
Shear stiffness k_t: 1.10×10^5 N/m	4×10^{-5} m^2/s
Friction coefficient μ: 0.30	Nozzle diameter b: 5 mm
Rolling friction μ_r: 0.1	Impingement height H: 70 mm
Restitution coefficient e: 0.2	Inlet velocity U_0: 1.9, 2.0,
Gravitational acceleration g: 9.81 m/s^2	and 2.2 m/s

The image sequences, obtained at the end of each simulation and based on particle positions, are post-processed to quantify the time evolution of the scour depth Δx from the crater area (as explained in subsection 3.4.2.2). Then the crater position $x(t) = x_0 + \Delta x(t)$ is calculated, especially its asymptotic value x_∞, reached at the equilibrium. Figure 3.32a shows the evolution of the non-dimensional crater depth $\frac{\Delta x}{\Delta x_\infty}$ versus time t for the simulation data. It is found that a simple exponential law of the form $1 - \exp(-Bt)$ can satisfactorily model the evolution. In this particular example, a coefficient $B = 2.31 \pm 0.05$ is obtained with a goodness of fit $R^2 = 0.9229$.

Next, we can turn to the interpretation model by plotting, based on both the input parameter ξ_0 and the measured value ξ_∞, the function $f(\xi) = \xi^{-5/2}(\xi - \xi_\infty)^{-1}$. Note that here, for simplicity, we first set the exponent $n = 1$ for the erosion law. Following this, a numerical integration of f is implemented for each ξ-value in-between ξ_0 and ξ_∞. One thus gets $\frac{t}{t_{er}} = -F(\xi) = \int_\xi^{\xi_0} f(\xi)d\xi)$, as shown in Figure 3.33.

Once again, when the non-dimensional crater depth $\frac{\Delta x}{\Delta x_\infty}$ calculated with the interpretation model is plotted versus the dimensionless time $\frac{t}{t_{er}}$ in Fig. 3.32b, an exponential law $1 - \exp(-A\frac{t}{t_{er}})$ can fairly well fit the analytical curve. In the present case, the value found for the parameter is $A = (470 \pm 1) \times 10^{-5}$ with a correlation coefficient $R^2 = 0.9988$.

Finally, the adjustment of the numerical data with the model allows the identification of the characteristic erosion time t_{er} as $t_{er} = A/B$. For the example shown in Fig. 3.32, one gets $t_{er} = A/B = (204 \pm 5) \times 10^{-5}$ s. Then k_d can be deduced from Eq. 3.19 and reads $k_d = (6.45 \pm 0.16) \times 10^{-3}$ m^3/N/s.

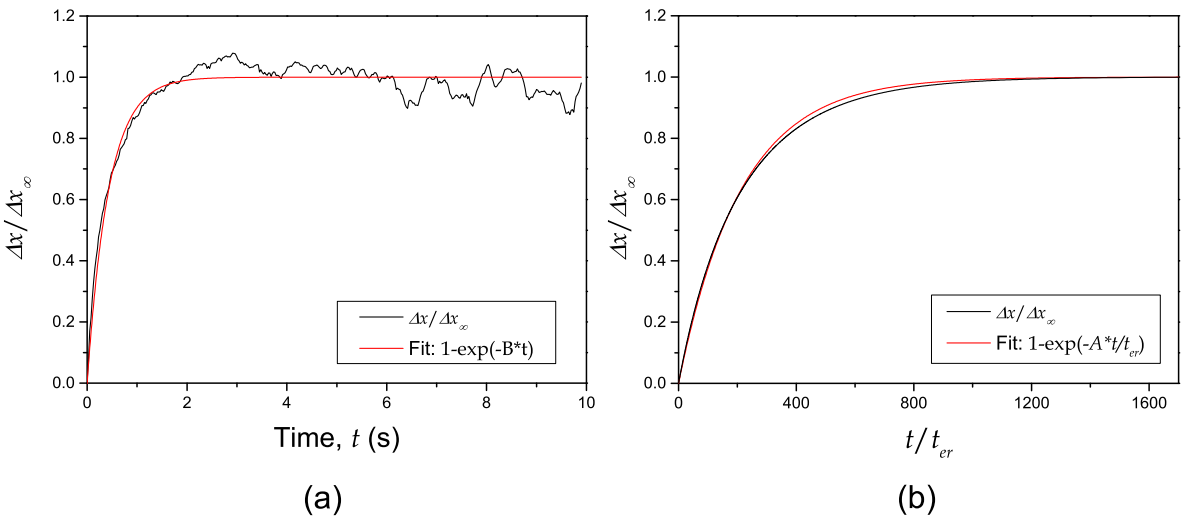

Fig. 3.32. Fit of the non-dimensional crater evolution. (a) Numerical data for $C = 1.2$ N and $U_0 = 2.0$ m/s; (b) Interpretation model with $\Delta x_\infty = 0.038$ m.

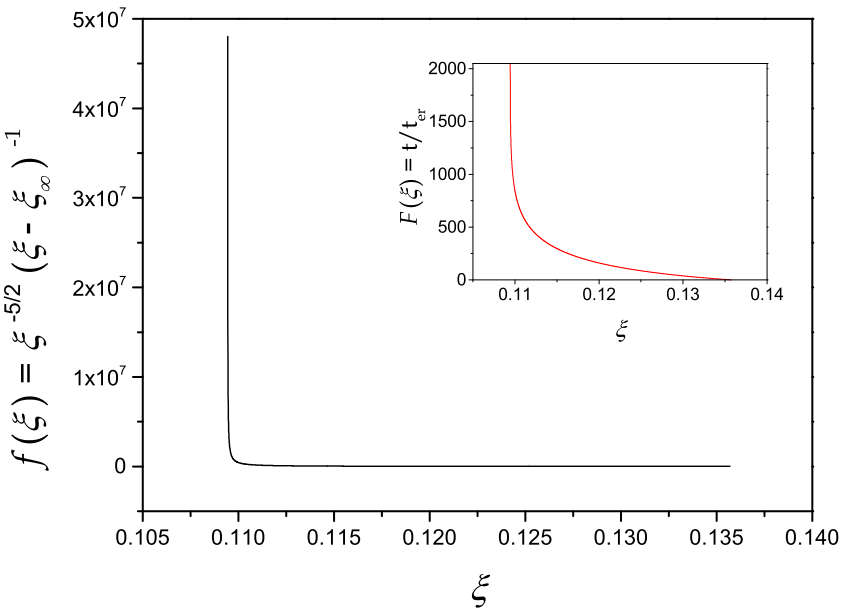

Fig. 3.33. Plot of $f(\xi)$ for $C = 1.2$ N and $U_0 = 2.0$ m/s. Insert: numerical integration of $f(\xi)$ in the corresponding range from $\xi_0 = 0.1357$ to $\xi_\infty = 0.1094$.

Figure 3.34 and Figure 3.35 present the erodibility parameters k_d and τ_c deduced from our JET simulations for different values of the cohesive bond strength C, respectively.

As regards k_d, it can be observed two important points. First, k_d consistently decreases when the cohesion strength gets higher. Second, for a given cohesion strength, the results vary moderately when the jet inlet velocity U_0 is changed, which is not expected as the erodibility parameters are supposed intrinsic of the material and should not be modified when the cohesion remains the same.

The same remarks hold for τ_c, but in a more pronounced manner. Indeed, for a given value of U_0, τ_c is poorly dependent on C, whereas an almost linear relation is expected from both Eq. 3.10 and the values obtained in the previous section as regards erosion onset. This means that the JET interpretation model over-predicts τ_c at low cohesive strength C and under-predicts it at high cohesive strength C values. Moreover, a strong and non-consistent sensitivity to the U_0-value is found. The shortcomings of the interpretation model are discussed and partly explained just below.

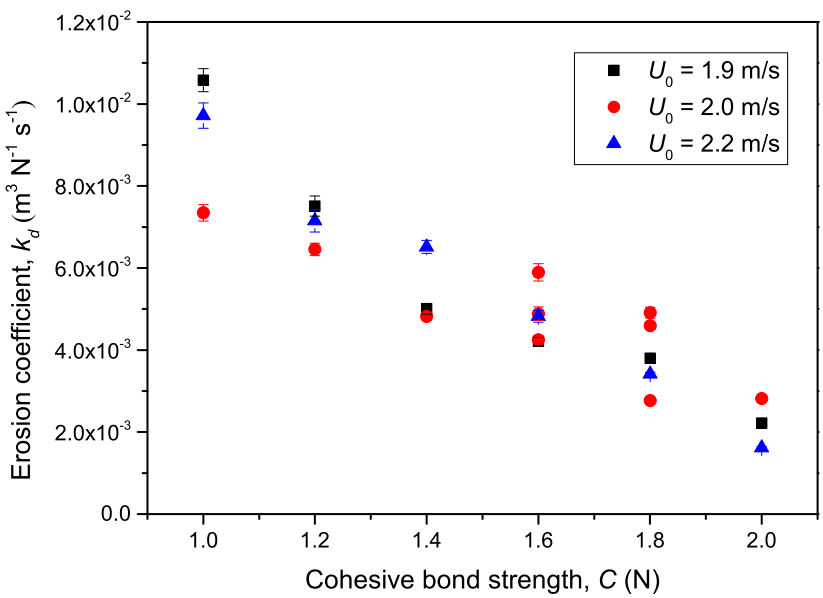

Fig. 3.34. Erosion coefficient k_d versus cohesive bond strength C obtained with three different inlet velocities: U_0 =1.9, 2.0, and 2.2 m/s.

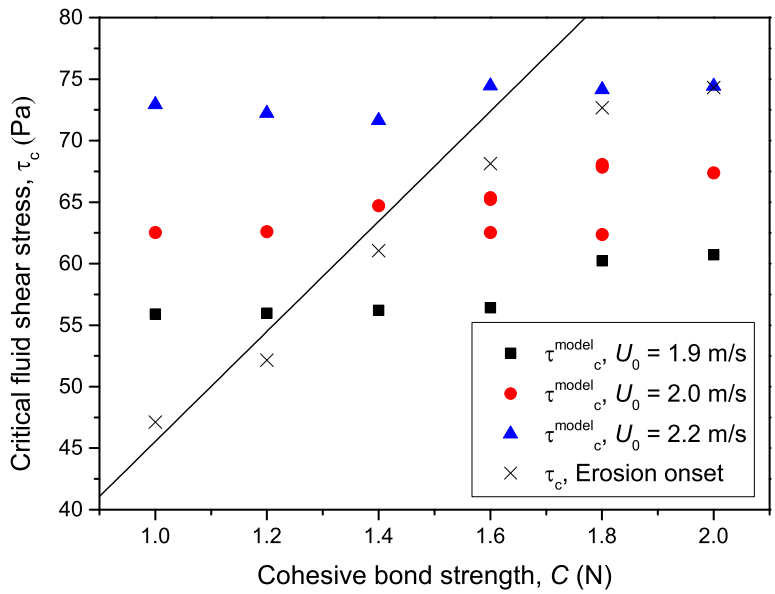

Fig. 3.35. Critical shear stress τ_c versus cohesive bond strength C obtained with three different inlet velocities: U_0 =1.9, 2.0, and 2.2 m/s. The data obtained for erosion onset in the previous section have been added ($\times$) while the solid line stands for Eq. 3.10.

3.4.2.4 Influence of the exponent n

The results presented above were obtained with a fixed value of the exponent $n = 1$. Here, we specifically examine the influence of the exponent n in the interpretation of the results and subsequent estimation of the erodibility parameters k_d and τ_c.

As a first observation on the basis of the model, the critical shear-stress τ_c is obviously independent of n (Eq. 3.15) and only an impact on the erosion coefficient τ_c is expected.

From Figure 3.36a, it is indeed observed that the exponent n affects only the characteristic time of erosion t_{er}, and thus k_d, but not the final scour depth that is solely ruled by τ_c. Moreover, the non-dimensional evolution of the crater depth $(\Delta x/\Delta x_\infty)$ for different n-values can be collapsed on a unique curve with the help of a fitting parameter χ_n as shown in Figure 3.36b. This parameter χ_n is obtained by adjustment of the dimensionless time t/t_{er} to the reference value for $n = 1$: $(t_{er})_n = \chi_n (t_{er})_{n=1}$. A linear variation of $\ln(\chi_n)$ versus n is found empirically in Figure 3.37 and reads: $\ln(\chi_n) = 4.55(n-1)$. Thus, for a given value of the exponent n, the erosion time t_{er} is simply deduced from its reference value obtained for $n = 1$ and, finally, the actual erosion coefficient reads:

$$k_{d_n} = k_{d_{n=1}} \times \exp\left[4.55(1-n)\right] \tag{3.22}$$

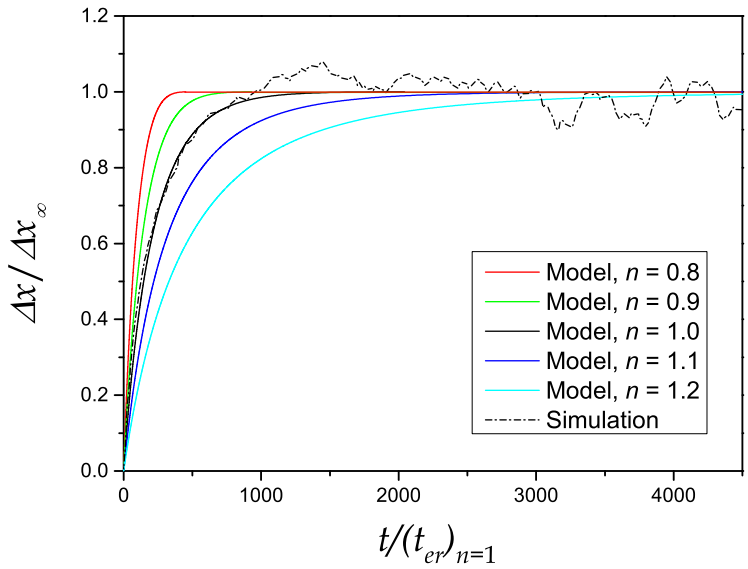

(a)

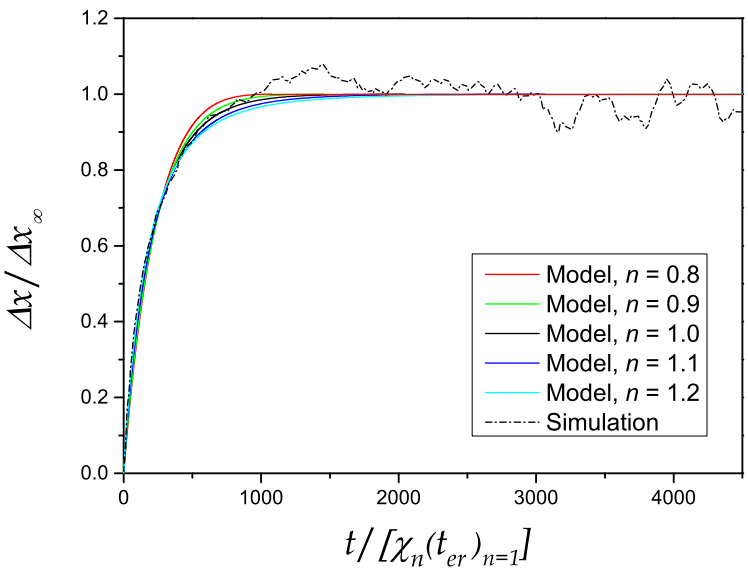

(b)

Fig. 3.36. Variation of the non-dimensional evolution of the crater depth $\frac{\Delta x}{\Delta x_\infty}$ for different values of the exponent n versus: (a) t/t_{er}; (b) $t/(\chi_n t_{er})$. The simulation parameters are: $C = 1.2$ N and $U_0 = 2.0$ m/s. The simulation data was normalized using the value of t_{er} calculated when $n = 1$.

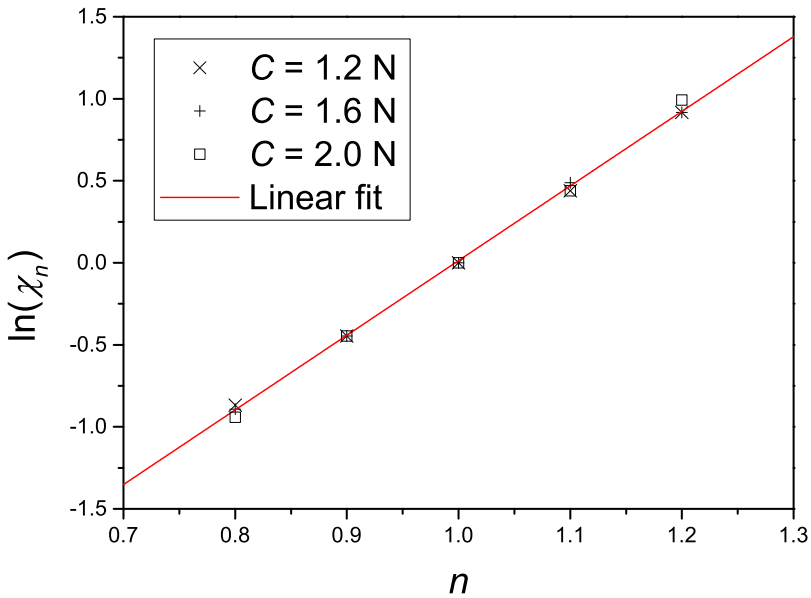

Fig. 3.37. Variation of $\ln(\chi_n)$ versus n for three different values of the cohesive strength C and for $U_0 = 2.0$ m/s. The red solid line corresponds to a linear fit of the data according to equation: $\ln(\chi_n) = 4.55(n-1)$ (with a correlation coefficient $R^2 = 0.9996$).

3.4.2.5 Critical discussion

Our interpretation model is clearly questionable: first, it gives different erodibility parameter values (k_d and τ_c) for different jet inlet velocity U_0 but with a same cohesion strength C; second, the critical shear-stress deduced from the model is not consistent with direct measurements at erosion onset. Such issues have also been underlined in JET experimental studies when using different interpretation models. Khanal et al. (2016) observed indeed a rather similar variability of the erosion parameters with jet injection velocity, initial nozzle to soil distance, and time intervals between two successive measurements. These authors also observed a large dispersion of the results for three different JET interpretation models: the interpretation model based on the Blaisdell solution of the final scour depth and proposed by Hanson and Cook (2004); the scour depth method proposed by Daly et al. (2013); the iterative method proposed by Simon et al. (2011). Additionally, Brunier-Coulin et al. (2017) found a dependency between the erodibility parameters and the initial conditions of the JET test for experiments performed with super-hydrophobic sand. To conclude, although the JET test is relevant for characterizing soil resistance to erosion by estimating the erodibility parameters (k_d and τ_c), different and non-equivalent interpretation models exist, with a huge influence on the inferred values of soil's erodibility.

As regards, our numerical simulations applied to 2D JET with cohesive granular samples, some shortcomings can be underlined about the applicability of the revised interpretation model. Indeed, from an accurate observation of the simulation results for low cohesive bond strength and how illustrated in Figure 3.38, two layers of particles can be distinguished above the front of the cohesive matrix: First, a layer composed of eroded grains in motion and, second, another non-eroded layer, composed of both cohesion-less grains and a number of small cohesive aggregates, that is subjected to a moderate bedload transport, induced in particular by the jet's lateral oscillations. The estimation of the equilibrium depth Δx_∞ being based on the crater's profile, this could explain why the value directly deduced for the critical fluid shear stress τ_c appears over estimated for low cohesive bond strengths C compared to the erosion onset values of Eq. 3.10. In reality, both layers are constituted of small grains or aggregates that can be easily carried away in suspension by the water flow. This issue will be fixed in forthcoming Chapter 4 by deleting the eroded particles in the simulation. However, if used here, such a deletion induces both an under-estimation of k_d and an increase of k_d with C which is clearly non physical.

Obviously, a number of physically sounded criticisms can also be formulated, more generally, about several speculative assumptions and unrealistic over-simplifications in all the different models used for JET interpretation. First, the reference situation used to estimate the shear-stress on a scour crater is the one of an impinging jet on a flat and smooth wall that does not account for the flow re-circulation inside the crater and is surely a strong and poorly realistic assumption. Second, only the maximal shear stress value is used whereas the stress distribution on a flat wall is strongly heterogeneous and presents a stagnation point in-between two symmetrical peaks as shown in Chapter 1. However, our simulation results with a fixed granular

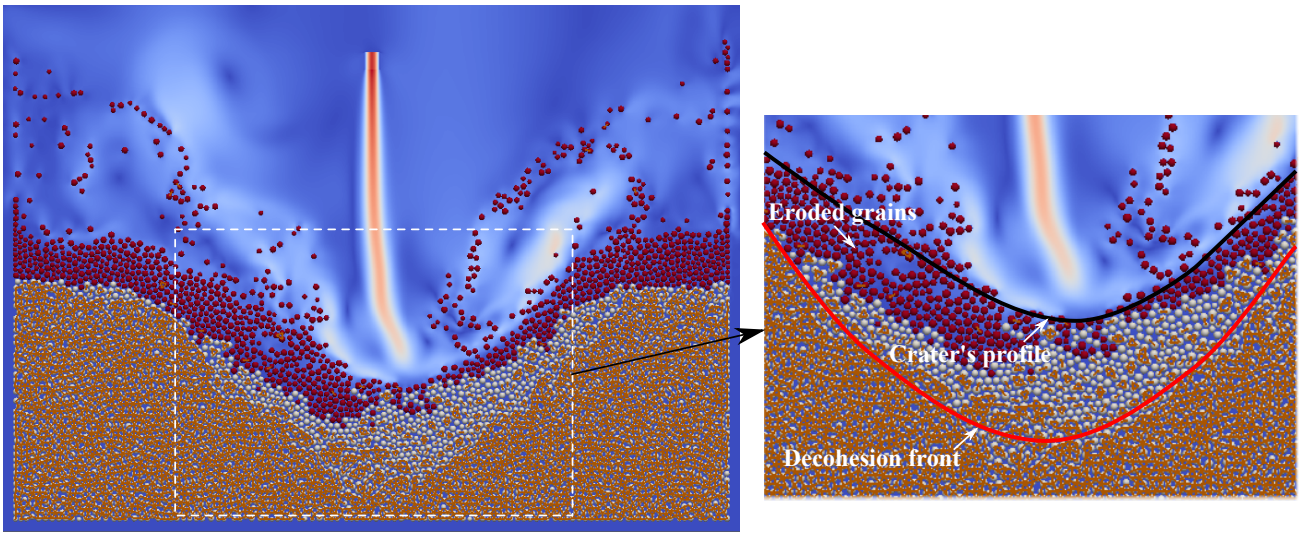

Fig. 3.38. JET simulation with $\nu = 40 \times 10^{-6}$ m^2/s, $U_0 = 1.9$ m/s, $C = 1.4$ N, and $x_0 = 70$ mm. The eroded grain are depicted in red while grey color is used for the others. The cohesive bonds are represented in orange color. Two layers profiles are shown in a zoom (right) where the crater shape and de-cohesion front profile from the cohesive soil matrix are depicted by a black and a red solid lines, respectively.

layer (section 3.2.2) exhibit substantial shear-stress fluctuations compared to the smooth wall case.

In next Chapter 4, this issue of spatially distributed and time dependent hydrodynamic stresses is circumvented by the use of a Couette flow which enables a uniform and stationary shear stress at the soil surface that is consequently kept flat.

Chapter 4

Couette shear flow erosion

Contents

4.1 Introduction

This study is dedicated to erosion induced by a laminar tangential Couette flow with the aim of imposing a constant shear-stress and measuring the corresponding erosion rate of a cohesive granular soil. Then, from such separate measurements of shear-stress and erosion rate, the relevance and use of empirical erosion laws can be checked and tested. Once such a law selected, erodibility parameters can be evaluated, especially the critical shear stress τ_c and the erosion coefficient k_d. Next, a parametric study is performed by varying the inter particle cohesion and the particle size to investigate the link between erodibility at sample scale and cohesive contact law at particle contact scale.

4.2 Model for 2D Couette flow erosion

4.2.1 Constant shear stress configuration

The present flow configuration consists of applying along the upper surface of a cohesive sample a constant shear fluid flow, also denoted laminar Couette flow, as shown in Figure 4.1. It is worth noting that there are however several options to keep the fluid shear stress constant. For example, an increase of the inlet velocity over time according to the mass loss, could be implemented, or a progressive lift upward of the soil sample as is achieved in the EFA test (see chap 1). The first choice would require increasingly large velocities that are not convenient for the LBM simulation. So, the second option is selected, except that a progressive displacement downward of the fluid inlet boundary condition is preferred to a global upward motion of the granular sample. This is sketch in Figure 4.2.

In the boundary layer, the fluid shear stress is defined as:

$$\tau = \rho_f \nu \frac{U_0}{e_0} \tag{4.1}$$

where U_0 is the imposed shear velocity at the upper boundary of the LBM domain, e_0 is the gap between the upper boundary and the sample surface, ρ_f and ν are the density and kinematic viscosity of the fluid, respectively.

The flow Reynolds number reads:

$$Re = \frac{U_0 e_0}{\nu}. \tag{4.2}$$

After Derksen (2011), the particle Reynolds number in such a shear configuration should be defined as:

$$Re_p = \frac{U_0 d^2}{e_0 \nu} \tag{4.3}$$

with d the particle diameter.

Table 4.1 summarizes the geometrical, material and model parameters used for our simulations of shear flow erosion.

Table 4.1. Input parameters for our parametric study of shear flow erosion

Solid phase	Fluid phase
Particle mean size, d_{mean}: 2, 3, and 5 mm	Density ρ_f: 1000 kg/m^3
Density ρ_g: 2500 kg/m^3	Kinematic viscosity ν: 2×10^{-4} m^2/s
Normal stiffness k_n: 1.10×10^5 N/m	Lattice speed, c : [50-100] m/s
Shear stiffness k_t: 1.10×10^5 N/m	Hydraulic radius factor, R_h: 0.8
Friction coefficient μ: 0.30	Shear fluid velocity, U_0: [1-10] m/s
Rolling friction μ_r: 0.1	BC's offset from surface, e_0: 5 mm
Restitution coefficient e: 0.2	Outlet pressure, P_{out}: 0 Pa
Gravitational acceleration g: 9.81 m/s^2	
Bond strength, C: [1-11] N	

4.2.2 Boundary conditions

The boundary conditions used for the shear flow erosion simulations are the following, as sketched in Fig.4.1: Outlet with zero pressure ($P_{out} = 0$) applied at the left, right, and at the bottom of the domain; Constant velocity inlet (U_0) imposed at the top of the domain in the x direction. The particles located at both sides and at the bottom are fixed (depicted in black in Fig. 4.1).

Note however that fixing these particles at the lateral boundaries could progressively form a kind of basin since they will act like as a solid wall. Consequently, to get a uniform bed throughout the top surface of the sample, the lateral grains will be progressively suppressed following the sample's mass loss over time. Thus, the fluid film thickness $e(t)$ increases as the mean height of non-eroded grains decreased (see Figure 4.2), according to the following equation:

$$e = H - 2y_{mean} \tag{4.4}$$

with H the domain height and $y_{mean} = \frac{1}{N_{ne}} \sum_i y_i$, where i represents a given non-eroded grain at altitude y_i within a total number N_{ne} of remaining non-eroded particles.

As will be used in the following, the slope of the evolution of e with time is directly equal to the soil's erosion rate.

The present configuration corresponds to a plane Couette flow over a flat smooth surface for which an analytical solution is given by the following self-similar relation (Tritton, 1959):

$$u_x(y,t) = u_x\left(\frac{y}{2\sqrt{\nu t}}\right) = U_0\left[1 - erf\left(\frac{y}{2\sqrt{\nu t}}\right)\right]. \tag{4.5}$$

Note that, in this flow configuration, a diffusion time $t_\nu = e_0^2/\nu$ is required in order to reach a stable (steady) solution (i.e. steady linear velocity gradient) starting from fluid at rest. To shorten the convergence time, the velocity at the fluid film

was initialized at initial time step $t = 0$ by the following analytical expression that already corresponds to the theoretical steady solution:

$$u(y) = \begin{cases} 0 & 0 < y < H - e_0 \\ U_0(y - (H - e_0))/e_0 & H - e_0 < y < H \end{cases} \tag{4.6}$$

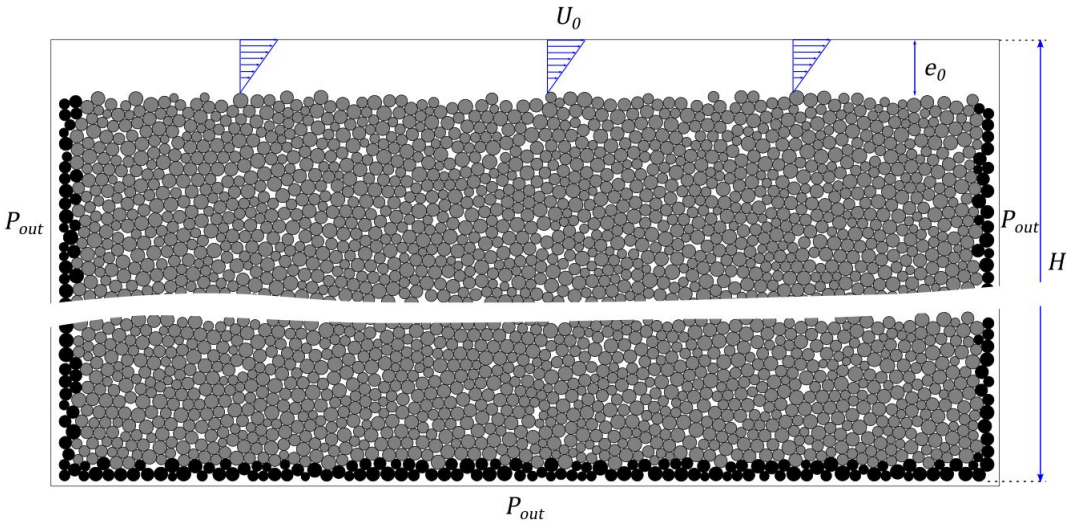

Fig. 4.1. Simulation domain and boundary conditions.

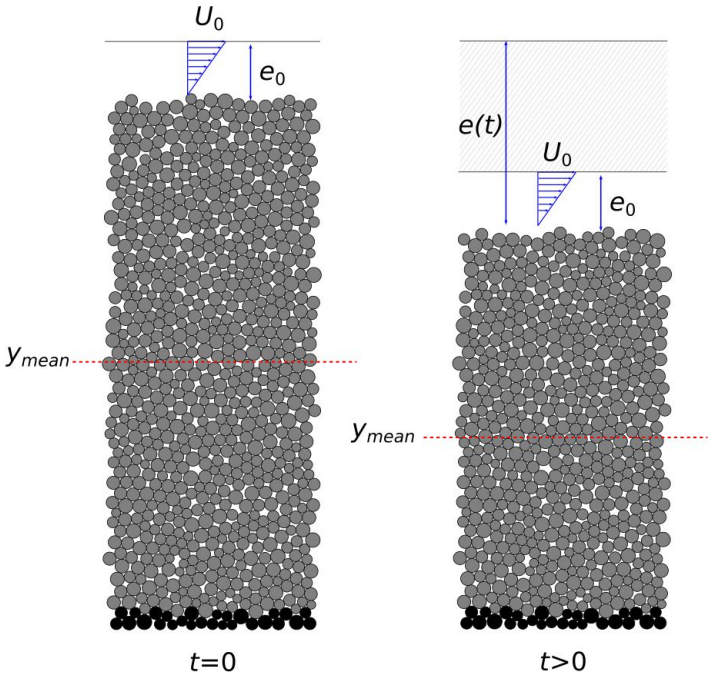

Fig. 4.2. Evolution with time of the velocity inlet boundary condition and fluid film thickness $e(t)$.

In this flow configuration, the TRT collision model is used with the combination of the PSM scheme, since this choice presents several advantages in this particular case. Indeed, as the PSM collision step is performed also inside the particle's nodes, a removal of the eroded grains from the system can be done easily, without significant changes to the algorithms. Only slight perturbations of the velocity and pressure fields after a grain's removal are observed and tend to be very short-lived, since they actually escape the system once they reach the outlet boundaries. Furthermore, the TRT scheme provides a smooth pressure field around the particles as already shown in the validation section (Sec. 2.6). Accordingly and as detailed just below, it is decided here that all eroded particles are removed from the LBM-DEM calculation. This way, we can focus exclusively on the erosion process, inhibiting any subsequent bedload transport of eroded particles. In return, a relevant criterion must be used to distinguish between eroded and non-eroded particles. In particular, an issue may arise when cohesion is very weak due to the bed load transport at the top of the bed which is induced by the shear flow. It is therefore difficult and rather arbitrary to determine a threshold for eroded, and consequently deleted, particles. For this reason, only high enough cohesive cases are studied here, namely for cohesive bond strength C in between 1 and 11 N as specified in Table 4.1.

4.2.3 Eroded grains criteria

The criterion for eroded grain is chosen based on both a total kinetic energy threshold (translation plus rotation) and a condition on the particle coordination number. In other words, once a grain reaches a kinetic energy above a given threshold and loses all contacts (i.e cohesive and non-cohesive contacts), it will not be considered further in the simulation and will be classified as eroded, with no more interaction with the fluid flow.

In Figure 4.3, different criteria are tested to distinguish between eroded and non eroded grains in a typical simulation. As can be seen, there exists a rather broad range of kinetic energy threshold giving rise to comparable values for the erosion rate. From a physical standpoint, an order of magnitude for the kinetic energy threshold can be obtained considering the inertial free fall of a single particle whose terminal settling particle velocity is $U = \sqrt{\frac{\Delta\rho}{\rho_f} gd}$. Thus the corresponding kinetic energy $E = \frac{1}{2}mU^2$ reads:

$$E = \frac{\pi}{8}\rho_g \frac{\Delta\rho}{\rho_f} g d^3 \tag{4.7}$$

As can be seen in Fig. 4.3, this expression is indeed in quantitative agreement with the previous blind test, and, furthermore, enables dimensional analysis to account for any change in particle size or densities. It will consequently be used in the following.

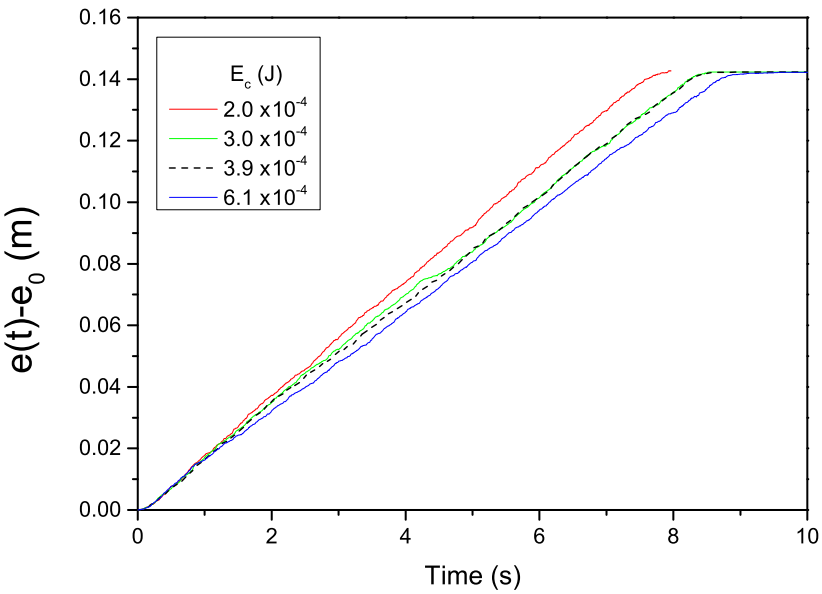

Fig. 4.3. Time evolution of the eroded particle height for different kinetic energy thresholds and with the following simulation parameters: $d = 3$ mm, $\nu = 200 \times 10^{-6}$ m^2/s, $U_0 = 4$ m/s, $e_0 = 5$ mm, and $C = 3$ N. The dashed line corresponds to the proposed expression in Eq. 4.7.

4.2.4 Erosion rate

As already mentioned, the erosion rate is measured based on the evolution of the fluid's shearing thickness e, which increases over time due to particle detachments from the cohesive granular medium at the bed surface. Since the initial fluid gap e_0 will be kept approximately constant during the simulation, the evolution of the fluid film thickness over time $e(t)$ is calculated based on Eq. 4.4. Thus the erosion rate $\dot{\epsilon}$ is simply the slope of the curve $e(t) - e_0$ versus time t.

Figure 4.4 shows a typical evolution of the system. The vertical position of the erosion front, i.e. $e(t) - e_0$, is displaced at a roughly constant rate $\dot{\epsilon}$ that depends on the shear velocity U_0 as displayed in Figure 4.5. The erosion rate obviously increases with U_0 as expected.

The same analysis can be repeated for different values of the fluid shear-stress τ and the corresponding erosion rates $\dot{\epsilon}$ are plotted against τ in Figure 4.6. A more or less linear evolution is found but the erosion rate does not continuously decrease to zero when the shear-stress is progressively reduced. A brutal jump is observed, defining just below a domain where no erosion is measured at sample scale although bonds degradation exists.

A closer examination of a cohesive soil stressed in this specific range points out the occurrence of a crack that opens quickly and develops downward, as shown in Fig. 4.6.

To overcome this shortcoming, our cohesive contact law is enriched by a damage model (see section 2.2.3 in chap 2) as explained in the next section.

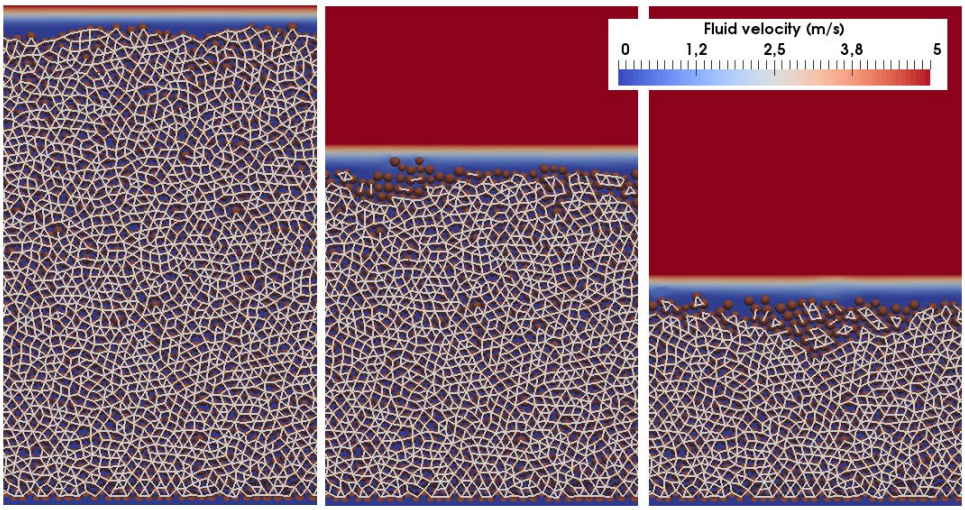

Fig. 4.4. Snapshots of the typical evolution of the sample erosion by a shear fluid flow at three successive times. Only part of the simulated domain is shown. The fluid velocity field is depicted through a color scale, from blue (0 m/s) to red (5 m/s). The cohesive bond network is coloured in white and the particles in red.

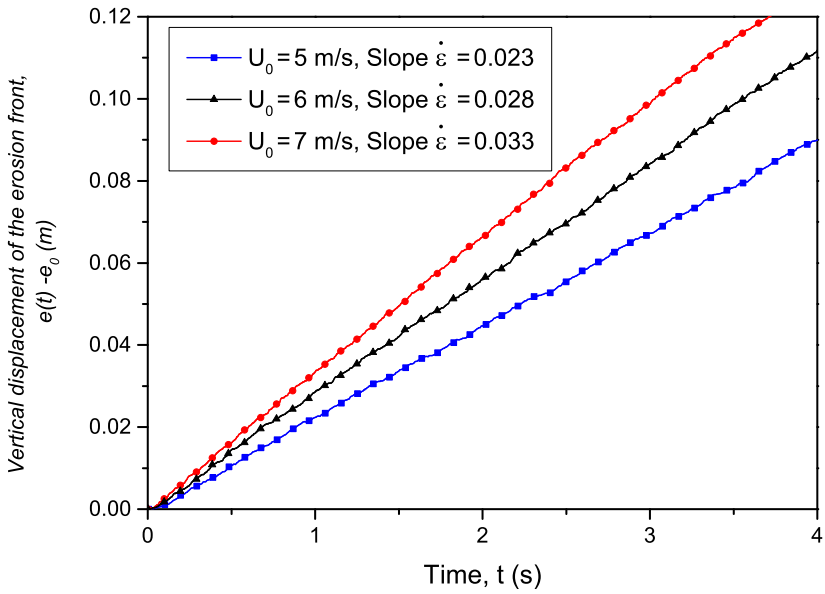

Fig. 4.5. Time evolution of the erosion front for a cohesive bond strength of $C = 3$ N (basic cohesion scheme without damage model) and with the following simulation parameters: d=3 mm, $\nu = 2.10^{-4}$ m^2/s, $e_0 = 5$ mm, and $U_0 = 5$ m/s (blue curve), 6 m/s (black curve), and 7 m/s (red curve).

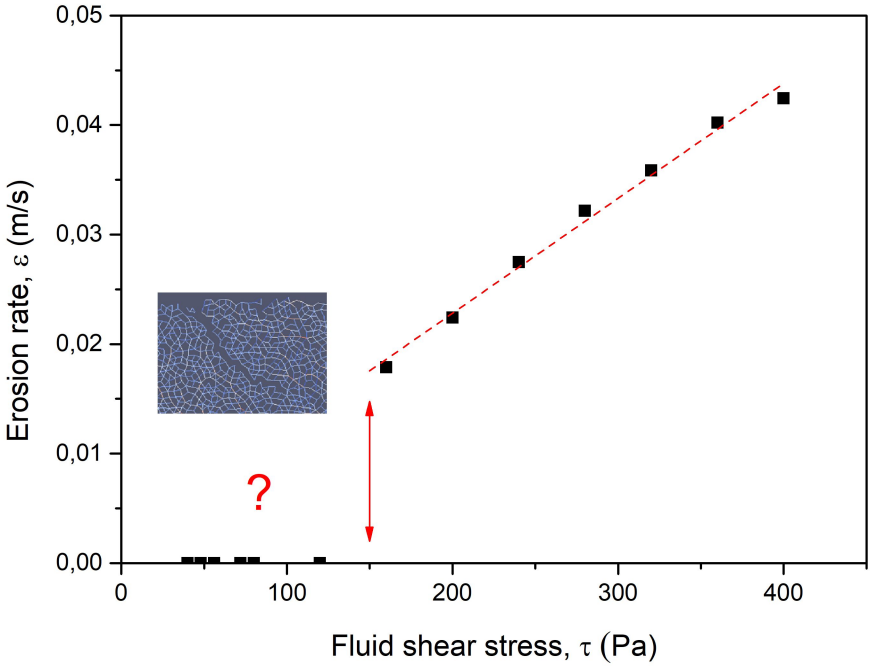

Fig. 4.6. Erosion rate $\dot{\epsilon}$ versus fluid shear stress τ (basic cohesion scheme without damage model). The dashed line stands for a linear trend. Inset: Non-eroded sample in a damaged state, with an oblique crack downward.

4.2.5 Addition of the damage model

As shown above, the basic cohesive bond scheme presented in section 2.2.2 fails to explore the lower range of fluid shear stress values due to the occurrence of large stationary cracks.

To inhibit such deep fracturing process, we propose here to include a damage model which can slow down the development of crack opening to the benefit of surface erosion of stressed particles in direct contact with the main fluid shear flow. This damage model is the one presented in section 2.2.3 with two main parameters: a damage threshold C_0 and a characteristic time η.

Figure 4.7 shows the influence of the damage time η on the temporal rate of the erosion front (i.e. $e(t)-e_0$) for a given damage threshold $C_0 = 0.1$ N. In this case (i.e. $C = 3$ N and $U_0 = 5$ m/s), it can be seen that the erosion rate is almost unchanged, meaning that η has no critical impact on the results. Then, if η is fixed to 0.01 and U_0 varied, the erosion rate can now be defined in the previously inaccessible range of fluid shear stress as shown in Figure 4.8.

To confirm this finding, a parametric study is performed by varying the cohesive strength C, the damage time η, and the fluid shear stress τ while fixing $C_0 = 0.1$ N. The results are displayed in Figure 4.9. On this basis, we find that the higher η the lower the erosion rate, up to values close to the no damage case. It is concluded that the characteristic time $\eta = 0.01$ does not influence the erosion rate for cohesion strength C in the range [1-5] N. This latter value will thus be used in this range, whereas $\eta = 0.1$ is more suitable for cohesion strength C in the range [7-11] N.

Another option is to find and fix an optimal ratio C/C_0 instead of varying η in each case. Since the initial damage threshold C_0 affects also the erosion rate and is directly in proportion to the damage time (i.e. the higher C_0 the faster the damage). This possibility is *a priori* more convenient but requires many simulation data and subsequently large simulation times.

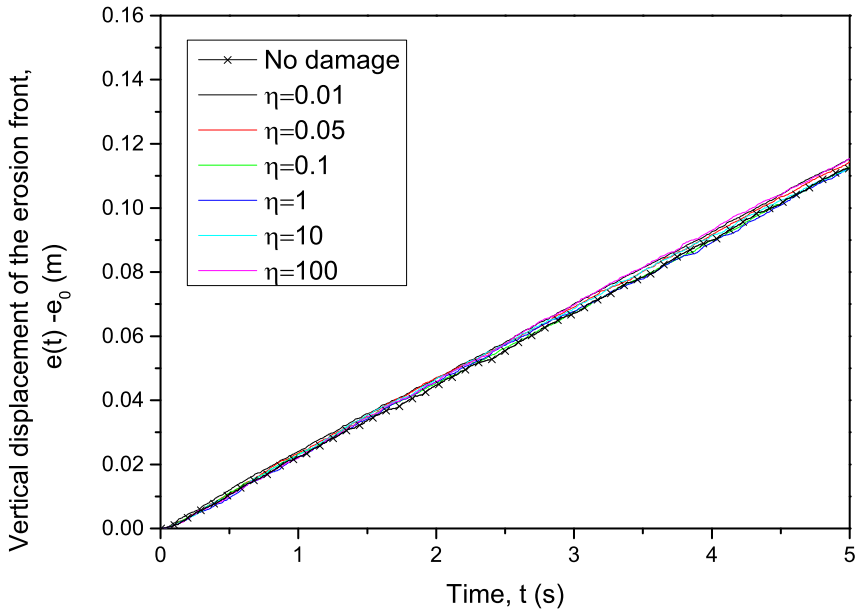

Fig. 4.7. Influence of the characteristic time of the damage model η for $C = 3$ N and $U_0 = 5$ m/s.

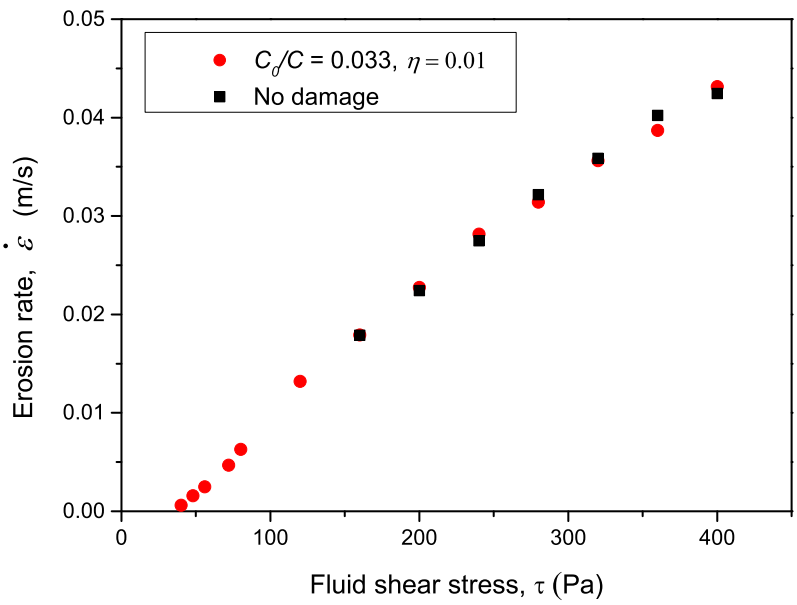

Fig. 4.8. Erosion rate $\dot{\epsilon}$ versus fluid shear stress τ for $C = 3$ N whether transient damage model is considered (red symbols) or not (black symbols). The damage threshold is $C_0 = 0.033 \times C$ and the characteristic time $\eta = 0.01$.

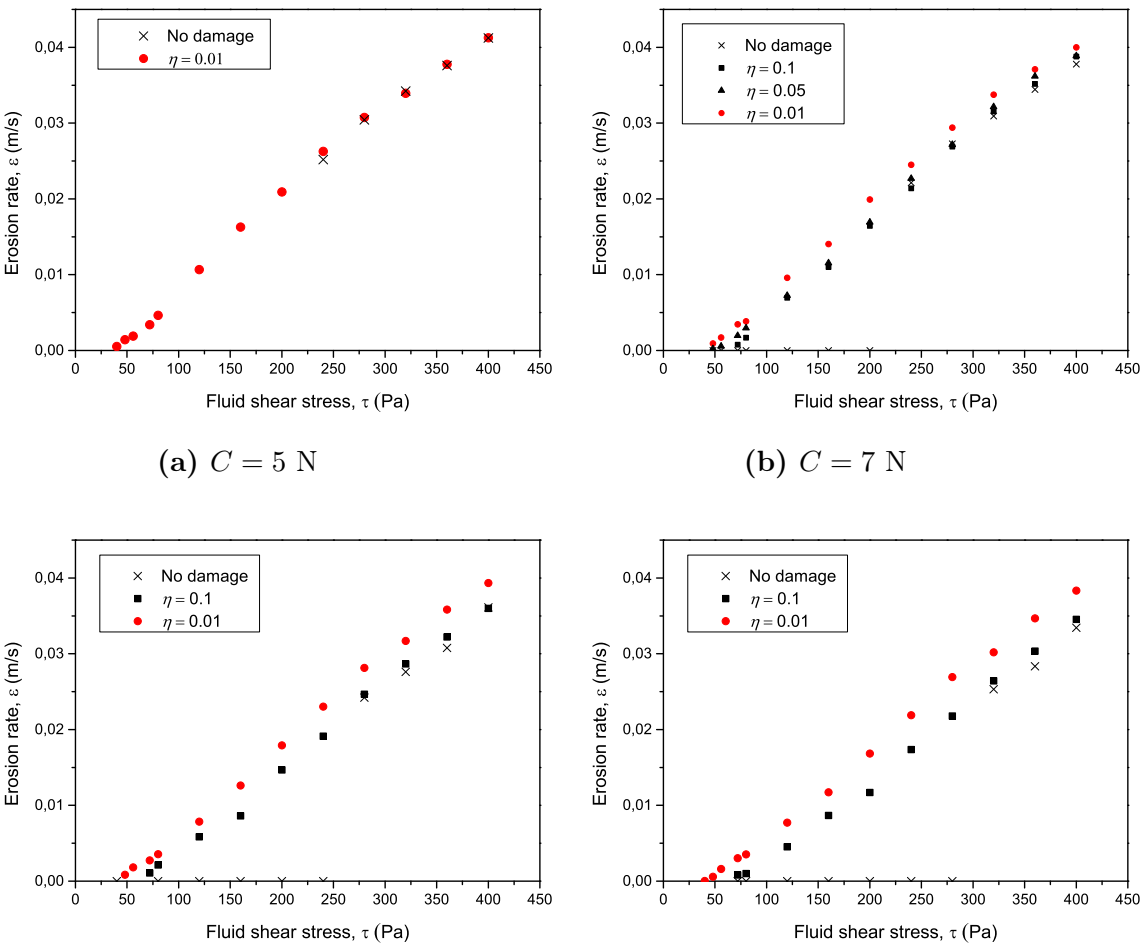

(a) $C = 5$ N **(b)** $C = 7$ N

(c) $C = 9$ N **(d)** $C = 11$ N

Fig. 4.9. Erosion rate versus fluid shear stress for different values of the cohesive strength C, without (cross symbols) or with (black and red symbols) the damage model using $C_0 = 0.1$ N and $\eta = 0.01$, 0.05, or 0.1.

4.3 Parametric study of the erosion law at sample scale

4.3.1 Choice of an accurate empirical law

As mentioned before, the variation of the erosion rate with the fluid shear stress is found approximately linear, except at large shear stress values where a less pronounced evolution is clearly observed, for instance in Fig. 4.8. Consequently, a linear erosion law as usually assumed in previous studies, namely $\dot{\epsilon} = k_d(\tau - \tau_c)$, is not sufficiently accurate. Thus, it is here abandoned in favour of a more general power law expression: $\dot{\epsilon} = k_d(\tau - \tau_c)^n$. Note that the previous linear law is recovered for $n = 1$.

As illustrated in Figure 4.10, the goodness of the fit is indeed improved when using the power law regression. In this particular example, fixing the exponent $n = 1$ gives $k_d = 1.34 \times 10^{-4}$ $\mathrm{m^3/N/s}$ and $\tau_c = 32.84$ Pa with a coefficient of correlation $R^2 = 0.9931$. Then, if n is used as a free parameter, one gets $k_d = 3.57 \times 10^{-4}$ (Note that k_d units are no more $\mathrm{m^3/N/s}$ but $\mathrm{m^{2n+1}/N^n/s}$), $\tau_c = 40.73$ Pa, and $n = 0.814$ with a coefficient of correlation $R^2 = 0.9968$ which is slightly increased. Such an improvement is systematically observed to benefit of the power law fit. Some examples of accurate adjustments are presented in Figure 4.11 for different values of the cohesive strength C and with corresponding exponents being either smaller, close, or larger than 1.

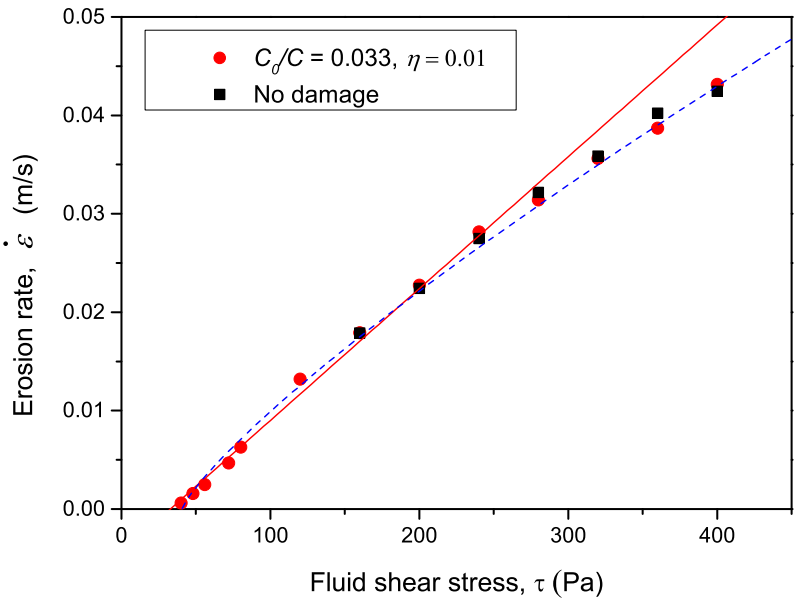

Fig. 4.10. Erosion rate $\dot{\epsilon}$ versus fluid shear stress τ for $C = 3$ N whether the transient damage model is considered (red symbols) or not (black symbols). The damage threshold is $C_0 = 0.033 \times C$ and its characteristic time $\eta = 0.01$. The solid line in red represents a linear fit of the damage data (red symbols) restricted to shear stresses lower than 300 Pa ($R^2 = 0.9931$). The dashed line in blue stands for a power law regression over the whole data range (red symbols), giving an improved coefficient of correlation $R^2 = 0.9968$.

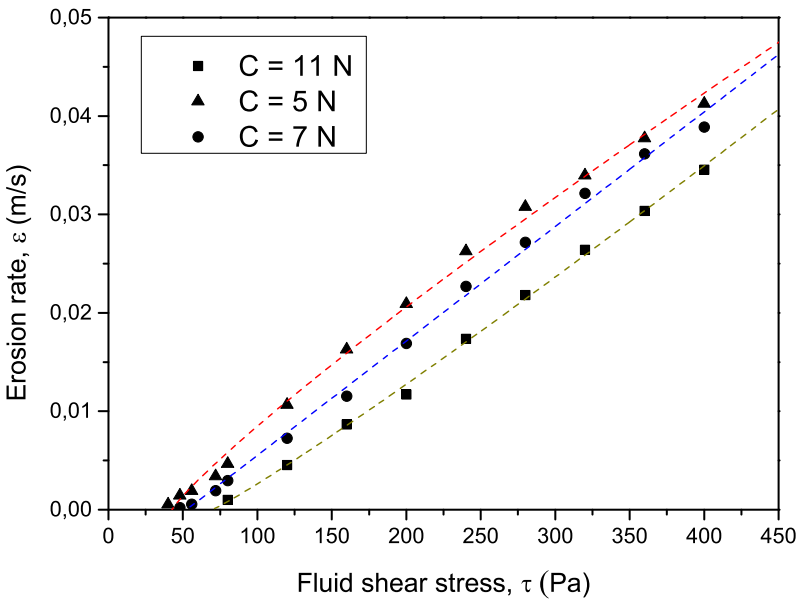

Fig. 4.11. Erosion rate versus fluid shear stress for different values of the cohesive strength C with use of the damage model ($C_0 = 0.1$ N, $\eta = 0.01$ for $C = 5$ N, and $\eta = 0.1$ for $C = 7$ and 11 N). The dashed lines represent power law regressions over the whole data range with the following fitting parameters: $n = 0.88$, $\tau_c = 42.67$ Pa, $k_d = 2.43 \times 10^{-4}$, and $R^2 = 0.9959$ for $C = 5$ N (triangle symbols); $n = 1.00$, $\tau_c = 52.34$ Pa, $k_d = 1.15 \times 10^{-4}$, and $R^2 = 0.9963$ for $C = 7$ N (circle symbols); $n = 1.08$, $\tau_c = 69.59$ Pa, $k_d = 6.50 \times 10^{-5}$, and $R^2 = 0.9977$ for $C = 11$ N (square symbols).

4.3.2 Influence of the parameters of the power erosion law (exponent n, τ_c, and k_d)

Figure 4.12 shows the variation of the empirical exponent n for different values of the cohesion strength C. We can see that n increases with C, approximately from 0.7 to 1.1 when C varies in-between $C = 1$ N at minimum and $C = 11$ N at maximum. As a reminder, the exponent n is usually taken equal to 1 for simplicity, which corresponds to the linear excess shear stress erosion law. In practice, the exponent n can however be higher or lower than 1 after the literature. Moreover, n appears merely as a fitting parameter of the experimental data, or also the numerical data as presented in previous Chapter 3, and does not provides a relevant physical significance (Bonelli and Brivois, 2008), contrarily to the two other erodibility parameters.

The variation of the critical shear stress τ_c versus the cohesive strength C is now presented in Figure 4.13. As expected, τ_c increases almost monotonously with C. Similarly, Figure 4.14 shows the erosion coefficient k_d versus the cohesive strength C. This time, k_d decreases as C increases which is fairly consistent with the general trend observed in experiments and in agreement with the commonly accepted idea

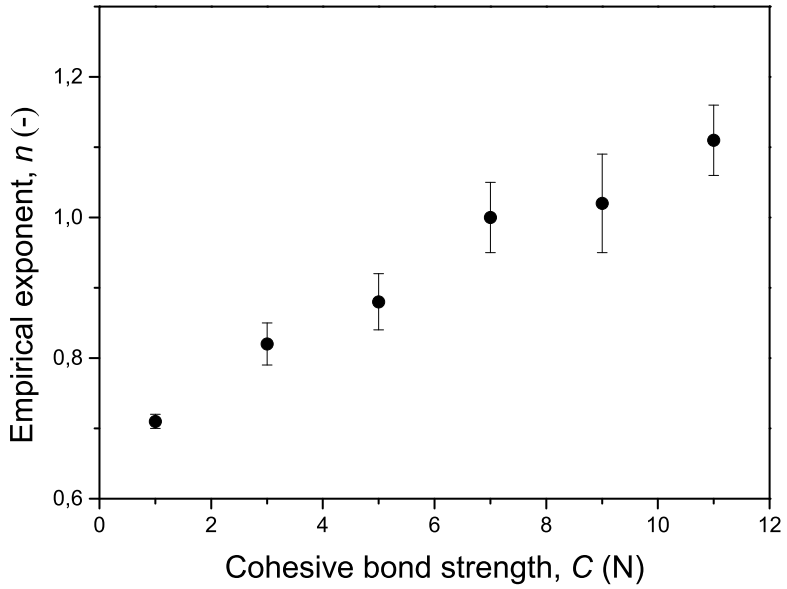

Fig. 4.12. Exponent n versus cohesive bond strength C for a mean particle diameter $d = 3$ mm.

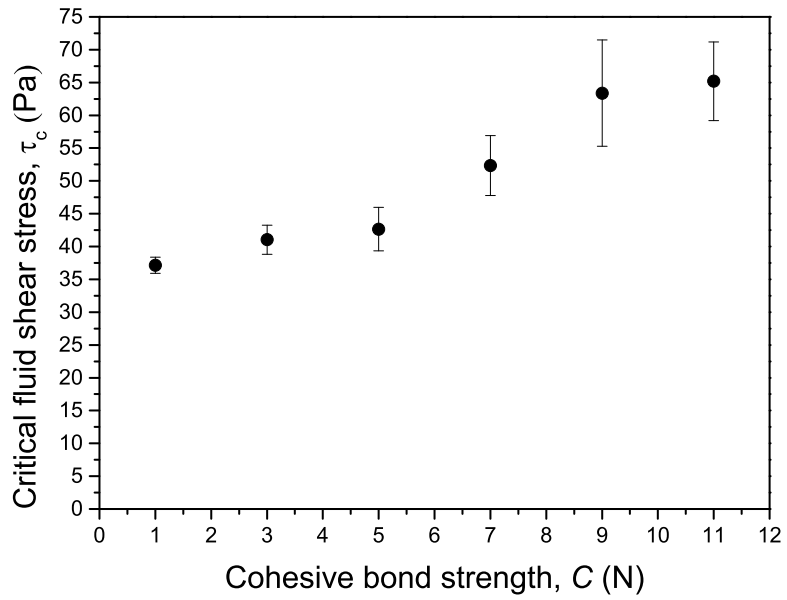

Fig. 4.13. Critical fluid shear stress τ_c versus cohesive bond strength C for a mean particle diameter $d = 3$ mm.

that the higher the cohesion strength, the less the material will be eroded.

It is worth pointing out that the critical shear stress τ_c for natural cohesive soil ranges from 0 to 10^3 Pa while the erosion coefficient k_{er} varies from 10^{-6} to 10^{-2} s/m (Mercier, 2013). As already explained, this coefficient k_{er} can be used alternatively to k_d, when the erosion rate is expressed as a mass loss per surface and time units instead of a volume. Consequently, the following relation holds between both coefficients: $k_{er} = \rho_d k_d$ with ρ_d the soil's dry density. For a common soil, $\rho_d \sim 1500 - 2000$ kg/m^3 and the corresponding range for k_d reads approximately 10^{-5} to 10^{-9} m^3/N/s. So, quantitatively and despite the fact that our simulation is bi-dimensional with circular bonded particles, the erodibility values obtained from our numerical results are comparable in terms of the critical shear stress and at least two orders of magnitude higher as regards the k_d values. The kinetics is consequently substantial faster in the simulation compared to real conditions.

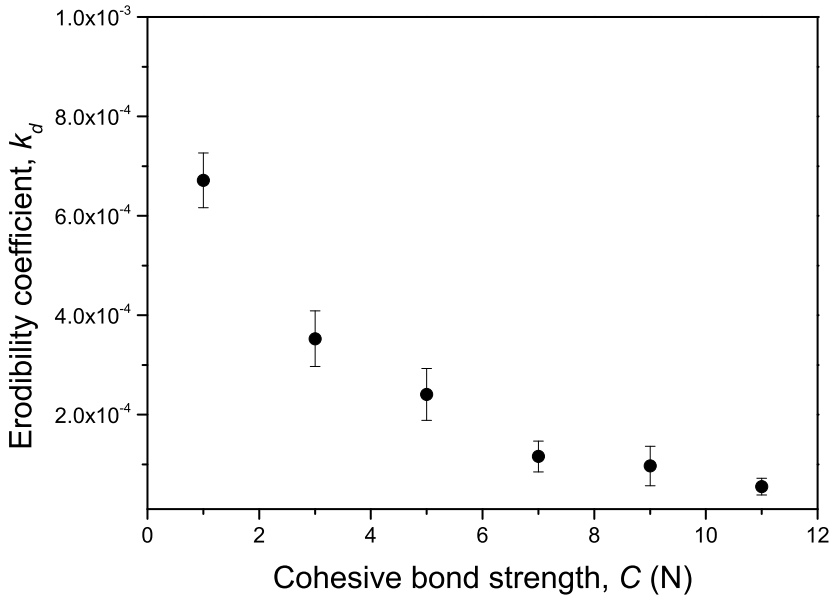

Fig. 4.14. Erosion coefficient k_d versus cohesive bond strength C for a mean particle diameter $d = 3$ mm.

As mentioned in Chapter 1, if some authors did not find any correlation between τ_c and k_d (Knapen et al., 2007), several others have suggested the existence of an underlying relation, generally through a power law of the form $k_d \propto \tau_c^{-\gamma}$. However, as we explained, the empirical values for the exponent γ found in the literature are quite dispersed, ranging from $\gamma \approx 0.4$ to $\gamma \approx 2.4$ (Daly et al., 2015; Julian and Torres, 2006; Karamigolbaghi et al., 2017; Karmaker and Dutta, 2011; Konsoer et al., 2016; Layzell and Mandel, 2014; Nguyen et al., 2017; Thoman and Niezgoda, 2008). Coming back to our numerical results, Figure 4.15 shows the erosion coefficient k_d plotted versus the critical shear stress τ_c. An approximate power law evolution of

k_d with τ_c can be proposed and reads:

$$k_d = 1.12 \times 10^6 \tau_c^{-5.88} \tag{4.8}$$

This value $\gamma \sim 5.9$ is even further away from the experimental ones, especially from $\gamma = 0.5$ which was initially found by Hanson and Simon (2001) and later suggested to be consistent with a dimensional analysis (Andreotti et al., 2013). As a consequence, the present result confirms that assuming a general relation between both erodibility parameters seems to be an hazardous postulate although an inverse correlation is clearly evidenced.

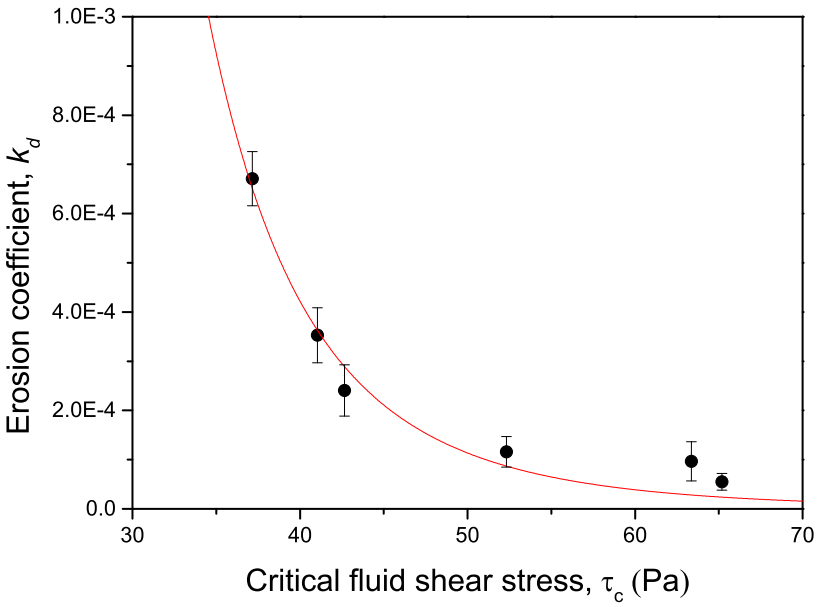

Fig. 4.15. Erosion coefficient k_d versus critical shear stress τ_c for a mean particle diameter $d = 3$ mm. The solid line in red stands for Eq. 4.8.

4.3.3 Influence of the mean particle diameter

The results presented above were obtained with only one value of the mean particle diameter, namely $d = 3$ mm. It is thus interesting to study the effect of varying the particle diameter on soil's erodibility (i.e. k_d and τ_c). To this end, two additional particles sizes are simulated: $d = 2$ and 5 mm. The evolution of both the critical fluid shear stress τ_c, the erosion coefficient k_d, and exponent n versus the cohesive bond strength C for different particle sizes are shown in Figure 4.16, Figure 4.17, and Figure 4.19, respectively.

Figure 4.18 shows evolution of erosion coefficient k_d versus critical shear stress τ_c for different particle mean diameters $d = 2$, 3, and 5 mm. It can be seen that the results for $d = 2$ and 3 mm are rather close, whereas the data for $d = 5$ mm do not follow the same evolution.

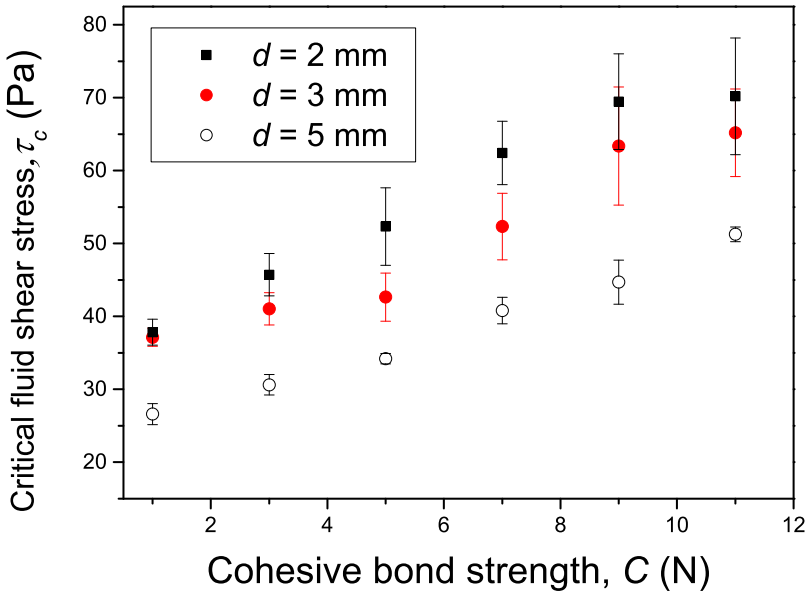

Fig. 4.16. Critical fluid shear stress τ_c versus cohesive bond strength C for different particle sizes: d=2, 3, and 5 mm.

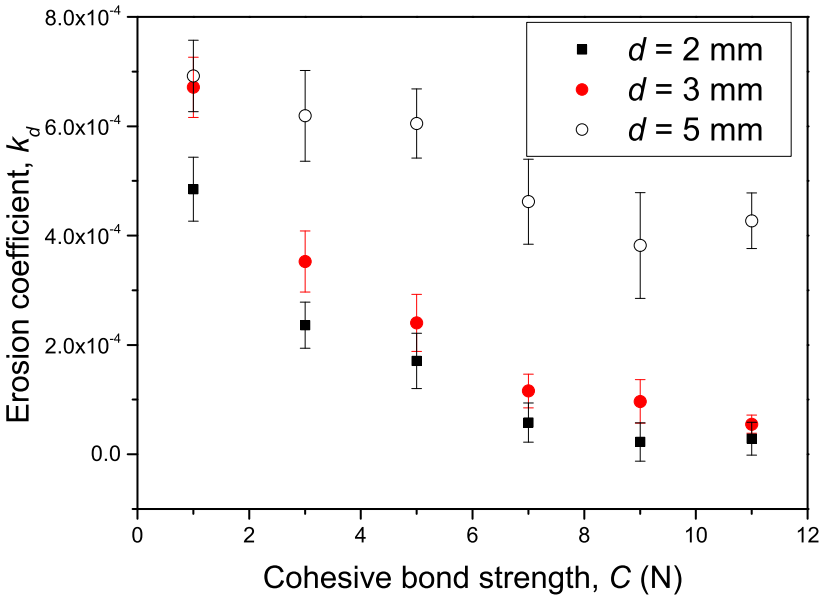

Fig. 4.17. Erosion coefficient k_d versus cohesive bond strength C for different particle sizes: d=2, 3, and 5 mm.

It can be seen that the smaller particle sizes require higher critical fluid shear

stress values τ_c in order to be eroded, whereas the larger particle sizes need lower values. This behaviour was already observed and explained in the previous chapter dedicated to the impinging jets case (see section 3.4.1). Conversely, for a given cohesion strength, the erosion coefficient k_d consistently increases with d, especially for $d = 5$ mm. Additionally, when plotting k_d versus τ_c in Figure 4.18, one can gather the data together accordingly to previous Eq. 4.8, except for the series obtained with $d = 5$ mm. The same difference for $d = 5$ mm is also observed for the exponent n of the erosion law as shown in Figure 4.19. The forthcoming section will test if the previous dimensional analysis developed in Chapter 3 can account for this influence of the particle size.

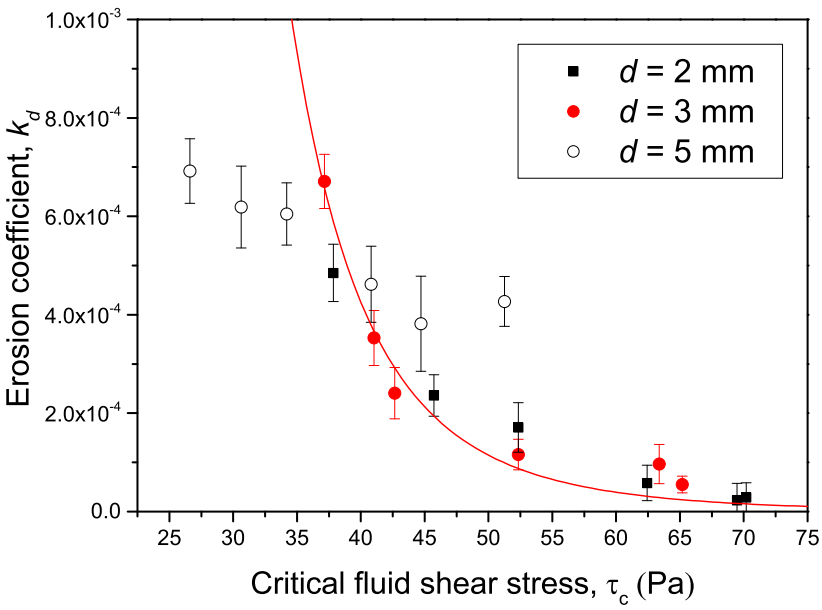

Fig. 4.18. Erosion coefficient k_d versus critical shear stress τ_c for different particle sizes: d=2, 3, and 5 mm. The solid line in red stands for Eq. 4.8.

Logically, the critical shear stress τ_c deduced from the erosion law should identify with the onset value measured directly at erosion initiation and reported in the classical Shields diagram. To this end, our data for critical shear stress τ_c for different mean particle sizes d are used to calculate both the usual critical Shields number Sh^*_τ and the generalized critical Shields number Sh^*_{coh} (from Eq. 3.8 with $\alpha = 2.7$) as well as the shear Reynolds number given by: $Re^*_\tau = \sqrt{\frac{\tau_c}{\rho_f}}\frac{d}{\nu}$. Then, both critical Shields numbers Sh^*_τ and Sh^*_{coh} are plotted versus the shear Reynolds number Re^*_τ in Figure 4.20 and Figure 4.21, respectively.

It can be seen that using directly Eq. 3.8 with $\alpha = 2.7$ for Couette shear flow erosion configuration fails not only to gather the data in the Shields diagram but also to agree, even roughly, with the Shields curve, except possibly for low cohesion strengths $C < 2$ N. As the value $\alpha = 2.7$ in the expression of the generalized Shields

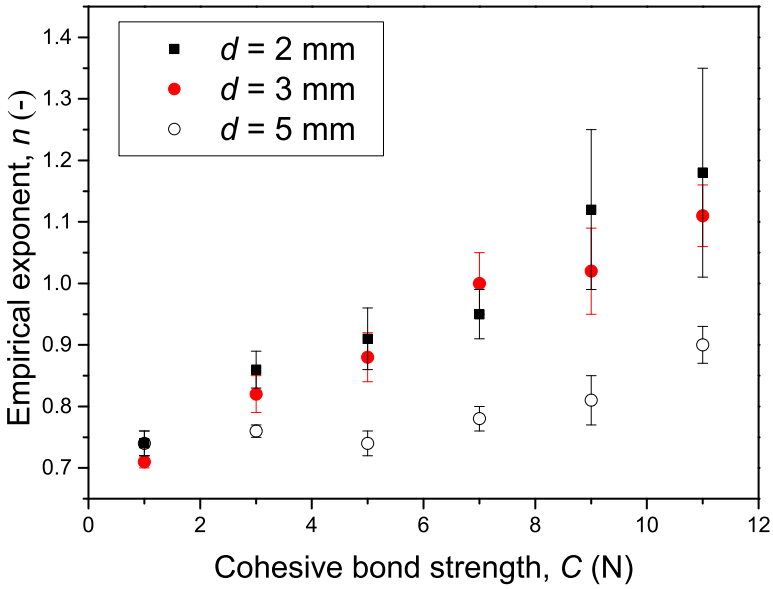

Fig. 4.19. Exponent n versus cohesive bond strength C for different particle sizes: d=2, 3, and 5 mm.

parameter in Eq. 3.8 was obtained for impinging jets with $0 < C < 3.2$, it may not be valid anymore outside this range of cohesive bond strength. To verify this, the ratio $\frac{Sh^*_{coh}}{Sh^*_{Guo}} - 1$ is plotted in Figure 4.22 as a function of the granular Bond number Bo_g calculated from Eq. 3.9, similarly to previous Fig. 3.26.

In this graph, if an approximate collapse of the data is now conceivable, the excepted proportional relation is however no more recovered, even when the coefficient α is used as a free parameter. An empirical alternative, but without any physical basis, could be to find a proper function $\Psi(Bo_g)$ able to interpolate the data while respecting the proportional law αBo_g at small granular Bond numbers. For instance, one can use:

$$\Psi(Bo_g) = A_\Psi \ln\left(1 + \frac{\alpha Bo_g}{A_\Psi}\right). \tag{4.9}$$

A regression based on this expression for Ψ provides a coefficient $A_\Psi = 9.8 \pm 0.5$ with a correlation coefficient $R^2 = 0.8906$. The function is plotted in Fig. 4.22 and gives a reasonable interpolation of the data. Nevertheless, the data quickly depart from the proportional law αBo_g that is also represented in the graph, typically as soon as $Bo_g > 5$, whereas this expression was found correct at least up to granular Bond numbers equal to 50 with previous impinging jet results (see Fig. 3.26).

Figure 4.23 shows the new empirical version of the generalized Shields diagram based on the following definition for Sh_{coh}:

$$Sh^*_{coh} = \frac{Sh^*_\tau}{1 + \Psi(Bo_g)} \tag{4.10}$$

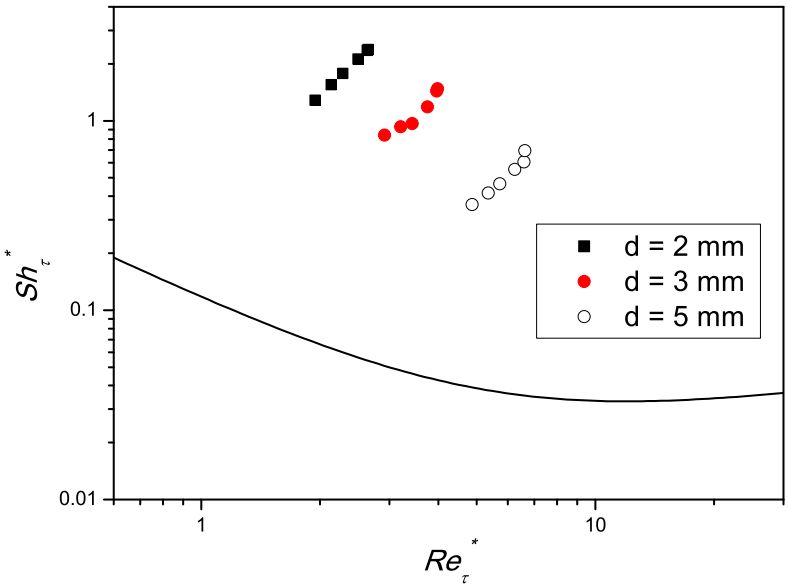

Fig. 4.20. Usual critical Shields number Sh_τ^* versus shear Reynolds number Re_τ^* for the simulated Couette shear flow erosion of cohesive granular beds with different values of mean particle size: d=2, 3, and 5 mm. The solid line represents the explicit formulation of the Shields curve in Eq. 1.13 (Guo, 1997).

with the interpolation function Ψ given by Eq. 4.9, $\alpha = 2.7$, and $A_\Psi = 9.8$.

To conclude this section, it can be seen that, although the results are indeed improved, this approach is poorly relevant and lacks strongly of generality, even by comparison of our simulations with the two flow configurations. Much work is consequently required to fully understand the competition between cohesion, flow stress, friction, and gravity with the final aim to propose an appropriate non-dimensionalisation, if any.

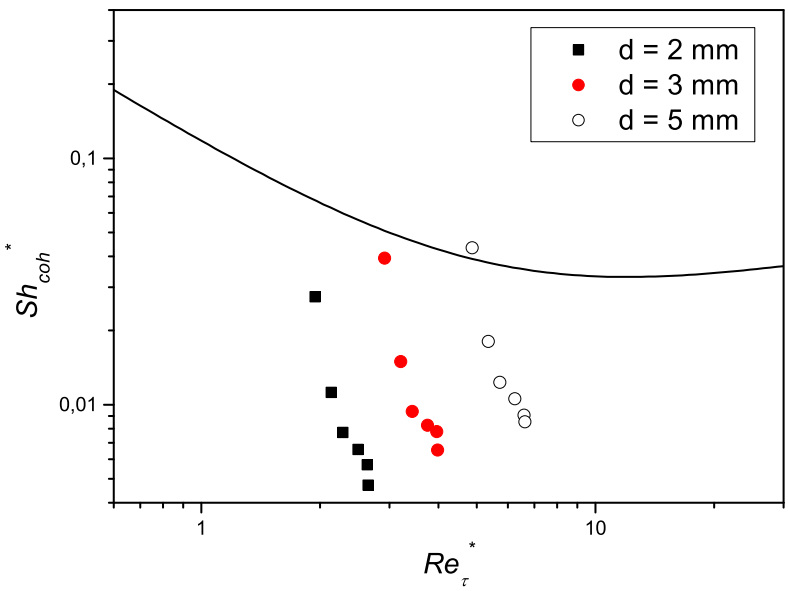

Fig. 4.21. Generalized critical Shields number Sh^*_{coh} versus shear Reynolds number Re^*_τ for the simulated Couette shear flow erosion of cohesive granular beds with different values of mean particle size: d=2, 3, and 5 mm. The solid line represents the explicit formulation of the Shields curve in Eq. 1.13 (Guo, 1997).

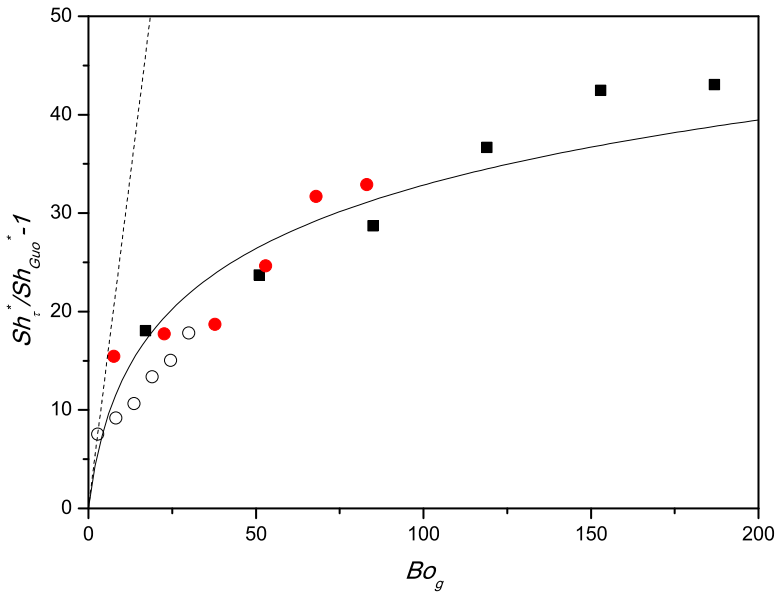

Fig. 4.22. $\frac{Sh_\tau^*}{Sh_{Guo}^*} - 1$ versus granular Bond number Bo_g for the three different mean particle sizes: d=2, 3, and 5 mm. Sh_τ^* is the usual critical Shields number obtained in the Couette simulation and Sh_{Guo}^* is given by the implicit formulation of Guo (1997). The solid line represents the best fit of function Ψ given by Eq. 4.9, with $\alpha = 2.7$ and $A_\Psi = 9.8$ ($R^2 = 0.8906$), and the dashed line stands for the previous proportional relation αBo_g.

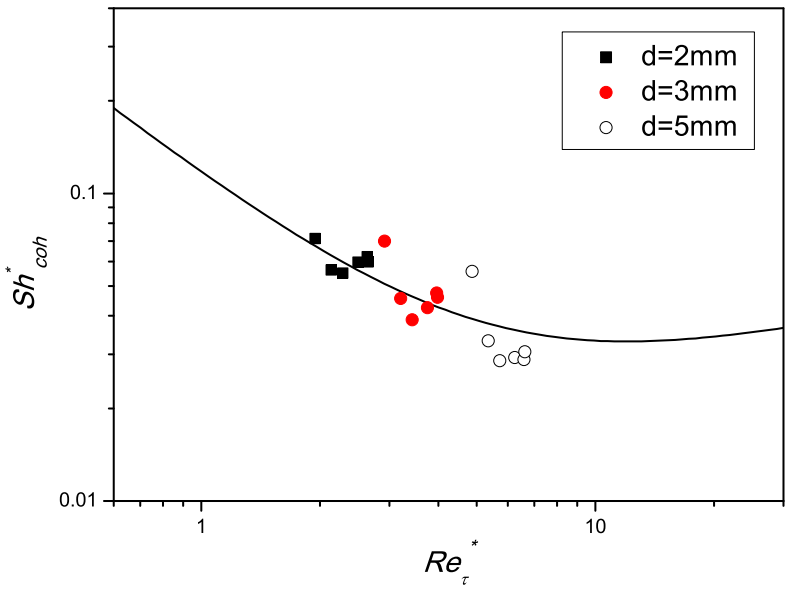

Fig. 4.23. Alternative generalized critical Shields number $Sh^*_{coh} = \frac{Sh^*_\tau}{1+\Psi(Bo_g)}$ versus shear Reynolds number Re^*_τ. The function Φ is given by Eq. 4.9 with $\alpha = 2.7$ and $A_\Psi = 9.8$.

4.3.4 A preliminary micro-mechanical analysis

As an illustration of the micro-mechanical investigations that can be conducted with our discrete numerical system, the particular forms of solid de-bonding taking place during the erosion process can be conveniently analysed with a ternary plot of the bond failure criterion (i.e. $(F_n/C_n) + (F_s/C_s)^2 + (M/M_b)^2 = 1$) where each de-bonding event is represented by a point P inside an equilateral triangle, accounting for the respective contribution of the traction, shear and bending solicitations, as shown in Figure 4.24.

Figure 4.25 shows a particular example of this micro-mechanical analysis of bond breakage. The corresponding results suggest that the most efficient types of de-bonding involve either pure traction (i.e. $(F_n/C_n) \sim 1$) or a combination of shear and bending solicitations with low levels of tensile forces, in the range of $(F_n/C_n) \sim [0.3-0.4]$. Furthermore, the micro-mechanical analysis also seems to indicate a preferential de-bonding direction around 60° during the erosion process that is roughly along the main direction of tensile efforts.

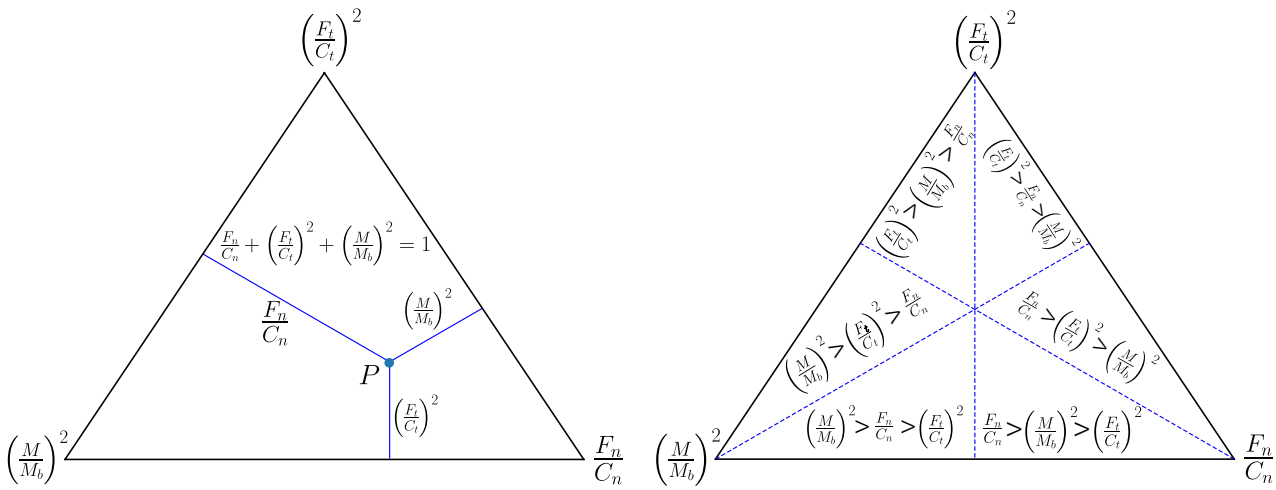

Fig. 4.24. Triangular representation of bond failure condition.

All these extents are supposed greatly dependent on both the particular flow conditions of the simulation and the chosen material behavior. They thus appear as a promising line of work for the selection of erosion-resistant materials within the general assessment of erosion countermeasures.

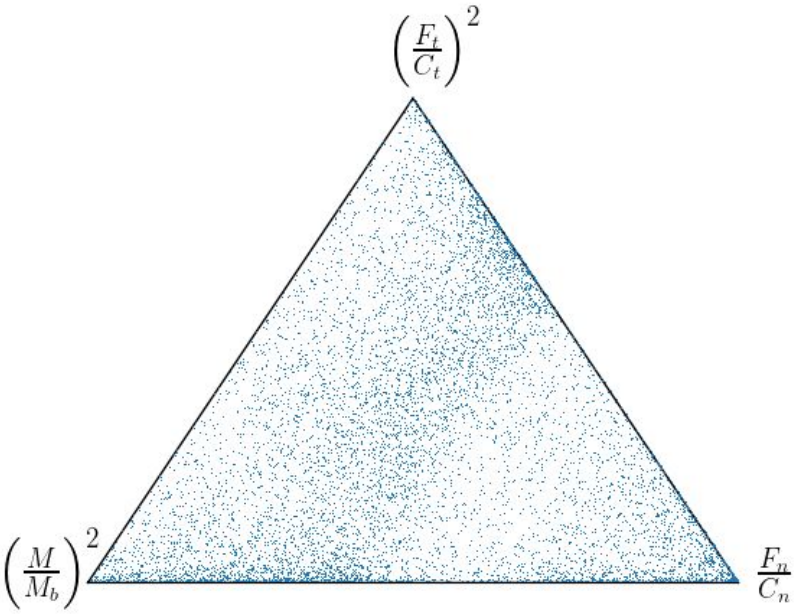

(a)

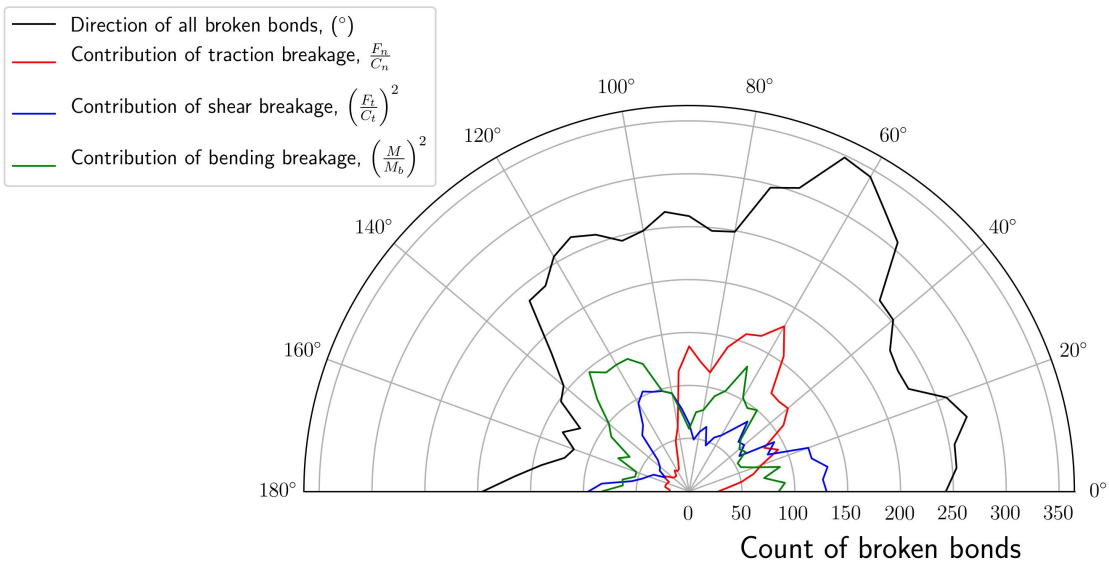

(b)

Fig. 4.25. Micro-mechanical features of the simulated shear flow erosion. (a) Ternary representation of bond failure conditions involving $d = 3$ mm, $\nu = 2.10^{-4}$ m^2/s, $U_0 = 5$ m/s, and $e_0 = 5$ mm; (b) Angular distribution of cumulative solicitations for all broken cohesive bonds (8647 in total) during the shear flow erosion.

4.4 Discussion

4.4.1 Different rupture modes

As pointed, the cohesive model used in the present study is quite rich, each debonding event during erosion involving a combination of three rupture mechanisms:

traction, shearing, and bending. It is thus interesting to examine the effect of excluding one or two breakage mechanisms on the overall behavior of the cohesive material under an eroding shear flow. Here, in practice, a given breakage mode can be inhibited by simply multiplying its corresponding threshold component by a factor 10. Four cases were implemented: (a) excluding shear breakage alone ($10 \times T$), (b) excluding bending breakage alone ($10 \times M$), (c) excluding traction breakage alone ($10 \times N$), (d) excluding simultaneously shear and bending breakages ($10 \times T$, $10 \times M$). The results are summarized in Figure 4.26 in terms of the previous micro-mechanical analysis.

First, the ternary representations confirm the effectiveness of the practical multiplication by 10 to inhibit a breakage mode, especially in cases (a), (b), and (d). This is less obvious in case (c), meaning that the contribution of tensile breakage still exists, even when the corresponding threshold is one order of magnitude higher. Considering now the angular distributions of cumulative solicitations, one can note on the graphs that case (a) and case (b) are very similar, shear and bending breakages playing almost exactly the same role, respectively, with a fairly increased contribution compared to the reference situation (see Fig. 4.25). The preferential de-bonding direction during erosion remains around 60°. For case (c), the distribution is more symmetric, but still giving rise to a preferential mode at about 60°. Finally, case (d) is an exceptional situation where shear and bending breakages are excluded, and, if the previous 60° direction still contributes substantially, the preferential angle is now around 90°, along indeed with the tensile efforts which thus appear significantly modified compared to the reference case.

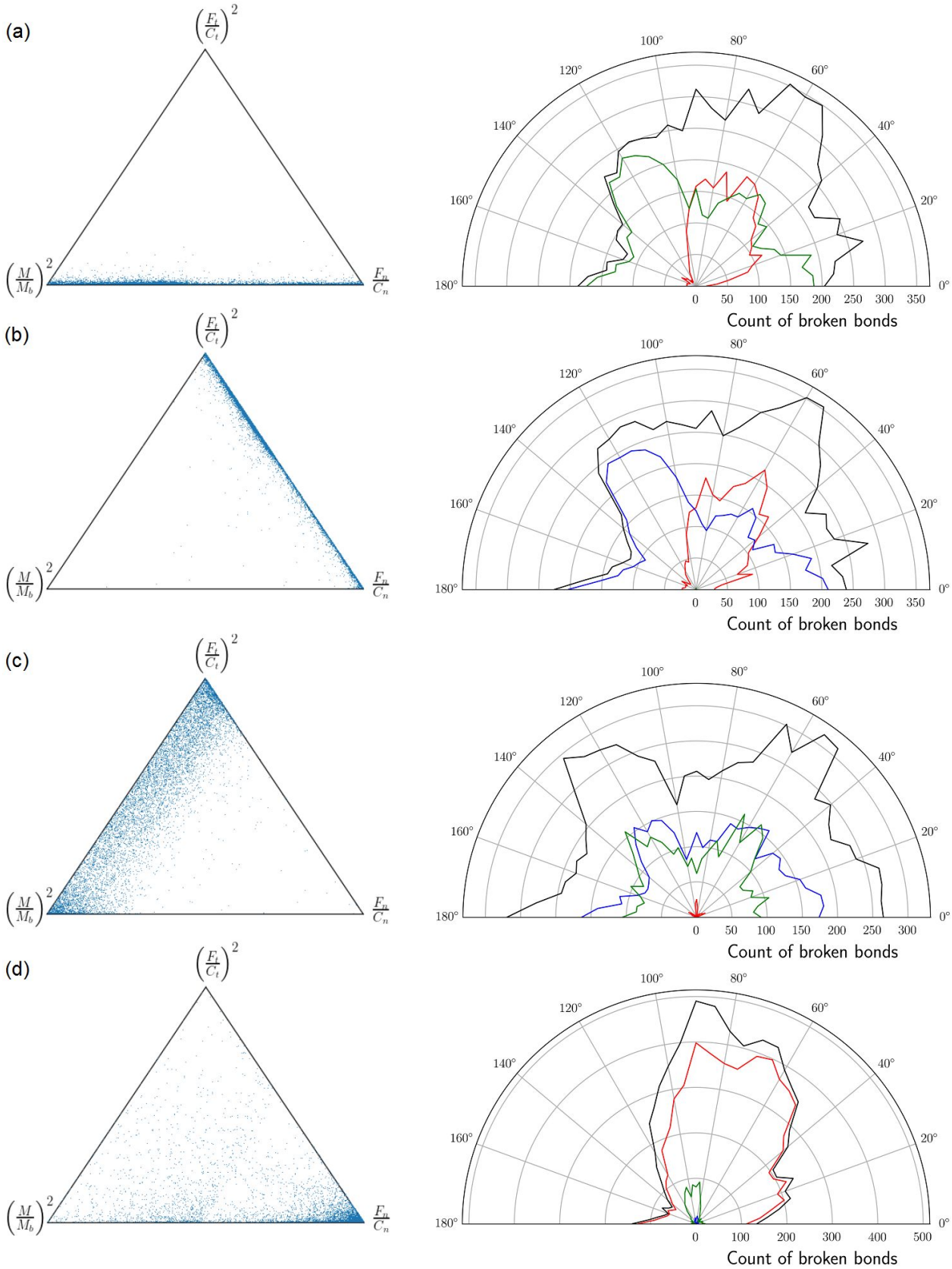

Fig. 4.26. Ternary representation of bond failure conditions with excluding shear breakage (left) and angular distribution of cumulative solicitations for all broken cohesive bonds (right) for: (a) excluding shear breakage ($10 \times T$), (b) excluding bending breakage ($10 \times M$), (c) excluding traction breakage ($10 \times N$), (d) excluding shear and bending breakage ($10 \times T$, $10 \times M$).

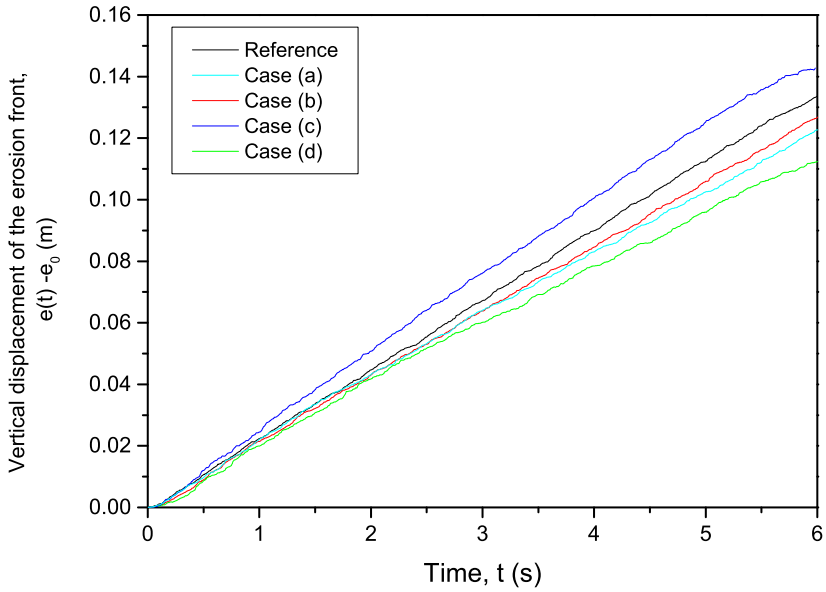

Fig. 4.27. Time evolution of the erosion front for the different cases with d=3 mm and for the following fluid flow conditions: $\nu = 2.10^{-4}$ m^2/s, $U_0 = 5$ m/s and $e_0 = 5$ mm.

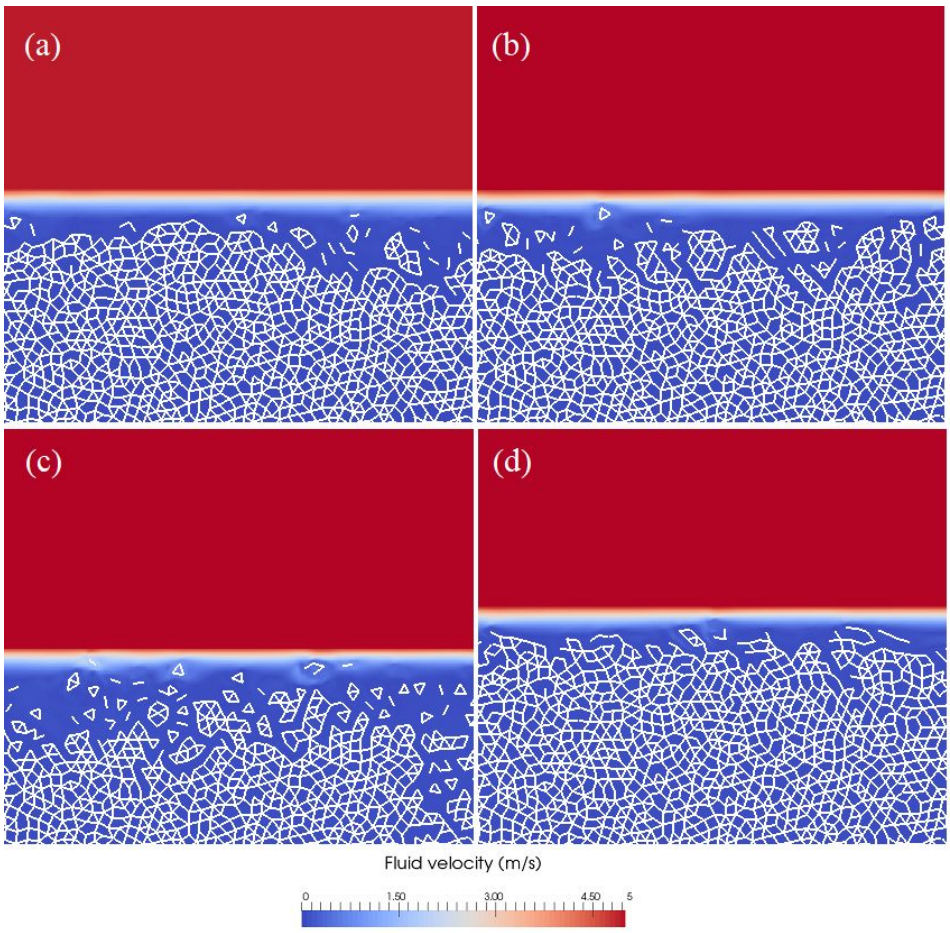

Fig. 4.28. Fluid velocity magnitude (color scale) and cohesive bond network (in white) contours for the 4 different rupture mode cases: (a) excluding shear breakage, (b) excluding bending breakage, (c) excluding traction breakage, (d) excluding both shear and bending breakage. The snapshots are zooms of the middle part of the channel taken at the same time $t = 2.4$ s. The solid particle and fluid flow conditions are the same as in Fig. 4.27.

The time evolution of the erosion front is shown in Figure 4.27 for the different cases. Here again, cases (a) and (b) are in very close agreement together and slightly above but comparable to the reference situation. On the contrary, case (c) is far less resistant to erosion. As regards case (d), it is rather similar to cases (a) and (b) during the first moments but the erosion rate then progressively decreases somewhat, meaning that a linear evolution of the erosion front is less obvious here.

To better understand the similarities and differences observed in the studied cases compared to the reference situation, the fluid velocity magnitude is plotted in Figure 4.28, together with the representation of the cohesive bond network. The corresponding snapshots are extracted at the same time t=2.4 s and only part of the domain is shown, basically the middle part of the channel. Once again, and even if their bond rupture modes are different, cases (a) and (b) show a similar scenario of erosion where only the superficial layers of the sample are damaged. Slight differences can however be detected as regards the occurrence of small oblique cracks which is favored in case (b). Stronger distinctions can be made for both cases (c) and (d). The first situation is characterized by an extended damaged depth with a substantial increase in the number of aggregates. The sample is more fragile when traction breakage is inhibited and erosion rate increases accordingly. On the contrary, when tensile bond ruptures are allowed, a higher resistant is observed through the occurrence of a significantly reduced extent of the superficial damaged depth. Even if less visible here, these observations are to a certain extent reminiscent to the previous exploratory study presented by Philippe et al. (2017) in the case of erosion by an impinging jet. An exhaustive analysis could be envisaged in the future by varying independently (which was not the case in this manuscript since they were assumed directly proportional to each other) and systematically the three bond rupture thresholds in traction, shearing, and bending.

4.4.2 Relevance of the shear stress

The fluid shear stress is widely used to quantify sediment transport and erosion rate whether for cohesive or cohesion-less soil. However, many researchers have suggested to quantify the erosion or sediment transport rate based on alternative flow quantities, as for example the stream power (Knapen et al., 2007; Marot et al., 2012). In turbulent flows, in addition to time average quantities such as shear stress, turbulent eddies exist and generate fluctuations in flow quantities (e.g velocity, pressure) which largely influence sediment erosion and transport, resulting for instance in chaotic motion of the particles. Consequently, erosion laws based on statistical distributions can be also envisaged alternatively (Van Prooijen and Winterwerp, 2010; Beguin et al., 2013).

In this section we question the relevance of the fluid shear stress as the appropriate flow quantity able to rule the soil's erosion rate through an erosion law. To do so, the flow shear stress τ as defined in Eq. 4.1 is kept constant while the inlet velocity U_0, the fluid gap e_0, and the fluid viscosity ν are varied. Four data set were simulated, corresponding to two shear stress values, namely $\tau = 100$ and 200 Pa, and two initial fluid gaps: $e_0 = 5$ and 8 mm. The results are summarized in Figure 4.29, which

shows the variation of the erosion rate $\dot{\epsilon}$ as a function of either the particle Reynolds number Re_p (Fig. 4.29a), calculated from Eq. 4.3, or the flow Reynolds number Re (Fig. 4.29b), calculated from Eq. 4.2.

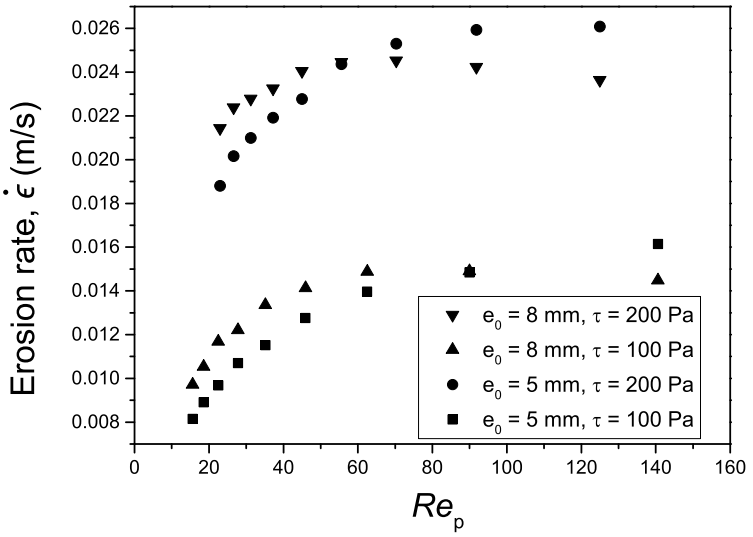

(a)

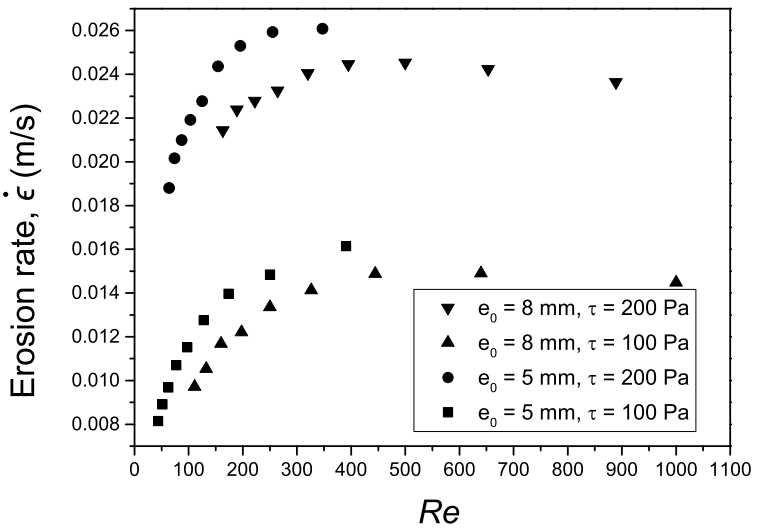

(b)

Fig. 4.29. Erosion rate versus (a) particle Reynolds number Re_p and (b) flow Reynolds number Re.

All the curves presented here, either versus particle or flow Reynolds number, have the same trend with a less and less increasing evolution until a final plateau is reached. Almost the same plateau values are found for a given shear stress τ value

while varying e_0, with a typical discrepancy around 10 to 15%. In all cases, the plateaus are reached for similar Reynolds numbers, around $Re_p \sim 50$ and $Re \sim 300$ in terms of the particle Reynolds number and the flow Reynolds number, respectively.

In conclusion, provided that the Reynolds number is high enough, namely $Re_p > 50$ or equivalently $Re > 300$, the fluid shear stress truly appears as the unique relevant quantity that rules erosion rate. Below this range, a substantial decrease in erosion is observed and the particle (or flow) Reynolds number should consequently be added as a second control parameter for erosion rate. Then, a closer examination would be required to pursue further in this direction.

Conclusion and perspectives

This work dealt with an in-depth study of the surface erosion phenomena through a numerical point of view. The approach adopted here is based on a coupled fluid-particle numerical model at the micro-scale by combination of the Lattice Boltzmann Method (LBM) for the fluid phase and the Discrete Element Method (DEM) for the solid phase composed of circular grains, including a cohesion model with time dependent damage to account for solid cohesive bonds at particle contacts. In this study, we aimed at validating and subsequently implementing an efficient code constructed from these methods to simulate two common flow configurations generating surface erosion of our cohesive granular soils : impinging jet, that is particularly relevant for the Jet Erosion Test (JET), and constant shear flow from which an appropriate erosion law was selected before related erodibility parameters were extracted and analysed systematically.

The numerical methods (LBM-DEM) used in this work were properly described, along with the coupling technique between both methods, highlighting the relevance of the model when dealing with particulate flows, including many fluid/particle interactions. During this thesis work, we have succeeded in parallelizing and improving the efficiency of the original CPU version of our code using GPGPU (General Purpose Graphical Processing Unit) computing approach, since the combined methods are highly costly in terms of computational resources and simulation time. Thus, the whole structure of the code is now adapted to be executed in GPUs where the "CUDA c/c++" programming language was chosen. The model was ultimately validated by comparison of classical particle settling situation for either a unique grain, where relevant drag coefficients were recovered, and a pair of particles through the so-called DKT-pattern (drafting-kissing-tumbling) which was found to be correctly simulated.

Before making full use of the capabilities of our code, 2D jet flow configurations were first investigated with the Lattice Boltzmann Method (LBM), namely free jet and impinging jet on either a smooth wall and a fixed horizontal granular surface. In this latter case, the coupling technique was turned on in the code while the particles remained fixed in the DEM part. The results obtained for the free jet could be very well described by the self-similarity theory for various jet Reynolds numbers through the introduction of the virtual origin λ for which a relevant expression was proposed. This study also further validated our model as regards the LBM flow calculation.

The following analysis of the configurations of impinging jets on a smooth wall and on a fixed granular surface was another step towards a better understanding

of jet flow erosion through relevant estimates of crucial hydrodynamic quantities, restricted here to the laminar regime. In that respect, the maximal tangential velocity near the impingement surface was found to be simply proportional to the theoretical center-line velocity of the self-similar free jet model evaluated at the same downstream distance (i.e. the distance from the nozzle exit to the impingement surface including the virtual origin λ). Moreover, the maximal center-line velocity from the free-jet theory allowed to provide an accurate estimate for the maximal bed shear stress and a complete expression has been proposed here in Eq. 3.5. This expression is notably based on the introduction of a friction coefficient that was found to be of Blasius type, that is inversely proportional to the square root of the jet Reynolds number.

From this point, the DEM part was fully activated in the model, starting with the case of cohesion-less granular samples whose erosion onset under jet impingement was found to be in close agreement with the results of Badr et al. (2014) obtained for plane impinging jets when using an inertial expression for the critical Shields number (Sh_u^*). Thanks to the previous expression of the shear stress in Eq. 3.5 coming from the preliminary study of impinging jets, both our numerical results and the experimental ones by Badr et al. (2014) could be successfully reported in the classical Shields diagram (Sh_τ^*), in reasonable agreement with the Shields curve.

Next, the solid bond model was added to the code with the aim of analysing impinging jet erosion of cohesive granular samples. To this end, the erosion threshold, defined as the initiation of bond breakage and particles detachment, was quantified for different particle sizes and fluid's viscosity. These values have been found to be well described by an extension of the classical Shields criterion used for cohesion-less materials to weakly cohesive soils. More precisely, as expressed in Eq. 3.10 or equivalently Eq. 3.11, an additional contribution of cohesion strength to the soil's resistance to erosion was included through a proper dimensional analysis providing a simple relation between the generalized Shields number (Sh_{coh}^*), the usual cohesion-less Shields number (Sh_τ^*), and the granular Bond number (Bo_g) which compares cohesion to buoyant weight.

The study was ultimately completed by the full simulation of 2D Jet Erosion Tests (JET) in the laminar regime, allowing to quantify the erodibility parameters of our cohesive granular samples after prior adaptation of the JET interpretation model to our 2D geometry and to a more general erosion law based on a power law relation including an exponent n in addition to the critical shear stress τ_c and erosion coefficient k_d. A parametric study was carried out by varying the cohesion strength C while fixing the jet inlet velocity. However, the overall result was not satisfying for the critical shear stress τ_c which, compared to the previous generalized critical Shields number, is over-predicted at low cohesion strength C and under-predicted for higher C values. Moreover, a non-expected dependence with the jet inlet velocity is found, especially for τ_c comparatively to k_d. This issue more generally confirms the intrinsic weaknesses of the JET interpretation model which requires several strong assumptions on the hydrodynamic quantities and disregards the existence of the crater depth inside which re-circulation flows increasingly grow.

Drawing on this conclusion, a second erosion configuration has been investigated

where the use of a Couette flow induces a uniform and stationary shear stress at the soil surface. This allowed to circumvent most of the complexity highlighted in the jet flow, notably the re-circulation flow once the crater is formed. Owing a relevant criterion to determine that a particle is eroded and next to removed it from the calculation, it was indeed possible to simulate a simple configuration where the top surface of the sample was kept flat during erosion and where the bed shear stress τ remained consequently constant, thus used as a control parameter. Therefore, a linear decrease of the sample thickness with time was found, enabling for a direct measurement of the erosion rate $\dot{\epsilon}$.

Without any a priori postulate as regards the mathematical expression of an erosion law relating, at the sample scale, erosion rate to fluid shear stress through intrinsic soil's erodibility parameters, it was next possible to investigate objectively and directly the relationship between $\dot{\epsilon}$ and τ. To this end, a remaining difficulty was first fixed since it was found that a sharp drop to zero of the erosion rate at low values of τ whereas a large crack occurs and develops downward in the sample. The full version of our code was then used by addition a time dependent damage law in the cohesive bond model and allowed to circumvent the problem. Afterward, a parametric study was carried out and a power erosion law, defined in Eq. 1.14, was found to fit fairly well our simulation data with a substantially increased accuracy compared to the most common linear law. The relevance of the shear stress as unique quantity that rules erosion was also questioned with a positive answer provided that the Reynolds number is high enough, expressed either at the particle or the flow scale. But less erosion was observed below this range.

Finally, as regards the relation between the erodibility parameters arising from the erosion law at the sample and the micro-scale quantities as the bond cohesive strength C and the particle diameter, original results were obtained, as for the new exponent n which increases almost linearly with C, but however with some inconsistency, especially about the critical shear stress whose values given by the erosion law do not coincide with the onset criterion from the generalized critical Shields number. Empirically, a modification of the previous relation could be proposed but without any satisfactory physical meaning. Further work is clearly needed to gain a better understanding on this issue and this last shear flow configuration appears particularly well suited for such an exhaustive investigation.

Perspectives

The present study suggests many perspectives and highlights several open questions. Among these, we can distinguish specific numerical aspects and more fundamental concerns about actual knowledge and remaining gap in our understanding of fluid flow erosion of cohesive soils.

Starting with the numerical tool developed and subsequently used during this work, several potential improvements can be summarized. First, although the computational speed was significantly improved using GPUs, there is still a room for improvement, especially in the LBM part, which was found to consume approximately 84% of the whole computational cost. This could be done by disregarding the use of the global memory to the benefit of the GPU's shared memory which is much faster to access. Furthermore, the actual LBM-DEM code is in 2D, thus it is difficult to compare directly the numerical simulations to the experimental results. However, the code could be rather easily extended to 3D, but large memory resources would be needed accordingly for the LBM part, since 15 (D3Q15 scheme) or 19 (D3Q19 scheme) velocity directions is required on each fluid node. Multi GPUs with domain decomposition may be required since one GPU has a fixed and small memory. The 3D version would eventually allow to model more realistic geotechnical applications.

As regards the physical aspects and related questions, several directions are envisaged. First, in the specific configuration of jet impingement, some investigation of the fluid flow could be started in the case of a solid surface with a pre-formed and realistically shaped crater, in order to estimate a more relevant shear stress value in the carter, possibly still based on the free jet velocity. Doing so, we may improve our jet interpretation model and thus gain a better estimation of soil's erodibility. As it was recently shown that the expression in Eq. 3.5 could be extended to 3D round impinging jet configuration in the laminar regime (Brunier-Coulin et al., 2019) and validates experimentally the generalized proposal of a critical Shields number for weakly cohesive soils, such an improvement of the JET interpretation model in laminar regime would become also relevant for more realistic situations.

The analysis of soil erosion under Couette flow configuration has not been satisfactorily completed and remaining efforts would be needed to better understand the underlying physical mechanisms of erosion based on an exhaustive study, by changing several parameters as particle size, density, or gravity, but, even more interestingly, by exploring all the different types of soils accessible through appropriate variations of the three breakage thresholds introduced in the cohesive bond model. To this end, the micro-mechanical analysis presented in section 4.3.4 appears as a promising way for such an investigation and could be further developed.

Additionally, a specific concern deals with the relation between the microscopic parameters and the more global quantities evaluated at sample scale. The latter involve erodibility, as studied in this thesis, but also more general mechanical resistances. To this end and as presented in Appendix A, a work has been initiated to simulate mechanical tests, particularly traction and shearing, at the sample scale

in order to study this micro-macro passage and check the relevance of the theoretical Rumpf formula (Pierrat and Caram, 1997). It is worth highlighting that, in parallel to the simulations, an experimental approach is already under progress in our research group and will be pursued, based on artificial materials made of large grains bonded by viscous or solid bridges, and a proper traction test that allows to measure the tensile yield force at the rupture, either at the sample scale or, locally, at the grain contact.

Finally, it should be noticed that, our coupled LBM-DEM code was used in this study to model only two flow configurations, namely impinging jet and tangential shear flow, it can be implemented for the study of various submerged fluid-particle interaction problems. This is already the case for the modeling of sinkhole occurrence within cohesive soil sublayer in karstic context (Luu et al., 2019) and preliminary results can also be cited about profile installation of an offshore monopile in fully saturated layered soil (Benseghier et al., 2019). Moreover, the in-house GPU code will be used and improved in the COMET[1] project starting in autumn 2019, mainly in two applications engineering fields: erosion of offshore foundations (e.g. triggering of superficial fluidization during the installation of a partially embedded suction bucket) and localized erosion of layered hydraulic infrastructures.

[1]COMET is a Franco-German ANR-DFG projet abbreviated from "Coupled micromechanical modelling for the analysis and prevention of erosion in hydraulic and offshore infrastructures."

Appendix A

Macro-scale tensile test

In the case of two bonded particles, the micro-scale tensile force required to break the bond is known in our model. However, there are little knowledge about the force needed to break at macro scale a stack of particles collectively connected by cohesive bonds. For this reason, we develop here a numerical macro-scale tensile test.

The tensile (traction) test aims to measure the resistance force to traction of our cohesive granular materials and also to verify Rumpf formula relating yield tensile force F_t^* and stress σ_t^*, as follows (Gilabert et al., 2007; Pierrat and Caram, 1997):

$$\sigma_t^* = \frac{1}{\pi} \frac{\langle d \rangle}{\langle d^D \rangle} z \phi F_t^* \tag{A.1}$$

where z denotes the coordination number, ϕ is the solid fraction, and D the dimension of space which is here $D = 2$. With our uniform diameter distribution, the mean and mean square diameter read $\langle d \rangle = d_{mean}$ and $\langle d^2 \rangle = d_{mean}^2$, respectively.

The test is divided into two parts. First, the sample preparation where we fill two cones connected by their smallest section. The particles are settled under gravity from the upper cone (see Figure A.1) before cohesion is activated. Second, the traction test is performed from the prior prepared cohesive sample and after the particles have been gathered into two separate groups, or clumps. As illustrated in Figure A.2, Clump 1, constituted of the particles in the upper cone, moves upward with constant velocity in y-direction whereas Clump 2 is fixed and contains of the particles in the bottom cone. When the two clumps separate, basically at the minimal section, we note the rupture force. The traction force is calculated by the summation of the cohesive forces between particles that belong to different clumps in y-direction.

The simulation parameters are summarized in Table A.1. The boundary conditions are set as follows: a constant velocity is applied at the upper clump in y-direction while the bottom clump is being fixed. Two different samples have been used with a same mean particle diameter and with different size ratio $L/d = 20$ and 30.

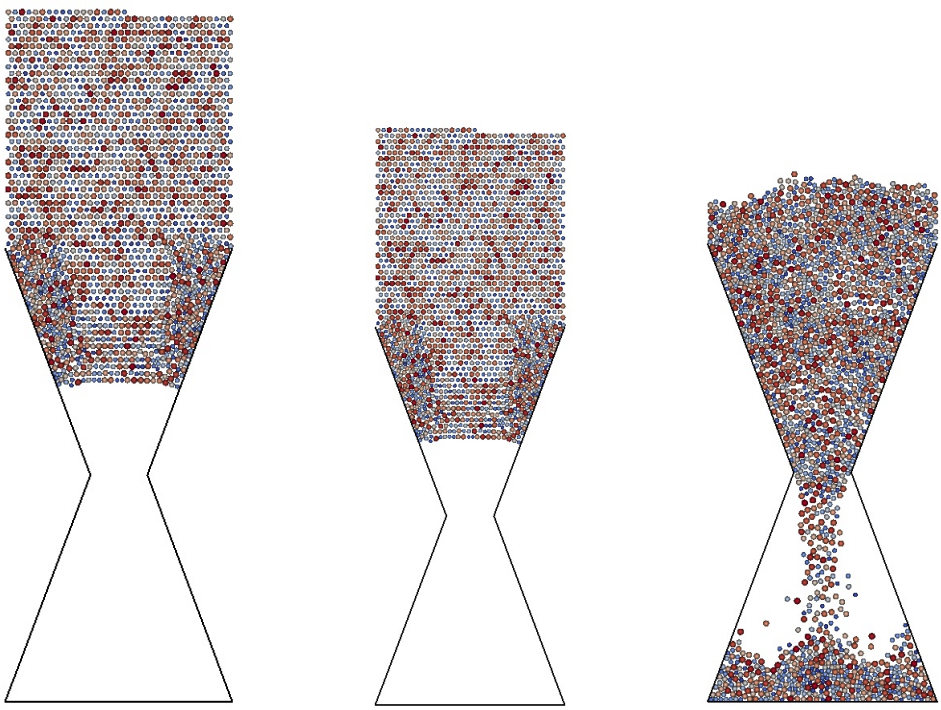

(a) (b) (c)

Fig. A.1. Time sequence of sample preparation for the traction test.

Table A.1. Parameters for our parametric study of traction tests

Particle mean size, d_{mean}: 3 mm
Density ρ_s: 2500 kg/m^3
Normal stiffness k_n: 1.10×10^5 N/m
Shear stiffness k_t: 1.10×10^5 N/m
Friction coefficient μ: 0.30
Rolling friction μ_r: 0.1
Restitution coefficient e: 0.2
Gravitational acceleration g: 0 m/s^2
Bond strength, C: [1-50] N
Displacement rate $\dot{\varepsilon} = V_y$: 0.0001 m/s
Sample 1
Number of particles N_g: 2491
Minimum section L: $20 \times d$
Coordination number z: 4.1
Solid fraction ϕ: 0.837
Sample 2
Number of particles N_g: 3500
Minimum section L: $30 \times d$
Coordination number z: 4.05
Solid fraction ϕ: 0.793

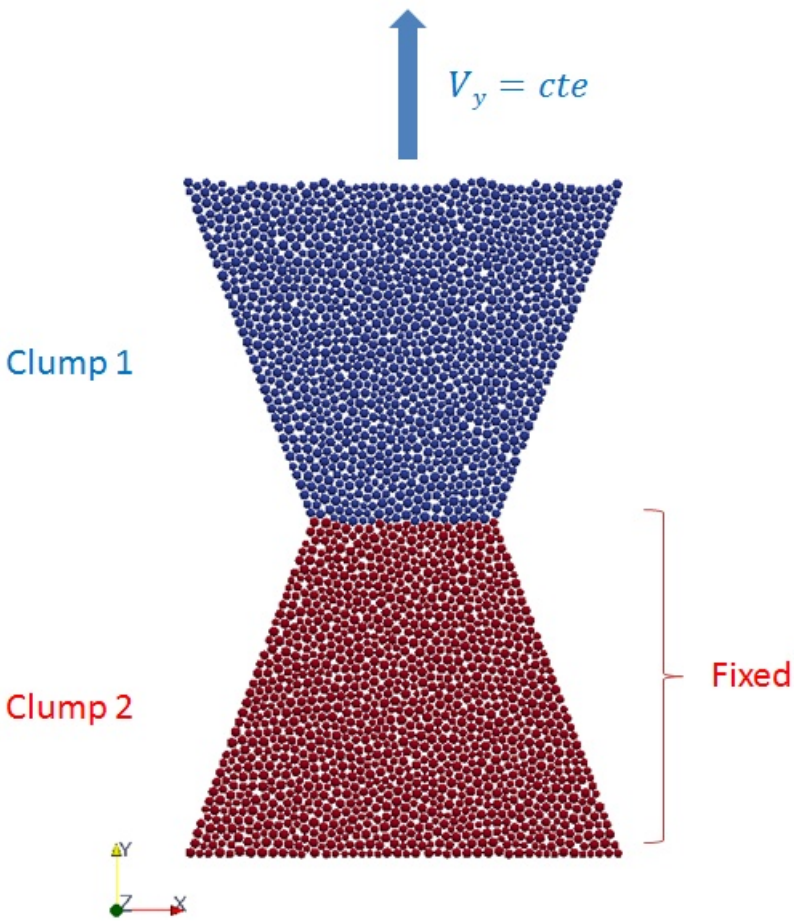

Fig. A.2. Snapshot showing the two clumps: clump 1 in blue with constant velocity, clump 2 in red being fixed.

Figure A.3 shows the evolution of the y component of the tensile force exerted between both clumps versus vertical displacement for different cohesive bond strength C values. The curves increase almost perfectly linearly until the rupture is reached and followed by a drastic decline in the force due to sudden separation of the two clumps. Also, it is observed that the rupture force indeed increases with the cohesion strength C.

A parametric study was carried out by varying the cohesion strength C ranging from 1 to 50 N. For each simulation, the rupture force is noted and plotted against C, as shown in Figure A.4. An obvious proportional relation is observed between the macro forces at the rupture and the micro cohesion strength C with a slope 24.84 ± 0.10 and a correlation coefficient $R^2 = 0.9998$.

By direct use of Rumpf's formula (Eq. A.1), one gets a rather close value for the slope: 21.86. It can be concluded that the formula is well verified by the simulation, at least in this particular conditions. An additional ratio $L/d = 30$ was also simulated and similar results were obtained. To compare the data each other, the tensile stress at rupture σ^* is plotted versus C/d in Figure A.5. According to

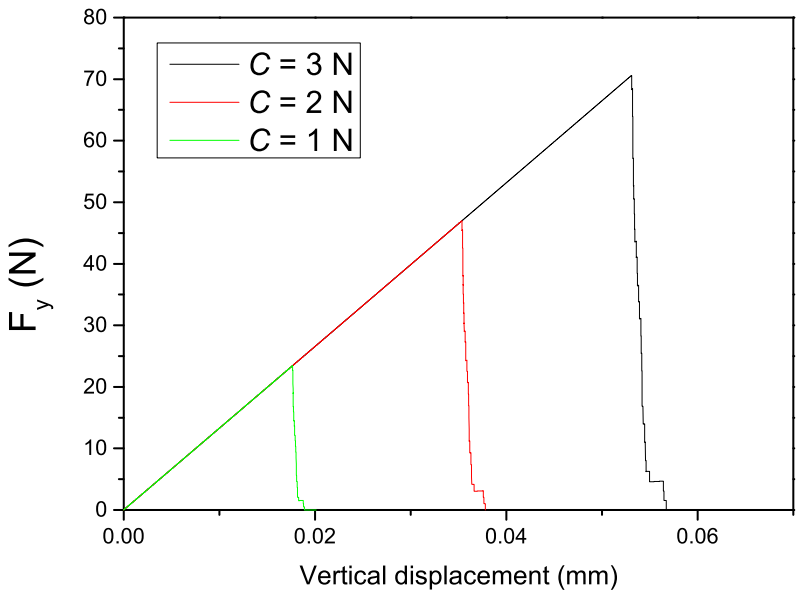

Fig. A.3. Evolution of the y components of tensile forces versus the vertical displacement of the upper clump for different cohesive strength C.

Rumpf formula, both results obtained for the two L/d ratios must almost coincide since they have close solid fraction ϕ and coordination number z values, and this is indeed the case.

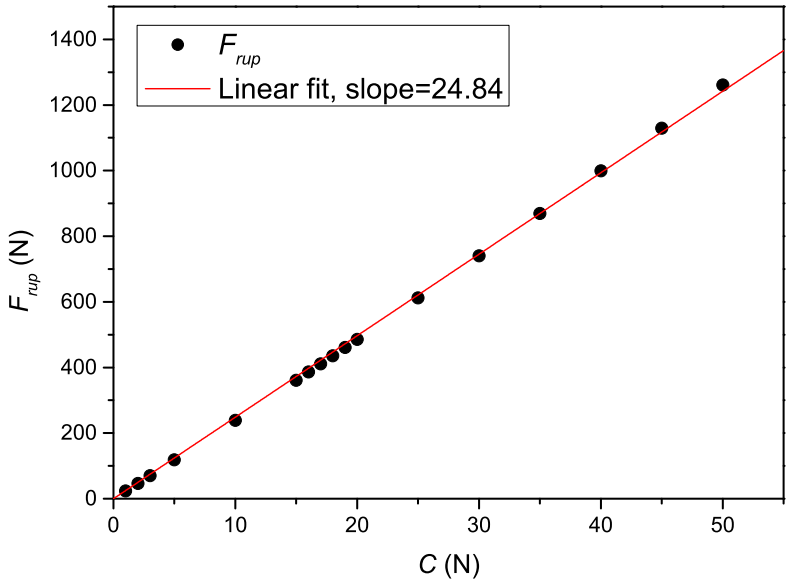

Fig. A.4. Rupture forces versus cohesive bond strength C values. The solid line stands for a proportional fit for $L/d = 20$ ($R^2 = 0.9998$).

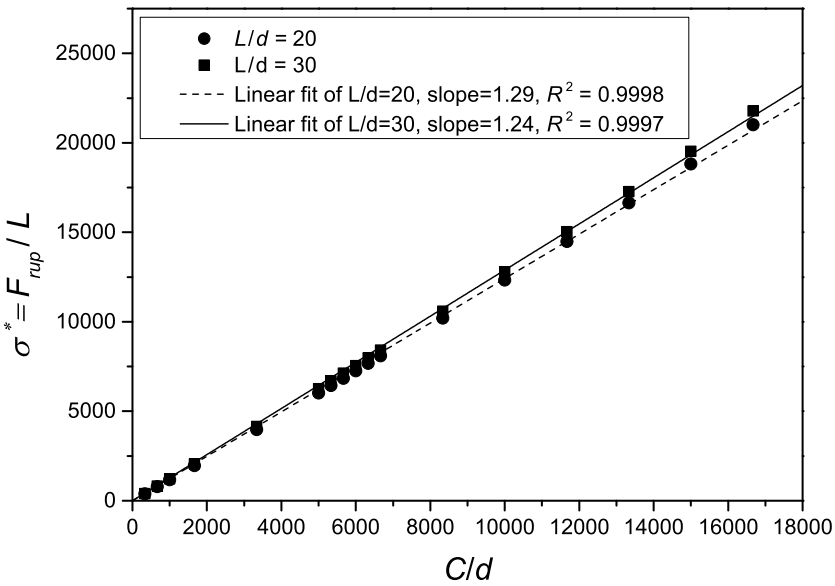

Fig. A.5. Rupture tensile stress versus C/d for $L/d = 20$ (solid circle) and $L/d = 30$ (solid square). The line stand for proportional fits for $L/d = 30$ ($R^2 = 0.9997$) (solid line) and for $L/d = 20$ ($R^2 = 0.9998$) (dashed line).

Appendix B

Résumé étendu en français

B.1 Contexte général

Le réchauffement global actuel induit un changement rapide du climat et une aggravation des catastrophes naturelles, entraînant des conséquences socio-économiques et écologiques majeures au niveau mondial. En particulier, l'élévation du niveau des océans et l'intensification des précipitations augmentent la fréquence et l'ampleur des inondations et, par conséquent, le risque potentiel de rupture des ouvrages de protection (digues, barrages, levées, etc).

Le principal phénomène responsable de la rupture de ces ouvrages hydrauliques en remblai est, très majoritairement, l'érosion des sols constitutifs de l'ouvrage par action de l'eau qui représente environ 95% des cas. En France, un exemple assez récent d'évènements dramatiques en termes d'érosion d'ouvrages de protection et de ruptures de digues concerne la crue du Gard de Septembre 2002 qui a coûté la vie à cinq personnes et causé pour pratiquement 1 milliard d'euros de dégâts. Au niveau international, les ruptures spectaculaires des digues de la Nouvelle-Orléans (Floride, US) à la suite de l'ouragan Katrina en 2005 restent dans toutes les mémoires. Katrina a tué au total plus de 1000 personnes et engendré un coût économique de l'ordre de 100 milliards de dollars. On comprend qu'il y ait une demande sociétale croissance pour à la fois une plus grande sûreté des ouvrages de protection existants et une meilleure gestion des réparations et constructions nouvelles en termes de durabilité, de résistance à l'érosion mais aussi de respect de l'environnement.

D'après Foster et al. (2000), les mécanismes d'érosion des ouvrages hydrauliques peuvent être classés en deux catégories : l'érosion interne et l'érosion externe. L'érosion externe fait référence à l'action hydrodynamique d'un écoulement d'eau à la surface extérieure de l'ouvrage, généralement due à une situation de surverse. Celle-ci dégrade l'ouvrage par entraînement d'une masse importante de sol pouvant conduire à la création d'une brèche et éventuellement à la rupture de la structure. Ce type d'érosion représente environ 50% des défaillances de barrages en terre. L'autre type d'érosion est dite interne et englobe, de façon générale, tous les processus d'entraînement et de transport de particules de sol à l'intérieur d'un ouvrage en terre. Ce phénomène, typiquement plus lent et beaucoup moins visible que l'érosion

externe, s'initie par infiltration d'eau à travers l'ouvrage ou ses fondations (voir Fig. 1.2b). Quatre mécanismes différents d'initiation de l'érosion interne ont été rapportés (Fell and Fry, 2007), comme résumé à la Fig. 1.3 : la suffusion, l'érosion de contact, l'érosion régressive et l'érosion par écoulement concentré.

L'érosion par écoulement concentré apparaît généralement le long d'un chemin hydraulique préférentiel au sein de l'ouvrage, causé par exemple par un tassement différentiel, par la fracturation hydraulique d'une couche argileuse, par dessiccation à proximité d'une paroi ou d'une conduite traversante, ou encore par présence de racines ou de terriers (Zhang et al., 2016). L'érosion régressive est d'abord initiée en pied aval d'ouvrage en cas d'écoulement d'infiltration important, par soulèvement ou fluidisation selon la nature du sol superficiel (cohésif ou granulaire). Une fois formée, la cavité initiale s'étend progressivement de l'aval vers l'amont, de façon régressive par rapport au sens de l'écoulement. L'érosion de contact est une érosion sélective des particules de sol les plus fines à l'interface entre deux couches de sols de compositions différentes. L'écoulement hydraulique se concentre dans la couche la plus grossière et érode la surface au contact de la couche de sol plus fin. Les particules érodées sont ensuite transportées et éventuellement filtrées plus loin dans l'ouvrage. La suffusion est également une érosion sélective des particules fines mais cette fois en volume, au sein d'un sol présentant une répartition granulométrique bimodale. On peut noter que ces quatre mécanismes d'initiation ont des cinétiques d'évolution lentes, typiquement sur plusieurs années, mais peuvent progressivement accélérer et se combiner à d'autres processus (tassement, colmatage, fontis, effondrement, ...) pour finalement mener à la rupture de l'ouvrage dès lors qu'il y a création d'un conduit continu connectant la réserve amont à l'aval. Ce mécanisme ultime de rupture est appelé érosion de conduit et se distingue par une cinétique extrêmement rapide, qui se compte plutôt en heures qu'en jours (Bonelli and Marot, 2011). Enfin, on pourra noter que ce processus d'érosion de conduit correspond localement, aux parois latérales, à une érosion de surface tout à fait comparable à l'érosion externe déjà évoquée. De même, l'érosion par écoulement concentré, l'érosion de contact et l'érosion régressive sont générées à petite échelle par l'érosion d'une couche de sol par un écoulement hydraulique superficiel. Les mêmes lois locales d'érosion pourront donc être a priori utilisées de façon générique pour la quasi-totalité des situations rencontrées au sein d'un ouvrage, à l'exception du cas de la suffusion.

La plupart des travaux portant sur l'érosion des sols cherchent à identifier les mécanismes déclencheurs ou bien, au contraire, les principaux facteurs inhibiteurs du phénomène. Dans ce but, de nombreux essais d'érosion ont été développés pour mesurer, en laboratoire ou in situ, la résistance d'un sol à l'érosion en fonction de ses propriétés mécaniques et physico-chimiques. Parmi les essais les plus courants, on peut citer l'essai d'érosion par jet (JET), l'essai d'érosion de conduit (HET) ou encore l'essai d'érosion tangentielle (EFA). On a ainsi défini l'érodibilité des sols qui est essentiellement caractérisée et quantifiée par deux paramètres : un coefficient d'érosion k_d et une contrainte fluide critique τ_c. Le coefficient d'érosion contrôle la cinétique du processus et peut permettre par conséquent de quantifier le temps restant avant la rupture de l'ouvrage en cas de crise. La contrainte fluide critique prédit quant à elle le seuil au-delà duquel l'érosion peut être activée et sera plutôt

utilisée comme une valeur de référence à ne pas dépasser lors de l'étude préalable d'un projet de construction ou de réhabilitation d'un ouvrage hydraulique. En pratique, ces deux quantités sont issues d'une régression linéaire des données expérimentales en se basant, pour l'érosion de surface, sur une loi linéaire reliant le taux d'érosion du sol à la contrainte fluide en excès (Eq. 1.14) proposée originellement par Partheniades (1965). La pente fournit le coefficient d'érosion k_d tandis que l'abscisse à l'origine donne la contrainte de cisaillement critique τ_c. Les différents essais d'érosion devraient ainsi permettre d'établir des relations empiriques entre les caractéristiques d'érodilibité du sol et les propriétés géo-mécaniques usuelles. Cependant, dans la pratique, ils reposent sur des modèles d'interprétation basés sur des hypothèses souvent réductrices et restent de ce fait encore insuffisamment fiables. Ainsi, par comparaison entre essais d'érosion, les résultats peuvent amener à des valeurs d'érodibilité notablement différentes pour un même sol, remettant en cause le caractère intrinsèque de ces grandeurs ou, tout du moins, le cadre théorique des modèles d'interprétation. D'un point de vue plus fondamental, le phénomène d'érosion de surface reste un terme très générique qui met en jeu des mécanismes complexes d'instabilité hydrodynamique et mécanique à petite échelle. Malgré le nombre croissant d'études menées sur le sujet, ces processus élémentaires au niveau de l'interaction entre grains et fluide restent encore mal compris, de même que le passage de l'échelle microscopique à celle intermédiaire de l'échantillon et, in fine, à celle globale de la rupture.

B.2 Objectifs et méthodologie

Ce travail de thèse porte sur la modélisation numérique de l'érosion des sols granulaires cohésifs induite par un écoulement fluide incompressible pour des nombres de Reynolds faibles à modérés (régime laminaire). La phase fluide est décrite par la méthode dite Lattice Boltzmann (LBM), basée sur une modélisation statistique de la dynamique des particules constituant le fluide. La phase solide est décrite par la méthode des éléments discrets (DEM) qui modélise un ensemble de grains sphériques interagissant via des lois de contact simples et se déplaçant selon les équations de Newton. Le calcul DEM inclut ici un modèle de cohésion inter-particulaire développé par Delenne et al. (2004), dans lequel est défini un critère de rupture d'un pont solide entre grains voisins suivant trois seuils : en traction, en cisaillement et en rotation. Ce modèle de cohésion a, par ailleurs, été enrichi par une loi d'endommagement temporelle du lien cohésif entre particules proposée originellement par Silvani et al. (2009).

Un des objectifs de cette thèse est de mener des simulations numériques pertinentes pour étudier l'érosion des sols à l'échelle des grains, en s'appuyant et en améliorant les outils numériques développés précédemment par J. Ngoma (2011-2014) lors de sa thèse de doctorat et P. Cuéllar (2014-2015) lors de son post-doctorat. Les simulations menées concernent deux cas pratiques : l'érosion par un jet fluide impactant et l'érosion par un écoulement de cisaillement (ou Couette). Dans ce travail de recherche, les questions scientifiques posées ont pour but de :

- prouver l'exactitude et la validité de notre modélisation numérique pour simuler de manière réaliste l'érosion d'un sol par un écoulement fluide ;
- tester la pertinence des lois empiriques d'érosion ;
- établir un lien entre les paramètres micro (force de liaison cohésive, diamètre des particules) et les paramètres macro (coefficient d'érosion, contrainte critique fluide) par des études paramétriques.

B.3 Amélioration et parallélisation du code en GPU

Les applications de la méthode LBM-DEM sont encore limitées à des études académiques à petite échelle. Ceci est en partie dû au coût de calcul extrêmement élevé qu'implique des simulations discrètes de sols à une échelle représentative (par exemple des millions de grains de sol interagissant au sein d'une structure de génie civil), en combinaison avec un degré de raffinement élevé du maillage de fluide, afin de résoudre complètement le problème autour des particules solides, environ 10 à 30 nœuds du domaine fluide par diamètre de grain étant requis en fonction de l'application (Tran et al., 2017).

Cependant, cette limitation peut être en partie surmontée grâce au calcul parallèle hautes performances (HPC). Plusieurs techniques de parallélisation sont utilisables, telles que OpenMP (Open Multi-Processing) ou bien MPI (Message Passing Interface). Il est à noter que ces deux méthodes de parallélisation sont basées sur les processeurs (Unité Centrale de Traitement UCT, ou Central Processing Unit, CPU en anglais). En raison de la moindre augmentation des performances des processeurs CPU au cours des dernières années par rapport à la croissance considérable de celles des processeurs graphiques, ou GPU (Graphics Processing Unit), nous avons choisi la technique de parallélisation GPU. L'environnement de programmation utilisé est CUDA (Compute Unified Device Architecture) qui permet aux cartes graphiques de type NVIDIA d'exécuter des programmes écrits en C, C ++, FORTRAN et plusieurs autres langages de programmation.

Concernant les développements nouveaux réalisés au cours de cette thèse, les méthodes et les algorithmes implémentés sont les suivants :

Pour la partie solide (DEM) :
L'algorithme de recherche des particules voisines (liste de Verlet) a été modifié par la technique de quadrillage régulier de l'espace. Ensuite, nous avons amélioré le stockage de la matrice des liens cohésifs entre les particules dans la mémoire globale de la carte à l'aide d'un algorithme de décomposition « Compressed sparse column (CSC) ».

Pour la partie fluide (LBM) :
La méthode PSM (Partially saturated method) proposée par Noble and Torczynski (1998) pour l'interaction solide-fluide a été implémentée et validée. Cette méthode

a l'avantage d'éviter toute interpolation au niveau de la condition de non-glissement entre fluide et parois solides. Elle réduit ainsi fortement l'utilisation de la mémoire GPU et augmente en retour les performances du calcul parallèle.

La vitesse de calcul obtenue en couplant ces deux méthodes est environ 90 fois plus rapide par rapport à l'ancienne version du code en simple précision. Nous avons effectué la validation du code LBM-DEM parallélisé à l'aide de deux benchmarks : la sédimentation d'une particule unique et la sédimentation de deux particules lâchées l'une au-dessus de l'autre et induisant un scénario DKT (drafting, kissing, tumbling). Nous avons obtenu un très bon accord entre nos résultats numériques et ceux de la littérature.

Les outils numériques ainsi développés et validés sont ensuite appliqués à deux configurations d'essais d'érosion, le Jet Erosion Test (JET) et l'érosion par écoulement tangentiel cisaillant de type Couette. Les hautes performances du code parallélisé ont permis d'étudier de manière systématique ces deux processus complexes en faisant varier de nombreux paramètres géo-mécaniques et fluides du modèle.

B.4 Erosion par jet impactant

Notre étude paramétrique de l'érosion par un jet impactant s'est intéressée au cas des sols cohésifs et non cohésifs, en se concentrant plus particulièrement sur le seuil d'érosion puis sur la cinétique d'affouillement.

Dans un premier temps, nous avons étudié et validé l'écoulement d'un jet libre laminaire bidimensionnel en s'appuyant sur la théorie du jet libre auto-similaire proposée par Bickley (1937); Schlichting (1960). En particulier, la vitesse longitudinale maximale suit quasi-parfaitement la prédiction théorique après ajout d'une origine virtuelle pour laquelle une relation empirique réaliste a été proposée. Ensuite, à partir d'un jet impactant soit une paroi lisse, soit une surface granulaire fixe, nous avons obtenu une formule empirique qui exprime la contrainte de cisaillement fluide maximale au niveau de la surface d'impact à l'aide du modèle auto-similaire de jet libre en régime laminaire et géométrie bidimensionnelle (Eq. 3.5). L'expression introduit notamment un coefficient de frottement de type Blasius qui est inversement proportionnel à la racine carrée du nombre de Reynolds du jet.

Dans un second temps, la partie de la modélisation de la phase solide discrète basée sur la DEM standard a été entièrement activée afin de simuler l'érosion par jet d'une couche de sol sans cohésion. Les résultats sont tracés dans le diagramme de Shields et comparés favorablement à des résultats expérimentaux antérieurs, notamment ceux de Badr et al. (2014), en utilisant une expression inertielle simplifiée pour le nombre de Shields Sh_u^* et le nombre de Reynolds particulaire Re_p^*. Pour aller plus loin, nos résultats numériques et ceux expérimentaux de Badr et al. (2014), ré-analysés pour l'occasion grâce à l'expression précédente de la contrainte de cisaillement maximale (Eq. 3.5), ont pu être reportés cette fois dans le diagramme classique de Shields avec formulation complète du nombre de Shields Sh_τ^* et utilisation du nombre de Reynolds Re_τ^* déduit directement de la contrainte de cisaillement. La comparaison entre simulation et expérience reste satisfaisante et l'accord avec la

courbe empirique de Shields, ou sa formulation explicite proposée par (Guo, 1997), est correct. Ensuite, le modèle de liens cohésifs a été ajouté dans al calcul DEM pour mener une démarche similaire dans le cas de sols granulaires cohésifs. Pour cela, le seuil d'érosion défini par les premières ruptures de ponts cohésifs et l'entrainement de grains, a été mesuré pour différentes tailles de particules et plusieurs valeurs de viscosité du fluide. Ces valeurs ne peuvent pas être décrites par le critère de Shields classique qui ne tient compte que du poids déjaugé et du frottement solide mais peuvent l'être de façon convaincante par une extension de celui-ci au cas de matériaux faiblement cohésifs. Plus précisément, l'expression que nous proposons (Eq. 3.8) tient compte de la contribution additionnelle des liens cohésifs à la résistance à l'érosion qui, par analyse dimensionnelle, est introduite dans un nombre de Shields généralisé Sh^*_{coh} par l'intermédiaire du nombre de Bond granulaire qui compare cohésion et poids déjaugé.

Cette étude a été finalement poursuivie par une analyse du processus de formation d'un cratère par jet impactant pour une version numérique bidimensionnelle de l'essai JET usuel. Par une méthode d'analyse d'images en post-traitement des simulations, un suivi de l'évolution de la profondeur du cratère (directement reliée au taux d'érosion) en fonction de la contrainte de cisaillement fluide maximale à la surface du lit granulaire a été obtenu. En adaptant le modèle d'interprétation mathématique de l'essai JET à notre cas spécifique bidimensionnel et laminaire et en élargissant le modèle à des lois d'érosion plus générales présentant un exposant n en plus des paramètres d'érodibilité standard, nous sommes parvenus à déduire implicitement les paramètres d'érodibilité des sols à l'échelle macro (c'est-à-dire l'exposant n, le coefficient d'érosion k_d et la contrainte de cisaillement fluide critique τ_c) pour différentes intensités de cohésion inter-particulaire C à l'échelle micro. Le résultat final s'est cependant révélé peu satisfaisant puisque, comparativement à l'évaluation directe du seuil d'érosion et à la prédiction précédente basée sur le critère de Shields généralisé, la contrainte critique τ_c trouvée ici est sur-estimée à cohésion faible et sous-estimée à cohésion plus forte. Par ailleurs, une dépendance est observée avec la vitesse de jet, surtout pout τ_c mais aussi pour k_d, remettant en cause le caractère intrinsèque des paramètres d'érodibilité ou, dans un premier temps, certaines des hypothèses parfois très simplificatrices du modèle d'interprétation, notamment le fait de ne pas considérer l'évolution de la topographie, qui passe progressivement d'un plan à un cratère de rapport d'aspect élevé, ou la présence d'une couche granulaire « protectrice » au-dessus de la matrice cohésive pour les faibles valeurs de C.

B.5 Erosion par écoulement de type Couette

Partant des limitations de la configuration précédente, la dernière partie de cette thèse présente une autre configuration d'érosion qui consiste à appliquer de façon uniforme et stationnaire un écoulement fluide en cisaillement à la surface supérieure d'un échantillon granulaire cohésif. Cette configuration d'écoulement, appelée aussi cisaillement de Couette, s'affranchit de certaines complexités inhérentes au JET,

notamment la recirculation de l'écoulement fluide une fois le cratère formé. Moyennant un choix raisonnable pour déterminer un critère objectif d'érosion d'un grain que l'on fait ensuite disparaître du calcul numérique, il est possible de maintenir tout au long du processus une surface approximativement plane au sommet du lit granulaire et de mesurer le taux d'érosion $\dot{\epsilon}$ à partir de la pente entre l'épaisseur du lit et le temps alors que la contrainte de cisaillement fluide appliquée τ est maintenue constante.

Grâce à cette configuration, il est possible de tracer directement, à l'échelle de l'échantillon homogène de sol, le taux d'érosion $\dot{\epsilon}$ en fonction de la contrainte de cisaillement τ sans recourir à aucune hypothèse a priori ou postulat quant à la loi d'érosion adaptée. Une dernière difficulté a dû être levée cependant car, pour les faibles contraintes fluides, l'échantillon de sol se trouvait dégradé mais pas érodé. En réalité, cela s'explique par la formation d'une fracture en profondeur dès le début de la simulation. Pour pallier à cela, nous avons utilisé ici la version complète de notre modèle dans laquelle la loi de contact cohésif est enrichie par un endommagement qui inhibe de ce fait la formation rapide d'une fracture au profit d'une érosion répartie en surface. A partir de là, une étude systématique a été menée et la meilleure loi empirique permettant de relier le taux d'érosion $\dot{\epsilon}$ à la contrainte de cisaillement τ s'est révélée être une loi de puissance, similaire à la loi linéaire usuelle mais avec un exposant n pouvant être différent de 1 et ainsi un meilleur degré d'ajustement. Par ailleurs, nous avons cherché à tester la pertinence du choix de la contrainte de cisaillement τ comme unique grandeur de contrôle de l'érosion. Ce choix apparaît justifié à condition que le nombre de Reynolds soit suffisamment élevé mais il y a en revanche une érosion moindre à valeur de τ maintenue égale quand le nombre de Reynolds de l'écoulement devient trop petit.

Enfin, une dernière étude paramétrique nous a permis d'analyser la relation entre l'érodibilité du sol à l'échelle d'un échantillon homogène et ses propriétés micromécaniques (force de cohésion, taille des particules). De façon assez logique, l'exposant n de la loi empirique proposée ainsi que la contrainte critique τ_c augmentent avec la force de cohésion entre les grains C, et le coefficient d'érosion k_d à l'inverse diminue. Certaines incohérences apparaissent cependant, notamment quant à la contrainte critique τ_c dont les valeurs déduites de la régression par la loi d'érosion ne coïncident pas avec le seuil tiré du nombre de Shields généralisé Sh^*_{coh}. Empiriquement, une expression modifiée de Sh^*_{coh} peut être proposée sans que cela ne soit satisfaisant physiquement. Des approfondissements sont clairement nécessaires pour mieux appréhender cette difficulté et la présente configuration d'écoulement de type Couette semble particulièrement bien adaptée pour mener les investigations systématiques attendues.

B.6 Perspectives

Au sortir de ce travail de thèse, plusieurs perspectives de recherche peuvent être évoquées ainsi qu'un certain nombre de problèmes restant ouverts. Parmi ceux-ci, on peut distinguer des aspects spécifiquement numériques et des questionnements

plus fondamentaux sur l'état actuel des connaissances et les verrous scientifiques non encore résolus quant à notre compréhension physique de l'érosion des sols cohésifs par action hydrodynamique et à sa modélisation.

Au sujet de l'outil numérique développé et déployé au cours de ce travail, plusieurs améliorations potentielles sont envisageables. Tout d'abord, bien que la vitesse de calcul ait déjà été très significativement augmentée par l'utilisation des GPU, il reste encore une marge de progression, particulièrement sur la partie LBM qui est la plus consommatrice en temps de simulation. Ainsi, il serait possible de supprimer le recours à la mémoire globale pour n'utiliser que la mémoire partagée des GPU dont l'accès est nettement plus rapide. Par ailleurs, notre code LBM-DEM actuel est bidimensionnel et les résultats de simulation qu'il produit s'avèrent, de ce fait, difficiles à comparer quantitativement à des observations expérimentales réalistes. Cependant, une extension en 3D du modèle est tout à fait envisageable mais requiert en retour des ressources mémoire en très fort augmentation, particulièrement pour le calcul LBM où, selon les schémas mis en œuvre (D3Q15 ou D3Q19), 15 ou 19 vecteurs vitesses de réseau sont nécessaires à chaque nœud. Des approches multi-GPU avec décomposition de domaine devront très vraisemblablement être envisagées puisque la mémoire GPU reste assez limitée en volume. Une version tridimensionnelle de ce type de code, même couteuse en temps de calcul, permettrait de simuler de façon beaucoup plus réaliste diverses applications en géotechnique.

D'un point de vue plus physique, plusieurs questions importantes demeurent comme autant de voies pour de futures investigations. Dans un premier temps, et en se restreignant à la configuration du jet impactant, des travaux pourraient être engagés sur la distribution des efforts hydrodynamiques à la surface d'une surface non plus plane mais présentant une forme de cratère réaliste, afin de proposer une estimation plus pertinente de la contrainte appliquée en cours d'affouillement, si possible encore basée sur le modèle de jet libre auto-similaire. Il serait ainsi possible d'améliorer significativement le modèle d'interprétation de l'essai JET, dont on a pu voir les limitations au cours de ce travail, et accéder alors à une évaluation plus fiable de la résistance à l'érosion. Cela a déjà été amorcé à travers l'extension à un jet axisymétrique réel de l'expression obtenue en 2D pour la contrainte maximale avec une validation expérimentale assez convaincante pour notre proposition d'un nombre de Shields généralisé (Brunier-Coulin et al., 2019).

L'analyse de l'érosion par écoulement de Couette n'a pas été totalement satisfaisante et des efforts importants restent à faire pour mieux comprendre les mécanismes physiques sous-jacents de l'érosion d'un sol cohésif à petite échelle. Le point de départ pourrait logiquement se baser sur cette configuration épurée et bien contrôlée en poursuivant l'analyse systématique déjà engagée ici, par variation de plusieurs paramètres physiques comme la taille des particules, leur densité ou la gravité, mais aussi, de façon encore plus intéressante, en explorant plus largement le modèle de cohésion utilisé, et notamment en modifiant indépendamment les 3 seuils de rupture locaux des ponts solides entre grains, afin d'accéder des comportements de sols dans une gamme beaucoup plus large et, potentiellement, plus réaliste. En cela, l'analyse micro-mécanique amorcée à la section 4.3.4 est une approche prometteuse et pourrait être poursuivie.

Une question aussi se pose quant à la relation existant entre les paramètres microscopiques et les grandeurs mesurées à plus grande échelle. Ces dernières englobent l'éridibilité, évoquée dans ce travail, mais aussi d'autres types de résistances mécaniques fortement contrôlées par la cohésion interne du matériau. Pour cela, et comme présenté à l'Annexe A, un travail a été initié pour simuler à l'échelle d'un échantillon de sol des tests mécaniques, notamment en traction et cisaillement direct afin d'étudier le passage micro-macro et de valider la pertinence de la formule théorique de Rumpf (Pierrat and Caram, 1997). Il est important de souligner que, parallèlement à l'approche numérique, des expériences sont également menées sur ce point dans notre équipe de recherche et seront poursuivies. Celles-ci s'appuient sur l'utilisation de matériaux cohésifs artificiels, constitués de grains collées entre eux par des ponts solides (résine, paraffine), et de différents dispositifs expérimentaux permettant de réaliser des tests de traction à une échelle macroscopique mais aussi directement à l'échelle du contact entre deux grains.

Finalement, pour conclure sur ces diverses perspectives, il est bon de noter que l'étude de plusieurs autres situations de couplage fluide-grains en condition immergée à l'aide de notre code LBM-DEM a déjà été amorcée ou le sera très prochainement. C'est ainsi le cas de la modélisation de l'apparition de fontis dans une couche superficielle de sol en contexte karstique, travail mené depuis plusieurs années en collaboration avec le BRGM (Luu et al., 2019). De premiers résultats préliminaires ont aussi été obtenus pour modéliser l'installation d'une fondation off-shore dans un sol sous-marin (Benseghier et al., 2019). Enfin, notre code sera utilisé et amélioré au cours du projet COMET, en démarrage effectif à l'automne 2019, qui s'intéresse spécifiquement à deux applications géotechniques : l'érosion et la fluidisation superficielle lors de l'installation d'une fondation off-shore par succion ; l'érosion localisée dans le sol stratifié d'un structure hydraulique.

Bibliography

Aboul Hosn, R., L. Sibille, N. Benahmed, and B. Chareyre (2018). A discrete numerical model involving partial fluid-solid coupling to describe suffusion effects in soils. *Computers and Geotechnics 95*, 30–39.

Ai, J., J.-F. Chen, J. M. Rotter, and J. Y. Ooi (2011). Assessment of rolling resistance models in discrete element simulations. *Powder Technology 206*(3), 269 – 282.

Albertson, M. L., Y. B. Dai, R. A. Jensen, and H. Rouse (1950). Diffusion of Submerged Jets. *Trans. ASCE 115*, 639–697.

Anand, A., J. S. Curtis, C. R. Wassgren, B. C. Hancock, and W. R. Ketterhagen (2009). Predicting discharge dynamics of wet cohesive particles from a rectangular hopper using the discrete element method (DEM). *Chemical Engineering Science 64*(24), 5268–5275.

Andrade, E. N. C. (1939). The velocity distribution in a liquid-into-liquid jet. Part 2: The plane jet. *Proceedings of the Physical Society 51*(5), 784–793.

Andrade, E. N. D. A. C. and L. C. Tsien (1937). The velocity-distribution in a liquid-into-liquid jet. *Proceedings of the Physical Society 49*(4), 381.

Andreotti, B., Y. Forterre, and O. Pouliquen (2013). *Granular Media: Between Fluid and Solid*. Cambridge University Press.

Badr, S. (2014). *Erosion of a granular bed by jet*. Theses, Université Paris Sud - Paris XI.

Badr, S., G. Gauthier, and P. Gondret (2014). Erosion threshold of a liquid immersed granular bed by an impinging plane liquid jet. *Physics of Fluids 26*(2), 23302.

Beguin, R., P. Philippe, and Y. H. Faure (2013). Pore-scale flow measurements at the interface between a sandy layer and a model porous medium: Application to statistical modeling of contact erosion. *Journal of Hydraulic Engineering 139*(1), 1–11.

Beltaos, S. and N. Rajaratnam (1973). Plane turbulent impinging jets. *Journal of Hydraulic Research 11*(1), 29–59.

Beltaos, S. and N. Rajaratnam (1974). Impinging Circular Turbulent Jets. *ASCE J Hydraul Div 100*(10), 1313–1328.

Beltaos, S. and N. Rajaratnam (1977). Impingement of axisymmetric developing jets. *Journal of Hydraulic Research 15*(4), 311–326.

Benahmed, N. and S. Bonelli (2012). Investigating concentrated leak erosion behaviour of cohesive soils by performing hole erosion tests. *European Journal of Environmental and Civil Engineering 16*(1), 43–58.

Bennett, S. J. and C. V. Alonso (2005). Kinematics of flow within headcut scour holes on hillslopes. *Water Resources Research 41*(9), 1–12.

Benseghier, Z., P. Cuéllar, L.-H. Luu, S. Bonelli, and P. Philippe (2019). A parallel GPU-based computational framework for the micromechanical analysis of geotechnical and erosion problems. *Computers and Geotechnics (submitted).*

Benseghier, Z., P. Cuéllar, L.-H. Luu, J.-Y. Delenne, S. Bonelli, and P. Philippe (2020). Relevance of free jet model for soil erosion by impinging jets. *Journal of Hydraulic Engineering 146*(1), 04019047.

Bhatnagar, P. L., E. P. Gross, and M. Krook (1954). A model for collision processes in gases. I. Small amplitude processes in charged and neutral one-component systems. *Physical Review 94*(3), 511–525.

Bickley, W. G. (1937). The plane jet. *The London, Edinburgh, and Dublin Philosophical Magazine and Journal of Science 23*, 727–731.

Black, K. S., T. J. Tolhurst, D. M. Paterson, and S. E. Hagerthey (2002). Working with natural cohesive sediments. *Journal of Hydraulic Engineering 128*(1), 2.

Blaisdell, F. W., C. L. Anderson, and G. G. Hebaus (1981). Ultimate Dimensions Of Local Scour. *Journal of the Hydraulics Division-ASCE 107*(3), 327–337.

Bonelli, S. and N. Benahmed (2011). Piping flow erosion in water retaining structures. *International Journal on Hydropower and Dams 18*(3), 94–98.

Bonelli, S. and O. Brivois (2008). The scaling law in the hole erosion test with a constant pressure drop. *International Journal for Numerical and Analytical Methods in Geomechanics 32*(13), 1573–1595.

Bonelli, S., O. Brivois, R. Borghi, and N. Benahmed (2006). On the modelling of piping erosion. *Comptes Rendus - Mecanique 334*(8-9), 555–559.

Bonelli, S. and D. Marot (2011). Micromechanical modeling of internal erosion. *European Journal of Environmental and Civil Engineering 15*(8), 1207–1224.

Boutt, D. F., B. K. Cook, B. J. McPherson, and J. R. Williams (2007). Direct simulation of fluid-solid mechanics in porous media using the discrete element and lattice-Boltzmann methods. *Journal of Geophysical Research: Solid Earth 112*(10).

Bouzidi, M., M. Firdaouss, and P. Lallemand (2001). Momentum transfer of a Boltzmann-lattice fluid with boundaries. *Physics of Fluids 13*(11), 3452–3459.

Briaud, J. L., F. C. Ting, H. C. Chen, Y. Cao, S. W. Han, and K. W. Kwak (2001). Erosion function apparatus for scour rate predictions. *Journal of Geotechnical and Geoenvironmental Engineering 127*(2), 105–113.

Brunier-Coulin, F. (2016). *Etude des mécanismes élémentaires de l'érosion d'un sol cohésif.* Theses, Aix Marseille Université.

Brunier-Coulin, F., P. Cuéllar, and P. Philippe (2017). Erosion onset of a cohesionless granular medium by an immersed impinging round jet. *Physical Review Fluids 2*(3), 34302.

Brunier-Coulin, F., P. Cuéllar, and P. Philippe (2019). Generalized Shields criterion for weakly cohesive granular materials. *Phys. Rev. Fluids (submitted).*

Brunier-Coulin, F., J. L. Sarrat, P. Cuéllar, and P. Philippe (2017). Experimental investigation of impinging jet erosion on model cohesive granular materials. In *EPJ Web of Conferences*, Volume 140, Montpellier, France, pp. 8002. EPJ Web of Conferences 140.

Buffington, J. M. (1999). The legend of A. F. Shields. *Journal of Hydraulic Engineering 125*(4), 376–387.

Castellanos, A. (2005). The relationship between attractive interparticle forces and bulk behaviour in dry and uncharged fine powders. *Advances in Physics 54*(4), 263–276.

Catalano, E. (2012). *A pore-scale coupled hydromechanical model for biphasic granular media.* Theses, Université de Grenoble.

Catalano, E., B. Chareyre, and E. Barthélémy (2014). Pore-scale modeling of fluid-particles interaction and emerging poromechanical effects. *International Journal for Numerical and Analytical Methods in Geomechanics 38*(1), 51–71.

Chareyre, B., A. Cortis, E. Catalano, and E. Barthélemy (2012). Pore-Scale Modeling of Viscous Flow and Induced Forces in Dense Sphere Packings. *Transport in Porous Media 94*(2), 595–615.

Chen, D., Y. Wang, B. Melville, H. Huang, and W. Zhang (2018). Unified formula for critical shear stress for erosion of sand, mud, and sand-mud mixtures. *Journal of Hydraulic Engineering 144*(8), 4018046.

Chen, S., H. Chen, D. Martnez, and W. Matthaeus (1991). Lattice Boltzmann model for simulation of magnetohydrodynamics. *Phys. Rev. Lett. 67*(27), 3776–3779.

Chen, S., D. Martínez, and R. Mei (1996). On boundary conditions in lattice Boltzmann methods. *Physics of Fluids 8*(9), 2527–2536.

Claudin, P. and B. Andreotti (2006). A scaling law for aeolian dunes on Mars, Venus, Earth, and for subaqueous ripples. *Earth and Planetary Science Letters 252*(1-2), 30–44.

Coleman, S. E. and V. I. Nikora (2008). A unifying framework for particle entrainment. *Water Resources Research 44*(4).

Cook, B. K., D. R. Noble, and J. R. Williams (2004). A direct simulation method for particle-fluid systems. *Engineering Computations (Swansea, Wales) 21*(2-4), 151–168.

Cuéllar, P., Z. Benseghier, L. H. Luu, S. Bonelli, J. Y. Delenne, F. Radjaï, and P. Philippe (2017). Numerical insight into the micromechanics of jet erosion of a cohesive granular material. *EPJ Web of Conferences 140*, 15017.

Cuéllar, P., P. Philippe, S. Bonelli, N. Benahmed, F. Brunier-Coulins, J. Ngoma, J. Y. Delenne, and F. Radjai (2015). Micromechanical analysis of the surface erosion of a cohesive soil by means of a coupled LBM-DEM Model. *Proceedings of the 4th International Conference on Particle-Based Methods - Fundamentals and Applications, PARTICLES 2015*, 519–528.

Cui, X., J. Li, A. Chan, and D. Chapman (2012). A 2D DEM-LBM study on soil behaviour due to locally injected fluid. *Particuology 10*(2), 242–252.

Cui, X., J. Li, A. Chan, and D. Chapman (2014). Coupled DEM-LBM simulation of internal fluidisation induced by a leaking pipe. *Powder Technology 254*, 299–306.

Cundall, P. A. and O. D. Strack (1979). A discrete numerical model for granular assemblies. *Geotechnique 29*(1), 47–65.

Daly, E. R., G. A. Fox, A. S. T. Al-Madhhachi, and D. E. Storm (2015). Variability of fluvial erodibility parameters for streambanks on a watershed scale. *Geomorphology 231*, 281–291.

Daly, E. R., G. A. Fox, A. T. Al-Madhhachi, and R. B. Miller (2013). A scour depth approach for deriving erodibility parameters from jet erosion tests. *Transactions of the ASABE 56*(6), 1343–1351.

Delenne, J. Y. (2002). *Granular media with solid behaviour - Modelling, experimental analysis of the cohesion, validation and applications.* Theses, Université Montpellier II - Sciences et Techniques du Languedoc.

Delenne, J. Y., M. S. El Youssoufi, F. Cherblanc, and J. C. Bénet (2004). Mechanical behaviour and failure of cohesive granular materials. *International Journal for Numerical and Analytical Methods in Geomechanics 28*(15), 1577–1594.

Derjaguin, B. V., V. M. Muller, and Y. Toporov (1994). Effect of contact deformations on the adhesion of particles. *Progress in Surface Science 45*(1), 131–143.

Derksen, J. J. (2011). Simulations of granular bed erosion due to laminar shear flow near the critical Shields number. *Physics of Fluids 23*(11), 113303.

Fell, R. and J.-J. Fry (2007). *Internal erosion of dams and their foundations*. London: Taylor & Francis.

Feng, Z. G. and E. E. Michaelides (2004). The immersed boundary-lattice Boltzmann method for solving fluid-particles interaction problems. *Journal of Computational Physics 195*(2), 602–628.

Fornberg, B. (1980). A numerical study of steady viscous flow past a circular cylinder. *Journal of Fluid Mechanics 98*(4), 819–855.

Foster, G. R. (1982). Modeling the erosion process. *Hydrologic modeling of small watersheds*, 295–380.

Foster, G. R. and L. D. Meyer (1972). Transport of Soil Particles By Shallow Flow. *Transactions of the American Society of Agricultural Engineers 15*(1), 99–102.

Foster, M., R. Fell, and M. Spannagle (2000). The statistics of embankment dam failures and accidents. *Canadian Geotechnical Journal 37*(5), 1000–1024.

Frisch, U., B. Hasslacher, and Y. Pomeau (1986). Lattice-gas automata for the Navier-Stokes equation. *Physical Review Letters 56*(14), 1505–1508.

Ghaneeizad, S. M., J. F. Atkinson, and S. J. Bennett (2014). Effect of flow confinement on the hydrodynamics of circular impinging jets: implications for erosion assessment. *Environmental Fluid Mechanics 15*(1), 1–25.

Gilabert, F. A., J. N. Roux, and A. Castellanos (2007). Computer simulation of model cohesive powders: Influence of assembling procedure and contact laws on low consolidation states. *Physical Review E - Statistical, Nonlinear, and Soft Matter Physics 75*(1), 11303.

Ginzburg, I., D. D'Humières, and A. Kuzmin (2010). Optimal stability of advection-diffusion lattice boltzmann models with two relaxation times for positive/negative equilibrium. *Journal of Statistical Physics 139*(6), 1090–1143.

Ginzburg, I., F. Verhaeghe, and D. D'Humières (2008). Study of simple hydrodynamic solutions with the two-relaxation-times lattice Boltzmann scheme. *Communications in Computational Physics 3*(3), 519–581.

Grabowski, R. C., I. G. Droppo, and G. Wharton (2011). Erodibility of cohesive sediment: The importance of sediment properties. *Earth-Science Reviews 105*(3-4), 101–120.

Guo, J. (1997). Discussion of the albert shields story by junke guo. *Journal of Hydraulic Engineering 123*(7), 666–666.

Guo, J. (2002). Hunter Rouse and Shields Diagram. In *Advances in Hydraulics and Water Engineering: Volumes I & II*, pp. 1096–1098. World Scientific.

Han, K., Y. T. Feng, and D. R. Owen (2007). Coupled lattice Boltzmann and discrete element modelling of fluid-particle interaction problems. *Computers and Structures 85*(11-14), 1080–1088.

Han, Y. and P. A. Cundall (2013). LBM-DEM modeling of fluid-solid interaction in porous media. *International Journal for Numerical and Analytical Methods in Geomechanics 37*(10), 1391–1407.

Hanson, G. J. and K. R. Cook (1997). Development of excess shear stress parameters for circular jet testing. *Paper - American Society of Agricultural Engineers 2*.

Hanson, G. J. and K. R. Cook (2004). Apparatus, test procedures, and analytical methods to measure soil erodibility in situ. *Applied Engineering in Agriculture 20*(4), 455–462.

Hanson, G. J., K. M. Robinson, and D. M. Temple (1990). Pressure and stress distributions due to a submerged impinging jet. In *Hydraulic Engineering - Proceedings of the 1990 National Conference*, pp. 525–530. ASCE.

Hanson, G. J. and A. Simon (2001). Erodibility of cohesive streambeds in the loess area of the Midwestern USA. *Hydrological Processes 15*(1), 23–38.

Hardy, J., Y. Pomeau, and O. De Pazzis (1973). Time evolution of a two-dimensional classical lattice system. *Physical Review Letters 31*(5), 276–279.

Higuera, F. J. and J. Jiménez (1989). Boltzmann Approach to Lattice Gas Simulations. *Europhysics Letters (EPL) 9*(7), 663–668.

Jacobs, W., P. L. Hir, W. V. Kesteren, and P. Cann (2011). Erosion threshold of sand–mud mixtures. *Continental Shelf Research 31*(10, Supplement), S14 – S25. Proceedings of the 9th International Conference on Nearshore and Estuarine Cohesive Sediment Transport Processes.

Jambunathan, K., E. Lai, M. A. Moss, and B. L. Button (1992). A review of heat transfer data for single circular jet impingement.

Johnson, K. L., K. Kendall, and A. D. Roberts (1971). Surface Energy and the Contact of Elastic Solids. *Proceedings of the Royal Society A: Mathematical, Physical and Engineering Sciences 324*(1558), 301–313.

Julian, J. P. and R. Torres (2006). Hydraulic erosion of cohesive riverbanks. *Geomorphology 76*(1-2), 193–206.

Karamigolbaghi, M., S. M. Ghaneeizad, J. F. Atkinson, S. J. Bennett, and R. R. Wells (2017). Critical assessment of jet erosion test methodologies for cohesive soil and sediment. *Geomorphology 295*, 529–536.

Karmaker, T. and S. Dutta (2011). Erodibility of fine soil from the composite river bank of Brahmaputra in India. *Hydrological Processes 25*(1), 104–111.

Khanal, A., K. R. Klavon, G. A. Fox, and E. R. Daly (2016). Comparison of linear and nonlinear models for cohesive sediment detachment: Rill erosion, hole erosion test, and streambank erosion studies. *Journal of Hydraulic Engineering 142*(9).

Kimiaghalam, N., S. P. Clark, and H. Ahmari (2014). An experimental study on the effects of physical, mechanical, and electrochemical properties of natural cohesive soils on critical shear stress and erosion rate. *International Journal of Sediment Research 31*(1), 1–15.

Knapen, A., J. Poesen, G. Govers, G. Gyssels, and J. Nachtergaele (2007). Resistance of soils to concentrated flow erosion: A review. *Earth-Science Reviews 80*(1-2), 75–109.

Koelman, J. M. V. A. (1991). A simple lattice boltzmann scheme for navier-stokes fluid flow. *Europhysics Letters (EPL) 15*(6), 603–607.

Konsoer, K. M., B. L. Rhoads, E. J. Langendoen, J. L. Best, M. E. Ursic, J. D. Abad, and M. H. Garcia (2016). Spatial variability in bank resistance to erosion on a large meandering, mixed bedrock-alluvial river. *Geomorphology 252*(SI), 80–97.

Kuang, S. B., C. Q. LaMarche, J. S. Curtis, and A. B. Yu (2013). Discrete particle simulation of jet-induced cratering of a granular bed. *Powder Technology 239*, 319–336.

Lachouette, D., F. Golay, and S. Bonelli (2008). One-dimensional modeling of piping flow erosion. *Comptes Rendus - Mecanique 336*(9), 731–736.

Ladd, A. J. (1994). Numerical Simulations of Particulate Suspensions Via a Discretized Boltzmann Equation. Part 1. Theoretical Foundation. *Journal of Fluid Mechanics 271*, 285–309.

Lallemand, P. and L. S. Luo (2000). Theory of the lattice Boltzmann method: Dispersion, dissipation, isotropy, Galilean invariance, and stability. *Physical Review E - Statistical Physics, Plasmas, Fluids, and Related Interdisciplinary Topics 61*(6), 6546–6562.

Lallemand, P. and L. S. Luo (2003). Lattice Boltzmann method for moving boundaries. *Journal of Computational Physics 184*(2), 406–421.

Latt, J., B. Chopard, O. Malaspinas, M. Deville, and A. Michler (2008). Straight velocity boundaries in the lattice Boltzmann method. *Physical Review E - Statistical, Nonlinear, and Soft Matter Physics 77*(5), 56703.

Layzell, A. L. and R. D. Mandel (2014). An assessment of the erodibility of Holocene lithounits comprising streambanks in northeastern Kansas, USA. *Geomorphology 213*, 116–127.

Lominé, F., L. Scholtès, L. Sibille, and P. Poullain (2013). Modeling of fluid-solid interaction in granular media with coupled lattice Boltzmann/discrete element methods: Application to piping erosion. *International Journal for Numerical and Analytical Methods in Geomechanics 37*(6), 577–596.

Looney, M. K. and J. J. Walsh (1984). Mean-flow and turbulent characteristics of free and impinging jet flows. *Journal of Fluid Mechanics 147*(7), 397–429.

Lu, N. and W. J. Likos (2013). *Origin of cohesion and its dependence on saturation for granular media*, pp. 1669–1675.

Luu, L.-H., G. Noury, Z. Benseghier, and P. Philippe (2019). Hydro-mechanical modeling of sinkhole occurrence processes in covered karst terrains during a flood. *Engineering Geology 260*, 105249.

Mansouri, M., M. S. El Youssoufi, and F. Nicot (2017). Numerical simulation of the quicksand phenomenon by a 3D coupled Discrete Element - Lattice Boltzmann hydromechanical model. *International Journal for Numerical and Analytical Methods in Geomechanics 41*(3), 338–358.

Marot, D., P. Regazzoni, and T. Wahl (2012). Energy-based method for providing soil surface erodibility rankings. *Journal of Geotechnical and Geoenvironmental Engineering 137*(12), 1290–1293.

Martin, H. (1977). Heat and Mass Transfer between Impinging Gas Jets and Solid Surfaces. *Advances in Heat Transfer 13*(C), 1–60.

McNamara, G. R. and G. Zanetti (1988). Use of the boltzmann equation to simulate lattice-gas automata. *Physical Review Letters 61*(20), 2332–2335.

Mei, R., D. Yu, W. Shyy, and L. S. Luo (2002). Force evaluation in the lattice Boltzmann method involving curved geometry. *Physical Review E - Statistical Physics, Plasmas, Fluids, and Related Interdisciplinary Topics 65*(4), 14.

Mercier, F. (2013). *Modélisation numérique de l'érosion d'un sol cohésif par un écoulement turbulent.* Theses, Aix Marseille Université.

Mercier, F., F. Golay, S. Bonelli, F. Anselmet, R. Borghi, and P. Philippe (2014). 2D axisymmetrical numerical modelling of the erosion of a cohesive soil by a submerged turbulent impinging jet. *European Journal of Mechanics, B/Fluids 45*, 36–50.

Montellà, E. P., M. Toraldo, B. Chareyre, and L. Sibille (2016). Localized fluidization in granular materials: Theoretical and numerical study. *Physical Review E 94*(5), 52905.

Mutabaruka, P., J. Y. Delenne, K. Soga, and F. Radjai (2014). Initiation of immersed granular avalanches. *Physical Review E - Statistical, Nonlinear, and Soft Matter Physics 89*(5), 52203.

Nearing, M. A. (1991). Probabilistic model of soil detachment by shallow turbulent flow. *Transactions of the American Society of Agricultural Engineers 34*(1), 81–85.

Ngoma, J. (2015). *Numerical and experimental study of the destabilization of a submerged granular bed by fluidization.* Theses, Aix Marseille Université.

Ngoma, J., P. Philippe, S. Bonelli, F. Radjaï, and J. Y. Delenne (2018). Two-dimensional numerical simulation of chimney fluidization in a granular medium using a combination of discrete element and lattice Boltzmann methods. *Physical Review E 97*(5), 52902.

Nguyen, V.-N., J.-R. Courivaud, P. Pinettes, H. Souli, and J.-M. Fleureau (2017). Using an Improved Jet-Erosion Test to Study the Influence of Soil Parameters on the Erosion of a Silty Soil. *Journal of Hydraulic Engineering 143*(8), 4017018.

Noble, D. R. and J. R. Torczynski (1998). A lattice-boltzmann method for partially saturated computational cells. *International Journal of Modern Physics C 9*(8), 1189–1201.

Obrecht, C., F. Kuznik, B. Tourancheau, and J. J. Roux (2013). Multi-GPU implementation of the lattice Boltzmann method. *Computers and Mathematics with Applications 65*(2), 252–261.

Papamichos, E. and I. Vardoulakis (2005). Sand erosion with a porosity diffusion law. *Computers and Geotechnics 32*(1), 47–58.

Parchure, T. M. and A. J. Mehta (1985). Erosion of soft cohesive sediment deposits. *Journal of Hydraulic Engineering 111*(10), 1308–1326.

Partheniades, E. (1965). Erosion and Deposition of Cohesive Soils. *Journal of the Hydraulics Division 91*(1), 105–139.

Phares, D. J., G. T. Smedley, and R. C. Flagan (2000). The wall shear stress produced by the normal impingement of a jet on a flat surface. *Journal of Fluid Mechanics 418*, 351–375.

Philippe, P., P. Cuéllar, F. Brunier-Coulin, L. H. Luu, N. Benahmed, S. Bonelli, and J. Y. Delenne (2017). Physics of soil erosion at the microscale. *EPJ Web of Conferences 140*, 8014.

Pierrat, P. and H. S. Caram (1997). Tensile strength of wet granular materials. *Powder Technology 91*(2), 83–93.

Poreh, M., Y. G. Tsuei, and J. E. Cermak (1964). Investigation of a turbulent radial wall jet. *Journal of Applied Mechanics, Transactions ASME 34*(2), 457–463.

Potapov, A. V., M. L. Hunt, and C. S. Campbell (2001). Liquid-solid flows using smoothed particle hydrodynamics and the discrete element method. *Powder Technology 116*(2-3), 204–213.

Qian, Y. H., D. D'Humières, and P. Lallemand (1992). Lattice bgk models for navier-stokes equation. *Epl 17*(6), 479–484.

Radjai, F. and F. Dubois (2010). *Modélisation numérique discrète des matériaux granulaires*. ISTE.

Rajaratnam, N. (1976). Turbulent jets. *Developments in Water Science*.

Revuelta, A., A. L. Sánchez, and A. Liñán (2002). The virtual origin as a first-order correction for the far-field description of laminar jets. *Physics of Fluids 14*(6), 1821–1824.

Righetti, M. and C. Lucarelli (2007). May the Shields theory be extended to cohesive and adhesive benthic sediments? *Journal of Geophysical Research: Oceans 112*(5).

Schlichting, H. (1960). *Boundary Layer Theory* (4th ed.). McGraw-Hill.

Shields, A. (1936). Application of Similarity Principles and Turbulence Research to Bed-Load Movement. *Mitt. Preuss. Versuchsanst. Wasserbau Schiffbau 26*(5-24), 47.

Sidorchuk, A. (2005). Stochastic components in the gully erosion modelling. *Catena 63*(2-3), 299–317.

Sidorchuk, A. Y. (2001). Calculation of the Rate of Erosion in Soils and Cohesive Sediments. *Eurasian Soil Science 34*(8), 893–900.

Silvani, C., T. Désoyer, and S. Bonelli (2009). Discrete modelling of time-dependent rockfill behaviour. *International Journal for Numerical and Analytical Methods in Geomechanics 33*(5), 665–685.

Simon, A., N. Pollen-Bankhead, and R. E. Thomas (2011). *Development and application of a deterministic bank stability and toe erosion model for stream restoration*, Volume 194, pp. 453–474. American Geophysical Union (AGU).

Stanley, O. and S. James A. (1988). Fronts Propagating with Curvature Dependent Speed: Algorithms Based on Hamilton-Jacobi Formulations. *Journal of Computational Physics 79*, 12–49.

Streeter, V. L. and E. B. Wylie (1975). *Fluid mechanics* (6th ed.). New York: McGraw-Hill.

Sukop, M. and D. Thorne Jr (2006). *Lattice Boltzmann Modeling Lattice Boltzmann Modeling: an Introduction for Geoscientists and Engineers*. Springer.

Swope, W. C., H. C. Andersen, P. H. Berens, and K. R. Wilson (1982). A computer simulation method for the calculation of equilibrium constants for the formation of physical clusters of molecules: Application to small water clusters. *The Journal of Chemical Physics 76*(1), 637–649.

Tejada, I. G., L. Sibille, and B. Chareyre (2016). Role of blockages in particle transport through homogeneous granular assemblies. *Epl 115*(5), 54005.

Ternat, F., P. Boyer, F. Anselmet, and M. Amielh (2008). Erosion threshold of saturated natural cohesive sediments: Modeling and experiments. *Water Resources Research 44*(11).

Thoman, R. W. and S. L. Niezgoda (2008). Determining erodibility, critical shear stress, and allowable discharge estimates for cohesive channels: Case study in the powder river basin of Wyoming. *Journal of Hydraulic Engineering 134*(12), 1677–1687.

Ting, J. M. and B. T. Corkum (1992). Computational laboratory for discrete element geomechanics. *Journal of Computing in Civil Engineering 6*(2), 129–146.

Tran, D. K., N. Prime, F. Froiio, C. Callari, and E. Vincens (2017). Numerical modelling of backward front propagation in piping erosion by DEM-LBM coupling. *European Journal of Environmental and Civil Engineering 21*(7-8), 960–987.

Tritton, D. J. (1959). Experiments on the flow past a circular cylinder at low Reynolds numbers. *Journal of Fluid Mechanics 6*(4), 547–567.

Urso, M. E. D., C. J. J. Lawrence, and M. J. Adams (2002). A two-dimensional study of the rupture of funicular liquid bridges. *Chemical Engineering Science 57*(4), 677–692.

Van Prooijen, B. C. and J. C. Winterwerp (2010). A stochastic formulation for erosion of cohesive sediments. *Journal of Geophysical Research: Oceans 115*(1).

Van Rijn, L. C. (1984). Sediment pick-up functions. *Journal of Hydraulic Engineering 110*(10), 1494–1502.

Vardoulakis, I., M. Stavropoulou, and P. Papanastasiou (1996). Hydro-mechanical aspects of the sand production problem. *Transport in Porous Media 22*(2), 225–244.

Verhoff, A. (1963). The two-dimensional, turbulent wall jet with and without an external free stream. Technical Report 626, PRINCETON UNIV NJ.

Walder, J. S. (2016). Dimensionless erosion laws for cohesive sediment. *Journal of Hydraulic Engineering 142*(2), 4015047.

Wan, C. F. and R. Fell (2004). Laboratory tests on the rate of piping erosion of soils in embankment dams. *Geotechnical Testing Journal 27*(3), 295–303.

Wang, L., Z. L. Guo, and J. C. Mi (2014). Drafting, kissing and tumbling process of two particles with different sizes. *Computers and Fluids 96*, 20–34.

Wang, M., Y. T. Feng, Y. Wang, and T. T. Zhao (2017). Periodic boundary conditions of discrete element method-lattice Boltzmann method for fluid-particle coupling. *Granular Matter 19*(3), 43.

Wautier, A., S. Bonelli, and F. Nicot (2017). Scale separation between grain detachment and grain transport in granular media subjected to an internal flow. *Granular Matter 19*(2), 22.

Winterwerp, J. C. and W. G. M. Van Kesteren (2004). *Introduction to the Physics of Cohesive Sediment Dynamics in the Marine Environment*, Volume 56. Elsevier.

Yang, G. C., L. Jing, C. Y. Kwok, and Y. D. Sobral (2018). A comprehensive study of coupled LBM-DEM with immersed moving boundary. *arXiv e-prints*, arXiv:1809.07008.

Yu, D., R. Mei, L. S. Luo, and W. Shyy (2003). Viscous flow computations with the method of lattice Boltzmann equation. *Progress in Aerospace Sciences 39*(5), 329–367.

Zhang, L., M. Peng, D. Chang, and Y. Xu (2016). *Internal Erosion in Dams and Their Foundations*, Chapter 6, pp. 67–126. John Wiley & Sons, Ltd.

Zhou, Y. C., B. H. Xu, A. B. Yu, and P. Zulli (2001, Jul). Numerical investigation of the angle of repose of monosized spheres. *Phys. Rev. E 64*, 021301.

Zhu, J. C., C. J. Gantzer, S. H. Anderson, R. L. Peyton, and E. E. Alberts (2001). Comparison of concentrated-flow detachment equations for low shear stress. *Soil and Tillage Research 61*(3-4), 203–212.

Zhu, Y. H., J. Y. Lu, H. Z. Liao, J. S. Wang, B. L. Fan, and S. M. Yao (2008). Research on cohesive sediment erosion by flow: An overview. *Science in China, Series E: Technological Sciences 51*(11), 2001–2012.

Zou, Q. and X. He (1997). On pressure and velocity boundary conditions for the lattice Boltzmann BGK model. *Physics of Fluids 9*(6), 1591–1598.